

# Precision Bragg spectroscopy of the density and spin response of a strongly interacting Fermi gas

*A thesis submitted for the degree of  
Doctor of Philosophy*

by

**Sascha Hoinka**



*Centre for Quantum and Optical Science  
Faculty of Science, Engineering and Technology  
Swinburne University of Technology  
Melbourne, Australia*

March, 2014



# Declaration

I, Sascha Hoinka, declare that this thesis entitled:

**“Precision Bragg spectroscopy of the density and spin response of a strongly interacting Fermi gas”**

is my own work and has not been submitted previously, in whole or in part, in respect of any other academic award.

Sascha Hoinka

Centre for Quantum and Optical Science (CQOS)  
Faculty of Science, Engineering and Technology  
Swinburne University of Technology  
Melbourne, Australia

March 3rd, 2014



# Abstract

This thesis presents precision measurements on strongly interacting Fermi gases using two-photon Bragg spectroscopy at high momentum ( $k = 4.2 k_F$ ). An optically trapped gas of  ${}^6\text{Li}$  atoms, equally populated in two hyperfine spin states, is brought to degeneracy by laser and evaporative cooling. Strong particle-particle interactions are established near the broad 832 G Feshbach scattering resonance. Such a setting constitutes a paradigm for fermionic many-body systems interacting via a short-range potential and large scattering length. Bragg spectroscopy is used to make precise measurements of the density and spin dynamic structure factors,  $S(k, \omega)$ . Improved methods for probing and analysing the Bragg spectra has led to two major results with low experimental uncertainty.

Firstly, I will present a high-precision determination of Tan's universal contact parameter in a strongly interacting Fermi gas [Hoi13]. The contact governs the high-momentum (short-range) and high-frequency (short-time) properties of these systems and can be inferred from the integrated density-density response giving the static structure factor,  $S(k)$ . For a harmonically trapped gas at unitarity, we find the contact to be  $3.06 \pm 0.08$  at a temperature of 0.08 of the Fermi temperature. This result also provides a new benchmark for the zero-temperature homogeneous contact which we have estimated to be  $3.17 \pm 0.09$ , and compared this with recent predictions from approximate strong-coupling theories including quantum Monte Carlo and many-body  $T$ -matrix calculations.

In a second series of measurements, I will describe the first experimental investigation of the dynamic spin response of a Fermi gas with strong interactions [Hoi12]. At large  $k$ , this observable is identical to the imaginary part of the dynamic spin susceptibility,  $\chi_S''(k, \omega)$ . By varying the detuning of the Bragg lasers, we show that either the spin or the density response can be measured independently allowing full characterisation of the spin-parallel and spin-antiparallel components of the dynamic and static structure factors. This opens the way to quantifying  $S(k)$  using Bragg spectroscopy at any momentum. Furthermore, we found that the spin response is suppressed at low energies due to pairing and displays a universal high-frequency tail, decaying as  $\omega^{-5/2}$ , where  $\hbar\omega$  is the probe energy.

# Contents

<b>Declaration</b>	<b>iii</b>
<b>Abstract</b>	<b>v</b>
<b>Contents</b>	<b>vi</b>
<b>List of Figures</b>	<b>viii</b>
<b>List of Tables</b>	<b>x</b>
<b>1 Introduction</b>	<b>11</b>
<b>2 Strongly interacting Fermi gases</b>	<b>15</b>
2.1 Introduction . . . . .	15
2.2 Degenerate ideal Fermi gases . . . . .	17
2.3 Interactions in ultracold Fermi gases . . . . .	20
2.3.1 Low-energy elastic collisions . . . . .	21
2.3.2 The broad Feshbach resonance of ${}^6\text{Li}$ . . . . .	23
2.3.3 BCS-BEC crossover – from weak to strong attraction . . . . .	28
2.3.4 Universal properties of Fermi gases . . . . .	34
2.3.5 Exact universal relations and Tan’s contact parameter . . . . .	36
2.4 Summary . . . . .	41
<b>3 Experimental setup and procedure</b>	<b>43</b>
3.1 Introduction . . . . .	43
3.2 Trapping neutral atoms . . . . .	43
3.2.1 Focussed-beam optical dipole traps . . . . .	44
3.2.2 Magnetic trapping with Feshbach coils . . . . .	46

3.3	Production of ultracold ${}^6\text{Li}$ quantum gases . . . . .	48
3.3.1	Vacuum system . . . . .	48
3.3.2	Laser layout and frequencies . . . . .	51
3.3.3	Cooling and preparation . . . . .	59
3.4	The new imaging system . . . . .	62
3.4.1	Absorption imaging . . . . .	63
3.4.2	Lasers and imaging optics . . . . .	67
3.4.3	Camera settings . . . . .	70
3.4.4	Calibrating the camera . . . . .	74
3.5	Summary . . . . .	75
<b>4</b>	<b>Precision measurement of the universal contact at unitarity</b>	<b>77</b>
4.1	Introduction . . . . .	77
4.2	Probing the density-density response using Bragg spectroscopy . . . . .	78
4.2.1	Bragg spectroscopy and dynamic structure factors . . . . .	78
4.2.2	Measuring density dynamic structure factors and the contact . . . . .	82
4.2.3	The new Bragg laser setup and frequency control . . . . .	89
4.2.4	Bragg transitions of ground state ${}^6\text{Li}$ atoms at high magnetic fields . . . . .	91
4.2.5	Bragg linearity measurements . . . . .	94
4.3	Characterisation of the trapped ${}^6\text{Li}$ gas . . . . .	97
4.3.1	Atomic recoil frequency and Bragg wave vector . . . . .	97
4.3.2	Image magnification . . . . .	99
4.3.3	Summary of the trapped cloud parameters . . . . .	102
4.4	Results at unitarity and the BEC-side of the crossover . . . . .	106
4.4.1	Bragg excitation spectra of a trapped strongly interacting Fermi gas . . . . .	106
4.4.2	Determining the trap-averaged contact $\mathcal{I}/(Nk_F)$ . . . . .	112
4.4.3	Extracting the homogeneous contact density $\mathcal{C}/(nk_F)$ at $T = 0$ . . . . .	115
4.5	Summary . . . . .	117
<b>5</b>	<b>Spin-Bragg spectroscopy of a strongly interacting <math>{}^6\text{Li}</math> gas</b>	<b>119</b>
5.1	Introduction . . . . .	119
5.2	Probing the spin response . . . . .	120

5.2.1	Bragg perturbation including finite laser detunings . . . . .	123
5.2.2	Energy level diagram for spin-Bragg scattering $^6\text{Li}$ atoms . . . . .	127
5.2.3	Bragg linearity for spin-response measurements . . . . .	128
5.3	Results at unitarity and the BEC-side of the Feshbach resonance . . . . .	131
5.3.1	Measuring spin dynamic structure factors . . . . .	132
5.3.2	Spin-parallel and spin-antiparallel responses . . . . .	135
5.3.3	Interpretation of the same- and opposite-spin response functions . . . . .	136
5.3.4	Universal behaviour of the high-frequency tail . . . . .	138
5.4	Summary . . . . .	140
<b>6</b>	<b>Summary and Outlook</b>	<b>141</b>
<b>A</b>	<b>Electronic level structure of <math>^6\text{Li}</math></b>	<b>147</b>
<b>B</b>	<b>Low-cost 4-channel digital direct synthesiser (DDS)</b>	<b>151</b>
	<b>References</b>	<b>155</b>
	<b>Publication list</b>	<b>171</b>
	<b>Acknowledgements</b>	<b>173</b>

## List of Figures

2.3.1	Tuning interactions via a magnetic Feshbach resonance . . . . .	24
2.3.2	Phase diagram of the BCS-BEC crossover . . . . .	29
3.3.1	Schematic of the vacuum system and the position of the magnetic coils . . . . .	49
3.3.2	Laser frequencies for laser cooling, imaging and Bragg scattering $^6\text{Li}$ atoms . . . . .	52
3.3.3	Schematic of the main and Zeeman diode laser systems . . . . .	54
3.3.4	New optical design for the MOT laser generation . . . . .	56

3.3.5 Laser setup for the optical dipole traps . . . . .	58
3.4.1 Schematic of the imaging laser setup . . . . .	68
3.4.2 Optical layout for the top imaging system . . . . .	69
3.4.3 Configuration of the CCD array in fast kinetics mode . . . . .	71
3.4.4 Pictorial diagram of the circuit generating short imaging pulses . . . . .	72
3.4.5 Timing diagram of the image sequence in fast kinetic mode . . . . .	72
3.4.6 Setup for the intensity calibration of the CCD sensor . . . . .	74
4.2.1 Schematic diagram of Bragg spectroscopy . . . . .	79
4.2.2 Absorption images and line profiles of a Bragg scattered unitary Fermi gas .	84
4.2.3 Comparison of conventional and differential centre-of-mass displacements .	86
4.2.4 Schematic of the Bragg laser setup and AOM frequencies . . . . .	90
4.2.5 Bragg-laser transitions for probing the density response . . . . .	92
4.2.6 Bragg lattice of parallel vs. orthogonal linearly polarised laser beams . . . .	93
4.2.7 Density-Bragg linearity measurements at 833G . . . . .	95
4.2.8 Density-Bragg linearity measurements at 783G . . . . .	96
4.3.1 Density line profiles and Bragg spectrum of a noninteracting Fermi gas . . .	99
4.3.2 Bragg spectroscopy as a tool for determining the image magnification . . .	101
4.3.3 Radial trapping resonance frequency of the optical dipole trap . . . . .	103
4.4.1 Density-density response of a strongly interacting Fermi gas at 783 and 833 G	107
4.4.2 Energy-momentum dispersion of a unitary Fermi gas in the density channel	110
4.4.3 Comparison of the static structure factor $S(k)$ with QMC calculations . . .	112
4.4.4 The trap-averaged contact parameter $\mathcal{I}$ as a function of $1/(k_F a)$ . . . . .	113
4.4.5 Homogeneous contact versus temperature for a unitary Fermi gas (overview)	116
5.2.1 Schematic illustration of probing the density and spin response . . . . .	122

5.2.2 Bragg-laser transitions for probing the spin response . . . . .	128
5.2.3 Spin-Bragg linearity measurements at 833G . . . . .	130
5.2.4 Spin-Bragg linearity measurements at 783G . . . . .	131
5.3.1 Spin and density dynamic structure factors of a two-component Fermi gas .	134
5.3.2 Spin-parallel and spin-antiparallel components at 833G . . . . .	136
5.3.3 Spin-parallel and spin-antiparallel components at 783G . . . . .	137
5.3.4 Universal frequency behaviour of $S_{\uparrow\downarrow}(k, \omega)$ . . . . .	138
A.0.1 Electronic level structure of a ${}^6\text{Li}$ atom at low magnetic field . . . . .	148
A.0.2 Electronic level structure of a ${}^6\text{Li}$ atom at high magnetic field . . . . .	149
B.0.1 Modified circuit diagram of the AD9959 DDS evaluation board . . . . .	152
B.0.2 Circuit of the electrically isolated BNC input for triggering the DDS . . . .	153

## List of Tables

4.1 Comparison of recently published values of the trapped contact parameter .	114
--	-----

# 1. Introduction

Over the last decade, ultracold atoms have established a new paradigm for studying strongly correlated many-body systems. Experiments on these novel “quantum materials” have reached a level of precision and complexity to address very specific problems in many-body physics. In particular, the realisation of fermionic superfluidity has connected the physics of ultracold gases to a vast range of research areas, from nuclear matter [Boh58] and neutron stars [Mig59] to superfluidity [Vol90], high-temperature superconductors [Che05] and even the quark-gluon plasma [Alf08] as well as string theory [Sch09].

Central to this are ultracold gases of neutral Fermi atoms which provide a versatile platform to study the crossover from a Bardeen-Cooper-Schrieffer (BCS) superfluid to a Bose-Einstein condensate (BEC) of composite bosons. This crossover is fascinating from a fundamental point of view as it involves the continuous evolution of a system whose physics changes from being dominated primarily by fermionic degrees of freedom to one dominated by bosonic degrees of freedom. The essential ingredient of the crossover are spin-1/2 particles in two (distinguishable) quantum states with an attractive interaction. Due to the attraction, constituent fermions (be they electrons, nucleons or atoms) can pair up providing access to bosonic degrees of freedom which are key to superfluidity and Bose condensation. The nature of the pairing varies widely with the strength of the attractive interaction relative to the Fermi energy.

Before the mid 2000s, nearly all systems that were known to lie in the BCS-BEC crossover existed essentially near one of the limiting cases. For example, Bose condensation was first encountered in superfluid  $^4\text{He}$  (He-II phase) [Kap38, Lon38], where a helium atom is comprised of many fermions bound together so tightly that in usual scenarios, fermionic degrees of freedom are inaccessible and instead the many-body behaviour is completely governed by interactions between point-like bosons, which corresponds to a system in the BEC limit. On the other hand, the BCS theory of superconductivity relies on the formation of weakly bound Cooper pairs on top of a Fermi sea whose spatial extent is much larger than the mean distance between fermions, such as encountered in an electron gas in conventional superconductors in some metals [Bar57] or a pair superfluid

## 1. Introduction

in fermionic  $^3\text{He}$  [Vol90]. Yet, it was shown that the ground state in the limits of tightly bound bosonic molecules (point like bosons) and a superfluid of Cooper pairs are smoothly connected [Kel68, Eag69, Leg80, Noz85].

Ultracold Fermi gases, whose interactions can readily be tuned via a Feshbach resonance, are different from all previous known examples of crossover materials in that the strength of the attractive interaction can be tuned to cover the full crossover. The atomic density ( $n$ ) and kinetic energy in such systems are sufficiently low so that two-body collisions encompass all relevant interactions. The associated  $s$ -wave scattering length ( $a$ ), determining the strength of the short-range scattering potential, can be conveniently controlled by an external magnetic field. Moreover, as the scattering properties are subject to Fermi statistics, the decay of pairs is strongly suppressed by the Pauli exclusion principle, allowing a stable many-body system to be scrutinised by precision measurements. Experimentally, ultracold gases near the Feshbach resonance rose to prominence with the creation of (Feshbach) molecules [Joc03b, Gre03, Zwi03] as well as the observation [Bar04, Zwi04, Reg04, Bou04] and characterisation [Kin04, Par05, Zwi05] of Fermi gases over the BCS-BEC crossover.

The range of the interaction potential for cold atoms is extremely small compared to other length scales, such as the scattering length  $a$ , the thermal deBroglie wavelength  $\lambda_{\text{dB}}$  and the mean separation between particles  $n^{-1/3}$ , meaning interactions can be treated as being of zero range. Consequently, the Fermi gas realises a universal system in the sense that microscopic interaction details play no role for the physical description, and the gas behaves like any other fermionic many-body system with a similar short-range behaviour irrespective of the energy and temperature scale [Ho04, Hau07, Hu07, Ada12].

Most significantly, one can readily tune to the unitarity limit, which lies in the middle of the crossover, where the  $s$ -wave scattering length diverges and no longer plays any role in the behaviour of the system. At this point, the elastic collision cross section takes on its maximum value allowed by quantum mechanics and provides a laboratory scale testbed for theories of strongly correlated many-body quantum systems which are notoriously difficult to validate [Blo08, Gio08].

In 2008, several exact theoretical relations were found for strongly interacting Fermi gases (now known as the Tan relations) that relate the microscopic properties to macroscopic parameters such as total energy and pressure [Tan08a, Tan08b, Tan08c]. These relations involve a single parameter, the universal contact parameter  $\mathcal{I}$ , which encapsulates all of the difficult many-body properties into a single number. The determination of this parameter has been a central challenge to researchers working with ultracold Fermi

gases in the past few years [Par05, Wer09, Kuh10, Ste10, Sag12] with different approaches (both theoretical and experimental) leading to different outcomes [Hu11].

In experimental physics, one of the simplest approaches one can take to learn about the structure of a new system is to scatter particles from it. A well known example is the inelastic scattering of neutrons from superfluid  $^4\text{He}$  where a collimated beam of neutrons is directed to the sample and the energy spectrum of the scattered neutrons in some direction is recorded [Gri93]. This gives direct access to the system's response as a function of the momentum and energy transfer of the probe particle. The measurable quantity is the dynamic structure factor which provides the maximum information possible in inelastic scattering experiments [Pin66]. Measurements in  $^4\text{He}$  not only revealed the condensate fraction in this quantum liquid but also facilitated the understanding of collective and quasiparticle excitations as well as correlations in strongly interacting many-body systems [Gly92].

We apply this principle here in the form of optical Bragg spectroscopy [Mar88, Ste99] to explore the response of a Fermi gas of lithium-6 ( $^6\text{Li}$ ) atoms in the strongly interacting regime of the BCS-BEC crossover to weak perturbations of the atomic density and spin density of the system. This allows us to make precise measurements of response functions from which we can determine the density dynamic structure factor and also the dynamic spin susceptibility. In cold atomic gases, measurements of the dynamic structure factor also provide a way to measure the universal contact parameter [Hu10b]. In superconductors, the spin susceptibility can provide information on pair-breaking excitations [Ran92] and can be used with cold atoms to check for the existence of pseudogap pairing, known to occur in high-temperature superconductors [Pla10].

There is a significant degree of uncertainty in theoretical predictions for the temperature dependence of pair formation [Str09, Mag11, Wla13] and the universal contact parameter [Com06a, Hau09, Gou10, Pal10, Dru11, Hu11] in a Fermi gas at unitarity, and the work in this thesis takes steps along the experimental path towards addressing these. Specifically we provide the most accurate determination of the contact parameter to date with an error bar at the few percent level as well as demonstrating a new type of Bragg spectroscopy, capable of directly measuring the dynamic spin response function which probes pair-breaking excitations exclusively.

## Thesis outline

The measurements described in this thesis utilise an apparatus for producing two-component ultracold Fermi gases and a setup for performing two-photon Bragg spectroscopy at

## 1. Introduction

high momentum. Based on the existing  ${}^6\text{Li}$  experiment at Swinburne University, several developments and upgrades were required to yield the results presented in the chapters four and five, all detailed in the thesis at hand which is structured as follows:

**Chapter 2** summarises main physical aspects of ultracold gases with fermionic  ${}^6\text{Li}$  atoms. After recalling important ideal gas properties, a brief discussion follows on two-component Fermi gases with Feshbach tunable  $s$ -wave interactions, used for the realisation and investigation of universal Fermi gases in the BCS-BEC crossover.

**Chapter 3** provides details on the apparatus and experimental procedure required for cooling and preparing atomic  ${}^6\text{Li}$ . The focus lies on upgrades and new developments in the setup, which were introduced in the course of completing this thesis. In addition, all steps of a typical experimental cycle will be explained.

**Chapter 4** presents the first main result, the precise determination of the contact of a strongly interacting Fermi gas in a low-temperature harmonic trap. Density-density responses at high Bragg momentum were measured to obtain dynamic and static structure factors used to obtain the contact. The result at unitarity serves as a reliable estimate of the homogeneous contact at zero temperature. Also included are procedural details on the performed Bragg measurements and data analysis that significantly reduces experimental uncertainties.

**Chapter 5** presents the second major result, the first measurements of the spin dynamic structure factor of a strongly interacting Fermi gas. Combined with the density response, this gives access to the structure factors of the individual same- and opposite-spin pair correlations in the gas. We have observed universal high-frequency tails which are predicted to appear at high momenta. A derivation based on a simple hamiltonian for the Bragg perturbation is given to show how the detunings of the Bragg lasers lead to the measured response functions, giving a probing scheme that directly applies to  ${}^6\text{Li}$  gas in the crossover.

**Chapter 6** summarises the key results described in the thesis and outlines possible future experiments on two-component Fermi gases using optical Bragg spectroscopy.

The result chapters four and five are based on my publications and hence are written in a more or less self-contained form. This inevitably leads to some instances of repetition which is intentional for the sake of readability. Additional material beyond the published text has been included in this thesis on experimental procedures, data analysis, mathematical derivations and a detailed physical interpretation of the results. Also, typical values of physical quantities used in the experiment are provided throughout the thesis.

## 2. Strongly interacting Fermi gases

### 2.1. Introduction

In this chapter, I will present basic facts on dilute atomic Fermi gases with tunable  $s$ -wave interactions. The discussion centres around the physical system we study in optical Bragg scattering experiments: A trapped, two-component, spin-balanced gas of  ${}^6\text{Li}$  atoms at nano-Kelvin temperatures, realising a fermionic superfluid with “ $s$ -wave symmetry”.

Atom-atom interactions in such gases are of short range; thus, in three dimensions (3D) they can be parameterised by the dimensionless interaction parameter,  $1/(k_F a)$ . By means of a Feshbach resonance, the  $s$ -wave scattering length  $a$  can be tuned to literally any value [Chi10]. The alkali  ${}^6\text{Li}$  in a mixture of its two lowest hyperfine states (cf. appendix A) has an extraordinarily broad (300 G) magnetic-field Feshbach resonance (located at 832 G) allowing for excellent control over the two-body interaction strength. A Fermi gas is said to be strongly interacting when  $|a|n^{-1/3} > 1$ , where  $n$  is the density, that is,  $a$  exceeds the mean interparticle spacing, which is of order of the inverse Fermi wave vector  $n^{-1/3} \simeq k_F^{-1}$ .

A gas of two types of fermions with attractive interactions can undergo pairing below a threshold temperature and ultimately form a pair condensate which exhibits superfluid properties. Depending on  $1/(k_F a)$ , the gas dramatically changes its behaviour from being dominated by fermionic degrees of freedom to bosonic degrees of freedom. Understanding the physics of this nontrivial many-body system is subject of the famous Bardeen-Cooper-Schrieffer (BCS) to Bose-Einstein condensation (BEC) crossover problem [Leg06].

Ultracold Fermi gases are dilute systems with atoms of low kinetic energy<sup>1</sup>. Atoms in a mixture of two different quantum states hence only collide pairwise (to lowest order). Interactions between three or more fermions are suppressed by the Pauli exclusion principle

---

<sup>1</sup>The typical density in a dilute atomic gas is  $n \sim 10^{14} \text{ cm}^{-3}$ , corresponding to a mean interparticle spacing of  $n^{-1/3} \sim 1 \text{ } \mu\text{m}$ . “Ultracold” usually refers to temperatures below the recoil temperature [Suo96], which for  ${}^6\text{Li}$  is  $3.5 \text{ } \mu\text{K}$  (although other texts are more generous using  $< 1 \text{ mK}$ ). The collision energy in a trapped Fermi gas is typically of order of the Fermi energy,  $E_F \sim 2\pi \times 10 \text{ kHz}$  or  $\sim 500 \text{ nK}$ .

## 2. Strongly interacting Fermi gases

due to the requirement of an overall antisymmetric wavefunction in the collision process. As far as short-range physics is concerned, this means that the complicated many-body behaviour of the system, even in the strongly interacting regime, can be separated into an effective two-body and a many-body problem. The two-body physics only takes into account short-range interactions between atoms through  $a$  while the many-body aspects, determining the macroscopic behaviour of the gas, can be captured in so-called universal functions, which in turn depend on the two-body parameter  $1/(k_F a)$  [Zha09].

So far, the BCS-BEC crossover has been experimentally realised in  $^6\text{Li}$  and  $^{40}\text{K}$ . Pairing in these gases (especially in  $^6\text{Li}$ ) is highly stable due to Pauli suppression of three-body losses [Pet04], allowing for a thorough characterisation of thermodynamic, transport and spectroscopic properties of these systems. Two physical regimes are very appealing from a theoretical point of view as they can be realised and investigated with these alkalis under well controlled laboratory conditions: The universal regime and the unitarity limit [Bru04].

In universal systems, as mentioned above, two-body interactions are completely specified by the single parameter  $a$ . In the unitarity limit, where atom-atom interactions are maximal,  $a$  diverges and drops out to leave  $n^{-1/3}$  and the thermal wavelength  $\lambda_{\text{dB}}$ , linked to the respective density and temperature of the gas, as the only length scales required for the physical description. In both cases, the exact details of the short-range interactions are not relevant; in the latter case, interactions are said to be scale invariant.

I start section 2.2 by briefly summarising some basics of ideal Fermi gases and then proceed to Fermi gases with Feshbach-tunable two-body interactions in section 2.3. This section also gives a qualitative overview of the phase diagram of the BCS-BEC crossover to illustrate fundamental properties of pairing in such a gas. Also, I will discuss universality in Fermi gases and Tan's contact parameter, a central many-body quantity that describes the short-range properties of a universal gas and plays key role in a set of exact relations. Where appropriate I will put the discussion into context of two-photon Bragg spectroscopy.

The field of strongly interacting Fermi gases has experienced dramatic experimental and theoretical progress over the past decade. An overview and a discussion of the main results are presented in the recently published textbooks [Ing07, Lev12, Zwe12, Sal13], which I highly recommend "to get the picture". The discussion in this chapter only scratches the surface of course and only presents facts required to help understand the results in chapters four and five. Beside these texts, I will also follow [Lew07, Blo08, Gio08, Ada12, Ran14] where the interested reader can find much more information, detailed explanations, derivations and further references. Additional references will be given throughout the chapter.

## 2.2. Degenerate ideal Fermi gases

An ideal Fermi gas has no collisions. At zero temperature, however, it provides important energy ( $E_F$ ), temperature ( $T_F$ ) and length scales ( $k_F^{-1}$ ) commonly used to parameterise an interacting Fermi gas in the BCS-BEC crossover. In this section, I will summarise key results for both a homogeneous and a harmonically trapped degenerate noninteracting 3D Fermi gas. More details on ideal fermionic systems, such as finite temperature results, can be found in numerous textbooks and articles, see for instance [But97, Pit03, Ket07].

A gas of indistinguishable fermionic atoms, or any other half-integer spin particles, are degenerate for temperatures  $T$  below the Fermi temperature  $T_F$  as its phase-space density

$$n_\sigma \lambda_{\text{dB}}^3 \gtrsim 1, \quad (2.2.1)$$

where  $\lambda_{\text{dB}} = \sqrt{2\pi\hbar^2/(mk_B T)}$  is the thermal wavelength,  $m$  the atoms' mass,  $\hbar$  the reduced Planck constant,  $k_B$  Boltzmann's constant and  $n_\sigma$  the density of atoms in a single spin state  $|\sigma\rangle$ . Then, the spatial extent of the de Broglie matter waves, representing one independent quantum state per atom, matches the interparticle separation  $n_\sigma^{-1/3}$ . The transition from a classical to a degenerate Fermi gas occurs gradually and is completed at  $T = 0$ .

By contrast, a gas of bosons (integer spin) undergoes a phase transition signalling the sudden onset of degeneracy at a critical temperature. In a BEC,  $\lambda_{\text{dB}}$  exceeds the interparticle spacing, and bosons prefer to macroscopically occupy the lowest single-particle momentum (ground) state to form a giant matter wave. This phase transition is a statistical effect requiring no interactions; thus, it also occurs in an ideal Bose gas [Ket99, Pit03, Pet08].

The quantum statistics of a Fermi gas is governed by the Fermi-Dirac distribution,  $f(\varepsilon, T)$ , which reflects the fundamental requirement for fermions to have an overall anti-symmetric many-body wavefunction. In thermal equilibrium, the mean occupation number of noninteracting fermions in a single-particle state of energy  $\varepsilon$  is given by

$$f(\varepsilon, T) = \frac{1}{e^{\beta(\varepsilon-\mu)} + 1}, \quad (2.2.2)$$

where  $\beta = 1/(k_B T)$  and  $\mu(n_\sigma, T)$  is the chemical potential. The value of  $f(\varepsilon, T)$  ranges between zero and one reflecting the Pauli exclusion principle. Note, a dilute gas whose properties are determined by quantum statistics is also referred to as “quantum liquid” [Leg06].

In the classical limit,  $e^{\beta(\varepsilon-\mu)} \gg 1 \forall \varepsilon$  which is equivalent to  $n_\sigma \lambda_{\text{dB}}^3 \ll 1$ . This can be realised, for example, by diluting the gas or raising its temperature. Then, the probability of an atom occupying a state with energy  $\varepsilon$  is much less than one, and on average no two atoms will take the same energy. The Fermi nature therefore no longer plays a role.

## 2. Strongly interacting Fermi gases

At zero temperature,  $f(\varepsilon, 0)$  in equation 2.2.2 is unity for energies less than  $\mu$  and zero otherwise, that is, the Fermi sea is filled up with one atom per available energy state, starting from the lowest energy. The Fermi energy  $E_F = k_B T_F$  is defined as

$$E_F \equiv \mu(n_\sigma, T = 0), \quad (2.2.3)$$

fixed by the density and refers to the energy of the highest occupied state in the gas.

In the semiclassical Thomas-Fermi description, the energy in equation 2.2.2 of a single atom with free kinetic energy confined by an external trapping potential  $U(\mathbf{r})$  is given by

$$\varepsilon(\mathbf{r}, \mathbf{p}) = \frac{\mathbf{p}^2}{2m} + U(\mathbf{r}), \quad (2.2.4)$$

where  $\mathbf{r} = (x, y, z)$  is the position and  $\mathbf{p} = (p_x, p_y, p_z)$  the momentum of the atom. This is the local density approximation (LDA) which assumes  $U(\mathbf{r})$  to vary slowly on a scale of the interparticle distance equivalent to a gas with a locally homogeneous density  $n_\sigma = n_\sigma(\mathbf{r})$ . It further assumes the spacing of the energy levels of  $U(\mathbf{r})$  to be much smaller than the chemical potential. The LDA is a convenient way to account for an external confinement in theoretical calculations on uniform gases in the thermodynamic limit (i.e. large  $N_\sigma$ ).

The total particle number and total energy of the system is then determined by the respective integrals

$$N_\sigma(T) = \int D(\varepsilon) f(\varepsilon, T) d\varepsilon, \quad (2.2.5)$$

$$E(T) = \int D(\varepsilon) f(\varepsilon, T) \varepsilon d\varepsilon, \quad (2.2.6)$$

valid in the limit of large atom number. The type of confinement determines the density of states<sup>2</sup>  $D(\varepsilon)$ . Equations 2.2.5 and 2.2.6 provide a normalisation condition for the equation of state,  $\mu(n_\sigma, T)$ , by fixing  $N_\sigma$ , and they can be used to obtain all other thermodynamic quantities, such as free energy  $F$ , pressure  $P$ , entropy  $S$  or specific heat  $C_V$ .

We now turn to a homogeneous ideal Fermi gas at  $T = 0$ . The trapping potential  $U(\mathbf{r})$  of such a system is a box of volume  $V$  with infinite walls enclosing  $N_\sigma$  uniformly distributed atoms giving a constant density,  $n_\sigma = N_\sigma/V$ . In momentum space, the Fermi wavenumber is defined by  $k_F = \sqrt{2mE_F/\hbar^2}$ , which corresponds to the radius of a fully occupied sphere. The density  $n_\sigma = k_F^3/(6\pi^2)$  of this ‘‘Fermi sphere’’ is simply the ratio of its volume  $4\pi k_F^3/3$  and the number of available phase-space cells  $(2\pi)^3$  within the sphere,

---

<sup>2</sup>In 3D, for a uniformly distributed gas  $D(\varepsilon) \propto \sqrt{\varepsilon}$  and for a gas in a harmonic trap  $D(\varepsilon) \propto \varepsilon^2$ .

in units of  $\hbar^3$ . By this we can express the respective Fermi energy and wave vector as

$$E_{\text{F}}^{\text{hom}} = \frac{\hbar^2}{2m} (6\pi^2 n_{\sigma})^{2/3} \equiv \mu(n_{\sigma}), \quad (2.2.7)$$

$$k_{\text{F}}^{\text{hom}} = (6\pi^2 n_{\sigma})^{1/3}. \quad (2.2.8)$$

From equation 2.2.6 two important thermodynamic ideal gas results can be computed, which are the respective mean energy per particle and pressure,

$$\frac{E}{N_{\sigma}} = \frac{3}{5} E_{\text{F}}, \quad (2.2.9)$$

$$P = - \left( \frac{\partial E}{\partial V} \right)_{S, N_{\sigma}} = \frac{2}{5} E_{\text{F}} n_{\sigma}, \quad (2.2.10)$$

taking finite values at zero temperature due to the Pauli exclusion principle. This contrasts the classical description where both quantities go to zero as  $T \rightarrow 0$  ( $E_{\text{cl}} = 3N_{\sigma}k_{\text{B}}T/2$ ).

A second important example is an ideal Fermi gas in a quadratic potential given by an experimentally easy to realise harmonic trap,

$$U(\mathbf{r}) = \frac{m}{2} (\omega_x^2 x^2 + \omega_y^2 y^2 + \omega_z^2 z^2), \quad (2.2.11)$$

leading to spatially varying density  $n_{\sigma}(\mathbf{r})$ . The Fermi energy can be obtained in the LDA by introducing a local Fermi momentum  $\hbar k_{\text{F}}(\mathbf{r})$  in equation 2.2.4 and by setting  $\varepsilon \equiv E_{\text{F}}$ . In combination with equation 2.2.8 we then can define the local density

$$n_{\sigma}(\mathbf{r}) = \frac{1}{6\pi^2} \left[ \frac{2m}{\hbar^2} \mu(\mathbf{r}) \right]^{3/2}, \quad (2.2.12)$$

where the trapping potential is absorbed in  $\mu(\mathbf{r}) = \mu_0 - U(\mathbf{r})$ , thereby defining  $\mu_0 \equiv E_{\text{F}}$  as the chemical potential in the trap centre fixed by the density. Integrating equation 2.2.12, as per  $N_{\sigma} = \int n_{\sigma}(\mathbf{r}) \, \text{d}\mathbf{r}$ , the Fermi energy and wavenumber at  $T = 0$  reads

$$E_{\text{F}} = \hbar\bar{\omega} (6N_{\sigma})^{1/3}, \quad (2.2.13)$$

$$k_{\text{F}} = \sqrt{\frac{m\bar{\omega}}{\hbar}} (48N_{\sigma})^{1/6}, \quad (2.2.14)$$

where  $\bar{\omega} = (\omega_x \omega_y \omega_z)^{1/3}$  is the geometrical mean trapping frequency. In this case, the mean ground-state energy of noninteracting fermions in a harmonic trap is

$$\frac{E}{N_{\sigma}} = \frac{3}{4} E_{\text{F}}. \quad (2.2.15)$$

The zero-temperature spatial profile of the density in the harmonic trap is given by the Thomas-Fermi distribution

$$n_{\sigma}(\mathbf{r}) = \frac{8N_{\sigma}}{\pi^2 R_{\text{Fx}} R_{\text{Fy}} R_{\text{Fz}}} \left[ 1 - \left( \frac{x}{R_{\text{Fx}}} \right)^2 - \left( \frac{y}{R_{\text{Fy}}} \right)^2 - \left( \frac{z}{R_{\text{Fz}}} \right)^2 \right]^{3/2}, \quad (2.2.16)$$

## 2. Strongly interacting Fermi gases

where  $R_{\text{F}x,y,z} = \sqrt{\hbar\bar{\omega}/(m\omega_{x,y,z}^2)(48N_\sigma)^{1/6}}$  are the Thomas-Fermi radii at which the cloud density goes to zero. The corresponding momentum distribution is

$$n_\sigma(\mathbf{p}) = \frac{8N_\sigma}{\pi^2(\hbar k_{\text{F}})^3} \left[ 1 - \left( \frac{|\mathbf{p}|}{\hbar k_{\text{F}}} \right)^2 \right]^{3/2}, \quad (2.2.17)$$

which can be observed in an expanding cloud after switching off the trap. Note that the profile of  $n_\sigma(\mathbf{p})$  for an ideal gas is always isotropic even in an anisotropic harmonic trap; thus, possible observed deviations from isotropy would suggest the presence of interactions.

A fully spin-polarised  ${}^6\text{Li}$  or  ${}^{40}\text{K}$  Fermi gas effectively realises an ideal gas in ultracold dilute gas experiments at typical temperatures of  $\ll 1 \mu\text{K}$  as the only energetically allowed  $s$ -wave collisions are Pauli suppressed. Higher order partial-wave scattering can be neglected ( $p$ -wave collisions diminish below  $\sim 6 \text{ mK}$  for  ${}^6\text{Li}$  or  $\sim 100 \mu\text{K}$  for  ${}^{40}\text{K}$  [Ket07]). In this sense, the only effective “interaction” in such a gas is weak Pauli repulsion.

Quantum degeneracy in an alkali Fermi gas was first demonstrated at JILA in 1999 by cooling a gas of  ${}^{40}\text{K}$  atoms [DeM99, DeM01]. The observed deviations from the classical energy of a harmonically trapped gas ( $E_{\text{cl}} = 3N_\sigma k_{\text{B}}T$ ) were attributed to the effects of the Fermi-Dirac statistics. Shortly after, the onset of degeneracy in a  ${}^6\text{Li}$  gas was identified at Rice University, ENS, MIT and Duke University [Tru01, Sch01, Had02, Gra02].

Adding atoms with another spin state to the ideal Fermi gas enables interactions in form of collisions between now distinguishable fermions, as described in the next section.

### 2.3. Interactions in ultracold Fermi gases

The type of interaction considered in this section is scattering between spin-1/2 atoms in an unpolarised gas of two distinct hyperfine spin states ( $N/2 = N_\uparrow = N_\downarrow$ ). Collisional interactions in ultracold quantum gases are well understood at the two- and few-body level as the density of the gas is low enough to allow the short-range atomic potential to be approximated by simple scattering models [Wei99, Blu12, Pet13].

If two-body interactions are attractive and the temperature is sufficiently low, the gas develops correlated pairs along the entire BCS-BEC crossover, leading to remarkable many-body properties such as fermionic superfluidity, the neutral analog to BCS-superfluidity with electrons in conventional superconductors [Bar57]. In case of strong interactions, the superfluid becomes more stable and exists even at higher temperatures, making its experimental observation possible in the first place. Also, due to strong pair correlations the gas behaves like a strongly correlated quantum liquid. Accordingly, the gas is in

the collisional regime even in the normal phase so that transport properties, such as the density flow and collective oscillations, can be described hydrodynamically [Wri07]. Most surprisingly, all these phenomena are a consequence of two-body collisional interactions.

Quite generally, collisions can be classified to be either elastic or inelastic. In elastic collisions, usually dominant in the low-density regime, the individual kinetic energy of the collision partners can change while the kinetic energy of the relative motion remains unchanged. Inelastic collisions, which can be suppressed in Fermi gases, transfer energy between internal and relative kinetic energy and thus ultimately limit the achievable density. If the internal energy after the collision event is less than before, the energy difference was carried away in form of kinetic energy by the collision partners. This is usually accompanied by heating of the gas cloud and trap losses.

Both processes play important roles when preparing the gas. For example, during evaporative cooling Feshbach molecules (dimers) can be produced via inelastic three-body recombination by atom-dimer collisions [Joc03a] while subsequent elastic atom-atom, atom-dimer and dimer-dimer collisions rethermalise the Fermi cloud to attain thermal equilibrium.

### 2.3.1. Low-energy elastic collisions

In the following, important results for elastic two-body collisions in the partial-wave treatment are summarised. Collisions in ultracold dilute gases are dominated by  $s$ -wave scattering. While the gas constitutes a many-body system, the scattering problem can be fully understood in a two-body picture. This topic is discussed in standard textbooks, such as [Sak94, Ing99, Kre09] as well as in many review articles [Wei99, Bra08, Chi10].

The attractive short-range potential  $U_{\text{sc}}(\mathbf{r})$  that causes two atoms to collide can be parameterised by the  $s$ -wave scattering length  $a$  if the interaction range  $r_0$  (potential range) is much smaller than both the thermal wavelength and the average particle separation, i.e.  $r_0 \ll \lambda_{\text{dB}}, n^{-1/3}$ . In this case, even a simple spherical square well for the atomic scattering potential captures the main physics of the collision process. In ultracold Fermi gases,  $n^{-1/3}$  is of order of the inverse Fermi vector  $k_{\text{F}}^{-1} (\sim \lambda_{\text{dB}})$ .

The asymptotic ( $r \rightarrow \infty$ ) scattering solution of the Schrödinger equation for the relative motion of two point-like atoms can be expanded in terms of partial waves,  $\psi_l(r)$ , where  $l = 0, 1, 2, \dots$  ( $= s, p, d, \dots$ -wave) and  $r$  is the relative distance between the collision partners. Identical bosons (fermions) can only collide in even (odd) partial waves due to the exchange symmetry of the wavefunction predetermined by quantum statistics. For nonidentical particles collisions in all partial waves are allowed.

## 2. Strongly interacting Fermi gases

For an isotropic (central) interaction potential, where  $U_{\text{sc}}(\mathbf{r}) \equiv U_{\text{sc}}(r)$ , partial waves do not mix. At low temperatures, only the partial wave with zero-orbital angular momentum ( $l = 0$ ) contributes to the scattering wave. This requires for two colliding same-species fermions to be in different internal states. In the asymptotic region ( $r \gg r_0$ ), the wave can be expressed by  $\psi_0(r) \propto \sin[kr + \delta_0(k)]/r$ , where  $k$  is the relative wave number. This shows that a low-energy scattering process is fully specified by a phase shift, which in the effective-range expansion to the second order in  $k$  can be written as

$$k \cot[\delta_0(k)] = -\frac{1}{a} + \frac{r_{\text{eff}}k^2}{2}, \quad (2.3.1)$$

where  $r_{\text{eff}}$  is the effective range of the scattering potential. Equation 2.3.1 provides the standard definition of the  $s$ -wave scattering length:  $a = -\lim_{k \ll r_0^{-1}} [\delta_0(k)/k]$ . The second-order correction in equation 2.3.1 includes low-order contributions of the potential shape to the phase shift. If the scattering potential is attractive and  $a$  positive to give a collision energy lower than the dissociation threshold of  $U_{\text{sc}}(r)$  the two-body system may support bound states (Feshbach molecules or dimers in cold atoms language).

For  $r_0$  and  $|r_{\text{eff}}|$  small compared to  $|a|$  and  $k_{\text{F}}^{-1}$ , which is the case for  ${}^6\text{Li}$  or  ${}^{40}\text{K}$  in the entire BCS-BEC crossover, two-body collisions can be approximated in the zero-range limit<sup>3</sup> ( $r_0 \equiv 0$ ), replacing the true scattering potential by one with contact interaction such as this regular pseudo potential:  $U_{\text{sc}}^0(\mathbf{r}) = 4\pi\hbar^2 a/m \delta(\mathbf{r})(\partial/\partial r)r$  [Lee57]. This means that microscopic details of potentials with complicated shapes are irrelevant, and the parameter  $a$  suffices to quantify interactions – this is the characteristics of a universal gas (cf. section 2.3.4). Then, the scattered wavefunction can be even further simplified to capture the entire short-range physics:  $\psi_0(r) \propto 1 - a/r$ , where  $a$  locates the zero crossing.

The scattering amplitude for  $s$ -waves in the zero-range limit is given by

$$f_0(k) = \frac{1}{k \cot[\delta_0(k)] - ik} \approx \frac{-1}{1/a + ik}. \quad (2.3.2)$$

At low collision energies (weak interactions,  $ka \ll 1$ ), the scattering amplitude becomes  $f_0(k \rightarrow 0) = -a$ , whereas  $|a| \rightarrow \infty$  defines the unitarity limit,  $f_0(k) = i/k$ . In the latter case, the scattering amplitude depends on the collision energy ( $E = \hbar^2 k^2/m$ ) for finite  $k$  but is independent of two-body interactions. Moreover, at unitarity the scattering amplitude reaches its maximal value allowed by quantum mechanics, realising a system with the strongest possible interactions (relative to the temperature scale).

---

<sup>3</sup>Note that in general  $r_{\text{eff}} \neq r_0$ ; for example,  $r_{\text{eff}}$  can take large, even negative values at a narrow Feshbach resonance [Pet13]. However, for broad Feshbach resonances, as found in  ${}^6\text{Li}$  and  ${}^{40}\text{K}$  gases,  $r_{\text{eff}} \sim r_0$  holds in the entire strongly interacting regime ( $k_{\text{F}}|a| > 1$ ) [Cas07].

Since only  $s$ -waves are present in the system, the total scattering cross section for distinguishable particles is simply given by  $\sigma_0(E) = 4\pi|f_0(k)|^2$  so that in the

$$\begin{aligned} \text{low-energy limit:} \quad \sigma_0 &= 4\pi a^2, & \text{for } k \rightarrow 0, \\ \text{unitarity limit:} \quad \sigma_0(E) &= \frac{4\pi}{k^2} = 4\pi \lambda_{\text{dB}}^2, & \text{for } |a| \rightarrow \infty, \end{aligned}$$

showing an increase in  $\sigma_0(E)$  for decreasing energy and temperature in the strongly interacting case. Note that for identical bosons  $\sigma_0$  is twice as large as for distinguishable particles as required by quantum statistics.

The scattering length in many atomic gases with standard isotopes is naturally of the same order as the potential range (typically  $50 - 100 a_0$ , where  $a_0 = 5.29177 \times 10^{-11}$  m is Bohr's radius), interactions therefore often turn out to be very weak at experimentally achievable temperatures and densities. Also, the sign of  $a$  can be either positive or negative so that there is a priori no control over whether the respective interatomic interactions are repulsive or attractive. A famous example is  $^{133}\text{Cs}$ , where  $a$  ( $\gg r_0$ ) at zero magnetic field is extremely large preventing the achievement of BEC until 2003 due to strong loss processes [Web03]. Interactions in such gases however can be controlled by resonantly scattering atoms close to a Feshbach resonance, at which  $a$  can be tuned to any value thereby greatly exceeding the mean interparticle spacing. Using the example of  $^6\text{Li}$ , the next section shows what happens when  $a$  is controlled by simply tuning an external magnetic field.

### 2.3.2. The broad Feshbach resonance of $^6\text{Li}$

At high magnetic field, a broad magnetic Feshbach resonance exists for  $^6\text{Li}$  atoms in each pairwise combination of the three existing hyperfine ground states with an electronic-spin projection along the quantisation axis of  $m_S = -1/2$  [Hou98, Bar05]. The main results in this thesis were obtained by probing spin-balanced  $^6\text{Li}$  mixtures prepared in the two lowest spin states  $|F = 1/2, m_F = \pm 1/2\rangle$ , which we label  $|\uparrow\rangle$  and  $|\downarrow\rangle$ , near the 832 G Feshbach resonance<sup>4</sup>. These states provide high stability against spin relaxation. The energy levels of all hyperfine states of the  $D_2$ -transition for a  $^6\text{Li}$  atom as a function of an external magnetic field  $B$  are plotted in appendix A. For a detailed discussion on Feshbach resonances see for example [Köh06, Ing07, Bra08, Kre09, Chi10] and references therein.

The principle of a Feshbach resonance for two atoms, one in  $|\uparrow\rangle$  the other in  $|\downarrow\rangle$ , is illustrated in figure 2.3.1 (a) based on the two-channel model for  $^2S_{1/2}$  atoms, where the

---

<sup>4</sup>Formerly known as the famous 834 G Feshbach resonance.

## 2. Strongly interacting Fermi gases

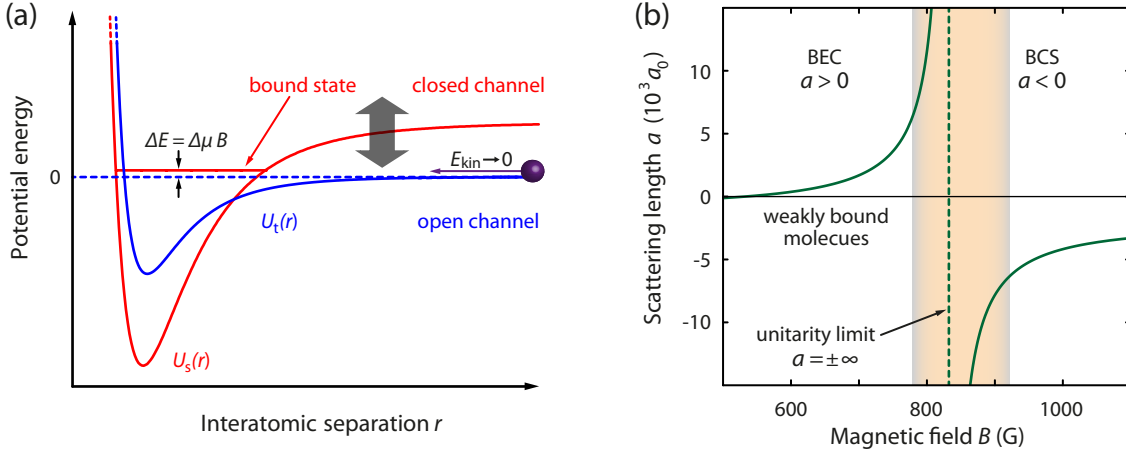


**Figure 2.3.1.:** Tuning interactions via a magnetic Feshbach resonance. (a) Two colliding atoms (relative distance shown by purple sphere) at near-threshold kinetic energy in the open channel resonantly couple to a molecular state in the closed channel. The channels can be shifted relative to each other by tuning  $B$  (black thick arrow). The energy difference of bound state and dissociation threshold is  $\Delta\mu B = E_{\text{closed}} - E_{\text{open}}$ . (b) Plot of  $a(B)$  (green) around the 832.2 G Feshbach resonance. The shaded area indicates the BCS-BEC crossover regime ( $k_{\text{F}}|a| > 1$ ) as realised in our experiments. The apparent slight asymmetry is due to the large triplet background scattering length.

interaction depends on the total electronic spin  $S = 0, 1$ . Binary collisions (approximately) involve a spin-triplet  $U_t(r)$  that couples to a spin-singlet  $U_s(r)$  molecular potential via spin-exchange (hyperfine) interaction. The singlet potential only admits bound states whereas scattering is initiated in the triplet potential; thus, they are referred to as “closed” and “open” channels, respectively. In this scenario the electronic spins are essentially parallel at large distances and antiparallel when two atoms are close together. The different orientation of the spins in the two channels leads to a differential magnetic moment  $\Delta\mu$ , which for  ${}^6\text{Li}$  is  $2\mu_{\text{B}}$  ( $\mu_{\text{B}} \simeq h \times 1.4 \text{ MHz/G}$  is Bohr’s magneton) [Bar05], allowing the potentials to be Zeeman shifted relative to each other by varying  $B$ . Energy conservation gives only access to bound states of the closed channel as the kinetic energy of two asymptotically free atoms is much lower than the scattering threshold of  $U_s(r)$ , see figure 2.3.1 (a).

A Feshbach resonance occurs when the energy of a bound state becomes near degenerate with the scattering threshold of the open channel leading to a strong enhancement of the scattering rate in the open channel [Tie93]. There are various standard treatments of this

scattering problem available in many textbooks, see in particular [Kre09]. The physical picture of this process is essentially that the zero-energy scattering state of two opposite-spin atoms in the open channel, colliding at small distance  $\sim r_0$ , resonantly couples to a weakly-bound (Feshbach) molecule in a different combination of spin states as a result of spin exchange interaction between electronic and nuclear spin [Dui04]. Although these Feshbach dimers are excited in the highest vibrational bound state ( $\nu = 38$ ) Pauli exclusion suppresses the rate for inelastic collisions which leads to decay into deeper internal states as the constituents are fermions, resulting in extraordinary long lifetimes [Pet04]. In particular, pairs of  ${}^6\text{Li}$  around the resonance position exhibit lifetimes of tens of seconds which is much larger than the inverse of the collision rate [Joc03a], hence they are considered as stable (in  ${}^{40}\text{K}$  lifetimes are  $\sim 100$  ms). This is due to the short interaction range ( $\ll \lambda_{\text{dB}}$ ), greatly reducing the probability for three-body reactions which would require two Fermi atoms in the same state to be close together. This contrasts gases of true bosonic atoms where dimer formation strongly enhances three-body decay (atom-molecule and molecule-molecule collisions), reducing dimer lifetimes to milliseconds at most.

The long-range behaviour of the interaction potentials for  $S$ -state atoms can be well approximated by the attractive van der Waals potential,  $-C_6/r^6$ , which simplifies the theoretical description of collisions and provides useful length and energy scales: The van der Waals length  $r_{\text{vdW}} = (mC_6/\hbar^2)^{1/4}$  and the van der Waals energy  $E_{\text{vdW}} = \hbar^2/(mr_{\text{vdW}}^2)$ . For  ${}^6\text{Li}$  ( $r_0 \equiv r_{\text{vdW}} \approx 62.5 a_0$  and  $E_{\text{vdW}} \approx \hbar \times 614$  MHz), the latter provides an estimate of the potential energy at  $r_0$ . Here  $C_6 = 1393$  a.u. is the van der Waals dispersions coefficient and  $m = 6.015$  u ( $9.988 \times 10^{-27}$  kg) is the atom's mass.

The evolution of the  $s$ -wave scattering length across the Feshbach resonance is shown in figure 2.3.1 (b). The analytic expression of  $a$  for a universal gas reads [Moe95]

$$a(B) = a_{\text{bg}} \left( 1 + \frac{\Delta B}{B - B_0} \right), \quad (2.3.3)$$

where (values for  ${}^6\text{Li}$ )  $a_{\text{bg}} = -1405 a_0$  is the triplet background scattering length in the absence of interactions, and  $\Delta B \simeq 300$  G is the resonance width given by the distance in magnetic field between  $B_0$  and the zero crossing of  $a$  located at<sup>5</sup> 527.5 G [Du08]. A precise resonance position has been recently experimentally found at  $B_0 = 832.18(8)$  G [Zür13].

Figure 2.3.1 (b) further shows that above (below) the Feshbach resonance  $a$  is negative (positive) leading to an effective attractive (repulsive) interaction. The BEC side of the

---

<sup>5</sup>A good approximation for practical purposes provides the fitting formula  $a(B) = a_{\text{bg}}(1 + \Delta B/x)(1 + \alpha x)$ , where  $x = B - B_0$  and  $\alpha = 0.04 \text{ G}^{-1}$ , with an accuracy of greater 99% between 600 and 1200 G [Bar05].

## 2. Strongly interacting Fermi gases

resonance ( $a > 0$ ) supports molecules which are stable in a two-body picture. On the BCS side ( $a < 0$ ), two-body physics predicts energetically unstable molecules [a “virtual” bound state lies above the dissociation threshold of  $U_t(r)$ , cf. figure 2.3.1 (a)]; however, as later will be shown, this side can lead to bound Cooper pairs in the presence of the Fermi sea. The highlighted area around the resonance in figure 2.3.1 (b) indicates the strongly interacting regime of the BCS-BEC crossover ( $k_F|a| > 1$ ) where universal physics is valid [in our experiments  $1/k_F \simeq 3\mu\text{m} \approx 6000 a_0$ ]. The unitarity limit ( $a = \pm\infty$ ) is a special case since the two-body scattering length drops out of the system’s physical description, leaving the Fermi energy  $E_F$  and density as the only scaling parameters (cf. section 2.3.4).

In experiments, we are interested in the physics of universal Fermi gases which can be realised by a broad Feshbach resonance. “Broad” in this context means that the coupling strength between closed and open channel is much stronger than the collision energy of the scattered atoms which is of order of the Fermi energy. Quantitatively, a criteria for broad is given by [Leg06, Zha09]

$$E_F \ll \frac{(\Delta\mu\Delta B)^2}{2\hbar^2/(ma_{\text{bg}}^2)}, \quad (2.3.4)$$

where the right hand side is a measure for the interchannel coupling strength. This criteria is equivalent to  $k_F R^* \ll 1$ , where  $R^* \equiv -r_{\text{eff}}/2 = -\hbar^2/(\Delta\mu\Delta Bma_{\text{bg}}) > 0$  characterises the resonance width, as often found in literature. The effective range and the background scattering length is taken at the resonance position. Plugging in the numbers for the 832 G resonance into equation 2.3.4 we obtain  $\sim \hbar \times 7$  THz. This is not only orders of magnitude larger than  $E_F/\hbar = 10$  kHz, the typical value in our experiments, but also than  $E_{\text{vdW}}$ , indeed indicating extremely strong coupling [Han09]; thus,  ${}^6\text{Li}$  is the best candidate of all species used in ultracold gas experiments so far to realise and study universal physics.

The strong interchannel coupling has severe consequences for the pair wavefunction. In the two-channel model, Feshbach molecules are described as a superposition of the open-channel free atoms and closed-channel bare molecules. It turns out that the resulting “dressed” pair wavefunction for  ${}^6\text{Li}$  is to over 99.9% open-channel dominated throughout the BCS-BEC crossover [Par05]. As a consequence, the broad resonance can be described by an effective single-channel model. Then, the molecular properties ( $a > 0$ ) for a pair of  $|\uparrow, \downarrow\rangle$  atoms interacting via a (triplet) contact potential are fully captured by a universal Halo pair wavefunction, which in the asymptotic form ( $r \rightarrow \infty$ ) can be expressed by

$$\phi(r) = \frac{1}{\sqrt{2\pi a}} \frac{e^{-r/a}}{r}; \quad \text{and} \quad E_b = -\frac{\hbar^2}{ma^2} \quad (2.3.5)$$

is its binding energy<sup>6</sup> determining the long-range behaviour of these molecules. The so-called Halo regime is defined for  $a \gg r_{\text{vdW}}$  and  $E_b \ll E_{\text{vdW}}$ . The characteristic size of  ${}^6\text{Li}_2$  molecules in the highest bound state is  $\sim a$  ( $\simeq 2000 a_0$ ), and the momenta individual atoms is  $\sim \hbar/a$ . Note that for  ${}^6\text{Li}_2$   $|E_b|$  can reach values up to  $\hbar \times 2.5$  GHz which is more than three orders of magnitude smaller than the binding energies of the corresponding ground state molecules ( $\sim$  THz). Other atomic species that feature Halo molecules include fermionic  ${}^{40}\text{K}$  and the bosonic alkalis  ${}^{39}\text{K}$ ,  ${}^{85}\text{Rb}$ , and  ${}^{133}\text{Cs}$  (not  ${}^7\text{Li}$ !) [Chi10].

There is also a narrow  $s$ -wave Feshbach resonance for  ${}^6\text{Li}$  atoms in the  $|\uparrow, \downarrow\rangle$  states of roughly 100 mG width which is located at 543.25(5) G [Str03], not shown in figure 2.3.1 (b). The magnetic range of the universal region for this resonance is too small ( $\sim 1$  mG) to be easily accessible experimentally [Sim05]. Unlike broad resonances, distinct regimes of two-body bound states and many-body Cooper pairs cannot be clearly identified at such resonances as contributions of the closed channel can vary significantly as a function of the energy [Gur07]. This means that a molecular condensate can coexist with a BCS-type fermionic superfluid within the experimental resolution; such a many-body system is qualitatively different from the BCS-BEC crossover described in the next section.

Feshbach resonances, originally described by Fano and Feshbach [Fan61, Fes62], were first observed in ultracold atomic gases by the MIT group in 1998 in a BEC of  ${}^{23}\text{Na}$  atoms through detection of inelastic loss processes [Ino98], and shortly after in  ${}^{85}\text{Rb}$  via photoassociation spectroscopy [Cou98]. Since then, magnetic Feshbach resonances have been found in pretty much all single- and multi-species quantum gases with alkali, earth-alkali, rare-earth and other elements that were cooled to degeneracy. Resonant scattering has become an invaluable tool for realising strong interactions in ultracold atoms (for an extensive review on early experiments see [Blo08, Gio08]): In 2002, a strongly interacting Fermi gas was first observed at Duke University using  ${}^6\text{Li}$  [O'H02]; in 2003, molecular BEC's were produced in  ${}^6\text{Li}$  and  ${}^{40}\text{K}$  atomic gases [Joc03b, Gre03]; in 2004, pair condensation beyond the BEC regime in the crossover was detected using  ${}^6\text{Li}$  and  ${}^{40}\text{K}$  [Zwi04, Reg04]; and finally, signatures of fermionic superfluidity in the BCS-BEC crossover was revealed at MIT in 2005 by observing quantised vortices in rotating  ${}^6\text{Li}$  Fermi clouds [Zwi05].

Note that there are other ways to produce Feshbach resonances in cold Bose and Fermi gases such as optical Feshbach resonance where pairs of free atoms are coupled to an excited molecular state by a laser field [The04, Bau09, Fu13]. In contrast to magnetic Feshbach resonances, these enable the control of both the resonance width and location [Chi10].

---

<sup>6</sup>In the frame of relative motion, two colliding atoms of equal mass  $m$  carry the reduced mass  $m_r = m/2$ .

### 2.3.3. BCS-BEC crossover – from weak to strong attraction

In this section, I will give a basic overview of the BCS-BEC crossover with an emphasis on pairing and the features related to elementary excitations that can be probed by optical Bragg spectroscopy, following mainly [Ing07, Blo08, Gio08, SdM08, Zwe12, Ran14]. The system considered here is a fermionic mixture of single-species atoms ( $m_\uparrow = m_\downarrow \equiv m$ ) in a spin-balanced ( $n_\uparrow = n_\downarrow \equiv n/2$  and  $\mu_\uparrow = \mu_\downarrow \equiv \mu$ ), homogeneous, low-density ( $k_F r_0 \ll 1$ ) 3D configuration unless otherwise stated.

In subsequent chapters, we use Bragg spectroscopy to measure the density-density response of ultracold Fermi gases in the crossover regime where interactions are strong. All experiments in this thesis were performed at high Bragg momentum relative to the Fermi momentum ( $\hbar k = 4.2 \hbar k_F$ ). The Bragg response hence is determined by short-range pair correlations, and the energy transfer between Bragg lasers and gas can largely exceed  $E_F$ . As detailed in section 4.4.1 on page 106, such a setting can probe Bragg spectra of fermionic and bosonic excitations, which we interpret in a single-particle picture as the respective scattering of single atoms of mass  $m$  and not too largely sized pairs ( $2m$ ) [Vee08]. This picture is reasonable as the energy dispersion for pair and atom excitations is quadratic at this momentum, revealing the molecular character of the gas at high  $k$  [Com06a]; yet the question is: What is the nature of these pairs along the BCS-BEC crossover?

So far in this chapter, fermionic pairing has been considered as a two-body problem. Atoms in different spin states interact via Feshbach tunable  $s$ -wave collisions to form stable molecules for  $a > 0$ , while they scatter as free atoms in the continuum for  $a < 0$ . Pair formation at any  $a$  requires many-body effects such as the presence of a Fermi sea. Then, the many-body ground state of the Fermi gas comprises bound fermions that smoothly evolve from large Cooper pairs in a BCS-type superfluid into point-like molecules in a BEC (mBEC) while the interaction parameter  $1/(k_F a)$  ranges from  $-\infty$  to  $\infty$  crossing the unitarity limit,  $1/(k_F a) \equiv 0$  (recall figure 2.3.1). Adiabatically following the lowest energy branch, sweeping the scattering length links the scattering continuum to the two-body bound state, realising an attractive Fermi gas across the resonance [Pri04].

One way to get an intuitive feel for pairing in the BCS-BEC crossover is by examining its phase diagram as a function of temperature and interaction strength, as illustrated in figure 2.3.2 (inspired by [Hau99, SdM08]). The crossover can be divided in two distinct regimes highlighting the qualitative changes in the many-body properties of the gas that occur while the coupling strength (binding energy) between atoms in the  $|\uparrow\rangle$  and  $|\downarrow\rangle$  spin states (red and blue spheres in figure) is tuned from weak to strong. Then, the crossing point,  $\mu = 0$ , at  $1/(k_F a) \simeq 0.6$  on the BEC side of the Feshbach resonance

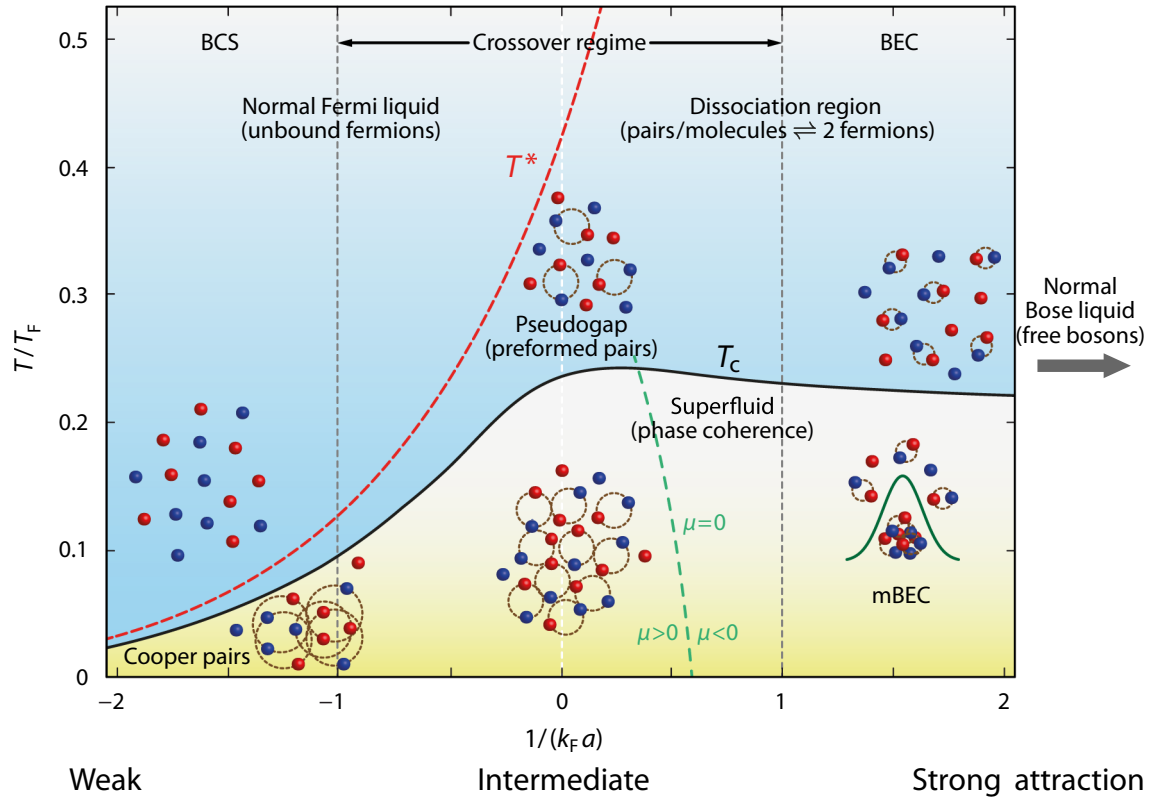


**Figure 2.3.2.:** Qualitative representation of the BCS-BEC crossover phase diagram of a two-component homogeneous Fermi gas relative to the dimensionless interaction strength  $1/(k_F a)$  and temperature  $T/T_F$ . Shown are correlations between “atoms” (red and blue) in the normal (blue area) and the superfluid (yellow area) phase of the gas. For weak attractive coupling, the gas is a Fermi liquid of single atoms, whereas for strong coupling it is a Bose liquid of (point like) bound molecules. Atoms pair up at  $T^*$  (red dashed curve), leading to pair correlations (brown circles) and ultimately to pair condensation at  $T_c$  (black curve). For an increase in coupling, the many-body ground state smoothly evolves from a BCS-superfluid of Cooper pairs into a BEC of molecules (mBEC). The crossing point,  $\mu = 0$ , separates BCS and BEC regime in view of many-body properties. Adapted from [Hau99, SdM08].

separates the BCS regime ( $\mu > 0$ ), where a Fermi surface is present and an energy gap exists at finite  $k = \sqrt{2m\mu/\hbar^2}$ , from the BEC regime ( $\mu < 0$ ), where the gas is described by bosonic molecules and a gap at  $k = 0$ . These regimes are smoothly connected and the system evolves continuously from one to the other by varying  $a$ . While the weakly

## 2. Strongly interacting Fermi gases

attractive (BCS) and repulsive (BEC) regimes, including the limits  $1/(k_F a) \rightarrow \pm\infty$ , are well understood, the crossover regime  $-1 < 1/(k_F a) < 1$ , where collisional interactions and thus correlations are strongest, is still an active field of theoretical and experimental investigations, and a accurate quantitative picture is not yet available. Note that the effective interaction in the BEC limit ( $+\infty$ ) is weak as the coupling energy is “used up” in molecular binding energy  $E_b$  (cf. equation 2.3.5) leaving weak Pauli repulsion of the constituent fermions to interact between bosonic pairs.

Figure 2.3.2 shows two characteristic temperatures signalling a transition of the degenerate Fermi gas into an energetically more favourable state. The pairing temperature  $T^*$  indicates the region where “red” and “blue” atoms become correlated as they pair up. A second-order phase transition at the critical temperature  $T_c$  marks the onset of pair condensation and superfluidity, which in 3D Fermi gases happens simultaneously. Composite pairs of spin-1/2 particles are integer spin bosons, and as such they can macroscopically occupy the many-body ground state with zero centre-of-mass momentum. This implies the constituent fermions of one pair of having equal but opposite momenta and zero total spin,  $(\mathbf{k}_\uparrow, -\mathbf{k}_\downarrow)$ . Note that the individual atoms in the pair can have considerable kinetic energy while the centre of mass of the pair rests.

The pair condensate is phase coherent, similar to the case of a BEC with bosonic atoms, giving rise to a nonzero (complex) order parameter for the superfluid state<sup>7</sup>. In the dissociation region,  $T_c < T < T^*$ , pairs and single atoms coexist in the normal liquid phase due to thermal pair-breaking excitations (the atom-pair ratio depends on  $a$  and  $T$ ). The contribution of such excitations to the normal density freezes out well below  $T^*$ . Note that a Fermi gas in the superfluid phase (yellow area in figure 2.3.2) comprises a normal, a condensate and a superfluid density which are all distinct quantities [Fuk07]. Interactions deplete the condensate by populating finite-momentum states even at zero temperature. This can be seen, for example, in the crossover regime where the condensate fraction of a low-temperature <sup>6</sup>Li gas only reaches a maximum of  $\sim 80\%$  around unitarity [Zwi04].

---

<sup>7</sup>In many-body language, the order parameter, characterising the so-called “off-diagonal long-range order” in the two-body density matrix (analogous to a single-body density matrix for bosonic particles) [Yan62], is a consequence of a “broken  $U(1)$  symmetry” in the wavefunction at the phase transition and is closely related to the physics of a gapless mode that “restores this symmetry” (Goldstone theorem) [Gri93]. This is interesting insofar as density fluctuations in the Fermi gas play important role in describing the order parameter, and they can in principle be probed by Bragg spectroscopy in the long-wavelength, low-energy limit [Oha03b]. This may open a way for Bragg spectroscopical studies of dynamic coherence properties of the order parameter in strongly interacting Fermi gases (see also footnote on page 108).

For a basic microscopic picture of pairing it is helpful to recall some important results from BCS-BEC crossover models. To date there is no exact analytical solution of this many-body problem other than the weakly interacting limits where analytic expressions can be obtained perturbatively in terms of  $k_F a$ . Pairing models for the crossover regime are based on sophisticated analytical and numerical methods, often relying on assumptions that need to be tested experimentally. Perturbative approaches are usually not suitable due to lack of a small expansion parameter or convergence. Most reliable unitarity results include diagrammatic, field theoretical and quantum Monte Carlo (QMC) approaches.

The “standard” description of the crossover many-body ground state at  $T = 0$  is given by BCS mean-field theory, introduced by Leggett [Leg80]. This model can be extended to finite temperature by including (pair) fluctuations. In this way, for instance, the Nozières and Schmitt-Rink (NSR) theory determines an approximate crossover function for  $T_c$  and provides corrections to BCS theory [Noz85, Ran96]. Also, the dynamics of pair correlations such as collective oscillations and pair-breaking excitations can be studied [Com06b], as well as the universal contact parameter [Hu11] (cf. section 2.3.5 for contact).

One representation of the BCS state is  $|\text{BCS}\rangle = \prod_{\mathbf{k}} (u_{\mathbf{k}} + v_{\mathbf{k}} \hat{c}_{\mathbf{k},\uparrow}^\dagger \hat{c}_{-\mathbf{k},\downarrow}^\dagger) |0\rangle$  describing a coherent collection of all pairs which do not interact. It smoothly connects both coupling limits and does not rely on any small parameter. Each pair state  $(\mathbf{k}_\uparrow, -\mathbf{k}_\downarrow)$  has probability of being occupied  $v_{\mathbf{k}}^2$  or empty  $u_{\mathbf{k}}^2$ , where  $v_{\mathbf{k}}^2 + u_{\mathbf{k}}^2 = 1$ , and  $\hat{c}_{\mathbf{k},\sigma}^\dagger$  is the fermionic creation operator. In a variational formulation, this wavefunction leads to two coupled equations,

$$\frac{m}{2\pi\hbar^2 a} = \int \frac{d\mathbf{k}}{(2\pi)^3} \left( \frac{1}{\epsilon_{\mathbf{k}}} - \frac{1}{E_{\mathbf{k}}} \right) \quad \text{and} \quad n = \frac{k_F^3}{3\pi^2} = \int \frac{d\mathbf{k}}{(2\pi)^3} \left( 1 - \frac{\epsilon_{\mathbf{k}} - \mu}{E_{\mathbf{k}}} \right), \quad (2.3.6)$$

which are the famous gap and number equations, respectively. The fermionic excitation (quasiparticle) energy is given by  $E_{\mathbf{k}} = \hbar\omega(\mathbf{k}) = \sqrt{(\epsilon_{\mathbf{k}} - \mu)^2 + \Delta^2}$ , where  $\epsilon_{\mathbf{k}} = \hbar^2 k^2 / (2m)$  is the kinetic energy of a free atom. Solving equations 2.3.6 results in monotonic crossover functions of the pairing gap  $\Delta$  and the fermionic chemical potential  $\mu$  [Eng97, Leg06].

In the BCS limit ( $\Delta \ll E_F$ ),  $\mu \equiv E_F$  and  $k_B T_c \simeq \Delta \propto E_F \exp[-\pi / (2k_F |a|)]$ , which is equivalent to the standard BCS weak-coupling results for conventional superconductors at  $T = 0$  [Bar57]. The BCS superfluid arises from pair correlations of, in the case of Fermi gases, neutral atoms in momentum space where Cooper pairs form near the Fermi surface in an exponentially narrow energy band of width  $\Delta$ . The pairing (or condensation) energy  $\Delta^2 / (2E_F)$  is a measure of reduction in energy when the Fermi liquid traverses from the normal into the superfluid state. Atoms with arbitrarily weak attractive two-body interactions cause an instability in the Fermi surface by forming bound pairs  $(\mathbf{k}_\uparrow, -\mathbf{k}_\downarrow)$  [Coo56]; thus, the excitation spectrum  $E_{\mathbf{k}}$  is gapped near  $k_F$ . Pauli blocking plays a crucial role

## 2. Strongly interacting Fermi gases

in stabilising pair formation by preventing atoms from scattering into occupied states in the Fermi sphere. In the weakly attractive regime, the excitation gap is equivalent to the order parameter as  $T^* \rightarrow T_c$ , that is, when pairs form they simultaneously condense. The minimum energy required to break a Cooper pair is  $2\Delta$ , where the factor two accounts for the creation of two free atoms (two quasiparticles) thereby destroying superfluidity.

In contrast to superconductors, BCS-like Cooper pairs are unlikely to be ever observed in ultracold atomic gases. For example, without access to a Feshbach resonance the critical temperature in  ${}^6\text{Li}$  would be  $T_c \approx 0.28 T_F \exp[-\pi/(2k_F|a|)] \sim 10^{-4} T_F$  which is unfeasible with current experiments (here  $a$  is set to  $a_{\text{bg}}$ , cf. section 2.3.2). In this case, the mean pair size  $\xi_{\text{pair}}^{\text{BCS}} \propto k_F^{-1} \exp[\pi/(2k_F|a|)] \sim 10^3 k_F^{-1}$  greatly exceeds the mean interparticle distance. Consequently, Cooper pairs are highly overlapping and pair correlations in coordinate space are minuscule. Note that in this example the diameter of the pairs would be even larger than the spatial extend of atomic clouds in typical trapping confinements.

Tuning the Fermi gas into the crossover regime ( $\Delta \sim E_F$ ) however increases the binding energy of Cooper pairs to a point where the pair size is comparable to the mean atomic separation,  $\xi_{\text{pair}}^{\text{CO}} \simeq k_F^{-1}$ , as illustrated in figure 2.3.2. The chemical potential rapidly drops from around  $E_F$  to negative values in the BEC regime. Pairing in the crossover cannot be described by a simple intuitive picture anymore. Strong correlations between atoms greatly modify the Fermi sphere leaving the Fermi surface less well defined in the superfluid as well as normal gas, vanishing at  $\mu = 0$ . Concurrently, an emerging two-body bound state on the BEC side ultimately dominates pair formation leading to a strongly interacting molecular BEC. The Feshbach resonance lifts the critical temperature to experimentally accessible values and separates it from  $T^*$ . Cooper pairing at unitarity results from many-body effects ( $E_b \equiv 0$ ,  $T_c = 0.167 T_F$  [Ku12],  $2\Delta \simeq 0.88 E_F$  [Sch08a]); at the same time, clear signatures of short-range pair correlations in the atomic density are present.

As shown in figure 2.3.2, the unitary gas features the so-called pseudogap phase for  $T_c < T < T^*$ , in analogy with high- $T_c$  cuprate superconductors, showing a gapped energy dispersion in the normal state. In atomic gases, pair correlations are present but not the result of thermal molecules. This region is argued to be an example of a non Fermi liquid; however, experiments have not yet led to conclusive results, as discussed in [Ran14]. The pairing temperature in a uniform unitary gas is predicted to lie in the range  $(0.2 - 0.7) T_F$ .

By further increasing  $1/(k_F a)$ , the critical temperature depends only weakly on attractive interactions. After peaking just beyond unitarity,  $T_c$  converges towards the NSR result of a free Bose gas in the strong coupling limit ( $0.218 T_F$ ). This contrasts  $T^*$  which diverges as a function of  $|E_b|/k_B$ . In the weakly interacting BEC regime, the molecules condense

in real space as opposed the Cooper pairs in the BCS limit where condensation happens strictly in momentum space. The mBEC superfluid consists of tightly bound molecules of size  $\xi_{\text{pair}}^{\text{BEC}} \simeq a \ll k_{\text{F}}^{-1}$  which behave like weakly repulsive bosons. In this region of the phase diagram, short-range pair correlations are strong. BCS mean-field theory predicts  $\mu$  to be  $(\mu_{\text{M}} - |E_{\text{b}}|)/2$ , where  $\mu_{\text{M}} = 4\pi\hbar^2 a_{\text{M}} n_{\text{M}}/m_{\text{M}}$  is the molecular chemical potential,  $n_{\text{M}} = n/2$ ,  $m_{\text{M}} = 2m$ , and  $a_{\text{M}} = 0.6a$  is molecular elastic scattering length which differs from the mean-field result of  $a_{\text{M}} = 2a$  [Pet04]. The gap parameter  $\Delta = 4E_{\text{F}}/\sqrt{3\pi k_{\text{F}} a} \sim \sqrt{n}$  serves as normalisation condition and by itself has no physical meaning. Instead, the energy required to break a condensed molecule is  $2\sqrt{\mu^2 + \Delta^2} \approx |E_{\text{b}}| - \mu_{\text{M}} + 2\Delta^2/|E_{\text{b}}|$  for  $\mu < 0$  and reduces to  $2|\mu| \simeq |E_{\text{b}}|$  in the BEC limit where  $|\mu| \gg \Delta$ . Also in this limit, the normal gas is a Bose liquid of point-like elementary bosons.

In the context of Bragg spectroscopy to measure linear response functions [Pin66], two types of elementary excitations in the crossover superfluid are of primary interest: Pair (bosonic) and pair-breaking (fermionic) excitations [Com06b]. For Bragg energies  $\hbar\omega$  below  $2\Delta$  and sufficiently low momentum  $\hbar k$ , a gapless collective (Bogoliubov-Anderson) mode arises from exciting pairs. Physically this mode relates to a (zero) sound wave with a linear energy dispersion relation. In the BCS limit where  $E_{\text{k}} = c_{\text{s}}\hbar k$ , the linearity of this dispersion is limited to  $k \ll k_{\text{F}}$ , whereas at unitarity the dispersion remains linear for much higher  $k \lesssim k_{\text{F}}$ . Here,  $c_{\text{s}} = v_{\text{F}}/\sqrt{3}$  is the speed of sound and  $v_{\text{F}} = \hbar k_{\text{F}}/m$  the Fermi velocity. The mode is damped for excitations above the binding energy as it merges into the continuum of pair-breaking excitations. As the scattering length is scanned across the Feshbach resonance, the collective mode smoothly evolves into the Bogoliubov sound wave in a mBEC with  $E_{\text{k}} = \sqrt{c_{\text{s}}^2 \hbar^2 k^2 + [\hbar^2 k^2 / (2m_{\text{M}})]^2}$  and slope  $c_{\text{s}} = v_{\text{F}}/\sqrt{3\pi k_{\text{F}} a}$  and does not merge with the continuum (see also the discussion in section 4.4.1 on page 106).

It is interesting to note that Bragg scattering actually can probe the collective mode of Cooper pairs despite the fact that the associated Bragg velocity  $v = \omega/k$  exceeds Landau's critical velocity beyond which superfluidity breaks down and which in the BCS regime is given by pair breaking excitations,  $v_{\text{c}} = \min_{\text{k}}(E_{\text{k}}/k) < c_{\text{s}}$  [Com06b]. This is because the Bragg perturbation is sudden and weak, as required by linear response theory, hence it probes the gas in the physical state it was before the Bragg pulse is applied [Bru01].

While in this thesis we are interested in Bragg spectroscopy at high momentum to probe pair scattering and pair-breaking excitations, the observation of the sound mode requires low-momentum Bragg scattering of a Fermi gas [Min01, Oha03b] (cf. Outlook).

### 2.3.4. Universal properties of Fermi gases

In the following, I will briefly describe some properties of fermionic universality. Universal properties of Fermi gases in the BCS-BEC crossover and the unitarity limit are detailed in [Zwe12] and summarised in [Hu07, Ada12, Ran14].

Pairing in the BCS-BEC crossover can be considered universal in that it only depends on the parameters  $a$  and  $k_F$  but not on specific details of the system. This of course can be generalised to any other physical observables that describe the macroscopic properties of the Fermi gas. In the crossover regime, where the gas is dilute and strongly interacting, this leads to universal functions that essentially absorb all the complicated many-body effects to give surprisingly simple physical quantities. For example, the ground-state energies of single atoms in a BCS gas and molecules in a mBEC in the above discussed limits are, to lowest order and at  $T = 0$ , in the [Tan08c]

$$\text{BCS limit } (a \rightarrow 0_-): \quad \frac{E}{N} = \frac{3}{5} E_F \left( 1 + \frac{10}{9\pi} k_F a + \dots \right), \quad (2.3.7)$$

$$\text{unitarity limit } (1/|a| \simeq 0): \quad \frac{E}{N} = \frac{3}{5} E_F \left( \xi - \frac{\zeta}{k_F a} + \dots \right), \quad (2.3.8)$$

$$\text{BEC limit } (a \rightarrow 0_+): \quad \frac{E}{N_M} = E_b + \frac{2\pi\hbar^2 a_M n_M}{m_M} + \dots, \quad (2.3.9)$$

where  $\xi$  is the superfluid Bertsch parameter, a universal function which at unitarity reduces to a pure number,  $N_M = N/2$  and  $\zeta \approx 1$ . While BCS theory gives  $\xi = 0.59$  [Eng97], recent theoretical calculations predict  $\xi$  to range between  $0.36 - 0.46$  [Ada12, Zwe12]. Most recent measurements found  $\xi = 0.376(4)$  [Ku12],  $0.370(5)$  [Zür13] and  $\zeta = 0.93(5)$  [Nav10]. Equation 2.3.8 shows that the energy near unitarity corresponds to the ideal gas result with a small correction.

A strongly interacting Fermi gas is characterised by a large scattering length  $a \gg n^{-1/3}$  and a vanishing interaction range  $r_0, r_{\text{eff}} \ll n^{-1/3}$  relative to the mean interatomic separation. Interactions therefore can be described in terms of  $(k_F a)$ , while possible corrections to interactions due to finite range effects of the scattering potential may be expressed by  $(k_F r_{\text{eff}})$ . Such a system exhibits universal scaling properties at the few- and many-body level, that is, thermodynamic (e.g. equation of state), transport (e.g. viscosity) and hydrodynamic (e.g. collective oscillations) properties are identical for all gases like  ${}^6\text{Li}$  or  ${}^{40}\text{K}$  in the BCS-BEC crossover regime. Most remarkably, universality links the physics of ultracold Fermi gases to neutrons, nuclear and quark matter or any other two-component spin-1/2 system that features identical scattering symmetries and mass ratios between the collision partners [Hei01].

Universality implies that any physical quantity of the atomic system is a function of  $1/(k_F a)$  and  $(T/T_F)$ . For example, the total energy per particle can be written as

$$\frac{E}{N} = E_F f_E \left[ \frac{1}{k_F a}, \frac{T}{T_F} \right], \quad (2.3.10)$$

where  $f_E$  is a dimensionless scaling function. Analogous expressions exist for all other thermodynamic variables describing the many-body properties of the system in thermal equilibrium, such as entropy, compressibility, specific heat and sound velocity, which may have different universal functions.

One way to learn about the thermodynamics of the gas is to measure the equation of state (EoS) through the density distribution of the atomic gas, such as the pressure  $P(\mu, T)$  [Nas10, Ku12]. The pressure relates to the density via  $n = (\partial P / \partial \mu)_T$ . In general, the knowledge of one particular EoS suffices to obtain all other thermodynamic quantities using thermodynamic identities [Sch00].

Of particular interest is the unitarity limit where  $a$  is infinitely large compared to all other length scales of the gas. Then, the only relevant length scale is the atomic separation in the density so that the set of parameters to describe the system is merely  $T$  and  $k_F^{-1}$ . At zero temperature,  $f_E(0, 0)$  reduces to the mentioned Bertsch parameter, a real number given by the ratio of the interaction energy of the ground state at unitarity and the kinetic energy  $E_F = \hbar^2 k_F^2 / (2m)$  of the free Fermi gas at the Fermi level. With  $\xi = 5 f_E(0, 0) / 3$ , also sometimes written as  $\xi = (1 + \beta)$ , various universal results are available in closed form. Sophisticated strong coupling theories are required to determine the value of  $\xi$ .

A homogeneous and harmonically trapped unitary Fermi gas have energies per particle,

$$\frac{E}{N} = \frac{3}{5} E_F \xi, \quad \text{where} \quad E_F = \frac{\hbar^2}{2m} (3\pi^2 n)^{2/3} \quad (\text{uniform}), \quad (2.3.11)$$

$$\frac{E}{N} = \frac{3}{4} E_F \sqrt{\xi}, \quad \text{where} \quad E_F = \hbar \bar{\omega} (3N)^{1/3} \quad (\text{trapped}). \quad (2.3.12)$$

Other quantities take similar simple expressions such as the chemical potential  $\mu = \xi E_F$  and pressure  $P = \xi \frac{2}{5} n E_F$ . The sound velocity of the collective mode at unitarity, mentioned in the last section, is with  $c_s = \sqrt{\xi/3} v_F$  somewhat lower than the BCS result. Also, the radius  $R_F$  of the cloud in a harmonic trap rescales by  $\xi^{1/4}$  compared to the Thomas-Fermi radius of an ideal gas given in equation 2.2.16. This shows that the quantities for a unitary gas are reduced compared to a ideal gas due to attractive interactions.

Much effort has been undertaken to characterise the thermodynamics of a unitary Fermi gas and to find the correct EoS, as nicely summarised in [Ada12]. The most accurate measurements of the EoS focus on local quantities only (within the LDA approximation),

## 2. Strongly interacting Fermi gases

do not rely on any models and avoid model-dependent temperature measurements which are usually the source of most uncertainty. Two experiments are highly relevant for this thesis as they provide the currently most precise value for the critical temperature, and also a model-independent scheme for calibrating the cloud temperature.

By analysing the density profiles of a harmonically trapped  ${}^6\text{Li}$  gas at unitarity, the MIT group has precisely determined the density EoS  $n(P, \kappa)$  as a function of pressure  $P$  and isothermal compressibility  $\kappa$  which quantifies the change in density relative to a change in the local trapping potential [Ku12]. The local quantities  $P$  and  $\kappa$  follow directly from the true density distribution,  $n(x, y, z)$ , reconstructed from the absorption images via the inverse Abel transform [Dri02]. Several thermodynamic variables for the superfluid and normal phase of the gas, such as free energy  $F$ , entropy  $S$  and chemical potential  $\mu$ , were deduced as a function of  $T/T_F$ . Based on analysing the specific heat  $C_V$  exhibiting an unmistakably sharp peak (lambda feature) at the superfluid phase transition, they were able to obtain a precise value for the homogeneous critical temperature:  $T_c = 0.167(13) T_F$ .

In a closely related experiment, the density EoS  $n(\mu, T)$  was measured by the MIT group and directly compared to high- and low-temperature calculations for a normal unitary  ${}^6\text{Li}$  gas to find a precise theoretical curve for the EoS [vH12]. Reliable temperatures can be obtained in the normal phase. We use the result of this work to provide a fit function for the high- $T$  wings of the density profiles, where the gas is in the normal phase, to obtain temperatures with low error bounds for the measurements of the contact presented in chapter 4. The method for this temperature calibration will be outlined in section 4.3.3.

Next, I will describe a class of universal relations for fermionic systems which connect universal two- and many-body physics via the contact, known as the Tan relations.

### 2.3.5. Exact universal relations and Tan's contact parameter

In the following, I will summarise important Tan relations which yield exact universal results across the entire BCS-BEC crossover of an atomic Fermi gas in the zero-range limit ( $k_F r_0 \rightarrow 0$ ). For more details see for example [Ran14] and the excellent review in [Bra12] which also gives a nice overview of various derivations of the Tan relations.

Several of these relations were derived by Shina Tan based on a dilute two-component Fermi gas with large scattering length  $a$  [Tan08a, Tan08b, Tan08c]. Tan thereby introduced the universal contact  $\mathcal{I}$ , a key parameter for many-body systems sensitive to the short-range (large-momentum) and short-time (high-frequency) properties of two-body interactions. All exact universal relations discovered to date embody the contact, and so they are commonly referred to as the Tan relations. The contact and any of these relations

are defined for fermions with large momentum  $\hbar k$  in a range given by the inverse length scales present in the gas,

$$\frac{1}{|a|}, \frac{1}{k_F}, \frac{1}{\lambda_{\text{dB}}} \ll k \ll \frac{1}{r_0}. \quad (2.3.13)$$

The Tan relations link microscopic two-body scattering properties to macroscopic thermodynamic variables. They can be applied to numerous physical settings in a quite general context: Bose or Fermi gases (liquids), zero or finite temperatures, weak or strong interactions, superfluid or normal phases, few- or many-body, equilibrium or non-equilibrium, trapped or homogeneous and balanced or imbalanced spin mixtures. The central quantity is Tan's (total) contact parameter defined as

$$\mathcal{I} = \lim_{k \rightarrow \infty} k^4 n_\sigma(\mathbf{k}), \quad (2.3.14)$$

where  $n_\sigma(\mathbf{k})$  is the momentum density of either of the two spin states, normalised such that  $\int n_\sigma(\mathbf{k}) d\mathbf{k} / (2\pi)^3 = N_\sigma$ . Here  $N_\sigma$  is the total number of atoms in one spin state; note that  $N_\uparrow$  and  $N_\downarrow$  can be different. The Tan relation 2.3.14 implies that firstly the contact is identical for both spin states, secondly the contact has dimension ( $\text{m}^{-1}$ ) and thirdly the density distribution decays as  $n_\sigma(\mathbf{k}) \rightarrow \mathcal{I}/k^4$  at large  $k$  as a result of the interactions. The power-law dependence of the asymptotic tail was known before [Viv04], Tan found that the magnitude of the tail in the outermost part of the density wings is determined by the thermodynamics of the gas, expressed through  $\mathcal{I}$ .

The relation 2.3.14 has been experimentally verified in a trapped  $^{40}\text{K}$  Fermi gas [Ste10]. Also, the trapped contact was probed in a universal Bose gas ( $^{85}\text{Rb}$ ) but the results were inconclusive [Mak14]. Based on definition 2.3.14, it was demonstrated that the large- $k$  tail of the momentum density also provides a measure of the mean number of closed-channel Feshbach molecules, obtained through photoassociation measurements [Par05, Wer09].

The total contact  $\mathcal{I}$  is an extensive quantity, and so it can be obtained by integrating the local contact density  $\mathcal{C}(\mathbf{R})$  over space as per

$$\mathcal{I} = VC = \int \mathcal{C}(\mathbf{R}) d\mathbf{R}, \quad (2.3.15)$$

where  $\mathbf{R}$  is the centre-of-mass position of a pair of atoms. The volume  $V$  equals either the size of a homogeneous gas to give the average contact  $C$  or, for a trapped gas, extends over a region much larger than the trap size to include all confined atoms. Thus, the unit of the contact density is ( $\text{m}^{-4}$ ). In this thesis, and in general, we refer to

$$\frac{\mathcal{C}(\mathbf{R})}{n(\mathbf{R})k_F} \equiv \frac{C}{nk_F} \quad (\text{homogeneous}), \quad \frac{\mathcal{I}}{Nk_F} \quad (\text{trapped}),$$

## 2. Strongly interacting Fermi gases

as the dimensionless contact density and the dimensionless total contact, respectively.

While the derivation of the contact requires to some extent sophisticated theoretical methods, its physical interpretation is quite intuitive: The contact density quantifies the probability of finding two Fermi atoms in different spin states at separations much smaller than all other length scales in the system; or in other words, the contact is proportional to the number of closely spaced pairs. It is interesting to note that the number of pairs in a small volume scales as  $V_{\text{small}}^{4/3}$ , which is an unusual scaling behaviour [Bra09]. This is due to the strong pair correlations present in this small volume leading to a larger number of pairs than one would expect by considering the more intuitive scaling volume  $V_{\text{small}}^2$  for a noninteracting system.

Tan showed that the contact density contains all thermodynamic information of a universal gas, in fact,  $\mathcal{C}$  is determined, like all other thermodynamic quantities, by a dimensionless universal function specifying the many-body behaviour,  $\mathcal{C} = k_{\text{F}}^4 c[1/(k_{\text{F}}a), T/T_{\text{F}}]$ . A detailed knowledge of the contact density throughout the BCS-BEC crossover therefore allows not only to calculate  $\mathcal{I}$  via equation 2.3.15 together with the LDA (cf. section 2.2) but also, thanks to the Tan relations, to directly relate microscopic properties, such as pair correlations, to the (macroscopic) EoS of a homogeneous Fermi gas with strong interactions [Nav10].

An important Tan relation is the adiabatic sweep theorem which states that the contact is proportional to the rate of change of the total energy due to a small change in the inverse scattering length,

$$\left[ \frac{dE}{d(1/a)} \right]_{S,N} = -\frac{\hbar^2}{4\pi m} \mathcal{I}, \quad (2.3.16)$$

while keeping  $S$  and  $N$  fixed. Here, the energy is the sum of kinetic, potential and interaction energy,  $E = E_{\text{kin}} + E_{\text{pot}} + E_{\text{int}}$ . Note that this also works with the free energy  $F$  or the thermodynamic potential  $\Omega$ . From this all other thermodynamic functions are determined. However, this requires the a priori knowledge of the contact as a function of  $k_{\text{F}}a$  to calculate the accumulated energy after the adiabatic sweep. Equation 2.3.16, together with the generalised virial theorem,  $E_{\text{kin}} + E_{\text{int}} - E_{\text{pot}} = -\hbar^2 \mathcal{I}/(4\pi k_{\text{F}}a)$ , which is another Tan relation, has been experimentally verified by the JILA group in the BCS-BEC crossover of  $^{40}\text{K}$  atoms [Ste10].

The energy relation, which is yet another Tan relation, shows how the sum of kinetic and interaction energy of the gas relates to the momentum distribution via the contact,

$$E_{\text{kin}} + E_{\text{int}} = \sum_{\sigma=\uparrow,\downarrow} \int \frac{d\mathbf{k}}{(2\pi)^3} \frac{\hbar^2 k^2}{2m} \left[ n_{\sigma}(\mathbf{k}) - \frac{\mathcal{I}}{k^4} \right] + \frac{\hbar^2 \mathcal{I}}{4\pi a m}. \quad (2.3.17)$$

The terms proportional to the contact describe the interaction energy. This relation has no ultraviolet divergence as the  $1/k^4$ -term in  $n_\sigma$  is cancelled by the interaction term.

Tan's adiabatic sweep theorem can be used, by rearranging equation 2.3.16 and dividing both sides by the volume to get  $\mathcal{C} = 4\pi m a^2 / \hbar^2 (dE/da)$ , to calculate analytic expressions for the  $T = 0$  contact density of a spin-balanced homogeneous Fermi gas in the crossover limits where the low-order ground-state energies are well known (see previous section). To lowest order, the contact is in the [Bra12, Hu11]

$$\text{BCS limit:} \quad \mathcal{C} = 4(\pi n a)^2 \quad \Rightarrow \quad \frac{\mathcal{I}}{N k_{\text{F}}} = \frac{4}{3} (k_{\text{F}} a)^2, \quad (2.3.18)$$

$$\text{unitarity limit:} \quad \mathcal{C} = \frac{2\zeta}{5\pi} (3\pi^2 n)^{4/3} \quad \Rightarrow \quad \frac{\mathcal{I}}{N k_{\text{F}}} = \frac{512\zeta}{175 \xi^{1/4}}, \quad (2.3.19)$$

$$\text{BEC limit:} \quad \mathcal{C} = \frac{4\pi n}{a} \quad \Rightarrow \quad \frac{\mathcal{I}}{N k_{\text{F}}} = \frac{4\pi}{k_{\text{F}} a}. \quad (2.3.20)$$

The short-range properties of Fermi gases prompts a Tan relation which is particularly useful for high-momentum Bragg spectroscopy where  $k \gg k_{\text{F}}$  (see chapter 4). The instantaneous pair correlations between  $|\uparrow\rangle$  and  $|\downarrow\rangle$  atoms are governed by the density-density correlation function  $g_{\uparrow\downarrow}$  which for small  $r$  is given by the square of the two-particle wavefunction  $\phi(r)$  so that  $g_{\uparrow\downarrow}(r \ll k_{\text{F}}^{-1}) \equiv \int \langle \hat{\rho}_{\uparrow}(\mathbf{R} - \mathbf{r}/2) \hat{\rho}_{\downarrow}(\mathbf{R} + \mathbf{r}/2) \rangle d\mathbf{R} = |\phi(r)|^2$ , where  $\hat{\rho}_\sigma$  is the atomic density operator of one spin state [Zha09]. In this limit, this corresponds to the short-range expansion of the Halo wavefunction introduced in equation 2.3.5,

$$\phi(r) = A \left( \frac{1}{r} - \frac{1}{a} \right) + \mathcal{O}(r) \quad \text{for} \quad r \rightarrow 0. \quad (2.3.21)$$

It turns out that the square of the coefficient  $A \equiv A(\mathbf{R})$  in front of  $\phi(r)$ , describing the centre-of-mass motion of a pair with centre-of-mass position  $\mathbf{R}$ , is nothing else than the contact density and hence integration leads to  $\mathcal{I} = 16\pi^2 \int |A(\mathbf{R})|^2 d\mathbf{R}$  [Tan08c]. By this, the Tan relation for the two-body pair distribution function yields

$$g_{\uparrow\downarrow}(r \rightarrow 0) = \frac{\mathcal{I}}{16\pi^2} \left( \frac{1}{r^2} - \frac{2}{ar} \right) \quad (2.3.22)$$

revealing a  $1/r^2$ -divergence at small distances. The two-body correlator is related to the static structure factor of the antiparallel spin component through [Com06a]

$$S_{\uparrow\downarrow}(k) = \frac{n}{2} \int [g_{\uparrow\downarrow}(r) - 1] e^{i\mathbf{k}\cdot\mathbf{r}} d\mathbf{r}, \quad (2.3.23)$$

where  $n$  is the total density. The Fourier transform of  $g_{\uparrow\downarrow}(r)$  in equation 2.3.22 then leads directly to a universal relation for the antiparallel static structure factor [Hu10b]

$$S_{\uparrow\downarrow}(k \gg k_{\text{F}}) = \left( \frac{\mathcal{I}}{N k_{\text{F}}} \right) \frac{k_{\text{F}}}{4k} \left[ 1 - \frac{4}{\pi k_{\text{F}} a} \frac{k_{\text{F}}}{k} \right], \quad (2.3.24)$$

## 2. Strongly interacting Fermi gases

showing a simple linear dependence on the contact. In combination with the static structure factor for correlations of parallel spins,  $S_{\uparrow\uparrow}(k)$ , approaching unity in the limit of large momenta due to autocorrelations, the total static structure factor  $S(k) = 2[S_{\uparrow\uparrow}(k) + S_{\uparrow\downarrow}(k)]$  allows to directly measure the contact using two-photon Bragg spectroscopy [Vee08].

In previous experiments, we measured the trap-averaged contact as a function of interaction strength  $1/(k_F a)$  [Kuh10], and for a unitary Fermi gas also as a function of temperature [Kuh11b].  $S_{\uparrow\downarrow}(k) = S(k)/2 - 1$  was obtained by normalising and integrating measured Bragg spectra (as will be explained in section 4.2 on page 78 ff.). As the relative probe momentum ( $k/k_F$ ) can be determined to high accuracy, the only unknown quantity is the contact. We found that  $\mathcal{I}[1/(k_F a), T/T_F]/(Nk_F)$  follows a monotonous decreasing function for decreasing  $1/(k_F a)$ , and also monotonously decreases for increasing temperatures as seen at  $1/(k_F a) = 0$ . These results will be complemented by new high-precision measurements of the low-temperature contact presented in chapter 4, section 4.4.2.

Universal short-time properties of strongly interacting Fermi gases can be examined by probing high-frequency tails of various spectral functions. They all are proportional to  $\mathcal{I}/\omega^\gamma$ , where  $\gamma$  depends on the actual measured dynamic quantity [Ran14]. Two standard techniques in cold atom experiments that probe response functions are radio-frequency (RF) [Chi04, Shi07, Ste08] and two-photon Bragg spectroscopy [Ste99, Vee08]. Universal behaviour should be visible for  $\omega \rightarrow \infty$ , which in real experiments means the excitation frequencies have to range in the interval  $\hbar k_F^2/(2m) \ll \omega \ll 1/(mr_0^2)$ .

One example of an observable that features a universal high-frequency tail is the spectrum of the shear viscosity,  $\eta(\omega) \propto \mathcal{I}\omega^{-1/2}$ . It was shown that at unitarity the bulk viscosity  $\zeta(\omega) \equiv 0, \forall \omega, T$  so that the spectrum only contains information of  $\eta(\omega)$  alone. As  $\eta(\omega)$  turns out to be proportional to the dynamic structure factor for  $k \rightarrow 0$  it should in principle be possible to observe this universality in a low-momentum Bragg spectrum ( $k \ll k_F$ ) of a unitary homogeneous Fermi gas [Son10, Tay10, Ens11]. (The dynamic structure factor,  $S(\mathbf{k}, \omega)$ , is defined in section 4.2.) Whether the response in the Bragg signal is strong enough for reliable data analysis however remains an open question.

Universal features can also be revealed in a RF spectrum of the integrated response of the single-atomic spectral function over all momenta. In a strongly interacting Fermi gas,  $I(\omega) \propto \mathcal{I}\omega^{-3/2}$  when final-state effects are small (this means, there are only weak interactions between two atoms after RF transferring one atom of the pair into an unpopulated spin state) [Bra10]. Such universal behaviour in  $I(\omega)$  was used to extract the contact in a series of measurements verifying Tan relations [Ste10].

Last but not least, the respective high-frequency tails of the large-momentum spin and density dynamic structure factors,  $S_{S,D}(\mathbf{k}, \omega)$ , are proportional to  $\mathcal{I}\omega^{-5/2}$  and  $\mathcal{I}\omega^{-7/2}$ . We have confirmed the universal behaviour of  $S_S(\mathbf{k}, \omega)$  by measuring high-frequency Bragg spectra of the individual spin components. This will be described in detail in chapter 5, section 5.3.4.

## 2.4. Summary

In this chapter, I revised basic facts on ultracold Fermi gases based on  ${}^6\text{Li}$  atoms in an 3D optical dipole trap with the intention to provide an adequate physical background of the system we study, and, to point to references for a more detailed treatment on specific topics.

After summarising some fundamentals on noninteracting Afermions, I focussed on two-component Fermi gases with tunable  $s$ -wave interactions. The discussion includes a brief summary of the principles of low-energy atomic collisions and a qualitative description of broad Feshbach resonances, the standard tool for tuning two-body interactions between nonidentical Fermi atoms. After that, I described the phase diagram of an attractive BCS-BEC crossover in order to convey an intuitive physical picture of fermionic pairing in the normal and superfluid phase as a function of interaction strength and temperature.

The chapter continues with a brief description of universal properties of two-component Fermi gases, a remarkable feature that allows to put the results of ultracold atom experiments into a more general context of strongly correlated fermionic many-body systems. Universal relations were described based on thermodynamic quantities to show that these observables are essentially ideal gas equations scaled by universal many-body functions.

Finally, exact Tan relations and in particular the contact parameter were discussed to make a connection with chapter four and five, where precision Bragg spectroscopical measurements of dynamic structure factors as well as the contact will be presented.



## 3. Experimental setup and procedure

### 3.1. Introduction

The starting point of all our experiments is a gas of ultracold  ${}^6\text{Li}$  atoms prepared in an equal mixture of the two hyperfine states  $|F = 1/2, m_F = \pm 1/2\rangle$ , labelled  $|\uparrow\rangle$  and  $|\downarrow\rangle$ . Many aspects on the production of such a gas and the usage of our apparatus have been detailed in earlier theses of our group [Fuc09, Vee09, Dyk10]. In this chapter, I will therefore focus on the essential experimental steps required to create degenerate Fermi gases and include references for further details. Special attention however is drawn to upgrades and improvements of the setup and procedures made as part of this thesis, mostly as a result of experience gained over the past few years working with this machine.

The following section explains how we confine lithium atoms in a combined optical and magnetic trap using a far-detuned focussed laser beam along with the Feshbach coils. In section 3.3, I will summarise the  ${}^6\text{Li}$  production cycle up to that point at which Bragg scattering experiments can be performed. Section 3.3.2 highlights the modifications made to the laser system for the magneto-optical trap (MOT) to improve its performance, in particular to the tapered amplifier. Our new absorption imaging system will be described and characterised in detail in section 3.4.

### 3.2. Trapping neutral atoms

Trapping ultracold neutral atoms is commonly accomplished through magnetic or optical trapping potentials or a combination of both [Met99]. Magnetic traps represent a prime example for nearly ideal conservative traps, and, their potential shape can be designed to be almost purely harmonic [Ber87]. The downside is that magnetic trapping restricts the internal atomic states available to be trapped. Thus, experiments which depend on a varying magnetic field or altering atomic states (spin flips) can quickly become unfeasible. Lithium, for example, cannot be trapped magnetically in any of the three lowest hyperfine

### 3. Experimental setup and procedure

ground states in the presence of a moderate to strong external magnetic field ( $\gtrsim 50$  G). In contrast, optical traps can confine atoms with sufficiently low kinetic energy in any spin state at any applied homogeneous magnetic field and are therefore ideal for our experiments. We use single-beam optical dipole traps to confine and evaporatively cool lithium atoms. (In fact, for trapping we use a combination of magnetic and optical fields, as discussed in detail in the following sections.) Typically, the maximum attainable trap depths can reach up to 100 mK for magnetic traps and 1 mK for optical traps.

#### 3.2.1. Focussed-beam optical dipole traps

The first optical trapping experiment on cold neutral atoms was realised by Chu *et al.* in 1986 [Chu86]. Since then, optical dipole traps have become a powerful tool to confine and manipulate atomic gases. An introduction to this topic can be found in [Met99, Pet08], a comprehensive discussion of trapping alkali atoms in far-detuned optical traps is given in the review article [Gri00].

Optical trapping utilises electric dipole interactions between atoms and spatially inhomogeneous intensity of an optical field,  $I(\mathbf{r})$ . Atoms in the presence of light, for example laser beams, become polarised through induced dipole moments. The resulting dipole potential shifts the electronic energy levels of these atoms proportional to the light intensity. This effect is known as the AC-Stark shift. If the intensity is spatially varying, a nonzero conservative force derives from the gradient field of the dipole potential,  $\mathbf{F}_{\text{dip}} = -\nabla U_{\text{dip}}$ . With suitable laser beam geometry such dipole forces can facilitate a three dimensional confinement for neutral atoms.

The trapping laser frequencies  $\omega$  are often chosen to be far from an atomic resonance  $\omega_0$  frequency to keep the atoms mostly in the ground state by avoiding absorption and spontaneous emission. In this case, the  $D$ -line doublet transitions of alkali atoms simplify to that of a two-level atom, and the potential depth takes the form<sup>1</sup>

$$U_{\text{dip}}(\mathbf{r}) = -\frac{\hbar\Gamma^2}{8} \left( \frac{1}{\omega_0 - \omega} + \frac{1}{\omega_0 + \omega} \right) \frac{I(\mathbf{r})}{I_{\text{sat}}} \approx \frac{\hbar\Gamma^2}{8\Delta} \frac{I(\mathbf{r})}{I_{\text{sat}}}, \quad (3.2.1)$$

where  $\Gamma = 2\pi \times 5.87$  MHz is the natural line width,  $I_{\text{sat}} = \hbar\Gamma\omega_0^3/(12\pi c^2) = 2.54$  mW/cm<sup>2</sup> the saturation intensity and  $\Delta = \omega - \omega_0$  is the detuning (values for lithium [Geh03]).

---

<sup>1</sup>Note that for frequency detunings in the range of the splitting of the  $D_1$  and  $D_2$  lines and below the internal atomic electron structure as well as the polarisation of the trapping laser become important and may modify the expressions for  $U_{\text{dip}}$  and  $\Gamma_{\text{sc}}$  [Gri00].

Atom-light interactions also generate dissipative effects in atomic gases due to photon absorption and spontaneous re-emission processes in random directions. This is widely used for laser cooling techniques but undesired for trapping ultracold atoms. The heating power, hence the associated radiation pressure, is proportional to the photon scattering rate

$$\Gamma_{\text{sc}}(\mathbf{r}) = \frac{\Gamma^3}{8} \left( \frac{\omega}{\omega_0} \right)^3 \left( \frac{1}{\omega_0 - \omega} + \frac{1}{\omega_0 + \omega} \right)^2 \frac{I(\mathbf{r})}{I_{\text{sat}}} \approx \frac{\Gamma^3}{8\Delta^2} \frac{I(\mathbf{r})}{I_{\text{sat}}}. \quad (3.2.2)$$

Typically,  $1/\Gamma_{\text{sc}}$  should remain small compared to the time scale of the experiment. The approximations given in both equations provide reasonably accurate values at small detuning  $|\Delta| \ll \omega_0$  and are commonly used for practical purposes<sup>2</sup>. Comparing both equations, one sees that the scattering rate falls off as  $I/\Delta^2$ , whereas the trap depth only decreases as  $I/\Delta$ . Thus, for a given laser power, optical dipole traps usually use large detunings to keep the scattering rate as low as possible. Furthermore, equation 3.2.1 indicates that for red detuning ( $\Delta < 0$ ) the potential is negative and the dipole force attracts atoms towards the intensity maximum of the trap, while for blue detuning ( $\Delta > 0$ ) the potential is positive and the interaction repels atoms out of the field.

The simplest way to trap atoms optically is focussing a laser beam shaped by a TEM<sub>00</sub> Gaussian mode at frequencies below the atomic resonance frequency. The intensity profile  $I(\mathbf{r})$  for such a cylindrically symmetric beam, assuming propagation in  $z$ -direction, can then be written as

$$I(r, z) = \frac{2P}{\pi w^2(z)} \exp\left(-2\frac{r^2}{w^2(z)}\right). \quad (3.2.3)$$

Here,  $r = \sqrt{x^2 + y^2}$  is the radial distance from the beam axis and  $P$  the total laser power. The waist radius  $w(z)$  defines the radial distance at which the intensity drops to  $1/e^2$  of its peak value and varies as

$$w(z) = w_0 \sqrt{1 + \left(\frac{z}{z_{\text{R}}}\right)^2}, \quad (3.2.4)$$

where  $z_{\text{R}} = \pi w_0^2/\lambda$  is the Rayleigh range. The maximum intensity,  $I_0 = 2P/(\pi w_0^2)$ , occurs at the beam centre with minimum waist radius  $w_0$ . Note, the coordinate system throughout this work is right handed with the  $z$ -axis collinear to the propagation direction of the trapping laser used for all Bragg scattering experiments.

---

<sup>2</sup>Example for <sup>6</sup>Li: A detuning  $\Delta$  of  $\pm 10\%$ , which corresponds to a shift in wavelength of  $\pm 70$  nm, leads to an error in the potential depth of about  $\pm 5\%$ .

### 3. Experimental setup and procedure

To trap any atoms the potential has to be significantly deeper than the temperature  $T$  of the atoms. When  $T \ll U_{\text{dip}}(\mathbf{r})/k_B$  the atomic sample stays close to the trap centre. Then, the deepest part of the potential is harmonic to leading order of the Taylor-expanded equation 3.2.1, combined with equation 3.2.3, giving

$$U_{\text{dip}}(r, z) \simeq -U_0 \left[ 1 - 2 \left( \frac{r}{w_0} \right)^2 - \left( \frac{z}{z_R} \right)^2 \right], \quad (3.2.5)$$

where  $U_0 = \hbar\Gamma^2 P / (4w_0^2 \Delta I_{\text{sat}})$  for a Gaussian mode. Comparing this expression for  $U_{\text{dip}}$  with that of a harmonic oscillator,

$$\omega_{\text{opt}(r)} = \sqrt{\frac{4U_0}{mw_0^2}} \quad \text{and} \quad \omega_{\text{opt}(z)} = \sqrt{\frac{2U_0}{mz_R^2}} \quad (3.2.6)$$

can be inferred as the oscillation frequencies for the radial and axial direction, respectively. Typical focal waist sizes of the optical traps in our experiments lie in the range of several 10 to some 100  $\mu\text{m}$  (cf. the description of the experiment in section 3.3).

The aspect ratio of the trap,  $\omega_{\text{opt}(r)}/\omega_{\text{opt}(z)} = \sqrt{2}\pi w_0/\lambda$ , points out that for such beams the confinement in the axial direction is often far too weak to trap any atoms. However, the next section describes how we circumvent this issue by taking advantage of the residual magnetic field curvature produced by the Feshbach coils.

#### 3.2.2. Magnetic trapping with Feshbach coils

All Bragg scattering experiments in this thesis are carried out at high magnetic fields,  $\mathbf{B}$ , where a cold gas of  ${}^6\text{Li}$  atoms in the  $|\uparrow\rangle$  and  $|\downarrow\rangle$  states exhibit a broad Feshbach resonance close to 832 G. An overview of all relevant electronic states and their dependence on an external magnetic field is given in appendix A. When the magnetic field exceeds  $\sim 50$  G these atoms become high-field seeking, and the magnetic dipole interaction pulls them towards regions of strong fields in the presence of a magnetic gradient.

The ‘‘Feshbach’’ field is produced by a set of Helmholtz coils capable of creating a near homogeneous magnetic field up to 1500 G. The orientation of this field is parallel to earths gravity. Since the separation of the coils is slightly larger than that of an ideal Helmholtz configuration, the Feshbach field features a residual curvature,  $\mathbf{B}''$ . For high-field seeking states, this leads to a rotationally symmetric confinement in the  $xz$ -plane (horizontal) and an anti-trapping potential in the  $y$ -direction (vertical).

The vertical axis defines the symmetry axis of the split pair coil. The magnetic potential, which always superposes the confinement of the optical dipole trap, can be harmoni-

cally approximated, for example, along the  $z$ -axis by

$$U_{\text{mag}} = -\frac{\mu_B}{2} \frac{\partial^2 \mathbf{B}}{\partial z^2} z^2 = -\frac{1}{2} m \omega_{\text{mag}}^2 z^2, \quad (3.2.7)$$

where  $\mu_B$  is Bohr's magneton and  $m$  the atom's mass. The curvature was calculated to be  $B'' = 0.0306 \text{ G/cm}^2$ . Due to rotational symmetry, the anti-trapping frequency  $\omega_{\text{anti}}$  has to be  $(i\sqrt{2})$  times the trapping frequency  $\omega_{\text{mag}}$ .

The frequencies of the magnetic trap were previously measured by parametrically heating atomic clouds in a crossed optical dipole trap [Fuc09], and, by observing sloshing motion of atoms in a single beam optical dipole trap [Dyk10]. Sloshing is accomplished by quickly switching an auxiliary magnetic field gradient for several milliseconds which displaces the atomic sample and triggers an oscillation. In the course of precision measurements on unitary Fermi gases we have repeated the frequency measurements of the magnetic trap at 833 G using the sloshing method and find for

$$\text{trapping: } \omega_{833\text{G}} = 2\pi \times 24.5 \text{ Hz}, \quad \text{anti-trapping: } \omega_{i833\text{G}} = 2\pi \times i34.6 \text{ Hz}. \quad (3.2.8)$$

We use the value for trapping to calculate magnetic trapping frequencies at any magnetic field, according to  $\omega_{\text{mag}} = \omega_{833\text{G}} \sqrt{B(\text{G})/833\text{G}}$ . The total optical and magnetic trapping frequencies combine in quadrature to

$$\omega_{x,z} = \sqrt{\omega_{\text{opt}(x,z)}^2 + \omega_{\text{mag}}^2} \quad \text{and} \quad \omega_y = \sqrt{\omega_{\text{opt}(y)}^2 + \omega_{\text{anti}}^2}. \quad (3.2.9)$$

The measurement of the optical trapping frequencies  $\omega_{\text{opt}}$  is described in section 4.3.3. For trapping with single focussed beams, the frequency in the laser propagation direction is  $\omega_z \simeq \omega_{\text{mag}}$  as the magnetic contribution to the confinement usually completely dominates. The atoms in the combined trap appear as an elongated cigar-shaped cloud and experience a total geometric mean trapping frequency of

$$\bar{\omega} = (\omega_x \omega_y \omega_z)^{1/3}. \quad (3.2.10)$$

The vertical position of the atoms happens to be slightly below the symmetry centre of the Feshbach coils. Without compensation, this causes an upwards acceleration of the atoms after switching off optical trapping. This drift is canceled by an installed pair of quadrupole coils producing a vertical magnetic field gradient. For a given Feshbach field, we adjust the magnetic force such that the centre-of-mass position of the cloud remains stationary without the optical trap. This offers the advantage that the cloud does not leave the imaging plane during time-of-flight measurements (cf. section 3.4.1).

### 3. Experimental setup and procedure

**Feshbach coils:** The following briefly summarises the main specifications of the high-field magnets in Helmholtz configuration. Each of the coils comprises 51 turns of Kapton insulated, square cross section ( $3.3 \times 3.3 \text{ mm}^2$ ), hollow (1.6 mm diameter circular hole) copper tubing glued on a reel made of hard plastic to reduce Eddy currents. An inductance of 433  $\mu\text{H}$  was measured allowing field switching times from zero to 833 G in about 80 ms with current electronics. The inner diameter of the coils is 70 mm, the outer 110 mm. Including the reel, the inner diameter reduces to 55 mm. The coils are separated by 35 mm (distance between inner surfaces). The magnetic field is voltage controlled through a 16 bit analog IO-card that is part of the experiment computer. The field is actively stabilised to the control voltage by a home-made PI-servo connected to the power supply with feedback provided by an ultra stable current transducer that has an overall accuracy of 0.0044 %. The current carrying wire passes through the transducer twice leading to a 50 mG/mV resolution of the magnetic field. Further details can be found in [Fuc09]. In a typical experimental cycle, the Feshbach coils dissipate power of about 2.3 kW for several seconds. To improve the cooling efficiency of the coils, and hence to shorten the waiting time for cooling between cycles, I have replaced the original low-pressure tap water cooling system by a high-pressure closed loop cooling system driven by a chiller.

## 3.3. Production of ultracold ${}^6\text{Li}$ quantum gases

In this section, I describe the vacuum system, laser equipment as well as the main production steps required to obtain clouds of degenerate Fermi gases. Trapping, cooling, and state preparation takes place in an ultra-high vacuum environment to isolate the atoms from collisions with high-temperature background gas.

### 3.3.1. Vacuum system

The vacuum system is divided into a high (HV) and an ultra-high (UHV) vacuum chamber, as illustrated in figure 3.3.1. At the HV end, shown to the left of the in-line valve, an atomic oven produces lithium vapour with sufficient high densities for efficient laser cooling. The atomic oven contains pieces of 95 % enriched  ${}^6\text{Li}$  isotope (total mass  $\sim 2$  grams) inside a stainless steel tube that is wrapped with heating wire<sup>3</sup> and thermally insulated. As the

---

<sup>3</sup>We use a 3 m long resistance wire (RS order No. 749-6341, company Block) with 1.73  $\Omega/\text{m}$ , insulated by ceramic beads (RS order No. 764-8731), providing a maximal heating power of 180 W.

### 3.3. Production of ultracold ${}^6\text{Li}$ quantum gases

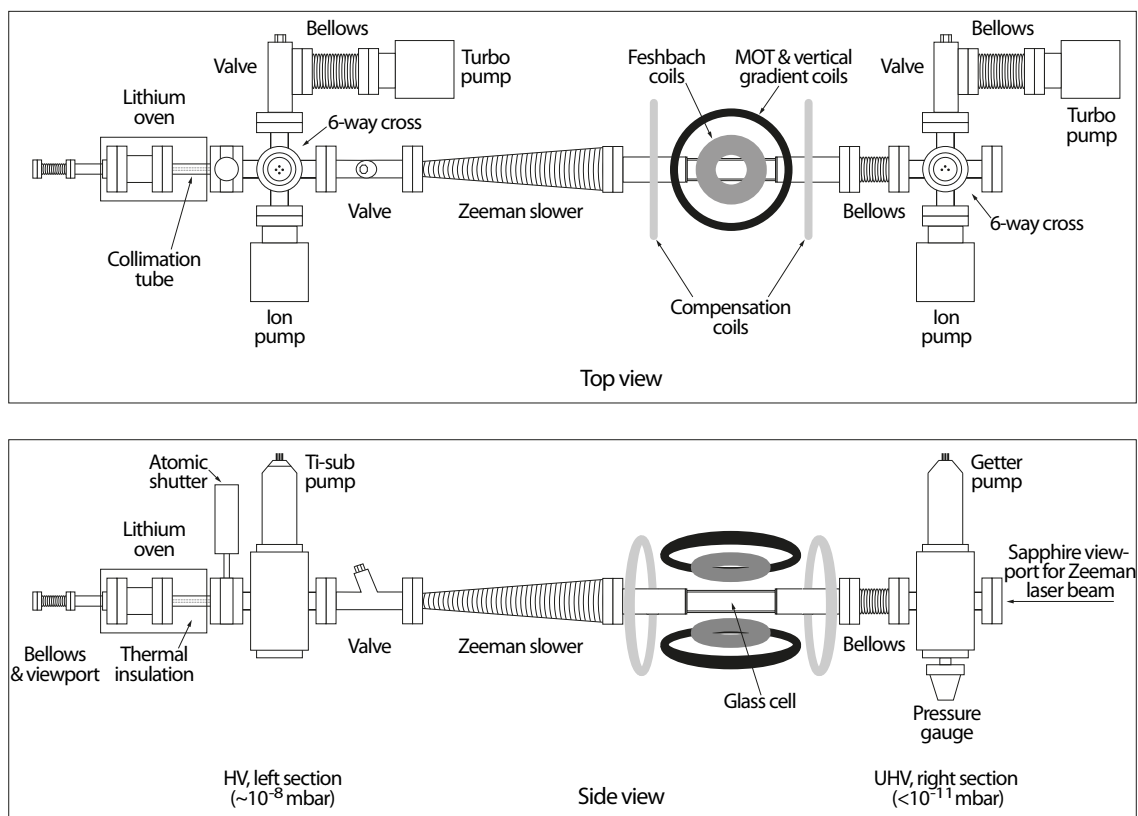


**Figure 3.3.1.:** Top and side view of the vacuum system of the apparatus (not to scale).

The main components are the lithium oven, Zeeman slower and glass cell. The overall length of the setup totals around 1.6 meters. Also shown are the locations of the magnetic coils relative to the glass cell.

amount of vapour produced by solid lithium at room temperature is minuscule we set the temperature of the oven to about  $360^\circ\text{C}$ . This corresponds to a vapour pressure of liquid lithium inside the oven of  $\sim 10^{-5}$  mbar. A stream of atoms exits the oven towards the UHV chamber at a mean velocity of about 1740 m/s through a collimating tube<sup>4</sup> of 10 cm length and an effective inner diameter of 4 mm. We have recently attached a viewport at the other end of the oven to facilitate the alignment of the Zeeman laser beam, as shown in figure 3.3.1. To reduce the deposit of lithium at the window, we fitted an aperture with a small hole of 1.2 mm diameter and 1.2 mm length inside the reducer flange and keep the window at room temperature by joining the viewport and oven with a bellows.

<sup>4</sup>The inner surface of the pipe is provided with a fine mesh woven stainless steel wire cloth to allow for recirculation of excess lithium back into the oven (wire spacing 0.1 mm, supplier Goodfellow).

### 3. Experimental setup and procedure

A six-way cross, which forms the HV chamber, connects the oven along with a 50 l/s ion pump, titanium sublimation pump, turbo molecular pump, mechanical shutter and a straight-through valve (figure 3.3.1). The pneumatically driven atomic shutter<sup>5</sup> is automatically controlled by the experiment control program. This is used to interrupt the flow of the atomic beam into the UHV region when there is no MOT loading. The in-line valve isolates the HV and UHV section when refilling lithium into the oven (this was necessary around mid-year of 2013 after more than six years of operation). Also, the permanently attached turbo pump is usually only required for re-evacuating the vessel after breaking the vacuum and is isolated by a valve.

The purpose of the Zeeman slower is twofold. Its main function is to slow down atoms using a spatially varying magnetic field in combination with laser light (more details in section 3.3.3). It also serves as a low-conduction tube for differential pumping to maintain a pressure difference between the two chambers by a factor of  $10^3$ . The Zeeman slower comprises a 300 mm tube divided into four sections with increasing inner diameters from the left to the right end. The length of the first two sections is 100 mm each with inner diameters of 4 mm and 6 mm, respectively. The inner diameter of the next two 50 mm long sections is 8 mm and 10 mm, respectively. With a resulting differential pumping speed through the Zeeman slower of roughly 0.1 l/s as well as the collimating tube of about 0.2 l/s, and, after firing the sublimation pump to coat its surrounding with a thin film of highly reactive titanium chemically binding some of the residual non-inert gas, we estimate the pressure inside the HV chamber to be less than  $10^{-8}$  mbar.

The heart of the apparatus, where the science takes place, is a customised glass cell made of Vycor quartz by Hellma with 100 mm long glass to metal transition sections fused to either side of the cell. The outer dimensions of the rectangular cell is  $120 \times 30.3 \times 30.3$  mm<sup>3</sup>, the wall thickness is 2.7 mm. Anti-reflection coating of the outside surface of the cell minimises back reflection of laser light at wavelengths of 671 nm and 1030 nm. On the right end, the glass cell is attached to an additional six-way cross via a bellows to reduce mechanical tension caused during the bake-out and by thermal expansion while operating the coils of the Zeeman slower, and to reduce mechanical vibrations when the turbo pumps are operating. Unfortunately, the left end of the glass cell is directly flanged to the Zeeman slower. Such a rigid construction is suboptimal as thermal expansion during each run of the experiment slightly moves the cell while taking experimental data. When imaging atoms,

---

<sup>5</sup>Viewport shutter with manual and pneumatic rotary drive, model: VPS38 by UHVdesign.com. Pneumatic valve: model EVK3120-5DO-01F-Q by SMC.

this can lead to fringes in the optical density images unless the time between consecutive images is rather short (which is the case as we use a camera in fast kinetics mode, see section 3.4.3). This suboptimal design, however, does help minimise the distance from the end of the Zeeman slower to the MOT collection region for efficient MOT loading.

The right section of the chamber consists of a 50 l/s ion pump and a non-evaporative getter pump, which are attached to a six-way cross. With these pumps UHV pressures below  $10^{-11}$  mbar are achieved (according to the pressure gauge!). Further components flanged to the six-way cross are a cold-cathode pressure gauge, an additional turbo pump and a sapphire viewport for optical access of the Zeeman slowing laser beam. We use sapphire instead of conventional glass as the deposit of lithium from the atomic beam at the window is highly corrosive to standard type glass. We also try to prevent lithium from coating the window by keeping the temperature of the viewport at  $80^\circ\text{C}$  (with only moderate success) and blocking the atomic beam when we take no data (with high success). The buildup of lithium at the viewport will ultimately lead to a decrease of the transmission of the Zeeman laser beam and hence the efficacy of the Zeeman slower.

The Zeeman laser system along with all other lasers required for cooling and manipulating  ${}^6\text{Li}$  atoms inside the vacuum chamber will be discussed in the next section.

#### 3.3.2. Laser layout and frequencies

In the following, I will describe the laser system and discuss the main technical improvements. The upgrades include a new setup of the laser beam optics for the MOT and a redesigned lithium vapour cell which was necessary after reoccurring problems with our old saturated absorption spectroscopy system.

Also, single-mode optical fibres now deliver all laser beams from the laser table to the experiment table. The benefits of using optical fibres are manifold: Free beam propagation can be significantly shortened resulting in beam paths less prone to mechanical instabilities, laser beams have well defined Gaussian profiles, sources of stray light can be minimised, and most importantly, replacement of broken laser diodes does not affect beam alignment on the experiment side.

For laser cooling and imaging of  ${}^6\text{Li}$  atoms we use a series of frequency stabilised diode lasers at wavelengths close to 671 nm. These are locked by one of the following schemes: Locking to the peak of an atomic transition via saturated absorption spectroscopy, injection locking and offset locking. Also, we utilise two commercial ytterbium doped high power fibre lasers for optically trapping atom clouds. The imaging laser also supplies the Bragg laser light. The Bragg laser system will be described in detail in the next chapter.

### 3. Experimental setup and procedure

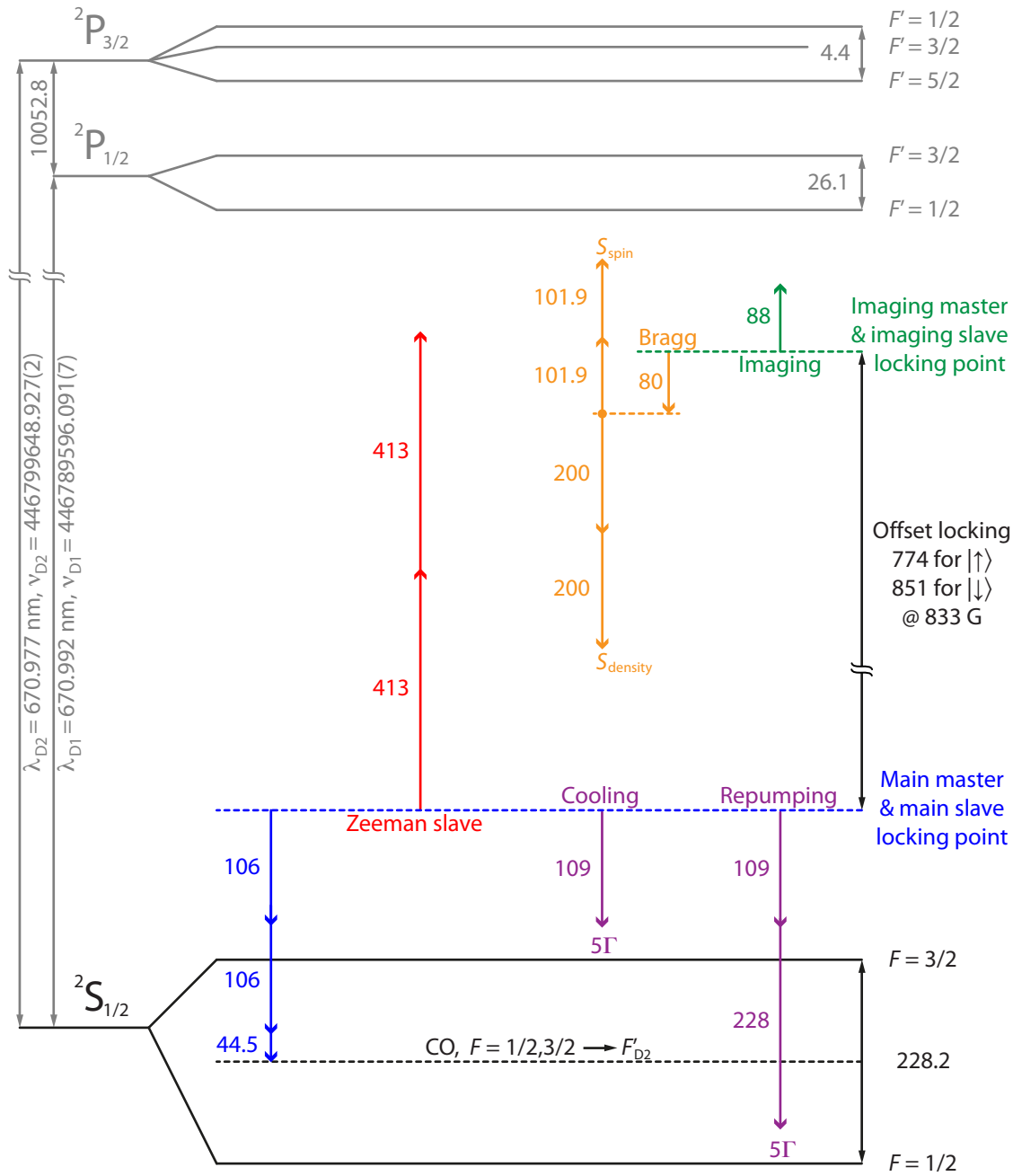


**Figure 3.3.2.:** Fine and hyperfine structure of the  ${}^6\text{Li}$  D-lines (not to scale) as well as laser frequencies (in units of MHz) used for cooling, imaging and Bragg scattering. Also shown are the locking points of the main and imaging laser, AOM frequency shifts (coloured arrows) and the beat frequency for imaging state  $|\uparrow, \downarrow\rangle$  at unitarity. Note, arrows pointing up (down) correspond to negative (positive) AOM frequency shifts. Atomic data from NIST [San11].

The energy levels of  ${}^6\text{Li}$  including all optical frequencies required for laser cooling, imaging and Bragg scattering are shown in figure 3.3.2. The coloured thick arrows in the diagram indicate laser frequency shifts by acousto-optical modulators (AOMs) relative to the locking point of the two master lasers (“main” and “imaging”). The AOMs are operated in either single- or double-pass configuration. The ideal cooling transition for the MOT using the  $D_2$ -line is  $|F = 3/2; m_F = 3/2\rangle \rightarrow |F' = 5/2; m_{F'} = 5/2\rangle$  which provides a closed cooling cycle. However, since the splitting between the excited states  $F' = 3/2$  and  $F' = 5/2$  is smaller than the linewidth of the atomic transition ( $2\pi \times 5.87$  MHz), simultaneous resonant excitation of the  $F' = 3/2$  state, which can decay into the  $F = 1/2$  state, is inevitable. Therefore, strong repumping light for depopulating atoms in  $F = 1/2$  is required to maintain efficient cooling. We found an optimum ratio for the cooling and repumping laser power of 2 : 1. Both cooling and repumping light are red-detuned to the transition by a about five natural linewidths during the MOT loading phase.

The “main master” diode laser serves as the reference frequency for all other diode lasers. The layout of the main master can be found in figure 3.3.3, along with its two amplification stages, a high power “main slave” diode laser and a tapered amplifier. The master laser consists of an external cavity diode laser (ECDL)<sup>6</sup> with a maximum optical output power of 10 mW. Its frequency is locked to the  $D_2$ -line crossover transition of the  $F = 1/2, 3/2$  hyperfine states via Doppler-free saturated absorption spectroscopy [Pre96]. A few milliwatts of the laser beam is branched off and directed via an AOM, in double-pass configuration shifting the frequency by  $2 \times 106$  MHz, to a heated lithium vapour cell. This AOM is also used to tune the MOT cooling and repumping light frequency during the compression stage (cf. section 3.3.3).

Figure 3.3.3 further shows that the diverted laser beam is split into a pump and probe beam, both passing through the cell in opposite direction. When scanning the laser frequency, the photodiode detecting the probe beam shows an enhanced absorption of the crossover resonance on the oscilloscope (in our case in form of a pronounced dip). Crossover transitions occur whenever the hyperfine splitting of two atomic transitions lie within the Doppler width; this strong feature provides an excellent reference point for locking. In alkali metals, such strong dips in the absorption spectrum only exists for lithium and potassium. The pump beam passes a 89 MHz AOM dithered by a 250 kHz oscillation. The resulting frequency modulation of the absorption by the probe laser leads to an intensity modulation on the photodiode generating an error signal for a feedback loop that is part

---

<sup>6</sup>Diode laser: Toptica, model DL100; laser controller: MOG Laboratories, model DLC-202.



an optical isolator. As the nominal lasing wavelength of the laser diode is 660 nm, a temperature of about 60°C is required to reach a free running wavelength near 671 nm, which in turn causes some instabilities of the injection lock. Therefore, the output of the slave laser is monitored by a Fabry-Perot spectrum analyser (etalon). The operation of the tapered amplifier (TA) on the other hand has become very stable after reconsidering the design of the MOT laser generation (see below). Recently (June 2012), I also replaced the old faulty TA chip<sup>9</sup>. Since then, the TA produces 324 mW optical power after an inbuilt optical isolator when seeding it with 27 mW from the main slave laser.

The setup to generate and monitor laser light for Zeeman slowing atoms from the oven is nearly identical to that of the main slave laser and uses the same models laser diode and mount. About 10 mW of the main slave light is fed back directly into the Zeeman slave laser after it has been shifted by  $2 \times 413$  MHz through an AOM. In addition, the laser diode current is RF modulated by 150 MHz after we found in previous experiments that sidebands on the Zeeman laser beam roughly doubles the number of laser cooled atoms in the MOT. The created optical sidebands might have some repumping effects on the Zeeman slowing transition assuming the splitting of the magnetic sub levels and the Doppler shift is roughly in the same range as the RF modulation. Due to the sidebands, however, the stabilisation of the Zeeman slave laser requires relatively high optical power for the seed beam. The Zeeman slower laser beam is delivered to the experiment via an optical singlemode fibre. Close to the vacuum chamber, the beam is expanded to 22 mm and has a power of approximately 5 mW. After passing a quarter wave plate, it is focused by a 1000 mm lens into the chamber through a sapphire viewport (cf. figure 3.3.1).

**New laser layout for the MOT:** The laser setup producing MOT cooling and repumping light has been redesigned. The AOMs, shifting the frequency of the master laser, are depicted in figure 3.3.4. In the old arrangement (not shown), these two AOMs were placed in front of the TA producing two beams that must perfectly overlap before seeding the TA. This design had two issues: The optical losses caused by the AOMs resulted in insufficient seed power for the TA, therefore the low optical power for the MOT generation required frequent optimisation, and, two seed beams of different frequencies can lead to an unstable operation of the TA with an unpredictable power in each of the output beams. This is because the amplification is very susceptible to mechanical instabilities of the input beams positions (due to the nonlinearity of the gain material in a TA-laser chip).

---

<sup>9</sup>New TA chip: Similar to model EYP-TPA-0670-00500-2003-CMT02-0000 by Eagleyard, 670 nm.

### 3. Experimental setup and procedure

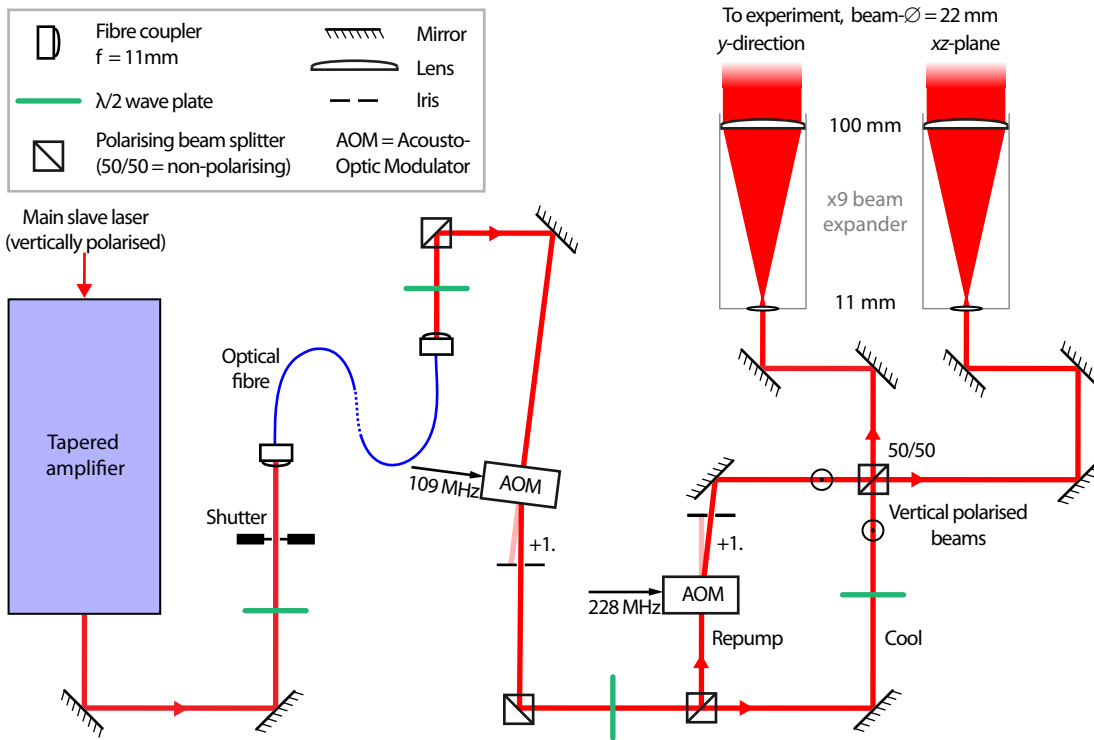


**Figure 3.3.4.:** Schematic of the new MOT laser setup. Two polarising beam splitters are used instead of mirrors to purify the vertical polarisation of the beam. The AOMs are at fixed frequencies,  $\pm 1$  indicates the direction of the frequency shifts.

The TA is located on the laser table whereas the AOMs, including optics, are placed on the experiment table. We limit the optical output power of the TA beam to 300 mW through the TA current. This gives about 200 mW at the other end of the singlemode fibre which suffices to produce MOT beams with intensities in the glass cell well above the saturation intensity of lithium. After shifting the frequency by 109 MHz, the beam is split into two beams; one for cooling and the other one passes a 228 MHz AOM for repumping, matching the ground state hyperfine splitting. We create two 22 mm diameter beams for a MOT setup in six-beam configuration, one for the horizontal plane with four beams, and the other one for two vertical beams. At the glass cell, the optical power of each horizontal beam is over 10 mW and of each vertical beam is over 20 mW.

In the vertical direction, the MOT beams propagate through the imaging optics, as will be explained in section 3.4.2. The excess in optical power not only helps to compensate losses caused by various optical elements but we also found that higher atom numbers can

be transferred into the optical dipole trap as the light pressure squeezes the MOT cloud vertically improving the mode match of cloud shape to the trapping beam.

**Lasers for optical dipole traps:** Our experimental setup utilises two far-red detuned single focussed optical dipole traps for cooling and trapping lithium atoms. The arrangement of the optics can be found in figure 3.3.5. A 100 W linear polarised multi-mode ytterbium fibre laser from IPG<sup>10</sup> with a centre wavelength of 1075 nm is used for forced evaporation after loading the laser cooled atoms into the focus of the beam. Being a fibre laser, the spot has an excellent spatial profile ( $M^2 \sim 1.1$ ). The laser intensity can be precisely controlled over roughly four orders of magnitude, at first directly via computer ( $> 13$  W laser beam power) followed by a 110 MHz AOM regulated through a commercial analog PID controller<sup>11</sup> ( $< 13$  W) while keeping the laser output power constant at 13 W via computer. The controller stabilises the laser intensity by measuring the actual intensity on a photodiode (bandwidth 10 kHz) and tuning the AOM to reach the desired intensity setpoint. The optical signal for the photodiode is obtained after the glass cell from residual light leaking through a  $45^\circ$  orientated dielectric coated mirror. Here, we avoid using a polarising beam splitter for the light pick up as the laser beam exhibits polarisation fluctuations at low optical power. The 100 W laser and optical setup for evaporation is not employed otherwise in the experiment since cooling atoms evaporatively is a delicate process and requires a high degree of optimisation. Instead, we add a further 10 W linear polarised single-frequency ytterbium fibre laser from IPG<sup>12</sup> with a wavelength of 1064 nm to our system which is solely dedicated for creating dipole traps with well defined trapping parameters that can be optimised for our Bragg scattering experiments.

Figure 3.3.5 shows the layout for the second trap used for all experiments described in this work. The laser produces a near pure  $\text{TEM}_{00}$  Gaussian mode at the fibre coupler output which then passes through a 110 MHz AOM. All optical components are attached to rigid mounts without any movable mechanical parts. The laser light is not actively intensity stabilised (however, this should be considered in future experimental upgrades). Instead, we monitor the laser intensity by an oscilloscope displaying a photodiode signal obtained from the back reflection of trapping light of the glass cell. The AOM acts as a fast switch and also allows for tuning the trap depth. Subsequently, the laser beam is filtered

---

<sup>10</sup>IPG Photonics, model YLR-100-1075-LP, emission bandwidth 2.5 nm, output beam diameter 5 mm.

<sup>11</sup>SRS Stanford Research Systems, model SIM960, bandwidth 100 kHz.

<sup>12</sup>IPG Photonics, model YLR-10-1064-LP-SF, output linewidth 70 kHz, output beam diameter 1.0 mm.

### 3. Experimental setup and procedure

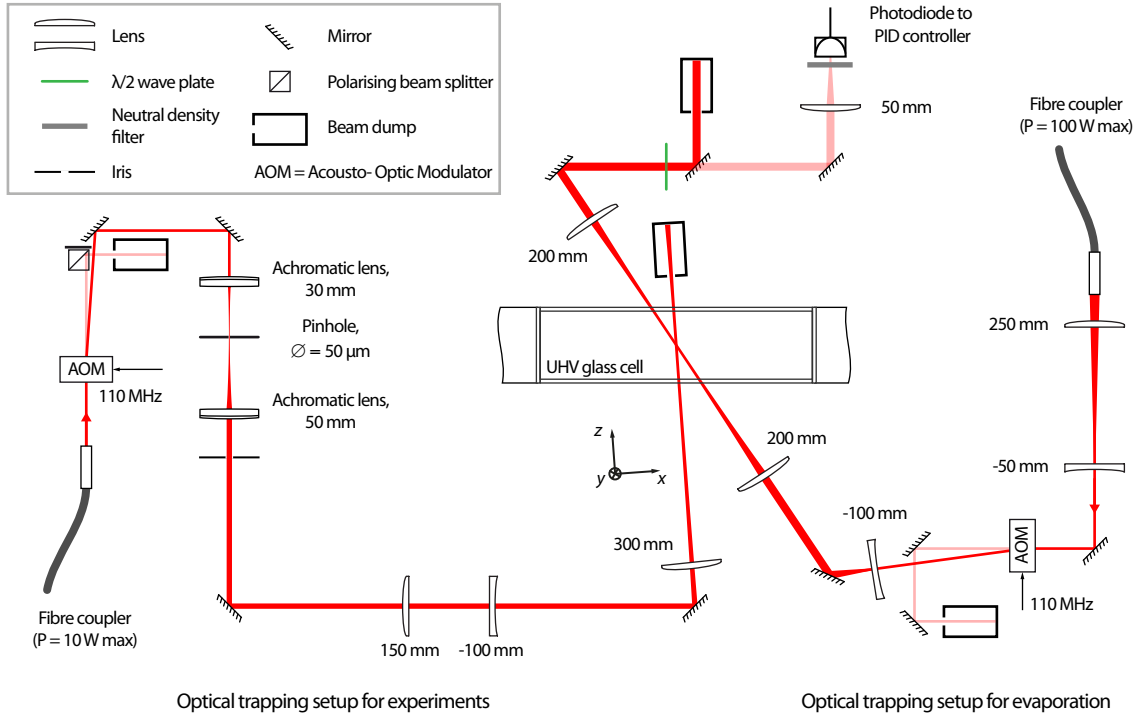


**Figure 3.3.5.:** Laser setup for both optical dipole traps. The trapping beams are vertically polarised to maximise the diffraction efficiency of the AOMs.

by a high-power  $50 \mu\text{m}$  precision pinhole<sup>13</sup>. To minimise lens aberrations, two achromatic lenses were chosen for focussing and recollimating the beam before and after the pinhole. The pinhole, mounted on a precision  $xy$ -translation stage, cleans the AOM diffracted laser beam. This is essential for realising a harmonical trapping confinement inside the glass cell as the AOM was seen to always introduce some high spatial frequency structure on the laser spot. Initially, we merely used a 300 mm lens for creating the trapping potential but as it turned out the shape of the atomic cloud became too elongated and the optical density too high for trap depths required in our experiments. Thus, a  $\times 1.5$  demagnifying telescope was inserted between the pinhole and the 300 mm lens to weaken the dipole trapping potential in radial direction resulting in atomic clouds with an aspect ratio of about 4 in the combined opto-magnetic trap.

The operational sequence of both dipole traps will be detailed in the next section where I explain how we produce ultracold lithium atoms. The parameters of the second dipole trap will be characterised in section 4.3.3.

<sup>13</sup>Thorlabs, model P50C.

### 3.3.3. Cooling and preparation

In this section, I will briefly go through all the steps carried out in a typical experimental cycle for producing a mixture of ultracold  ${}^6\text{Li}$  gas inside the UHV class cell of nearly an equal number of atoms in each of the two lowest hyperfine states,  $|F = 1/2, m_F = \pm 1/2\rangle$ , at temperatures as low as  $0.08 T/T_F$ . In addition, I will provide some technical and physical background to motivate each step. Further details can be found in the references given.

The experiment is computer controlled by a LabView program as well as analog and digital IO-cards<sup>14</sup>. Details of hard- and software can be found in an earlier thesis of this group [Fuc09]. For clarity, the cycle is divided in several stages each covering one main physical step in the process.

In the first stage, lithium atoms are laser cooled by the MOT and Zeeman slower for about 40 s. After opening the atomic shutter, the magnetic field of the Zeeman slower and the Zeeman laser beam is switched on to decelerate atoms from the oven by resonant radiation pressure within 30 cm from an initial mean velocity of around 1700 m/s down to a few tens of metre per second corresponding to the velocity capture range of our MOT.

Running at a current of 2.94 A, the spatially varying magnetic field of the Zeeman slower increases towards the glass cell and has a maximum field strength of 620 G at the end of the coil [Fuc09]. The inhomogeneous magnetic field keeps the atoms in resonance with the Zeeman laser during the slowing down process [Phi82]. For increasing magnetic fields and decreasing atomic velocities, the laser beam pushing the atoms requires  $\sigma^-$  polarisation. This configuration has the advantage of providing a large detuning of almost 1 GHz relative to the Zeeman cooling transition. Therefore, very little interaction between atoms in the MOT and the Zeeman laser field occurs while the Zeeman light travels through the MOT cloud. The downside is that this strong Zeeman magnetic field results in a large gradient at the end of the coil pulling the MOT trapping centre about one centimetre towards the Zeeman coil. This defines the position where we optimise the MOT loading. However, compressing the thermal cloud following the loading process (see below) takes place at the position of the trapping centre when the Zeeman coil is turned off. Thus, finding the balance between optimising the loading and compressing stage is a decisive factor for efficient laser cooling with our setup.

The transverse spread of the atomic beam in the glass cell is estimated to be the same size as the area cross-section of the cell. The MOT laser beams, which are set up in a six-

---

<sup>14</sup>National Instruments: One PCI-6733 16-bit card, two PCI-6713 12-bit cards, output range -10 V – 10 V.

### 3. Experimental setup and procedure

beam configuration, have diameters of 22 mm (limited by the free aperture of 1" optical mounts), and, in combination with the magnetic field of the anti-Helmholtz coils, only a few percent of the atoms from the atomic beam are collected.

We estimate the final atom number in the MOT to be of order of  $10^9$ . The MOT temperature prior compressing was determined in previous measurements to be  $280 \mu\text{K}$  [Dyk10]. This is surprisingly high when compared to the theoretical Doppler limited temperature of  $\hbar\Gamma/(2k_B) = 140 \mu\text{K}$  achievable for laser cooling  ${}^6\text{Li}$  [Win79]. Sub-recoil laser cooling techniques, such as polarisation-gradient cooling [Let88, Bar94] commonly applied to other alkali elements, are not suitable for our species due to the narrow hyperfine structure of the excited state. However, recently two different cooling methods on  ${}^6\text{Li}$ ,  ${}^7\text{Li}$  and fermionic  ${}^{40}\text{K}$ , all of them featuring closely spaced hyperfine levels, have been demonstrated achieving much colder MOT temperatures: A MOT operating in the ultraviolet region led to temperatures for  ${}^6\text{Li}$  of  $59 \mu\text{K}$  [Dua11], and cooling potassium atoms using grey molasses was used to reach temperatures seven times below its Doppler limit [Fer12]. The same method as used for potassium was later applied to cool  ${}^7\text{Li}$  to  $60 \mu\text{K}$  [Gri13]. Implementing one of these schemes into our experiment would most likely enable us to achieve quantum gases at significantly lower temperatures with larger atom numbers after evaporation, entailing an increase in signal-to-noise for Bragg scattering and all other experiments.

In order to load the pre-cooled atoms into the optical dipole trap for further cooling, the phase-space density of the MOT cloud is increased through compression. This allows a more efficient transfer of the atoms – which again is only a few percent. For this, the gradient of the quadrupole magnetic field initially is ramped from 20 to 50 G/cm within 20 ms, while the 100 W high power fibre laser is linearly ramped up in 10 ms to a maximum optical power of 90 W. This corresponds to a potential depth at the trapping centre of  $k_B \times 2.3 \text{ mK}$  (using equation 3.2.5 of section 3.2.1, and a waist radius of  $w_0 = 38 \mu\text{m}$ ). Concurrently with the magnetic ramp, the intensity of the cooling and repumping light is lowered by a factor of 50 and 150, respectively. Also, the frequency of both lasers is detuned closer to resonance from  $5\Gamma$  to approximately half the atomic linewidth,  $\Gamma/2$ . Just before the end of this stage the atoms are pumped within  $200 \mu\text{s}$  into the  $F = 1/2$  hyperfine state by turning off the repumping light, populating the magnetic states  $m_F = \pm 1/2$ .

For quantum degeneracy, unity phase-space density is required. At this point the phase-space density of the MOT is still more than five orders of magnitude too low. One way to attain the necessary density is by forced evaporative cooling, which for an optical trap can be achieved by simply continuously lowering the trap depth in a well defined manner. In general, this process effectively decreases the cloud temperature by removing the high-

energy component of a thermal cloud from the trap while allowing the remaining atoms to re-thermalise through two-body collisions [Ket99]. However, due to the Pauli blocking, two fermionic alkali atoms only collide if they are in two distinct quantum states once the temperature is low enough so that only  $s$ -wave collisions are energetically allowed.

In our system, evaporative cooling of the atomic sample is achieved by lowering the intensity of the dipole trap from 90 W to a few milliwatt (for the coldest clouds) by successive use of LabView generated functions. First we apply two linear ramps with different slopes followed by an exponential curve. The total evaporation lasts for about 8 s. At the beginning of the evaporation we also quickly turn on the Feshbach coils and tune the magnetic field to the BEC-side of the Feshbach resonance at 785 G. As a result, the atoms arrive at the resonance as a strongly interacting repulsive Fermi gas. This system constitutes a metastable state with a high three-body recombination rate that has a decay channel into a two-body bound state [Pri04]. Thus, three atoms can form a loosely bound Feshbach molecule plus an extra atom along with the release of the binding energy as kinetic energy going to the constituents [Fer08]. However, it is noteworthy that with this cooling method both prevalent types of collisions present in the cloud work in our favour: Inelastic collisions for producing bosonic molecules and elastic collisions for cooling the gas through those. Since the trap is twice as deep for pairs of atoms or molecules than it is for single atoms, unpaired atoms are preferentially evaporated. In this way, we are able to produce clouds with a nearly perfectly balanced 50/50 mixture of atoms prepared in the two lowest spin states. The final atom number can reach up to of  $3 \times 10^5$  per state for clouds below  $0.1 T/T_F$ .

In the final stage, we adiabatically transfer the quantum degenerate gas into the second dipole trap, produced by the 10 W fibre laser, which is specifically designed for Bragg scattering experiments. Simultaneously, the magnetic field is either tuned right to unitarity at 833 G or to any other position of the BCS-BEC crossover<sup>15</sup>. Inside the glass cell the centres of the first and second trap overlap perfectly. For a smooth transfer the second trap is ramped up linearly in 150 ms followed by linearly turning off the first trap in 100 ms. We do not observe any significant heating or trap loss resulting from the transfer. The optical power of the second trap is set to 2.6 W for all experiments in this work creating a deep harmonic trapping confinement. The peak trap depth amounts to  $k_B \times 2.5 \mu\text{K}$ , which is about ten times the Fermi energy of the gas. At unitarity, where

---

<sup>15</sup>An additional vertical gradient field is applied to compensate vertical shifts of the cloud position caused by a residual gradient field of the Feshbach coils, which depends on the strength of the magnetic field.

### 3. Experimental setup and procedure

inelastic collisions and heating are suppressed by Pauli exclusion [Pet03], a trapping hold time of typically 500 ms allows enough time for the transferred cloud to re-equilibrate before measurements take place. For samples prepared on the BEC-side we reduce the hold time due to increased heating caused by three-body collisions of more tightly bound Feshbach molecules. Optionally, the temperature of the cloud can be precisely increased by a release and recapture method involving suddenly switching off and on the second trap. The recaptured atoms heat up by converting their potential energy into kinetic energy.

In conclusion, after each cycle the experiment produces a gas of ultracold  ${}^6\text{Li}$  atoms at temperatures as low as  $0.08 T/T_F$  prepared in the two lowest spin states ( $|\uparrow, \downarrow\rangle$ ) each containing up to  $3 \times 10^5$  atoms. Imaging the atoms with our new imaging system is topic of the next section.

#### 3.4. The new imaging system

This section is devoted to the new absorption imaging system which I designed and incorporated into the setup at the beginning of my research work. This includes the implementation of a new imaging lens system with better optical resolution than any of our previous imaging systems and a new camera featuring fast kinetics mode. We image atomic clouds from two perpendicular orientations in our setup which we refer to as “top” (vertical) and “side” (horizontal) imaging. All results presented were obtained with the new top imaging system whose imaging axis is parallel to gravity and the Feshbach field.

Top imaging offers the advantage that atomic clouds can be fully optically accessed across their long axis. The downside is that the imaging and vertical MOT light must share the same optical path so that more optics and mechanics is needed. Side imaging is currently only used for measuring radial trapping frequencies of the dipole traps and will not be discussed here. More details about our side imaging can be found in [Dyk10].

This section starts with a brief summary of absorption imaging along with the experimental steps required to create images of the atom clouds (cf. section 4.2.2 for procedural details about imaging Bragg scattered clouds in the precision measurements). Then, I will describe the imaging laser setup and the new imaging system. Finally, the fast kinetics mode settings and calibration of the top camera will be discussed.

### 3.4.1. Absorption imaging

We study atomic properties and pair correlations of strongly interacting  ${}^6\text{Li}$  gases in the  $|\uparrow, \downarrow\rangle$ -spin states by analysing spatial density distributions. In particular, centre-of-mass displacements, temperatures and atom numbers of atomic clouds are all obtained from resonant absorption images. In general, at the end of an experimental cycle a short pulsed laser beam, ideally with a uniform intensity distribution, illuminates the cloud where it is partially absorbed. The transmitted light is then focussed via the imaging optics onto a CCD (Charge-Coupled Device) camera which images the shadow of the cloud to give the two-dimensional density profile  $n_{2\text{D}}$ . As this method is destructive, each image requires the preparation of a new cloud [Ket99].

We are interested in density profiles of atomic clouds in either spin states for each run of the experiment. For this, two shadows of atom clouds are consecutively recorded on a single CCD frame while quickly tuning the frequency of the imaging laser by about 77 MHz to image both states. Each frame comprises three images to give the integrated column density  $n_{2\text{D}}$  for each state. The first image contains  $|\uparrow\rangle$  atoms plus imaging beam, the second  $|\downarrow\rangle$  atoms plus imaging beam and the third only imaging beam but no atoms. An example of how these raw images appear on the CCD camera is given in figure 3.4.3.

As high magnetic fields are present to produce strongly interacting Fermi clouds, the optical transitions for imaging become particularly simple (cf. appendix A). A strong Zeeman magnetic field leads to an almost full decoupling of the electronic and nuclear spins so that atoms can undergo effectively closed transitions preserving the nuclear spin projection  $m_{\text{I}}$ . We use imaging light that is  $\sigma^-$  polarised and propagates along the  $y$ -direction, parallel to the Feshbach field. The imaging transitions are therefore

$$\begin{aligned} |m_{\text{F}} = +1/2; m_{\text{J}} = -1/2\rangle &\longrightarrow |m_{\text{F}'} = -1/2; m_{\text{J}'} = -3/2\rangle \text{ for } |\uparrow\rangle \text{ and} \\ |m_{\text{F}} = -1/2; m_{\text{J}} = -1/2\rangle &\longrightarrow |m_{\text{F}'} = -3/2; m_{\text{J}'} = -3/2\rangle \text{ for } |\downarrow\rangle. \end{aligned}$$

In the following, the image analysis we perform to obtain optical densities will be explained based on the standard derivation of Beer's law including saturation [Rei07]. The shadow profiles on the CCD are related to the integrated column density by  $n_{2\text{D}} \equiv n(x, z) = \int n(x, y, z) dy$  of the atomic density distribution  $n(x, y, z)$  depending non-linearly on the absorption. The intensity of a resonant collimated laser beam in  $y$ -direction attenuates while travelling through the probed gas as

$$\frac{dI}{dy} = -I\sigma(I)n(x, y, z). \quad (3.4.1)$$

### 3. Experimental setup and procedure

This expression embodies the effective cross section  $\sigma(I) = \sigma_0/(1 + I/I_{\text{sat}})$ , which reduces to the absorption cross section of a two-level atom,  $\sigma_0 = 3\lambda^2/(2\pi)$ , in the limit of  $I \ll I_{\text{sat}}$ .

Separating the variables of equation 3.4.1 and integrating both sides leads to

$$\int_{I_b}^{I_a} \frac{dI}{I\sigma(I)} = - \int_{-\infty}^{+\infty} n(x, y, z) dy. \quad (3.4.2)$$

The limits of the integrals are chosen such that they reflect the actual experimental situation when taking absorption images. The imaging optics for the camera is focussed on the  $xz$ -plane where the centre of the atomic clouds are located.  $I_a = I_{\text{atom}}(x, z) - \bar{I}_{\text{back}}(x, z)$ , referring to as the ‘‘atom’’ image, comprises a 2D-intensity profile that corresponds to the first acquired image containing the shadow of the atoms.  $I_b = I_{\text{beam}}(x, z) - \bar{I}_{\text{back}}(x, z)$ , referring to as the ‘‘beam’’ image, serves as a reference and is taken second showing only the 2D-intensity distribution of the imaging beam without atoms.

For technical reasons, a background image  $\bar{I}_{\text{back}}$  is subtracted from both atom and beam images to eliminate additional background counts on the camera chip. These arise mainly due to dark counts, an inherent feature of CCD cameras constantly generated by charge buildup in the pixel wells over time, and, scattered residual light shining onto the chip while the camera shutter is open. The bar over  $\bar{I}_{\text{back}}$  indicates that we smooth the 2D-background profiles by averaging many of them ( $> 10$ ) to keep the noise in the final images  $I_a$  and  $I_b$  roughly at the same level as without subtraction.

The integral limits on the right hand side of equation 3.4.2 reproduce the column density. Carrying out the integration we obtain

$$n_{2\text{D}} = -\frac{1}{\sigma_0} \left[ \ln \left( \frac{I_a}{I_b} \right) + \frac{I_a - I_b}{I_{\text{sat}}} \right]. \quad (3.4.3)$$

At low intensities,  $I_a, I_b \ll I_{\text{sat}}$ , the second term becomes negligible and  $\sigma_0 n_{2\text{D}}$  simplifies to the standard definition of the optical depth,  $\text{OD} = -\ln(I_a/I_b)$ . This expression yields reliable results for the column density of dilute gases with ODs well below 0.1 [San10].

The experiments in chapter 4 and 5 are performed on large atomic clouds with ODs of up to 5 since we aim for strong response signals spread out over many pixels for a high signal-to-noise. Such dense clouds require imaging intensities of up to  $5 I_{\text{sat}}$  to saturate the atoms making the cloud transparent. In this case, the second term in equation 3.4.3 contributes significantly to the OD and the absolute value of the intensity, in units of pixel counts, has to be known precisely. We thus carried out a careful calibration of the imaging system including the  $I_{\text{sat}}$  value, as discussed in section 3.4.4.

We modify equation 3.4.3 by introducing two parameters,  $\Phi$  and  $\beta$ , to account for additional considerations due to imperfect imaging and obtain the final expression for the column density<sup>16</sup>,

$$n_{2D} = -\frac{1}{\sigma_0} \left[ \ln \left( \frac{I_a/\beta + (\Phi - 1)I_b}{\Phi I_b} \right) + \frac{I_a - \beta I_b}{I_{\text{sat}}} \right]. \quad (3.4.4)$$

The  $\Phi$  correction is based on an idea described in [Kin06] and considers the fact that the imaging light may not have a perfect  $\sigma^-$  polarisation, that is, any light with the wrong polarisation will be far detuned from an atomic transition so will be transmitted. Owing to the large Zeeman splitting at  $\sim 833$  G, only the  $\sigma^-$  component can be absorbed by the atoms. Circular polarised light can easily change its polarisation when reflecting off dielectric mirror surfaces or by the anti-reflection coating of the glass cell. Also birefringence effects of the cells glass material or, as in our case, the unfortunate presence of dust particles, sticking to the glass surface inside the cell, from which the imaging light scatters off can depolarise the light. This “wrong” light distorts the shape of the density profiles in the images and has to be accounted for.

To find the value for  $\Phi$ , the following procedure can be applied (more details in [Kin06]): For a given pulse duration, the intensity of the imaging light is weakened until the fraction of light passing through the cloud saturates to a minimum value and the centre region of the cloud appears flat. This effect shows up more pronounced in 1D-density profiles. If the light was fully  $\sigma^-$  polarised all the light would be absorbed and the pixel counts on the CCD chip at the cloud centre would go to zero (after background subtraction). In reality, some counts are recorded at the centre even for saturated images. The ratio of the counts in the central flat-top region and the counts of an imaging region that shows only the (flat) background with no atom cloud gives  $\Phi$ . We found  $\Phi$  to be 93%.

The scaling factor  $\beta$  allows us to take beam images with very high intensities ( $\gg 5 I_{\text{sat}}$ ) to reduce the photon shot noise which is the dominate source of noise in our images. The benefit of using intense laser beams is that, before we subtract  $I_b$  from  $I_a$ , the signal in the reference (beam) image and hence the average amplitude of the noise is scaled down by the respective factors  $\beta$  and  $\sqrt{\beta}$  thus adding less noise to the subtracted images. Currently,

---

<sup>16</sup>In previous experiments of our group [Kuh11a], we included an effective saturation intensity  $\alpha^* I_{\text{sat}}$  as discussed in reference [Rei07].  $\alpha^*$  corrects for specific atomic properties such as different coupling strengths of Zeeman sub levels of the optical transition and polarisation effects of the imaging beam. However, this method does not really reflect our imaging situation as in our case the optical transition is effectively that of a two-level system.

### 3. Experimental setup and procedure

the technical limit for  $\beta$  is 3 (for  $15 I_{\text{sat}}$ ) reducing the noise only by a factor of  $\sqrt{3}$ , which is fairly small. However, if the laser setup was changed such that the maximum intensity in  $I_b$  is  $185 I_{\text{sat}}$ , limited by the maximum pixel counts the top camera can accept at its current setting, then the amplitude of the photon shot noise in  $I_b$  could be reduced to around 16 % of the average noise amplitude in  $I_a$ , which would be a clear improvement.

Once the true column density is known, the atom number  $N_\sigma$  per spin state  $|\sigma\rangle$  can be calculated by summing over all pixels of the image via

$$N_\sigma = A \sum_{\text{pixel}} n_{2\text{D}}, \quad (3.4.5)$$

where  $A = (13 \mu\text{m}/M)^2$  is the effective area of a single camera pixel with side length  $13 \mu\text{m}$ , and  $M = 4.58$  is the measured magnification of the imaging system. As the atom number is a critical quantity for the determination of the universal contact parameter (cf. section 4.4.2), we developed a robust method for finding the true magnification using Bragg scattering of non-interacting atoms. This is explained in more detail in section 4.3.2. We cannot perform, for example, drop experiments on the clouds to find  $M$  since firstly, a magnetic gradient field of the Feshbach coils prevent the atoms from free falling, and secondly, the imaging axis is along the direction of gravity anyway.

In practise we find that direct application of equations 3.4.4 and 3.4.5 still underestimate the true atom number due to additional nonlinear effects that occur at high density [Est08]. For this reason, we also use an independent calibration of  $N$ , based on the cloud size, as described in section 4.3.3 on page 102.

High-intensity imaging of lithium can also be compromised due to its low atomic mass and therefore large photon recoil energy. This leads to significant Doppler shifts of the atoms in the cloud after absorbing a relatively small number of resonant photons. A quick check of the number of photons scattered during imaging is therefore advisable. The number of scattered photons for a two-level atom on resonance is given by

$$N_{\text{ph}} = \frac{\Gamma\tau}{2} \frac{I/I_{\text{sat}}}{1 + I/I_{\text{sat}}}. \quad (3.4.6)$$

For our typical experimental values,  $I = 5 I_{\text{sat}}$  and  $\tau = 1 \mu\text{s}$  (imaging pulse duration), around 15 photons are scattered. As the photon recoil energy for  ${}^6\text{Li}$  is 147 kHz, atoms are red-shifted out of resonance by 2.2 MHz. However, at such high intensities the transition linewidth is power broadened by a factor of  $\sqrt{1 + I/I_{\text{sat}}} \approx 2.45$ . Comparing both we find

$2.2 \text{ MHz}/(2.45 \times 5.9 \text{ MHz}) \ll 1$ , so this is a small effect. Consequently, the irradiated atoms should be re-excited sufficiently during imaging and fully contribute to the optical density.

Also there is a random isotropic change in momentum of atoms in any direction due to photon recoil kicks after repeated spontaneous emission processes. The spatial blurring that results from this can be estimated according to  $\sqrt{N_{\text{ph}}/3}v_{\text{rec}}\tau$  [Jof93], where  $v_{\text{rec}} = 9.89 \text{ cm/s}$  is the recoil velocity for  ${}^6\text{Li}$ . With this expression we find that the blurring of the atoms does not exceed  $2.2 \mu\text{m}$ . As the atoms stay within an area with radius comparable to  $2.84 \mu\text{m}$ , the optimum theoretical resolution of our imaging system, imaging at  $5 I_{\text{sat}}$  does not degrade the optical resolution. Next, I will describe the lasers and optics for the top imaging system.

### 3.4.2. Lasers and imaging optics

A commercial “master” laser and “slave” diode laser provide the light for the side and top imaging setup as well as the Bragg setup (cf. section 4.2.3 on page 89), as illustrated in figure 3.4.1. The lasers, controllers and the realisation of the master-slave configuration are of the same type as for the main diode laser setup (cf. section 3.3.2 for more details). Here, we refer to the master and slave laser as “imaging master” and “imaging slave”, respectively. The frequency stabilisation of the imaging master is realised by a computer controlled offset-locking scheme enabling a high-frequency tuning range. This allows us to easily take images of atom clouds in either ground state at any point over the entire BCS-BEC crossover.

Operational details about the offset-lock and a schematic diagram of the electronic and RF circuit, generating an error signal based on an optical beat signal [Sch99], are described in a previous thesis [Vee09]. In brief, the beat signal results from the frequency difference of the main and imaging lasers. The laser beams are overlapped using a 50/50 non-polarising beamsplitter and the co-propagating beams produce a beat signal which is detected by a fast photodiode<sup>17</sup>, as shown in figure 3.4.1. Deviations of the beat frequency from the reference frequency of a local oscillator results in a nonzero error signal fed back into the internal PID circuit of the imaging laser controller. The two lasers are locked to each other when the frequencies of the beat and local oscillator are identical (within a finite linewidth). Figure 3.3.2, summarising all AOM frequencies, shows precise values of the beat frequency for atoms in the  $|\uparrow\rangle$  and  $|\downarrow\rangle$  spin states at unitarity, typically around

---

<sup>17</sup>Model: ET-2030A, silicon detector by Electro-Optics-Technology Inc., bandwidth 1 GHz.

### 3. Experimental setup and procedure

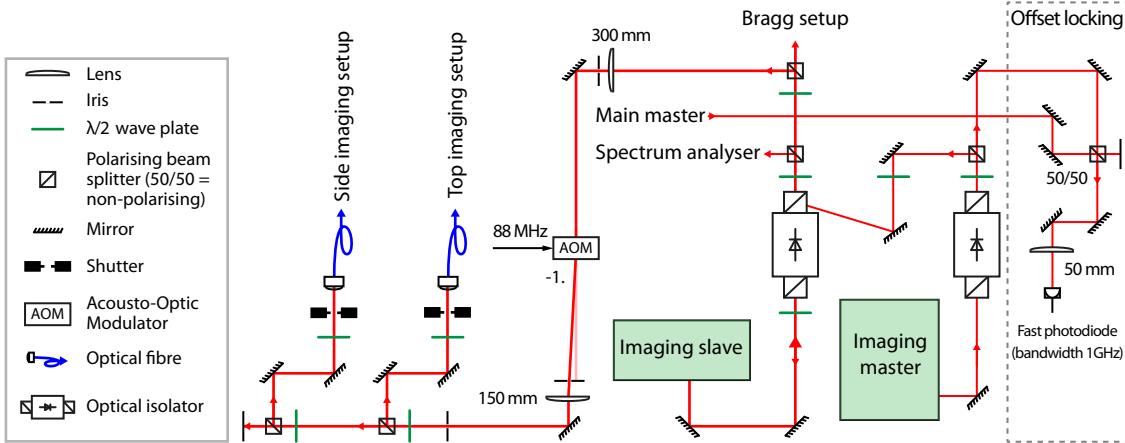


**Figure 3.4.1.:** Schematic of the imaging laser setup. The imaging master diode laser provides frequency stabilised light for the imaging slave diode laser. Imaging light is delivered to either side or top imaging via optical fibres, selectable by a half-wave plate. The laser system also supplies the light for the Bragg laser setup.

800 MHz. We actively monitor the linewidth of the beat signal with a spectrum analyser to keep it below 400 kHz by tweaking the current of the imaging master if necessary.

The laser beam of the imaging slave passes through an 88 MHz AOM, used for fast switching, before entering the coupling lens of single-mode fibres which delivers light to either the side or top imaging setup, selectable by a half-wave plate. The current setup can only provide sufficient optical power for one imaging branch. The mechanical shutter of the unused branch remains closed. We control the imaging intensity by a direct-digital synthesiser (DDS) driving the AOM, as described in the next section. Note that an AOM in double-pass configuration would be preferable as currently we face issues due to residual stray light coming from the zero order of the AOM crystal coupling into the fibres. This leads to some resonant heating of atomic clouds as soon the imaging shutter opens.

The imaging optics share a common path with the vertical MOT beams, as illustrated in figure 3.4.2. Space constraints require a compact lens design combining imaging and MOT beams. The MOT beams propagate parallel to the centre axis of the Feshbach and MOT coils whereas the imaging beam, entering the setup from below, follows a slight off-centred path at an angle of  $\sim 2^\circ$ . This is mainly to avoid capturing imaging light by the camera that has undergone multiple reflections from the surfaces of the glass cell leading to ghost images of the atomic cloud. A fibre coupling lens, with a focal length of

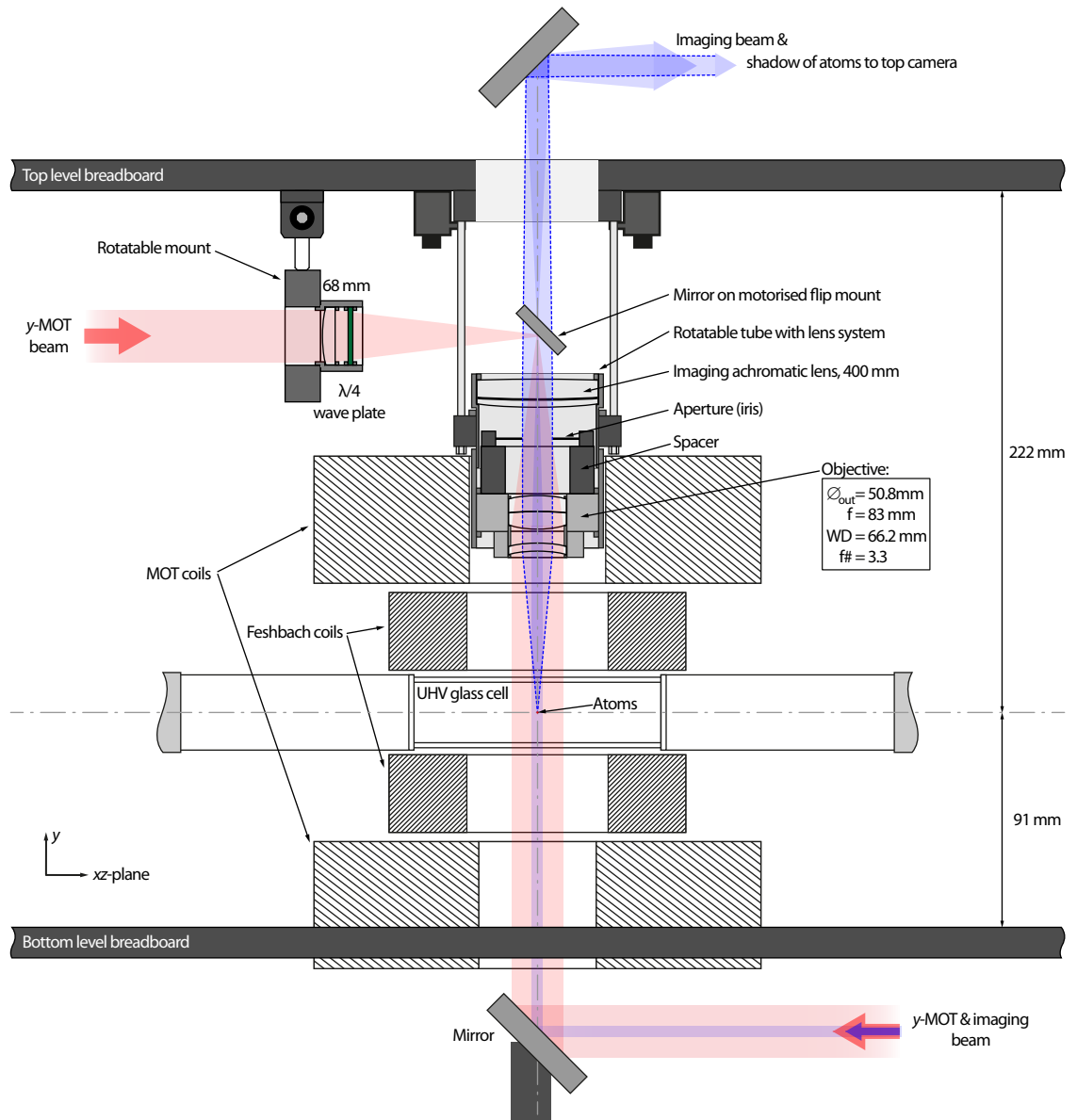


**Figure 3.4.2.:** Optical layout for the “top” imaging system. Imaging beam and MOT beams in  $y$ -direction share the same optical path through the centre of the Feshbach and MOT coils. A motorised flip mirror, guiding the MOT light, is activated to clear the path when taking an image. The objective consists of a combination of an aplanat and a meniscus lens (specs in figure). The imaging achromatic lens has a focal length of 400 mm. Not shown are the camera on the upper breadboard and the fibre output coupling lens for the imaging laser beam placed on the optical table below the lower breadboard.

### 3. Experimental setup and procedure

18.4 mm, for shaping a beam of 6 mm diameter and the quarter-wave plate for generating  $\sigma^-$ -polarised light are not shown in figure 3.4.2.

The main components of the imaging optics consists of an objective and imaging lens mounted into a 2" lens tube. The lens tube is mounted into a threaded cage plate such that the lenses can be shifted down- or upwards by rotating the tube clock- or anticlockwise, respectively (cf. figure 3.4.2). This allows for fine adjustments of the focus. The objective comprises a matched aplanat and aplanatic-meniscus lens combination<sup>18</sup> with a combined focal length of 83 mm and a clear aperture of f/3.3 to give a Rayleigh resolution of about  $3 \mu\text{m}$ . The working distance is 66.2 mm which is the distance between the last element of the objective and imaging plane. The specifications are summarised in figure 3.4.2. The imaging lens is a standard 400 mm achromat from CVI Melles Griot.

We purposely lower the imaging resolution to (at least) twice the Rayleigh limit to ensure that all of the cloud lies within the imaging depth of focus by placing an aperture with a 12 mm diameter opening in between the objective and imaging lens. This leads to a depth of focus<sup>19</sup> of roughly  $30 \mu\text{m}$ .

During MOT loading, the vertical MOT beams enter the glass cell from two sides. The beam from above enters via a motorised flip mirror<sup>20</sup> in rest position. Both beams have to propagate through the imaging lenses. Thus, an additional lens of 68 mm focal length is placed in front of the flip mirror so that the upper MOT beam is collimated inside the glass cell. Prior taking images, the flip mount is activated to move the mirror out of the way for the imaging beam. We have observed good mechanical stability and repeatability of the flip mirror such that the operation of the MOT is unaffected by multiple activations. The camera, which will be characterised in the following sections, is placed on the top level breadboard, not shown in figure 3.4.2.

#### 3.4.3. Camera settings

In this and the next section, I will describe technical details of the camera setup relevant for our experiment. For imaging in vertical direction, we employ an air-cooled camera from Princeton Instruments (model PIXIS 1024) that features fast kinetics timing mode. Figure 3.4.3 schematically shows the CCD chip located at the frontside of the camera

---

<sup>18</sup>Aplanat: LAP-125.0-25.0-PM, meniscus lens: APM-125.0-25.0-PM by CVI Melles Griot.

<sup>19</sup>Assuming an increase in waist of a Gaussian beam by 5 %, the depth of focus reads  $2.56 \lambda (f/\#)^2/\pi$ .

<sup>20</sup>Motorised flipper for one inch optics, model 8892-K by New Focus.

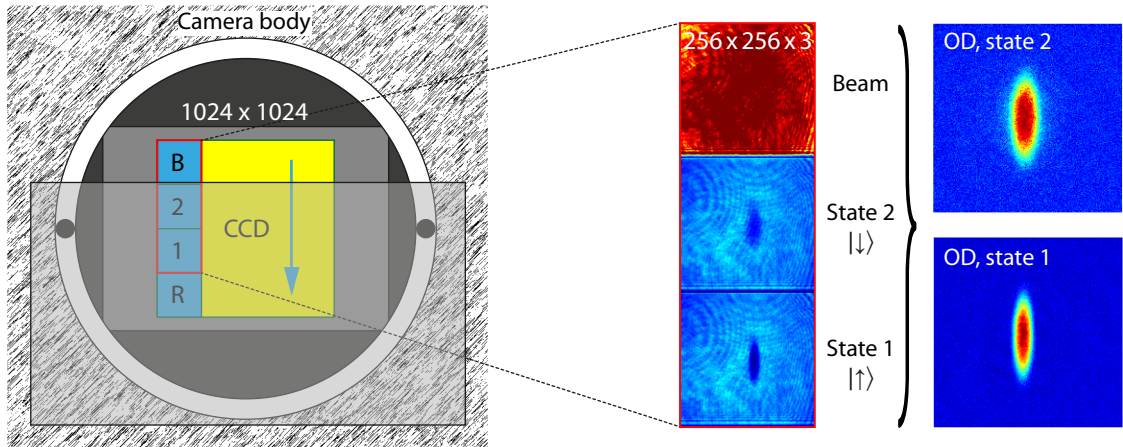


**Figure 3.4.3.:** Configuration of the CCD array in fast kinetics mode. Left: A narrow strip (blue,  $256 \times 1024$  pixels) of the array (yellow) is used for exposure. Most of the CCD area is masked by a razor blade (light grey rectangle). Right: The CCD readout contains shadow images of atom clouds in either spin state and a beam image at high intensity to give density profiles.

(yellow and blue area on the left side in the figure). The chip comprises an array of  $1024 \times 1024$  square pixels, each of size  $13 \times 13 \mu\text{m}^2$ . To improve the signal to noise, the chip temperature is set by default to  $-70^\circ$  Celsius. The large grey shaded semi-transparent rectangle in figure 3.4.3 indicates a razor blade, directly attached to the camera housing, serving as a knife edge to mask a well defined region of the CCD sensor and to leave only a small imaging window for exposure.

Fast kinetics mode allows the acquisition of consecutive images within milliseconds. This enables us to image both spin states of the same atom cloud over short time scales. Only a small area of the CCD is exposed to obtain images of, as in our case,  $256 \times 256$  pixels that are transferred into a hidden part of the array acting as a temporary memory. Once all images are recorded, the CCD is read out. Note, here “image” refers to a subimage of  $256 \times 256$  pixels, whereas “frame” denotes the entire CCD array. The time it takes to shift an image across the CCD is  $819 \mu\text{s}$ . This results from multiplying the vertical image size by the vertical shift rate (set to  $3.2 \mu\text{s}$ ) defining the time it takes to transfer the content of the pixels by one row. Obviously, the smaller the vertical image size the shorter is the time between taking successive images, also, the smaller the horizontal image size the shorter is the read-out time of the CCD frame.

As further shown in figure 3.4.3, the chip is set up to record four images per frame,

### 3. Experimental setup and procedure

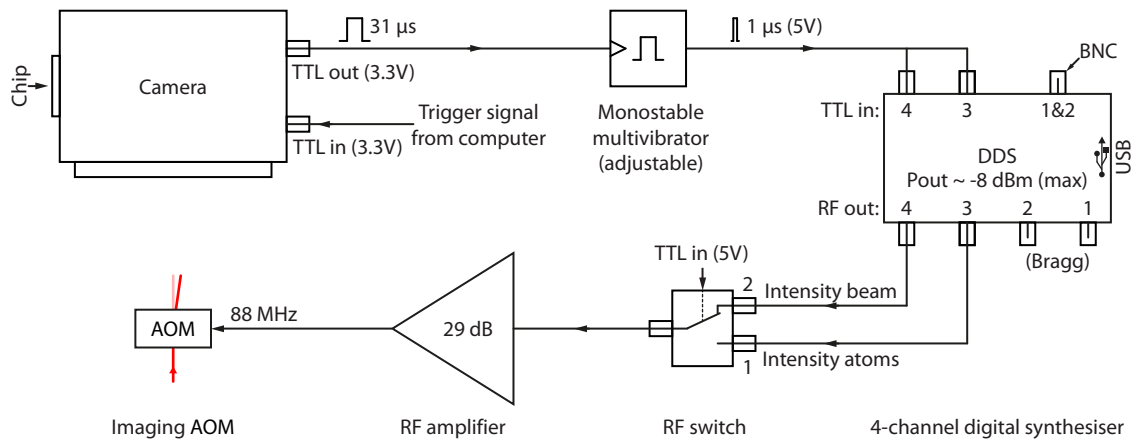


**Figure 3.4.4.:** Pictorial diagram of the circuit generating short imaging pulses. Two channels of the DDS produce a RF signal of 88 MHz with two different amplitudes. The camera is triggered by the experiment computer.

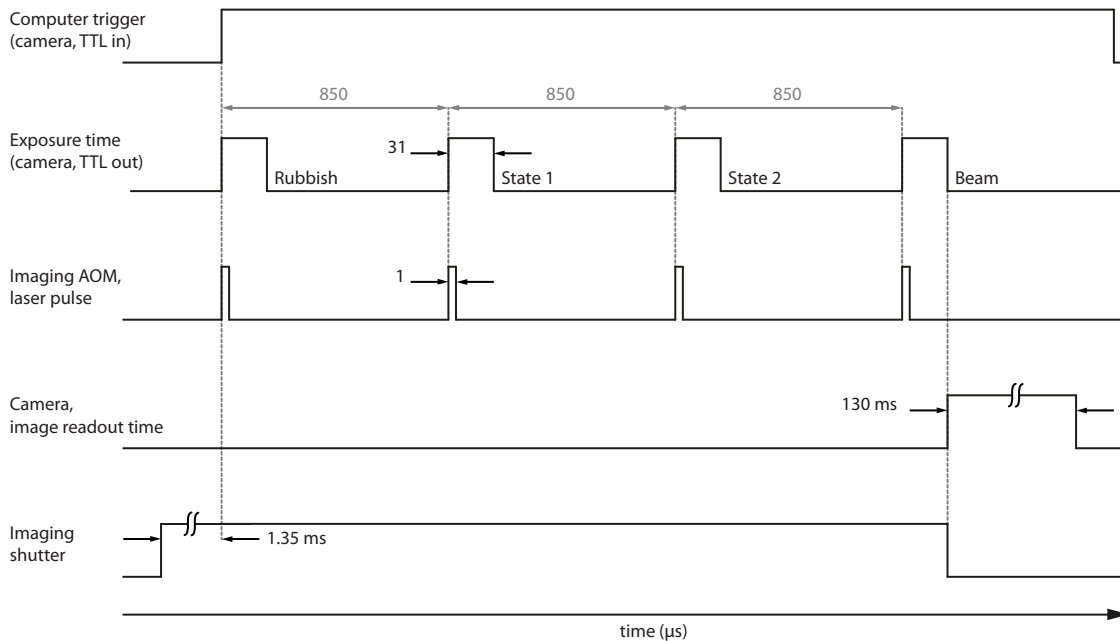


**Figure 3.4.5.:** Timing diagram of the image sequence in fast kinetic mode. Four images are recorded on a single frame within 2.6 ms upon triggering the camera, while the CCD readout with about 130 ms takes much longer. The shutter for the imaging laser beam is fully open after 1.35 ms.

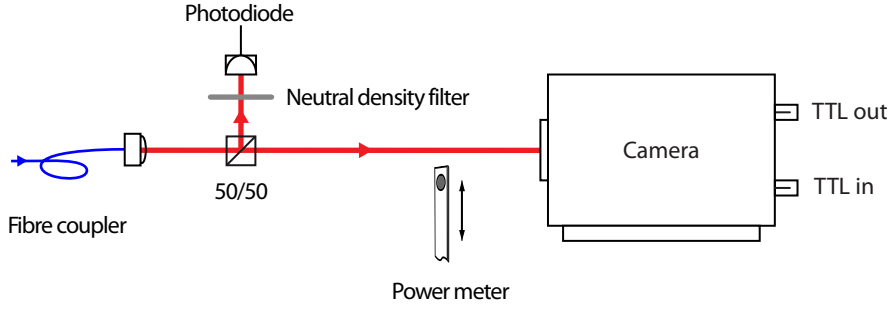
labelled R, 1, 2 and B, which stands for Rubbish, atomic state 1, atomic state 2 and Beam, respectively. The latter three images give the density distribution of clouds in each spin state after separately applying equation 3.4.4. On the right side of figure 3.4.3 examples of such density distributions ( $n_{2D}$ ) are shown (after background subtraction). For technical reasons the image sequence always begins with a “Rubbish” image that consists of background counts accumulated while the camera shutter is open, several seconds before acquiring the desired images.

Figure 3.4.4 schematically shows the circuit that includes all components required to control the imaging AOM (cf. figure 3.4.1). We make use of the camera’s auxiliary TTL output to trigger the DDS that generates an 88 MHz radio frequency (RF) driving pulse for the AOM. This allows for conveniently synchronising imaging laser pulses with the timing of the camera in kinetics mode. The TTL output provides a 3.3 V signal while the CCD is on exposure. The exposure time is purposely set to 31  $\mu\text{s}$  to give a total time for acquiring a single image of 850  $\mu\text{s}$  (exposure plus shift time), corresponding to an integer multiple of the time resolution of the experiment control program (which is 50  $\mu\text{s}$ ). This allows for synchronising the timing for the imaging sequence, set by the camera, with the outputs of the computer card used, for example, for tuning the frequency of the offset lock when imaging both atomic states.

The pulse length of the TTL output can be reduced by a home-made adjustable monostable multivibrator and is typically set to 1  $\mu\text{s}$ . As indicated in figure 3.4.4, we exploit two channels of the DDS for imaging that are set to the same RF frequency but with a different amplitude. Channel three (four) provides the signal for the atom (beam) image at low (high) intensity. The reason for this is detailed in section 3.4.1 ff.. The DDS can be either soft- or hardware controlled (for technical details see appendix B). One of the many advantages of a DDS over our standard analog AOM drivers is that the RF output can be fully switched off eliminating residual leakage light that can contribute to resonant heating of atoms once the imaging shutter opens.

The timing for exposing a series of images on a single CCD frame is summarised in figure 3.4.5. The camera autonomously acquires four images after a single electronic trigger pulse from the experiment computer. In this way, three individual frames are recorded in each experimental cycle: After opening the camera shutter, the first frame is taken for technical reasons to clean the CCD sensor. This step is required as we cannot use the inbuilt “continuous cleaning” mode due to timing issues leading, as mentioned before, to saturated pixels after some time. The second frame contains the images of the atomic clouds, as shown in figure 3.4.3, and the last frame, following immediately the second,

### 3. Experimental setup and procedure



**Figure 3.4.6.:** Setup for the intensity calibration of the CCD sensor. Pulses of a collimated laser beam with small beam diameter illuminate the CCD. A calibrated photodiode gives correct optical power reading for short laser pulses.

collects a series of background (dark) images.

#### 3.4.4. Calibrating the camera

We determine the atom number from measured density profiles of optically thick clouds that were resonantly imaged. As this requires high laser intensities, the second term in equation 3.4.4 cannot be neglected. We therefore have to calibrate the pixel counts of the CCD to the absolute laser intensity. Basically, we want to express the saturation intensity, which for  ${}^6\text{Li}$  is  $I_{\text{sat}} = 2.54 \text{ mW/cm}^2$ , in units of average pixel counts for a given pulse duration of the imaging beam,  $\tau_{\text{im}}$ .

The setup for the calibration is illustrated in figure 3.4.6. We use a test laser beam with a variable pulse length and intensity to illuminate the CCD. A calibrated photodiode (bandwidth 10 kHz) monitors the optical power of the beam. It is obviously crucial that the readout of the power meter can be trusted; thus, check its calibration date. The setup is fully covered to ensure that no room or other stray light can reach the CCD. In a series of measurements, we separately determine the total counts over all pixels  $N_c$  after shining light at different optical powers  $P_{\text{test}}$  and pulse lengths, for example  $1.5 \leq \tau_{\text{test}} \leq 15 \mu\text{s}$ , onto the chip. We choose  $P_{\text{test}}$  and  $\tau_{\text{test}}$  such that the laser beam does not saturate any pixels. The results are then related to the saturation intensity through

$$I_{\text{sat}}[\text{pixel}] = \frac{\eta}{M^2} \frac{N_c}{N_p} \frac{P_{\text{sat}}}{P_{\text{test}}} \frac{\tau_{\text{im}}}{\tau_{\text{test}}}, \quad (3.4.7)$$

where  $P_{\text{sat}} = A I_{\text{sat}}$ ,  $N_p$  the number of pixels in a given area  $A$  and  $\tau_{\text{im}}$  is the imaging pulse length that is used in the actual experiments. Note that  $A$  can be of arbitrary size as long it surely includes all photons. And of course all photons of the test laser should hit

the pixels. For example, we used  $A = 1 \text{ cm}^2$ , which was much larger than the beam size, giving  $P_{\text{sat}} = 2.54 \text{ mW}$ . Then, the number of pixels enclosed by this area is  $N_p = 591716$ .

After including the imaging magnification  $M = 4.58$  (cf. section 4.3.2), and the transmission  $\eta$  of all optical elements between the imaging plane where the atoms reside and the CCD, which we have measured separately to be 89.0%, the average value for the saturation intensity of a  $1 \mu\text{s}$  imaging pulse results in  $I_{\text{sat}} = 135 \pm 1 \text{ counts/pixel}$ .

### 3.5. Summary

This chapter was intended to give an overview of the current experimental setup we use in the Fermi gas laboratory. It hopefully assists new students in finding all relevant information and references in one place and getting a quick start on the equipment.

The main components of the experimental setup were described including the vacuum chamber, optical dipole traps and the Feshbach magnetic coils. Also, all setups of the diode lasers and the TA-laser system for laser cooling and imaging  $^6\text{Li}$  atoms were detailed. The discussion focusses on technical upgrades and changes in the optical layouts that have significantly improved the reproducibility of the experiment.

A new imaging system has been designed and implemented into the existing experiment to improve the optical resolution of atomic clouds in the vertical imaging direction. The imaging optics and the calibration of the “top” camera as well as the camera settings were described in detail. The camera operates in fast kinetics mode which enables imaging atomic clouds on short (sub milliseconds) time scales.

A brief step-by-step guide of a typical cooling cycle and the preparation of a spin balanced  $^6\text{Li}$  Fermi mixture in the optical traps was given. The results presented in the following two chapters, precision measurements of the contact parameter in the BCS-BEC crossover and spin Bragg spectroscopy, greatly benefited from these major improvements.



# 4. Precision measurement of the universal contact at unitarity

## 4.1. Introduction

In this chapter, I will present precise measurements of the density dynamic structure factor  $S(\mathbf{k}, \omega)$  of a strongly interacting Fermi gas in the unitarity limit and the molecular BEC regimes, utilising two-photon Bragg spectroscopy at high momentum ( $k = 4.20 k_F$ ) [Hoi13]. The static structure factor  $S(\mathbf{k})$  at unitarity was evaluated for a high-precision determination of the universal contact parameter  $\mathcal{I}$ . In a trapped gas, we find  $\mathcal{I}/(Nk_F) = 3.06 \pm 0.08$  at a temperature of 0.08 of the Fermi temperature of the harmonic trap. We use this result for  $\mathcal{I}$  to obtain a constraint on the zero-temperature homogeneous contact.

Strongly interacting Fermi systems are a challenging many-body problem as low-order perturbative approaches usually fail due to the absence of small parameters. The thermodynamics of such systems implies a universal contact which governs the high-momentum (short-range) properties [Bra09]. While exact calculations of  $\mathcal{I}$  are not available, various approximate strong-coupling theories and quantum Monte Carlo (QMC) simulations exist but vary in their predictions by as much as 10 % [Hu11]. Our results set a new benchmark for the contact parameter with an uncertainty small enough (3 %) to differentiate between different theoretical predictions.

In addition, there are a number of qualitative predictions for the dynamic structure factor of a strongly interacting Fermi gas, see for example [Min01, Com06a, Str09, Guo10]. However, a theory that precisely quantifies  $S(\mathbf{k}, \omega)$  of such a gas is unavailable, except at high temperatures ( $T \gtrsim T_c$ ) [Hu12b] and at high frequencies [Son10, Tay10], where exact results for the universal dynamic structure factor exist. Our low-temperature Bragg spectra may thus help to check future strong-coupling calculations of  $S(\mathbf{k}, \omega)$  against experimental data [Hu12a], and they also can provide input for the development of advanced QMC calculations [Ast13]. Note that I use Bragg spectrum as a synonym for the response of the trapped Fermi gas to a perturbation with momentum  $\hbar\mathbf{k}$  and energy  $\hbar\omega$ .

## 4. Precision measurement of the universal contact at unitarity

Section 4.2 starts with a detailed discussion on how we obtain Bragg spectra. The Bragg laser setup is described in section 4.2.3 and 4.2.4, and the calibration of the Bragg laser intensities is given in section 4.2.5. Section 4.3 characterises all experimental parameters relevant for the contact. The main results are reported in section 4.4. After describing the features in the observed Bragg spectra in section 4.4.1, the results for the trapped and homogeneous contact are presented in section 4.4.2 and 4.4.3, respectively.

### 4.2. Probing the density-density response using Bragg spectroscopy

Cold and ultracold atoms are highly amenable to optical Bragg spectroscopy, where inelastic light scattering is used to induce weak perturbations to the momentum distribution of an atomic cloud [Mar88, Koz99]. In early two-photon Bragg scattering experiments on single-species Bose gases, phonon- and particle-like Bogoliubov excitations were studied by measuring density-density responses of atomic BECs [SK99, Ste99]. In previous experiments, we deployed two-photon Bragg spectroscopy on balanced spin mixtures of  ${}^6\text{Li}$  atoms in the states  $|\sigma = \uparrow, \downarrow\rangle$  to probe density-density responses in the BCS-BEC crossover [Vee08, Kuh11c]. Our observations were quite different to the ones in Bose gases as the response is strongly affected by pair correlations between atoms in different spin states and strong interactions, leading to a very different shape of  $S(\mathbf{k}, \omega)$ . To be sensitive to the density-density response, the coupling between Bragg lasers and all particles should be identical. For Fermi gases this means the coupling to each spin state is essentially the same, resulting in a perturbation of the total density,  $\rho_D = \rho_\uparrow + \rho_\downarrow$ . By contrast, probing the spin response in Fermi gases requires the Bragg lasers to couple to the spin density,  $\rho_S = \rho_\uparrow - \rho_\downarrow$ , which will be described in detail in the next chapter.

#### 4.2.1. Bragg spectroscopy and dynamic structure factors

The principles of Bragg spectroscopy in Fermi gases and dynamic structure factors have been extensively described in previous theses of our group [Vee09, Kuh11a]; therefore, I will only briefly summarise the main aspects. In addition, I will outline how the Bragg response of the atomic system relates to pair correlations and the dynamic structure factor.

Two-photon Bragg scattering is a Raman scattering process involving the stimulated absorption and emission of a photon between an atom and two optical fields thereby transferring momentum  $\hbar\mathbf{k}$  and energy  $\hbar\omega$ . Figure 4.2.1 shows the probing scheme we apply

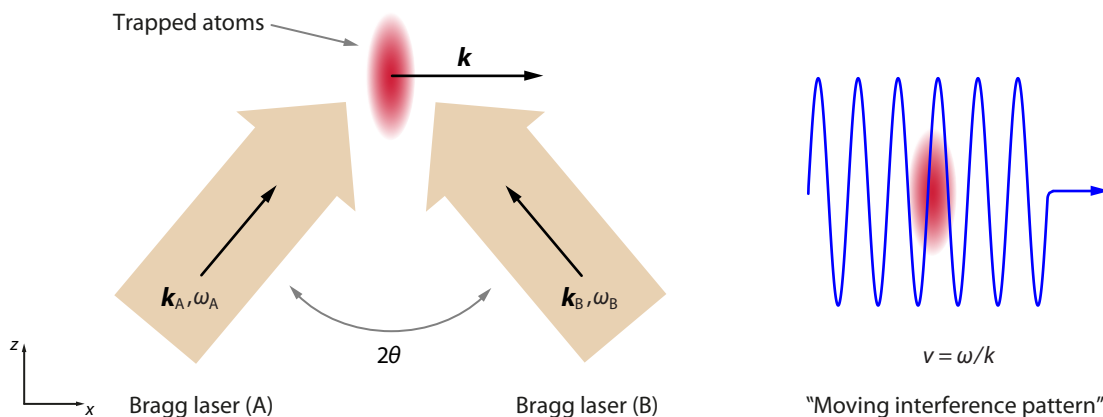


**Figure 4.2.1.:** Bragg spectroscopy involves two collimated laser beams, (A) and (B), with wave vector  $\mathbf{k} = \mathbf{k}_A - \mathbf{k}_B$  and frequency detuning  $\omega = \omega_A - \omega_B$ , where  $\omega \ll \omega_{A,B}$ , to create a Bragg grating that moves with velocity  $v = \omega/k$ .

on Fermi gases. Two collimated laser beams, intersecting at an angle of  $2\theta$ , illuminate a trapped atomic cloud. The difference in the wave vectors defines the momentum transfer,  $\hbar\mathbf{k} = \hbar\mathbf{k}_A - \hbar\mathbf{k}_B$ , while their frequency difference defines the amount of energy transferred,  $\hbar\omega = \hbar\omega_A - \hbar\omega_B$ . An intensity modulation, such as  $I(\mathbf{r}, t) = \sqrt{I_A I_B} \cos(\mathbf{k} \cdot \mathbf{r} - \omega t)$  where  $I_{A,B}$  are the mean laser intensities, is created at the intersection. For  $\omega_A > \omega_B$ , the Bragg lattice moves in positive  $x$ -direction with velocity  $v = \omega/k$ , as indicated in the figure.

In a single particle picture, resonant Bragg scattering occurs when  $\hbar\omega$  is equal to the change in kinetic energy of the atom being scattered. The absorbed and emitted photons result in a momentum kick of  $\hbar k = \sqrt{(\mathbf{k}_A - \mathbf{k}_B)^2} = 2\hbar k_L$ , where to a good approximation  $k_A \simeq k_B \simeq k_L = (2\pi/\lambda) \sin \theta$ , and  $\lambda = 671 \text{ nm}$  is the wavelength of the Bragg lasers. Based on the fundamental laws of conserving energy and momentum, the Bragg resonance condition for an atom, initially at rest, is given by the atomic recoil frequency

$$\omega_{\text{rec}} = \frac{\hbar k^2}{2m} \quad \text{where} \quad k = \frac{4\pi}{\lambda} \sin \theta. \quad (4.2.1)$$

The appearance of the atomic mass in the Bragg condition allows to distinguish the scattering of single atoms ( $m$ ) and molecules or pairs which have twice the atomic mass ( $2m$ ).

The number of scattered particles  $N_{\text{sc}}$  in a dilute atomic cloud with a total of  $N (\gg N_{\text{sc}})$  atoms is proportional to the number of particles that satisfy the Bragg condition. Any elastic collisions following the Bragg pulse preserve the total momentum imparted to the cloud, leading to the key quantity we seek to measure for a Bragg spectrum,

$$\Delta \mathbf{P} = \hbar \mathbf{k} N_{\text{sc}}. \quad (4.2.2)$$

#### 4. Precision measurement of the universal contact at unitarity

We use Bragg spectroscopy to probe the response of the atomic system as a function of the excitations energy  $\hbar\omega$ , given by the frequency detuning between the two lasers at wave vector  $k$  fixed by  $2\theta$  (Bragg spectrum). The probe field of the Bragg lasers is weakly coupled to the total density of the two spin species,  $\rho = \rho_\uparrow + \rho_\downarrow$ , so that the response of the system is linear [Pin66]. In this regime, interactions of the atoms with the Bragg modulation can be expressed in perturbation by the hamiltonian [Bru01],

$$\hat{H}_{\text{Pert}} = U_{\text{Br}} \left[ \hat{\rho}^\dagger(\mathbf{k}) e^{-i\omega t} + \hat{\rho}(\mathbf{k}) e^{i\omega t} \right], \quad (4.2.3)$$

where  $\hat{\rho}(\mathbf{k}) = \sum_{\mathbf{j}} e^{-i\mathbf{k}\cdot\mathbf{r}_{\mathbf{j}}}$  is the total density operator in momentum space, quantifying the fluctuations of the particle density about its average  $\delta\hat{\rho} = \hat{\rho} - \langle\hat{\rho}\rangle$ . The strength of the perturbation,  $U_{\text{Br}} = \hbar\Omega_{\text{Br}}$ , where we define  $\Omega_{\text{Br}} = \hbar\Gamma^2/(4\Delta)\sqrt{I_{\text{A}}I_{\text{B}}}/I_{\text{sat}}$  as the two-photon Rabi frequency (cf. section 3.2.1 on page 44 for values of  $\Gamma$ ,  $\Delta$  and  $I_{\text{sat}}$ ), is set by the laser intensities  $I_{\text{A,B}}$  as well as the laser detunings relative to the atomic transitions from the spin states,  $\Delta_\sigma$  (here  $\Delta_\uparrow \approx \Delta_\downarrow \equiv \Delta$ ).

In such a setting, the linear response is sensitive to spatio-temporal pair correlations. This leads to the generalised pair correlation function,  $G(\mathbf{r}, t)$ , introduced by van Hove in the context of neutron and x-ray inelastic scattering experiments [vH54]. For atoms in the  $|\sigma\rangle$ -spin states it can be defined as

$$\begin{aligned} G_{\sigma\sigma'}(\mathbf{r}, t) &= \frac{1}{N} \left\langle \sum_{\mathbf{i}, \mathbf{j}, \sigma, \sigma'} \int \delta[\mathbf{r}' + \mathbf{r} - \mathbf{r}_{\mathbf{j}, \sigma}(t)] \delta[\mathbf{r}' - \mathbf{r}_{\mathbf{i}, \sigma'}(0)] d\mathbf{r}' \right\rangle \\ &= \frac{1}{N} \left\langle \int \hat{\rho}_\sigma(\mathbf{r}' + \mathbf{r}, t) \hat{\rho}_{\sigma'}^\dagger(\mathbf{r}', 0) d\mathbf{r}' \right\rangle \\ &= \frac{1}{N} \langle \hat{\rho}_\sigma(\mathbf{r}, t) \hat{\rho}_{\sigma'}(0, 0) \rangle, \end{aligned} \quad (4.2.4)$$

analogous to the definition given in [Han86]. Here,  $\hat{\rho}_\sigma(\mathbf{r}, t) = \sum_{\mathbf{j}, \sigma} \delta[\mathbf{r} - \mathbf{r}_{\mathbf{j}, \sigma}(t)]$  is the space- and time dependent density operator and  $\langle \dots \rangle$  indicates that the average is taken over all possible eigenstates of the many-body system. The physical interpretation of  $G_{\sigma\sigma'}(\mathbf{r}, t)$  is that it essentially gives the probability of finding an atom in state  $|\sigma\rangle$  at position  $\mathbf{r}$  and time  $t$  while another atom in state  $|\sigma'\rangle$  is located at  $\mathbf{r} = 0$  at the time  $t = 0$ . This includes the correlation of an atom with itself, referred to as autocorrelation.

The Fourier transform of this pair correlation function leads directly to the dynamic structure factor per particle, according to [vH54, Gri93]

$$\begin{aligned} S_{\sigma\sigma'}(\mathbf{k}, \omega) &= \frac{1}{2\pi} \int G_{\sigma\sigma'}(\mathbf{r}, t) e^{i(\mathbf{k}\cdot\mathbf{r} - \omega t)} d\mathbf{r} dt \\ &= \frac{1}{2\pi N} \int \langle \hat{\rho}_\sigma(\mathbf{k}, t) \hat{\rho}_{\sigma'}^\dagger(\mathbf{k}, 0) \rangle e^{i\omega t} dt, \end{aligned} \quad (4.2.5)$$

## 4.2. Probing the density-density response using Bragg spectroscopy

where  $\hat{\rho}_\sigma(\mathbf{k}, t) = \sum_{\mathbf{j}, \sigma} e^{-i\mathbf{k}\cdot\mathbf{r}_{\mathbf{j}, \sigma}(t)}$ , satisfying the identity  $\hat{\rho}^\dagger(\mathbf{k}, 0) \equiv \hat{\rho}(-\mathbf{k}, 0)$ . The dynamic structure factor is the central quantity for our Bragg scattering experiments. For a spin-balanced two-component Fermi gas, the spin-parallel and anti-parallel components of the response function can be combined to give the total dynamic structure factor [Com06a]

$$S(\mathbf{k}, \omega) = 2[S_{\uparrow\uparrow}(\mathbf{k}, \omega) + S_{\uparrow\downarrow}(\mathbf{k}, \omega)], \quad (4.2.6)$$

where  $S_{\uparrow\downarrow}(\mathbf{k}, \omega) \equiv S_{\downarrow\uparrow}(\mathbf{k}, \omega)$  and  $S_{\uparrow\uparrow}(\mathbf{k}, \omega) \equiv S_{\downarrow\downarrow}(\mathbf{k}, \omega)$ . By this, the transition probability per atom and unit time into an excited momentum state, that is, the atom remains internally in the ground state but the Bragg lasers have transferred energy  $\hbar\omega$  and momentum  $\hbar\mathbf{k}$ , can be written using Fermi's golden rule

$$\mathcal{P}(\mathbf{k}, \omega) = 2\pi\Omega_{\text{Br}}^2 S(\mathbf{k}, \omega). \quad (4.2.7)$$

As an example, at high momentum the Bragg spectrum of a zero-temperature ideal Fermi gas in a single spin state is simply given by its momentum distribution  $n_\sigma(\mathbf{p})$ , as per equation 2.2.17 on page 20, centred at the atomic recoil frequency  $\omega_{\text{rec}}$ . This can be shown by using the so-called impulse approximation for  $S(\mathbf{k}, \omega)$ , valid in the limit of high-momentum transfer [Zam00].

The linear density-density response function or dynamic susceptibility  $\chi(\mathbf{k}, \omega)$  describes spatio-temporal fluctuations in a many-body system at the characteristic length ( $1/k$ ) and time ( $1/\omega$ ) scales as a result of weak perturbations by an external probe potential. The response is fully specified by the properties of the system. The density dynamic structure factor  $S(\mathbf{k}, \omega)$  directly measures the excitation spectrum of these density fluctuations and is proportional to the coherent part of the differential scattering cross-section of the system. The dynamic structure factor is linked to the imaginary (dissipative) part of the dynamic susceptibility by

$$\chi''(\mathbf{k}, \omega) = \pi[S(\mathbf{k}, \omega) - S(-\mathbf{k}, -\omega)] \quad (4.2.8)$$

via the fluctuation-dissipation theorem [Pin66]. The difference term on the right hand side in equation 4.2.8 implies that energy transfer can occur from the probe into the system [ $S(\mathbf{k}, \omega)$ ], and vice versa [ $S(-\mathbf{k}, -\omega)$ ]. At high  $k$  and low  $T$ , used throughout this thesis, only the first term on the right hand side of equation 4.2.8 contributes so I will interchange the terms “density-density response” and “dynamic structure factor” in this thesis as the respective quantities follow from the other.

In the following, I will describe the preparation of the atomic system, the sequence for measuring Bragg spectra, and the image analysis for extracting the density-density response function. I will label the measured response, given by a Bragg spectrum, by  $R(\mathbf{k}, \omega)$  and explain how this quantity relates to  $S(\mathbf{k}, \omega)$ .

## 4.2.2. Measuring density dynamic structure factors and the contact

### Experiment in a nutshell

The experiments which follow are performed on clouds of  ${}^6\text{Li}$  atoms prepared in an equal mixture of the spin states  $|F = 1/2, m_F = +1/2\rangle \equiv |\uparrow\rangle$  and  $|F = 1/2, m_F = -1/2\rangle \equiv |\downarrow\rangle$ , evaporatively cooled in a 100 W single-beam optical dipole trap. Details about the experimental procedure are given chapter 3. In the final stage, a cloud with approximately  $N/2 = (300 \pm 25) \times 10^3$  atoms per spin state is confined in a second optical dipole trap, produced by a 10 W single-beam fibre laser. This trapping beam is spatially filtered to create a large harmonic trapping region. The interactions are tuned to either the unitarity regime [ $1/(k_F a) = 0$ ] near the pole of the broad Feshbach resonance at a magnetic field of 833.0 G or to the BEC side of the crossover at 783 G [ $1/(k_F a) = 0.93$ ].

After holding the cloud in the second dipole trap for 500 ms to allow for equilibration, we apply a short rectangular shaped Bragg pulse of  $\tau_{\text{Br}} = 100 \mu\text{s}$  to the trapped gas and switch of the trapping potential immediately following the pulse. Both of these events happen on a time scale short compared to the inverse trapping frequency to ensure linearity. The cloud expands for  $\tau_{\text{tof1}} = 200 \mu\text{s}$  before an absorption image of atoms in state  $|\uparrow\rangle$  is taken. After a further delay of 850  $\mu\text{s}$  and quickly ramping the imaging laser frequency a second image of the atoms in state  $|\downarrow\rangle$  is taken, which corresponds to a time of flight of  $\tau_{\text{tof2}} = 1.05$  ms. Imaging at such short time intervals was achieved using the kinetics mode of the imaging camera (cf. section 3.4.3). Taking separate images of each spin state enables us to measure the differential centre-of-mass cloud displacement, as described below, which is insensitive to drifts in the trap position. Since we use a 50/50 Fermi mixture, and with large collisional coupling between the two spin states, the order in which we image states  $|\uparrow\rangle$  and  $|\downarrow\rangle$  makes no difference to the measured spectra.

### Obtaining Bragg spectra

As discussed in section 4.2.1, the key quantity in our Bragg experiments is the total momentum transfer  $\Delta\mathbf{P}(\mathbf{k}, \omega)$  which, in the linear response regime, is proportional to the measured dynamic response function  $R(\mathbf{k}, \omega)$ . More specifically, the momentum transfer is proportional to the convolution of the spectral content of the Bragg pulse, due to the finite pulse duration, with the difference of the positive and negative frequency dynamic structure factor [Bru01, Vee08]

$$R(\mathbf{k}, \omega) \propto \tau_{\text{Br}} \int [S(\mathbf{k}, \omega) - S(-\mathbf{k}, -\omega)] \text{sinc}^2 \left[ \frac{(\omega - \omega')\tau_{\text{Br}}}{2} \right] d\omega', \quad (4.2.9)$$

## 4.2. Probing the density-density response using Bragg spectroscopy

where  $\text{sinc}(x) = \sin(x)/x$ . To ensure linearity, a Bragg pulse of  $\tau_{\text{Br}}$  is 100  $\mu\text{s}$  is applied, which is short compared to the inverse two-photon Rabi frequency  $\Omega_{\text{Br}}^{-1}$  at the intensity we use. For  $|\mathbf{k}| > k_{\text{F}}, \lambda_{\text{dB}}^{-1}$ , de-excitation from the cloud into the Bragg beams is strongly suppressed and  $S(-\mathbf{k}, -\omega) \rightarrow 0$ . The Bragg pulse is long enough so that the finite spectral width of the Bragg pulse contributes little to the shape of the Bragg spectra. The convolution due to this pulse gives a Fourier width of  $\sim 9$  kHz which is narrow compared to the spectral features of interest. Under these experimental conditions, the momentum transfer can be written in a simplified form [Bru01],

$$\Delta P(\mathbf{k}, \omega) = 2\pi \hbar k \Omega_{\text{Br}}^2 \tau_{\text{Br}} S(\mathbf{k}, \omega), \quad (4.2.10)$$

where we find the number of scattered atoms to be  $N_{\text{sc}} \equiv \tau_{\text{Br}} \mathcal{P}(k, \omega)$  (cf. equation 4.2.7). Note, from now on we drop the vector notation of the Bragg wave vector as the response depends on  $|\mathbf{k}| = k_x \equiv k$  only (elastic collisions preserve the centre-of-mass motion).

We obtain the response  $R(k, \omega)$  through the total momentum  $\Delta P_x = P_x(\tau_{\text{Br}}) - P_x(0)$  imparted to the cloud, where  $P_x(0) \equiv 0$ . A Bragg pulse which scatters atoms at given  $\omega$  is applied in the  $x$ -direction, perpendicular to the long axis of the cloud. The momentum transfer can be quantified by calculating the centre-of-mass displacement  $\Delta X(\omega)$  which relates to the  $x$ -component of the momentum through the centre-of-mass velocity

$$\frac{\Delta X(\omega)}{\Delta t} = \frac{1}{m} P_x(k = 4.20 k_{\text{F}}, \omega), \quad (4.2.11)$$

where  $\Delta t \equiv \tau_{\text{tof}}$  is the time of flight of the released cloud and  $m$  is the particle's mass.

By taking several absorption images, we acquire two-dimensional density profiles  $n_\omega(x, z)$  of atomic clouds at a particular  $\omega$ . Integrating each image along the  $z$ -direction leads to the line profiles  $n_\omega(x)$ . To determine  $\Delta X(\omega)$ , we evaluate the Bragg signal by calculating the centre of mass of each line profile, defined by its first moment

$$\langle x(\omega) \rangle = \frac{\sum_i x_i n_\omega(x_i)}{\sum_i n_\omega(x_i)}, \quad (4.2.12)$$

where the sum is along the  $x$ -direction over all pixels  $i$ . By comparing the first moment of each profile relative to the profile taken with a Bragg pulse at zero frequency, the Bragg spectrum at frequency  $\omega$  is obtained through

$$\Delta X(\omega) = \langle x(\omega) \rangle - \langle x(0) \rangle. \quad (4.2.13)$$

Figure 4.2.2 shows typical absorption images and the corresponding line profiles of Bragg scattered trapped unitary clouds at (a) zero frequency, (b) at  $\omega_{\text{rec}}/2$ , and (c) the

#### 4. Precision measurement of the universal contact at unitarity

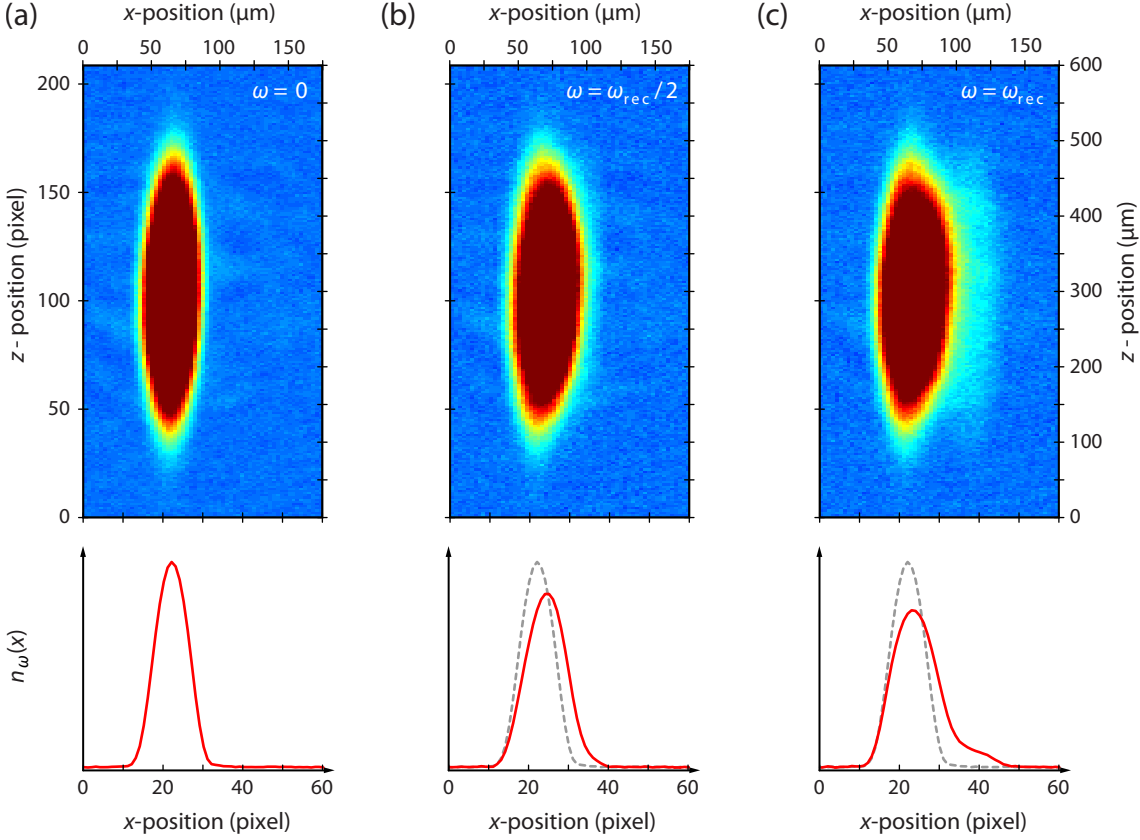


**Figure 4.2.2.:** Typical absorption images and line profiles of a unitary Fermi gas after Bragg scattering at (a)  $\omega = 0$ , (b)  $\omega = \omega_{\text{rec}}/2$ , and (c)  $\omega = \omega_{\text{rec}}$ . The expansion time is  $200\mu\text{s}$ . The images are saturated to amplify the Bragg signal, where blue indicates low and red high pixel counts. Integrating the clouds along the  $z$ -axis gives the line profiles  $n_\omega(x)$ . For comparison, the unperturbed profile from (a) is plotted as a dashed grey line in (b) and (c). The Bragg lattice moves in positive  $x$ -direction.

atomic resonance frequency  $\omega_{\text{rec}}$  after a time of flight of  $200\mu\text{s}$ . The difference in pair ( $\omega_{\text{rec}}/2$ ) and single-atom scattering is evident. At  $\omega = \omega_{\text{rec}}/2$ , we are sensitive to particles with twice the atomic mass, and the scatter of pairs, carrying double atomic mass, appears as a pure deformation of the cloud, while at  $\omega = \omega_{\text{rec}}$ , the cloud is deformed but also single atoms leave the Fermi sea and scatter into free space. In general, we find no obvious separation of pairs from the deformed parent cloud after longer expansion times ( $\sim\text{ms}$ ) in the strongly interacting regime of the BCS-BEC crossover, pointing towards the collective nature of pair scattering.

At this stage, the quality of the Bragg signal can be optimised by carefully selecting a region of interest that just includes the parent cloud and all scattered atoms. This is crucial for minimising noise contributions from the image background to the Bragg signal. It turns out that the background of our images contains some non-random structure as a result of diffraction when imaging dense atomic clouds. This effect can obviously not be cancelled by statistical averaging a large number of images (the structure is present in figure 4.2.2 but is barely visible). A flat background is particularly important at high  $\omega$  where the Bragg signal is inherently very weak. In the following, I will discuss several measures we have taken in the Bragg analysis to improve the quality of the data and also point out a solution to minimise the effects of the abovementioned structure.

### Improved Bragg analysis

In previous experiments, where we used Bragg spectroscopy based on momentum transfer, the centre-of-mass displacement was evaluated with the steps described above. However, the main issue was that  $\Delta X$  relies on a stable absolute trapping position, a requirement which is hard to realise over a long period of data collection. We observed long-term drifts and even sudden jumps in the trapping position by several camera pixels, a distance comparable to the actual Bragg signal! We primarily attribute these effects to thermal expansion of the Zeeman coils, heating up parts of vacuum chamber holding the glass cell, and, of the Feshbach magnetic coils which is attached to the post holding the mount for the top camera.

The accuracy of the Bragg spectra can be considerably improved by eliminating the dependency on the absolute trapping position. In our case, this is easy to accomplish thanks to having atoms in two different hyperfine states. We sequentially image spin state  $|\uparrow\rangle$  and  $|\downarrow\rangle$  after 250  $\mu\text{s}$  and 1.05 ms time of flight, respectively, and compute the first moment  $\langle x_\sigma(\omega) \rangle$  of the resulting line profiles using equation 4.2.12. In this way, we obtain the differential centre-of-mass displacement,

$$\Delta X_c(\omega) = \langle x_\downarrow(\omega) \rangle - \langle x_\uparrow(\omega) \rangle - [\langle \bar{x}_\downarrow(0) \rangle - \langle \bar{x}_\uparrow(0) \rangle], \quad (4.2.14)$$

where the index “c” refers to common-mode rejection, and the bar indicates that we average over many of zero-frequency profiles ( $\gtrsim 20$ ) before calculating the first moment. The reason for averaging is to compensate for any fluctuations in atom number.

In practise, however, we first subtract the normalised average of many zero-frequency line profiles from the normalised profile  $n_\omega(x)$ , and then compute the first moment of the

#### 4. Precision measurement of the universal contact at unitarity

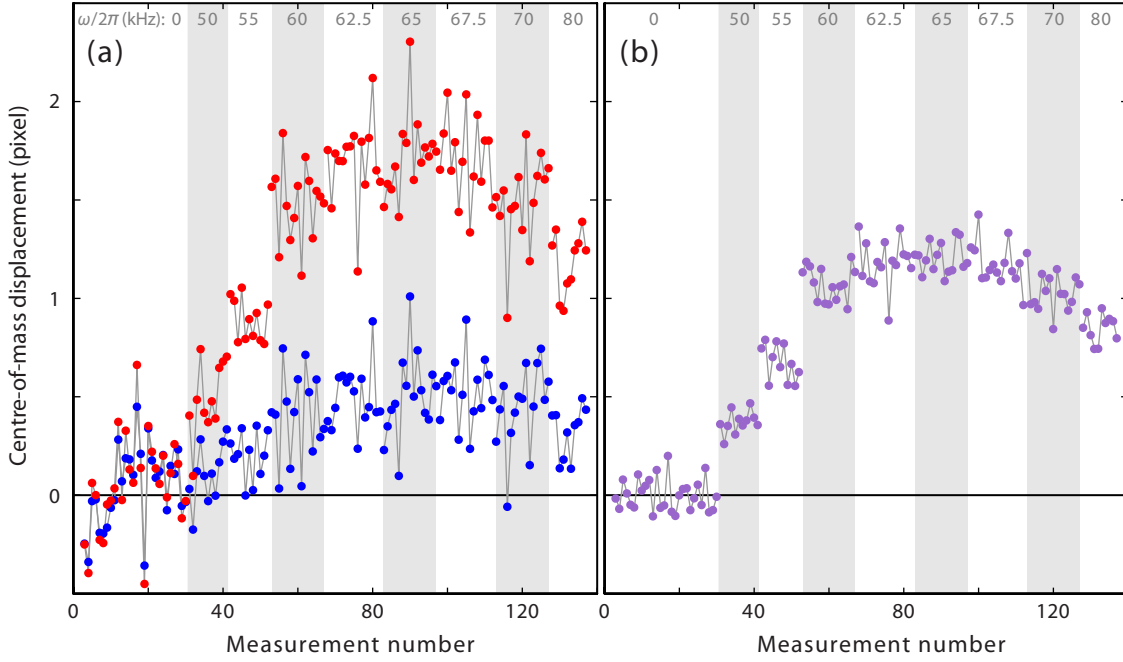


**Figure 4.2.3.:** Figure (a) displays centre-of-mass displacements of Bragg scattered clouds in the spin states  $|\uparrow\rangle$  (blue) and  $|\downarrow\rangle$  (red) after a time of flight of  $200 \mu\text{s}$  and  $1.05 \text{ ms}$ , respectively. The differential centre-of-mass displacement  $\Delta X_d(\omega)$  in (b) contains much less fluctuations and no drifts. The data ranges up to  $80 \text{ kHz}$ , as indicated by the grey and white vertical stripes. The Bragg laser intensities are kept constant in all measurements.

result, according to

$$\Delta \langle x(\omega) \rangle = \frac{\sum_i x_i n_\omega(x_i)}{\sum_i n_\omega(x_i)} - \frac{\sum_i x_i \bar{n}_0(x_i)}{\sum_i \bar{n}_0(x_i)} = \sum_i x_i \left[ \frac{n_\omega(x_i)}{\sum_i n_\omega(x_i)} - \frac{\bar{n}_0(x_i)}{\sum_i \bar{n}_0(x_i)} \right]. \quad (4.2.15)$$

This enables us to obtain only the difference in atom density in a 2D image from which we can calculate the centre of mass, and, to eliminate the abovementioned structure in the background which is essentially consistent for all Bragg frequencies. The final expression for the normalised Bragg spectrum at frequency  $\omega$  is given by

$$\Delta X_d(\omega) = \Delta \langle x_\downarrow(\omega) \rangle - \Delta \langle x_\uparrow(\omega) \rangle, \quad (4.2.16)$$

where  $\Delta \langle x_\sigma(\omega) \rangle$  refers to equation 4.2.15 applied to the profiles at two different expansion times. We typically acquire a number of values for  $\Delta X_d(\omega)$  ( $\gtrsim 10$ ) at each  $\omega$  for averaging purposes. The achieved improvement by using equation 4.2.16 is illustrated in figure 4.2.3.

Graph (a) displays  $\langle x_\sigma(\omega) \rangle$  of raw line profiles for the first 80 kHz of a typical Bragg spectrum. The blue (red) data points corresponds to the results of spin state  $|\sigma = \uparrow, (\downarrow)\rangle$ . The amplitude of the absolute fluctuations is large and a drift is clearly visible in the zero-frequency measurements. After applying equation 4.2.16, the drift has been eliminated and the fluctuations are significantly reduced, as shown in figure 4.2.3 (b). We found that the fluctuations in (b) can be further reduced by increasing the number of data points, which suggests that these fluctuations are essentially random in nature. We also confirmed that it plays no role which of the atomic states is imaged first.

A second major improvement on the Bragg spectra is to use high Bragg lasers intensities while operating in the linear regime. This enhances the Bragg signal which is proportional to  $\Omega_{\text{Br}}^2 \propto I_A I_B$ , where  $I_A$  and  $I_B$  is the intensity of the respective Bragg lasers (A) and (B). For this, a careful linearity check of the density response at several Bragg frequencies was performed (cf. section 4.2.5). Consequently, each  $\Delta X_d(\omega)$  is scaled by the corresponding intensity product ( $I_A I_B$ ), where the intensity in each beam is set to be equal, and then combined to give a complete Bragg spectrum,  $\Delta X(k, \omega)$ .

### Normalising Bragg spectra

We normalise a Bragg spectrum using the  $f$ -sum rule to directly obtain the dynamic structure factor per particle  $S(k, \omega)$  from the measurement of the total momentum transfer without the need of taking into account any prefactors in equation 4.2.10, in particular  $\Omega_{\text{Br}}$  which is hard to scale accurately. The  $f$ -sum rule is an identity from linear response theory and expresses the conservation of particle number. It relates the first or energy-weighted moment of the dynamic structure factor to the recoil energy  $\hbar\omega_{\text{rec}}$  via [Pit03]

$$\hbar \int S(k, \omega) \omega \, d\omega = \omega_{\text{rec}}. \quad (4.2.17)$$

This sum rule is independent of the many-body model, statistics and temperature and is valid at any momentum and frequency. Note that since  $S(k, \omega)$  is in units of  $1/N$ , the particle number does not appear on the right hand side in equation 4.2.17, as often found in literature. In the limit that the centre-of-mass displacement  $\Delta X$  is probing the density-density response, the measured response is given by

$$R(k, \omega) = \frac{\Delta X(k, \omega)}{\int \Delta X(k, \omega) \frac{\omega}{\omega_{\text{rec}}} \, d\omega} \equiv S(k, \omega), \quad (4.2.18)$$

where we have set  $\hbar \equiv 1$  for convenience. In this way, when plotted in units of  $\omega/\omega_{\text{rec}}$ , the response function, and likewise the dynamic structure factor  $S(k, \omega)$ , is expressed

#### 4. Precision measurement of the universal contact at unitarity

in units of  $\omega_{\text{rec}}/N$ . The value of the atomic recoil frequency,  $\omega_{\text{rec}} = \hbar k^2/(2m)$ , can be obtained with high accuracy, as will be demonstrated in section 4.3.1. Note that by this normalisation, the energy weighted integral  $\int R(k, \omega) \frac{\omega}{\omega_{\text{rec}}} d\omega \equiv 1$ . Since the determination of  $X(k, \omega)$  results directly from the high-momentum transfer in the linear regime, the Bragg spectrum after normalisation is equivalent to  $S(k, \omega)$ .

Remark: The difference in the Bragg laser detunings ( $\Delta_{\uparrow, \downarrow}$ ) leads in fact to a correction in the weight of the opposite-spin component  $S_{\uparrow, \downarrow}(\mathbf{k}, \omega)$  of equation 4.2.6 which amounts to about 1% for the detunings we use (cf. section 4.2.4). This will be relevant when comparing  $R(\mathbf{k}, \omega)$  with accurate calculations of  $S(\mathbf{k}, \omega)$ . For the calculations of the contact parameter in this chapter, this correction is not included as we found that the error introduced is smaller than other experimental uncertainties. In the next chapter (section 5.2.1), however, I will show how to include this correction in  $R(\mathbf{k}, \omega)$ . It turns out that this will directly lead to a scheme for measuring the dynamic spin response function,  $R_S(\mathbf{k}, \omega)$ , where the Bragg lasers couple to the spin density of the Fermi gas,  $\rho = \rho_{\uparrow} - \rho_{\downarrow}$ .

#### The static structure factor

The static structure factor gives access to the instantaneous pair correlations between atoms in same- and opposite spin states in the system and is defined by the Fourier transform of the pair distribution function [Com06a]

$$S(k) = 1 + n \int [g(r) - 1] e^{-i\mathbf{k}\cdot\mathbf{r}} d\mathbf{r}, \quad (4.2.19)$$

where  $g(r) = [g_{\uparrow\downarrow}(r) + g_{\downarrow\uparrow}(r)]/2$  is the sum of the pair correlation functions of the same- and opposite spin states.  $S(k)$  can be calculated via the zero moment of the dynamic structure factor,  $\hbar \int S(k, \omega) d\omega = S(k)$ . Due to the normalisation described above, the integral of the normalised Bragg spectra over  $\omega$  directly gives the total static structure factor,

$$\int R(k, \omega) d\omega \equiv \int S(k, \omega) d\omega = S(k) = S_{\uparrow\uparrow}(k) + S_{\uparrow\downarrow}(k), \quad (4.2.20)$$

where  $S_{\uparrow\uparrow}(k) \equiv S_{\downarrow\downarrow}(k)$  and  $S_{\uparrow\downarrow}(k) \equiv S_{\downarrow\uparrow}(k)$  for a spin-balanced Fermi gas. The improved results for the dynamic and the static structure factors will be used to determine a new high-precision value for the trapped (section 4.4.2) and homogeneous (section 4.4.3) universal contact parameter.

### 4.2.3. The new Bragg laser setup and frequency control

The Bragg laser setup was completely redesigned to obtain Bragg spectra under more repeatable conditions. Special attention was paid to stabilising intensity and beam paths of the lasers. Also, we now make use of a direct digital synthesiser (DDS) that controls the frequency difference  $\omega$  between the lasers to an accuracy better than 1 Hz. Technical details of the DDS including instructions on how to build it are given in appendix B.

Figure 4.2.4 depicts the layout of the new laser setup. For spatial filtering, and for more flexibility in handling the Bragg beams, linear polarised laser light is delivered through two separate polarisation-maintaining singlemode fibres prior entering the science cell. The fibre outcoupling units, outlined in figure 4.2.4 (a), consist of compact half inch optical mounts from Thorlabs each carrying a fibre coupling lens with a focal length of 13.86 mm, and a high contrast linear polariser sandwiched between two zero-order half-wave plates to allow for a precise adjustment of the polarisation<sup>1</sup>. Large collimated Bragg beams are required to uniformly illuminate the atomic cloud. We measured the  $1/e^2$ -beam diameter with a beam profiler and found 2.65 mm which is much larger than  $\sim 300 \mu\text{m}$ , the typical size of the cloud in the weakest trapping direction. The typical optical total power of the Bragg beams after the last optical element ranges between 1 – 100  $\mu\text{W}$ .

Two calibrated photo diodes (bandwidth 500 kHz) at the opposite side of the glass cell collect the light of the Bragg beams. Their signal voltages are continuously recorded by an oscilloscope. We use these signals to monitor pulse shape and intensity of the Bragg lasers during data acquisition, and to scale the measured spectrum  $\Delta X(k, \omega)$  by the intensity product (cf. section 4.2.2). The angle of the intersecting Bragg beams is  $2\theta = 83.9^\circ$  which we determined by measuring the atomic recoil frequency, as explained in section 4.3.1.

The light for the Bragg laser setup originates from the imaging slave diode laser, which is frequency stabilised via a seed and offset lock (cf. imaging laser setup in section 3.4.2). As illustrated in figure 4.2.4 (b), a number of AOMs are deployed to produce all necessary frequency shifts (figure 3.3.2 on page 52 gives a summary of all required laser frequencies), and to control  $\omega$ . The setup is designed to either probe density or the spin responses. For this, a polarising beamsplitter is used to select AOMs, set to +200.0 MHz and –101.9 MHz in double-pass configuration, as shown in figure 4.2.4 (b). These two AOMs also serve as a fast optical switch. The duration of the Bragg pulse depends on whether we measure density ( $\tau_{\text{Br}} = 100 \mu\text{s}$ ) or spin ( $\tau_{\text{Br}} = 50$  and  $25 \mu\text{s}$ ) responses.

---

<sup>1</sup>Polariser: Edmund optics, VIS-NR 12.5mm; Half-wave plate: Lens-optics, W2Z15-671

4. Precision measurement of the universal contact at unitarity

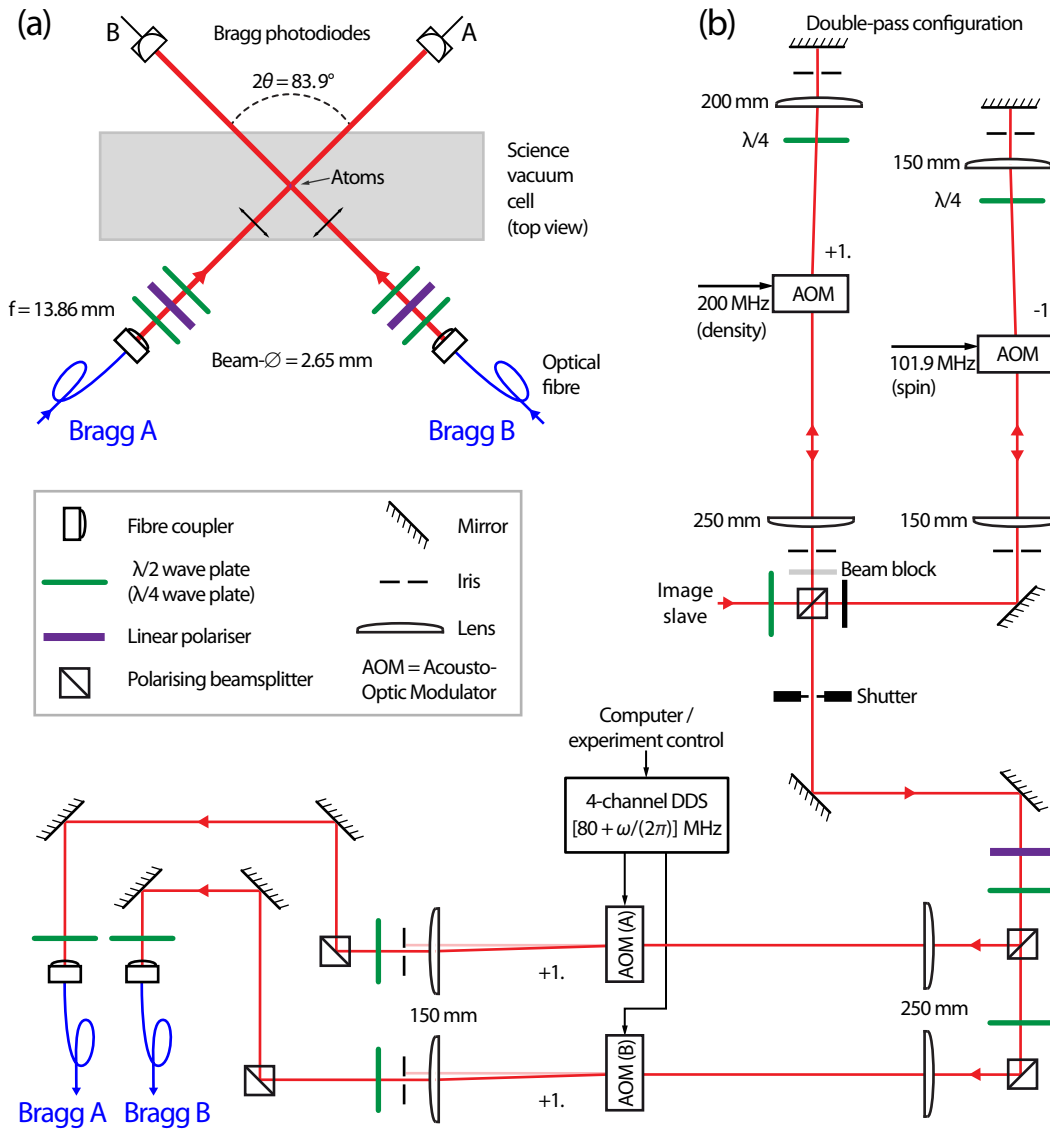


**Figure 4.2.4.:** Schematic of the Bragg laser setup. (a): Two collimated laser beams (red) with horizontal, linear polarisation enter the glass cell. (b): A set of AOMs shift the Bragg laser frequencies. Depending on the type of measurement, AOMs set to  $200.0 \text{ MHz}$  (density Bragg) and  $101.9 \text{ MHz}$  (spin Bragg) in double-pass configuration are used. The Bragg excitation frequency  $\omega$  is precisely defined by the frequency difference between AOM (A) and (B) (centre frequency  $80 \text{ MHz}$ ), driven by the DDS on two separate channels.

As further shown in figure 4.2.4 (b), the Bragg beam is split into two branches prior reaching AOM (A) and (B). These AOMs run continuously to ensure a high intensity

stability of the first diffracted order. AOM (A) and (B) are phase coherently driven by the DDS at the respective frequencies  $80 + \omega/(2\pi)$  and 80 MHz, which enables a precise control of the excitation frequency  $\omega$  (tuning range typically  $2\pi \times 500$  kHz). The DDS is controlled by the image acquisition computer. For coupling the Bragg beams (A) and (B) into the two optical fibres, we employ low drift stainless steel mirror mounts from Thorlabs, model Polaris-K1. They have proven to be very stable, and readjustments of the input coupling over a period of one day are in general not required.

#### 4.2.4. Bragg transitions of ground state ${}^6\text{Li}$ atoms at high magnetic fields

The study of Fermi gases in the BCS-BEC crossover takes place in the vicinity of the broad Feshbach resonance of the  $|\uparrow\rangle$  and  $|\downarrow\rangle$  spin states, centred around 833 G. At such high magnetic fields, the atomic nuclear spin is essentially fully decoupled from the electronic spin (Paschen-Back regime) and therefore the nuclear spin cannot be flipped by the Bragg lasers. This situation turns out to work in our favour when selecting Bragg transitions as effectively closed transitions can be realised.

Figure 4.2.5 illustrates the Bragg scheme for measuring response functions at unitarity. We blue-detune the frequency  $\omega_L$  of the two Bragg lasers relative to the atomic transitions,  $m_J = -1/2 \rightarrow m_{J'} = -3/2$ , with detunings  $\Delta_\uparrow = 584$  MHz and  $\Delta_\downarrow = 662$  MHz. The nuclear spin projection  $m_I$  is +1 for the  $|\uparrow\rangle$  and 0 for the  $|\downarrow\rangle$  ground state. Only transitions changing  $m_J$  and preserving  $m_I$  are possible (see also appendix A for a detailed diagram of the  ${}^6\text{Li}$  electronic structure).

As pointed out in the previous section, the Bragg laser beams (A) and (B) are horizontally polarised which corresponds to a direction perpendicular to the Feshbach magnetic field. For ideal horizontal polarisation, only  $\sigma^\pm$  transitions are allowed. We use the strong  $\sigma^-$  transitions,  $|\uparrow\rangle \rightarrow |m_{F'} = -1/2, m_{J'} = -3/2\rangle$  and  $|\downarrow\rangle \rightarrow |m_{F'} = -3/2, m_{J'} = -3/2\rangle$ . Due to the large Zeeman splitting of approximately 80 MHz it is straightforward to selectively excite each of the ground states. Contributions from other excited  ${}^2P_{3/2}$  levels are present but small ( $\sim 8\%$ ). In our case, the possible  $\sigma^+$  transitions are 3 times weaker than the  $\sigma^-$  transitions [Met99] (the corresponding levels are not shown in figure 4.2.5). Also, detunings from  $\omega_L$  to any of these  $\sigma^+$  transition are  $\sim 4$  times larger than  $\Delta_{\uparrow,\downarrow}$  (of order 1.5 GHz). The overall coupling to  $\sigma^+$  transitions is therefore about 12 times weaker. In addition, transitions to any  $m_{J'} = -1/2$  levels of  $|e'\rangle$  are forbidden by selection rules. We hence can treat the selected Bragg transitions as atom-light interactions of a simple two-level atom.

#### 4. Precision measurement of the universal contact at unitarity

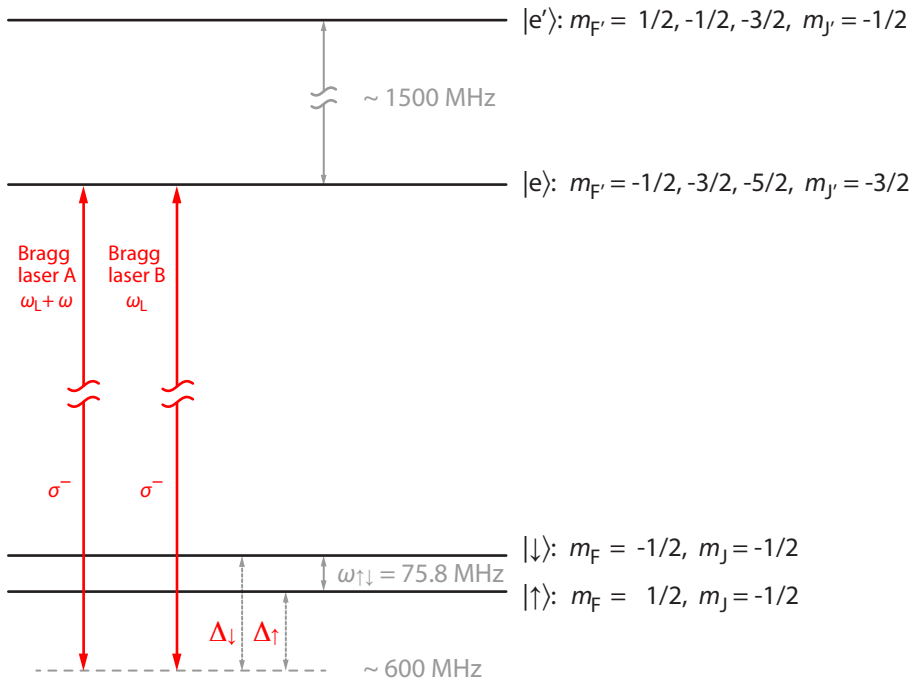


**Figure 4.2.5.:** Atomic energy diagram of the  ${}^6\text{Li}$   $D_2$ -line and Bragg-laser transitions for probing the density response at unitarity (not to scale). Both Bragg lasers with frequency  $\omega_L$  are blue detuned by  $\Delta_{\uparrow,\downarrow} \sim 600$  MHz relative to the optical transitions. Note that  $\omega_L \gg \Delta_{\uparrow,\downarrow} \gg \omega$ , where  $\omega$  is Bragg excitation frequency. The distance to neighbouring excited levels is more than 1.5 GHz.

#### Bragg lasers with orthogonal polarisation

I will briefly comment on the, at first glance, unusual configuration of the polarisation: The intensity distribution of a Bragg lattice is created by two intersecting laser beams with perpendicular polarisation. When probing a trapped atomic gas in Bragg experiments, a moving intensity pattern with spatially periodic structure is required to transfer momentum  $\hbar\mathbf{k}$  into the gas.

Standard descriptions on the formation of intensity gratings used for Bragg spectroscopy are usually based on the interference of two parallel (vertical) linear polarised plane waves intersecting at an angle of, let's say,  $2\theta$ . This scenario is illustrated in figure 4.2.6 (a). It is well known that for waves with identical field amplitude and a fixed phase relation the interference in the overlapping region creates a sinusoidal one-dimensional lattice with spatially varying intensity,  $I_{\text{Bragg}} = I_0 \cos^2(\frac{kx}{2}) = I_0 \cos^2(\frac{\pi x}{d})$ , where  $I_0$  is the modulation

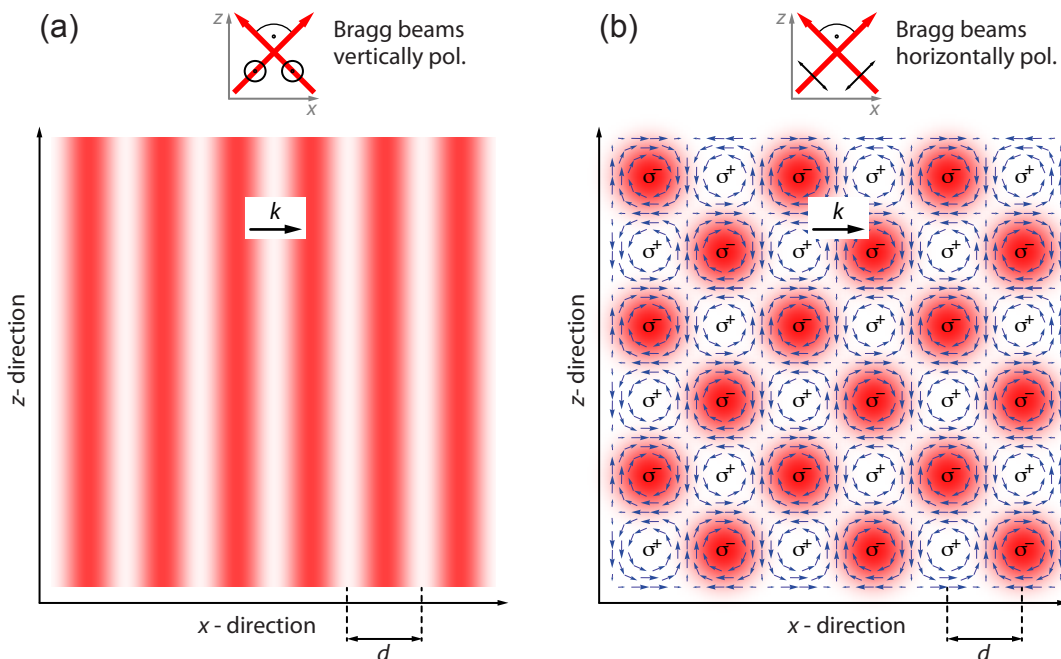


**Figure 4.2.6.:** Intensity distribution of Bragg lattices created by two intersecting collimated laser beams with parallel (a) and perpendicular (b) linear polarisation. The diagrams show intensity pattern in a small section of the overlapping region, looking from the top. Intensity maxima and minima are indicated in red and white, respectively. The lattices move to the right.

strength,  $k = 2\pi/d$  is the Bragg wave vector, and  $d = \lambda/(2\sin\theta)$  the distance between two intensity maxima (red) or minima (white). If the two waves differ in frequency  $\nu$ , the light sheets travel at velocity  $v_{\text{lat}} = \nu d$  in the direction of  $\mathbf{k}$ , here parallel to the  $x$ -axis.

In our case, however, the polarisation vectors of the Bragg lasers, intersecting at an angle of  $2\theta \simeq 84^\circ$ , lie in the plane of the two beams and therefore are almost orthogonal. Consequently, no intensity grating in the usual sense exists, in fact, the total intensity  $I_{\text{Bragg}}$  is essentially constant (if we ignore the Gaussian beam profile). However, atoms scatter off the Bragg lattice for the following reason: The Bragg field in the overlapping region can be decomposed into waves with alternating left ( $\sigma^+$ ) and right ( $\sigma^-$ ) circularly polarised light, periodically varying in space, as shown in figure 4.2.6 (b) [Mor06]. For slightly different laser frequencies, the array of  $\sigma^\pm$  light moves along the  $x$ -axis as shown in the figure. Since our Bragg scheme only allows  $\sigma^-$  transitions, the atoms are only perturbed by a potential created by the square of the electric amplitude of the right-

#### 4. Precision measurement of the universal contact at unitarity

circular polarised field component, which is arranged in an array of one-dimensional tube-like intensity maxima (red) separated from areas with effectively zero intensity (white), as visualised in figure 4.2.6 (b). Note that since the lattice travels diagonal relative to the intensity maxima the lattice constant  $d$  is identical to Bragg lasers with vertically polarised beams.

##### 4.2.5. Bragg linearity measurements

To ensure that Bragg spectra are probed in the linear response regime, we have carefully checked the intensity dependence of the dynamic response. We aim to find laser intensities that maximise the Bragg signal at given frequency  $\omega$ . In the linear regime, the momentum imparted to the cloud by the Bragg lasers (A) and (B) (Bragg signal) will grow linearly with the product of the Bragg laser intensities,  $I_A I_B$ . Matching the two intensities provides the largest Bragg response for a given total intensity while minimising spontaneous emission. The linear response regime also depends on the Bragg frequency; therefore we have a range of Bragg frequencies to map this dependence.

The response is obtained by applying a short Bragg pulse to a trapped atom cloud and measuring the momentum transferred to the cloud by releasing the cloud from the trap and measuring the resultant centre-of-mass displacement  $\Delta X_d(\omega)$ , as described in section 4.2.2. A Bragg pulse duration of  $\tau_{\text{Br}} = 100 \mu\text{s}$  was used for the density response at  $1/(k_F a) = 0.0$  and  $0.93$ . In the linear regime, the momentum imparted to the cloud is proportional to the product of the Bragg laser intensities  $I_A I_B$  multiplied by the pulse duration, while the number of spontaneously scattered photons is proportional to the total intensity,  $I_A + I_B$ , multiplied by  $\tau_{\text{Br}}$ .

The panels (a) and (b) in figure 4.2.7 show the density response of a cloud at unitarity, and, figure 4.2.8 shows the density response for a cloud on the BEC side of the Feshbach resonance at an interaction strength of  $1/(k_F a) = 0.93$ . Bragg laser intensities are quoted in units of the saturation intensity,  $I_{\text{sat}} = 2.54 \text{ mW}$ , for the  $D_2$ -line of  ${}^6\text{Li}$ . The different colours indicate different Bragg frequencies with the red triangles corresponding to the atomic recoil frequency  $\omega_{\text{rec}}$ . The data at  $\omega_{\text{rec}}/2$  (blue circles) and  $\omega_{\text{rec}}/4$  (green squares) are dominated by pairing and have a different intensity dependence compared to the response at higher frequencies,  $\omega_{\text{rec}}$  (red triangles) and  $2\omega_{\text{rec}}$  (black inverted triangles), which is dominated by single-atom excitations.

The density response in both figures, 4.2.7 and 4.2.8, stays linear at  $\omega_{\text{rec}}/2$  only up to squared intensities of approximately  $4 \times 10^{-3} I_{\text{sat}}^2$  for both unitarity and on the BEC side, whereas the response at  $\omega_{\text{rec}}$  stays linear up to  $2 \times 10^{-2} I_{\text{sat}}^2$  at unitarity and  $6 \times 10^{-2} I_{\text{sat}}^2$

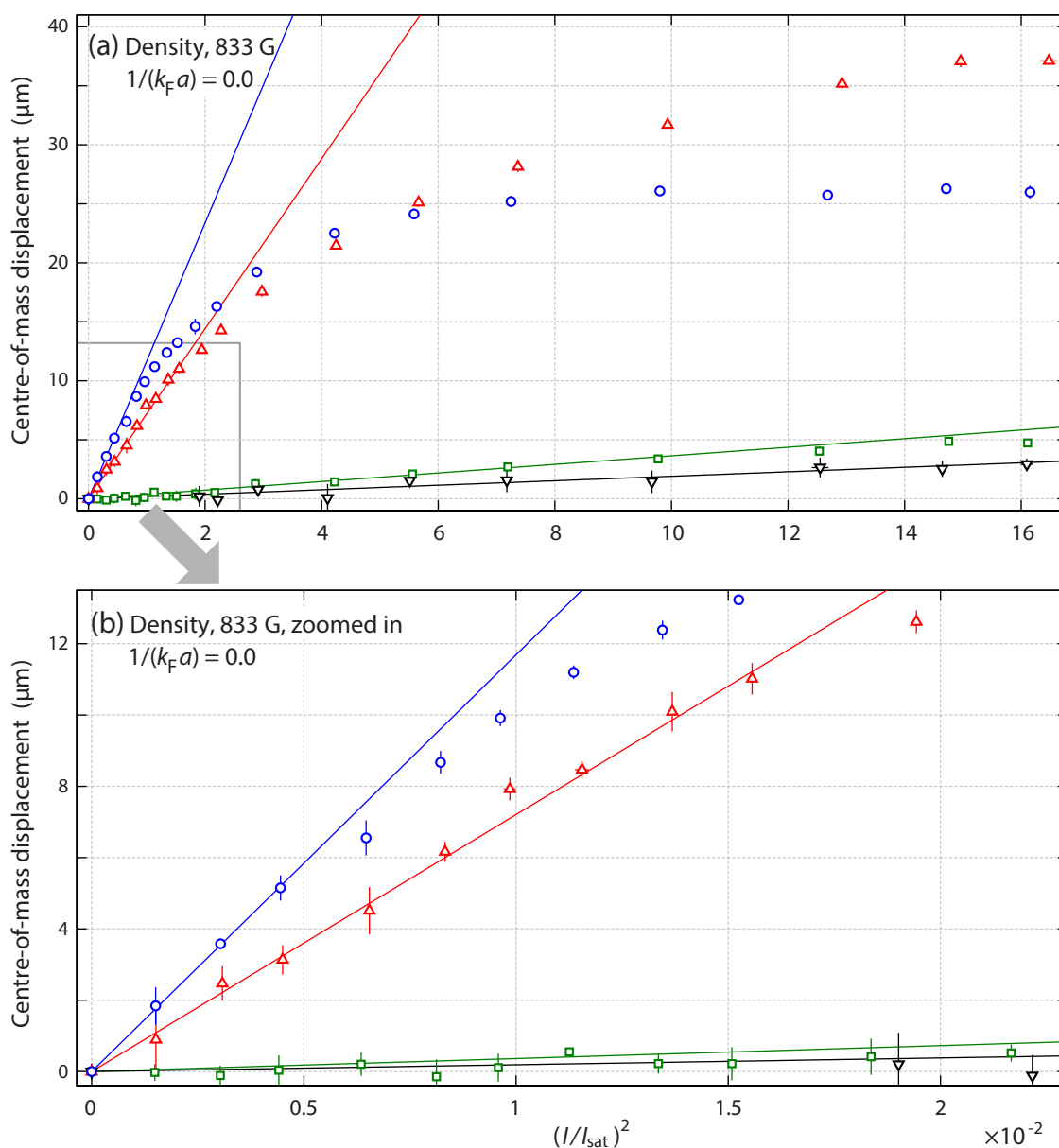


**Figure 4.2.7.:** Measurements of the centre-of-mass cloud displacement versus the squared Bragg laser intensity at four different frequencies. Shown are density-responses for a unitary Fermi gas. Green squares were taken at  $\omega = \omega_{\text{rec}}/4$ , blue circles at  $\omega = \omega_{\text{rec}}/2$ , red triangles at  $\omega = \omega_{\text{rec}} = 132 \text{ kHz}$  and black inverted triangles at  $\omega = 2\omega_{\text{rec}}$ . The straight lines are fits to the low intensity linear response portion of the data. Figure (a) shows data for squared intensities up to  $16 \times 10^{-2} I_{\text{sat}}^2$ , figure (b) zooms in on the same data.

#### 4. Precision measurement of the universal contact at unitarity

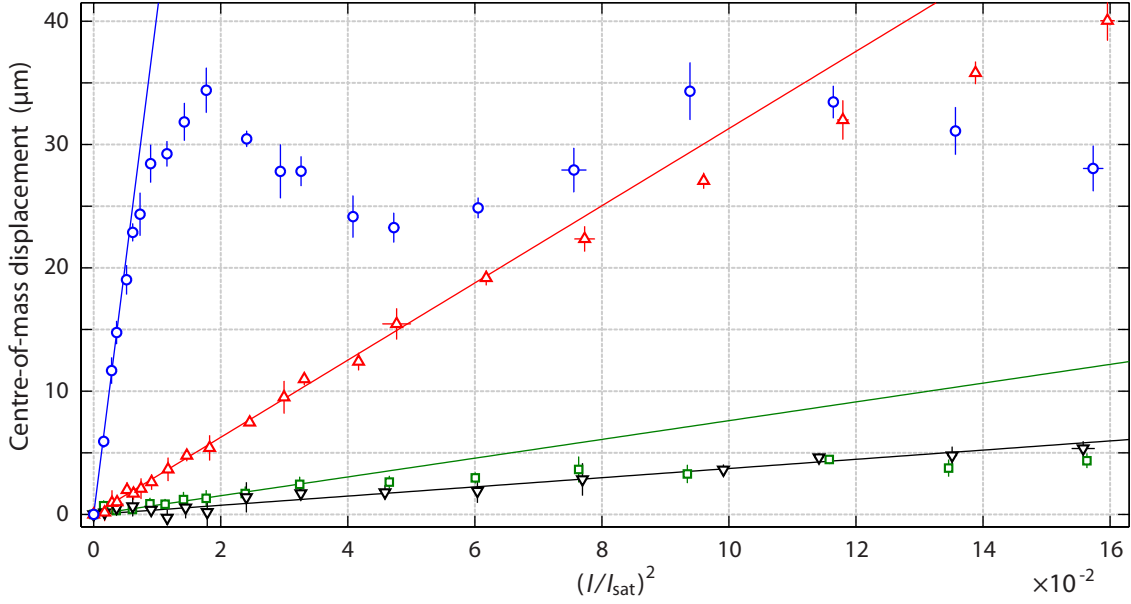


**Figure 4.2.8.:** Measurements of the centre-of-mass displacement of atomic clouds prepared at 783 G versus the squared intensity of the Bragg lasers for a selection of excitation frequencies  $\omega$  in units of the atomic recoil frequency  $\omega_{\text{rec}} = 132$  kHz. Green squares were taken at  $\omega = \omega_{\text{rec}}/4$ , blue circles at  $\omega = \omega_{\text{rec}}/2$ , red triangles at  $\omega = \omega_{\text{rec}}$ , and black inverted triangles at  $\omega = 2\omega_{\text{rec}}$ . The straight lines are fits to the low intensity linear response portion of the data. The pair response at  $\omega = \omega_{\text{rec}}/2$  exhibits damped Rabi oscillations.

on the BEC side. At even higher frequencies,  $\gtrsim 2\omega_{\text{rec}}$ , the density response is linear up to much higher intensities. The BEC response, figure 4.2.8, shows damped Rabi oscillations for  $\omega = \omega_{\text{rec}}/2$  corresponding to the coherent excitation of the momentum states of weakly bound molecules. This (Landau) damping can arise from the overlap of the pair excitations with the continuum of single-atom excitations as well as elastic collisions (cf. section 4.4.1).

Knowing the Bragg laser intensities needed to remain in the linear regime, we can optimise the intensities as we vary the Bragg frequency  $\omega$  in such a way that spectra are obtained using the largest possible linear signal and hence greatest signal-to-noise ratios. For density Bragg spectra, we gradually increase the laser intensities for frequencies above  $\omega_{\text{rec}}$  and scale the measured momentum by the product of the intensities.

### 4.3. Characterisation of the trapped ${}^6\text{Li}$ gas

Before proceeding to the results in the next section, I will discuss some more technical aspects of the atomic system, namely the calibration of experimental parameters including their uncertainties, that are required for determining the contact. These are quantities such as the trapping frequencies  $\omega_{x,y,z}$ , the total atom number  $N$ , and the Bragg wave vector  $k$  which we infer from the atomic recoil frequency  $\omega_{\text{rec}}$ . I will also describe how we determine the relative temperature  $T/T_{\text{F}}$  of a harmonically trapped unitary Fermi gas.

It turns out that the uncertainty in atom number dominates the uncertainties of all other quantities of interest here. This is due to the notorious difficulties that arise from determining atom numbers of optical dense clouds, and, due to shot-to-shot fluctuations over the course of the experiments.

As I was not directly involved in the final calibration measurements of the atom number and the temperature, I will only briefly summarise the applied procedures. A more thorough discussion is deferred to a future thesis. However, I do not want to miss the opportunity of describing two neat procedures I carried out utilising Bragg spectroscopy on a noninteracting Fermi gas as a tool to precisely determine the value of  $k$  based on measuring the atomic recoil frequency, and, to obtain the magnification  $M$  of the imaging system, an important quantity to calculate  $N$  from absorption images.

#### 4.3.1. Atomic recoil frequency and Bragg wave vector

We determine the magnitude of the Bragg wave vector  $k$  by measuring the dynamic structure factor of a noninteracting  ${}^6\text{Li}$  Fermi gas at high-momentum transfer. The peak of the spectrum gives the atomic recoil frequency  $\omega_{\text{rec}}$ , and thus  $k$  via the atomic Bragg resonance condition. For the calculation of the contact and for comparison of the measured static structure factor with theoretical predictions we need to know a precise value of  $k$ .

The magnitude of the Bragg wave vector is given by  $k = (4\pi/\lambda) \sin \theta$ , which depends on the angle  $\theta$  and the wavelength  $\lambda$  of the two intersecting Bragg laser beams. The wavelength is known to high accuracy from the  $D_2$ -line (670.9773... nm). The obvious way to find  $\theta$  would be to use a ruler and measure the positions of the beam paths. Since the beams are aligned at vertical and horizontal angles, to reach the atom cloud in the vacuum glass cell, this method turns out to be somewhat cumbersome, given the limited access to the beams for placing the ruler and the lack of proper reference points. We tried it anyway and found an angle of  $(84 \pm 1)^\circ$ .

To improve the accuracy of this measurement, we take a second approach and obtain

#### 4. Precision measurement of the universal contact at unitarity

$k$  directly by making use of the atomic Bragg resonance condition,

$$\omega_{\text{rec}} = \frac{\hbar k^2}{2m} \quad (4.3.1)$$

which relates the square of the Bragg wave vector to the atomic recoil frequency. According to the impulse approximation [Zam00], the dynamic structure factor of an ideal Fermi gas in a harmonic trap at high-momentum transfer,  $S_{\text{IA}}(k > 2k_{\text{F}}, \omega)$ , provides an immediate measure of atomic momentum distribution  $n_{\sigma}(\mathbf{p})$  (cf. equation 2.2.17 on page 20). In this case, the peak of  $S_{\text{IA}}(k, \omega)$  coincides with the position of  $\omega_{\text{rec}}$ , simply reflecting the fact that the atoms at zero  $x$ -momentum are located at the centre of the momentum distribution, the region of the cloud with highest density.

To measure the response function, we start by preparing a balanced mixture of atoms in the  $|\uparrow\rangle, |\downarrow\rangle$  spin states until the last step of the evaporation in the first dipole trap, as described in section 4.2.2. A noninteracting Fermi gas can be realised for example in the weakly interacting BCS regime by removing atoms in one of the spin states from the trap. To lower the collision rate between the atoms, the magnetic field of the Feshbach coils is tuned from 833 to 980 G [ $1/(k_{\text{F}}a) = -1.4$ ], the highest magnetic field where imaging of  $|\uparrow\rangle$  atoms is possible with our current setup. A flash of the imaging laser for 4  $\mu\text{s}$  follows to resonantly excite the  $|\uparrow\rangle$  atoms and effectively blast them out of the trap. The purified cloud with the remaining  $|\downarrow\rangle$  atoms are then loaded into the second dipole trap while ramping the magnetic field to 920 G, corresponding to the highest magnetic field to image the  $|\uparrow\rangle$  state. After a hold time of 500 ms, a Bragg pulse of  $\tau_{\text{Br}} = 100 \mu\text{s}$  is applied. Switching off the trap immediately following the pulse, the cloud is imaged after a time of flight of 1.35 ms.

To obtain the spectrum  $\Delta X_{\text{d}}(k, \omega) \equiv S_0(k, \omega)$ , the above steps were repeated for a range of Bragg frequencies  $\omega$ . Two sets of ten data points were collected for each  $\omega$  with atoms scattering out of the parent cloud in either the positive or negative direction, as illustrated in figure 4.3.1 (a) and (b). Probing both directions serves as a consistency check. The Bragg laser intensities were set to 20  $\mu\text{W}$  per beam. Note that the displacement of the scattered component of the noninteracting Fermi gas is independent of the intensity of the Bragg lasers. The sets of data points were combined to give averaged centre-of-mass displacements  $\Delta X_{\text{d}}(\omega)$  from the line density profiles. By determining the maximum amplitude of a fitting function of the form  $\propto \exp(-|x - a|^{2.32}/b^2) + cx$  to the resultant spectrum, the atomic recoil frequency was found to be  $\omega_{\text{rec}} = 2\pi \times (131.6 \pm 0.3) \text{ kHz}$ , see figure 4.3.1 (c). Note that this somewhat arbitrary function was chosen to provide a good fit to the data which allows us to accurately determine the centre frequency.

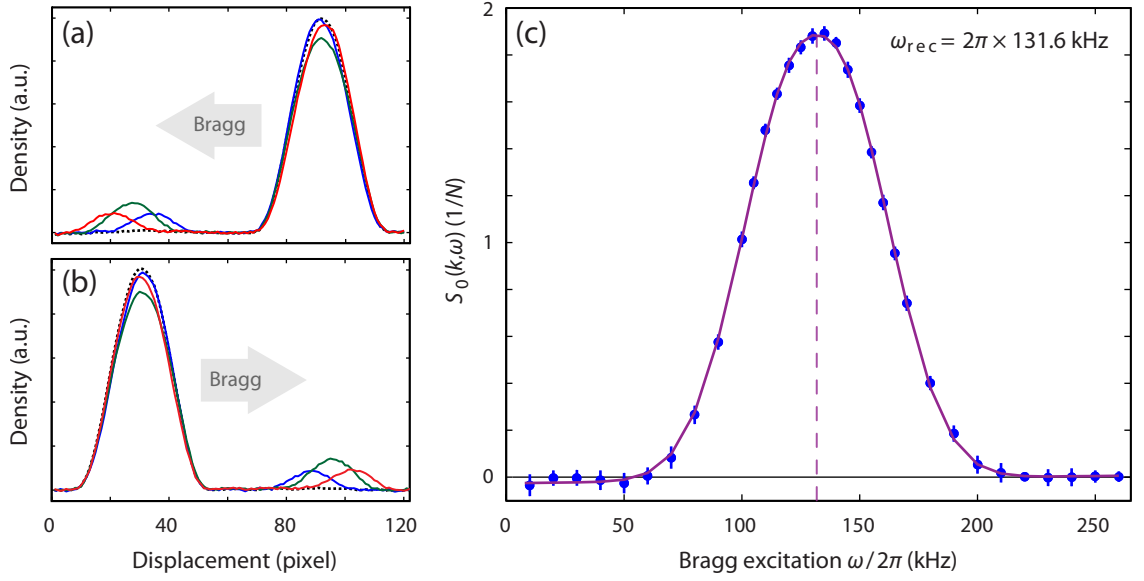


**Figure 4.3.1.:** Line density profiles  $n_\omega(x)$  (a,b) and the resultant Bragg spectrum (c) of a trapped noninteracting Fermi gas at 920 G. Atoms are scattered in the negative (a) and positive (b) direction at frequencies  $\omega/(2\pi)$  of 100, 130, 160 and 0 kHz (blue, green, red and dashed black). The peak of the spectrum in (c) is located at  $\omega_{\text{rec}}/(2\pi) = 131.6$  kHz obtained by a fit function (purple).

Using equation 4.3.1, the magnitude of the Bragg wave vector  $k$  therefore amounts to  $(12.51 \pm 0.01) \mu\text{m}^{-1}$ , which corresponds to an angle of  $2\theta = (83.86 \pm 0.12)^\circ$  of the two intersecting Bragg lasers. This results shows, the job with the ruler was not so bad. As an additional check, it is worth noting that the static structure factor,  $S_{1A}(k)$ , of the measured Bragg spectrum has a value of  $0.995 \pm 0.008$  which confirms the expected value of unity for an uncorrelated ideal Fermi gas [Pin66].

### 4.3.2. Image magnification

The magnification  $M$  of the imaging system was determined by comparing the measured centre-of-mass positions of two adjacent Bragg scattered noninteracting Fermi gas clouds at different time of flights in a weak magnetic trapping potential with the motion of a particle in a simple harmonic oscillator at different travel times.

The dimensionless contact parameter  $\mathcal{I}/Nk_F$  for a harmonically trapped Fermi gas at unitarity is specified relative to the Fermi wave vector  $k_F = (24N)^{1/6} \sqrt{m\bar{\omega}/\hbar}$ , where  $\bar{\omega} = (\omega_x\omega_y\omega_z)^{1/3}$  is the mean trapping frequency. Although the dependency of the total atom number  $N$  is comparably weak a reliable measure of this quantity is still required

#### 4. Precision measurement of the universal contact at unitarity

for the contact. In fact, as described in the next section, determining  $N$  for an optically dense Fermi gas has turned out to be more challenging than anticipated.

When analysing images, a key quantity relevant for determining  $N$  is the magnification which scales the pixel area of the CCD camera proportional to  $1/M^2$  (cf. equation 3.4.5 on page 66). Due to the lack of access to the imaging objective lens in our setup for measuring its working distance to the atom cloud, and also due to the absence of adequate calibration objects in the imaging plane, the exact magnification can only be determined indirectly. We have performed a reliable calibration of  $M$  in the following way: We start by taking a series of Bragg scattered clouds images, produced in the same way as described in section 4.3.1 but for three different expansion times using a noninteracting gas.

Figure 4.3.2 (a) shows such clouds displaced in the positive direction after time of flights of  $\tau_{1,2,3} = 0.7, 1.35, 2.0$  ms. The relative time difference between adjacent clouds hence is  $\Delta\tau = 650 \mu\text{s}$ . Following the Bragg pulse, the clouds are immediately released from the optical trap but remain confined in the (very harmonic) magnetic potential with a precisely known trapping frequency of  $\omega_{\text{mag}} = 2\pi \times 25.75$  Hz, created by the residual magnetic field curvature of the Feshbach coils at 920 G (cf. section 3.2.2).

Figure 4.3.2 (b) shows the average of ten measured line density profiles for all used expansion times. From these profiles, the positions of all centre of masses on the positive side  $x_{i=1,2,3}$  in units of pixel ( $\hat{=} 13.0 \mu\text{m}$ ) are evaluated using a fit function. In this way, the relative displacement of two separate clouds can be computed. In contrast, the relative shift of two objects in units of length can be calculated using the trajectory of a simple harmonic oscillator, as illustrated in figure 4.3.2 (c). By comparing the measured and calculated relative shifts, the magnification can be determined. For example, the mass centres of cloud  $1_{\text{pos}}$  and  $3_{\text{pos}}$ , with a relative time difference of  $2\Delta\tau$ , have a relative displacement of  $\Delta x_{13} = \alpha v_{\text{rec}}/\omega_{\text{mag}} \{\sin[\omega_{\text{mag}}(t_1 + 2\Delta\tau)] - \sin[\omega_{\text{mag}}t_1]\}$ , where  $v_{\text{rec}} = \hbar k/m = 13.22$  cm/s is the atomic recoil velocity and  $\alpha, t_1$  have to be determined as follows.

For a rectangular shaped Bragg pulse with a pulse length of  $\tau_{\text{Br}} = 100 \mu\text{s}$ , the reference time  $t_1 \neq \tau_1$  but rather approximately 0.75 ms as in the linear regime, on average, 50% of the scattered atom cloud starts moving after the time  $\tau_{\text{Br}}/2$ . This is the time when the number of scattered atoms has reached half of its maximum value. The actual value of  $t_1$  was found to be  $757 \mu\text{s}$  by evaluating the ratios of the measured cloud positions in pixels  $x_i/x_j$  where  $i, j = 1, 2, 3$ , see also figure 4.3.2 (b). The slightly higher value of  $t_1$  suggest that this measurement was performed just outside the linear response regime, however, this does not affect the outcome. This ratio is the same for clouds in the negative direction. The parameter  $\alpha$  ( $= 0.9936$ ) accounts for a small timing issue which we have

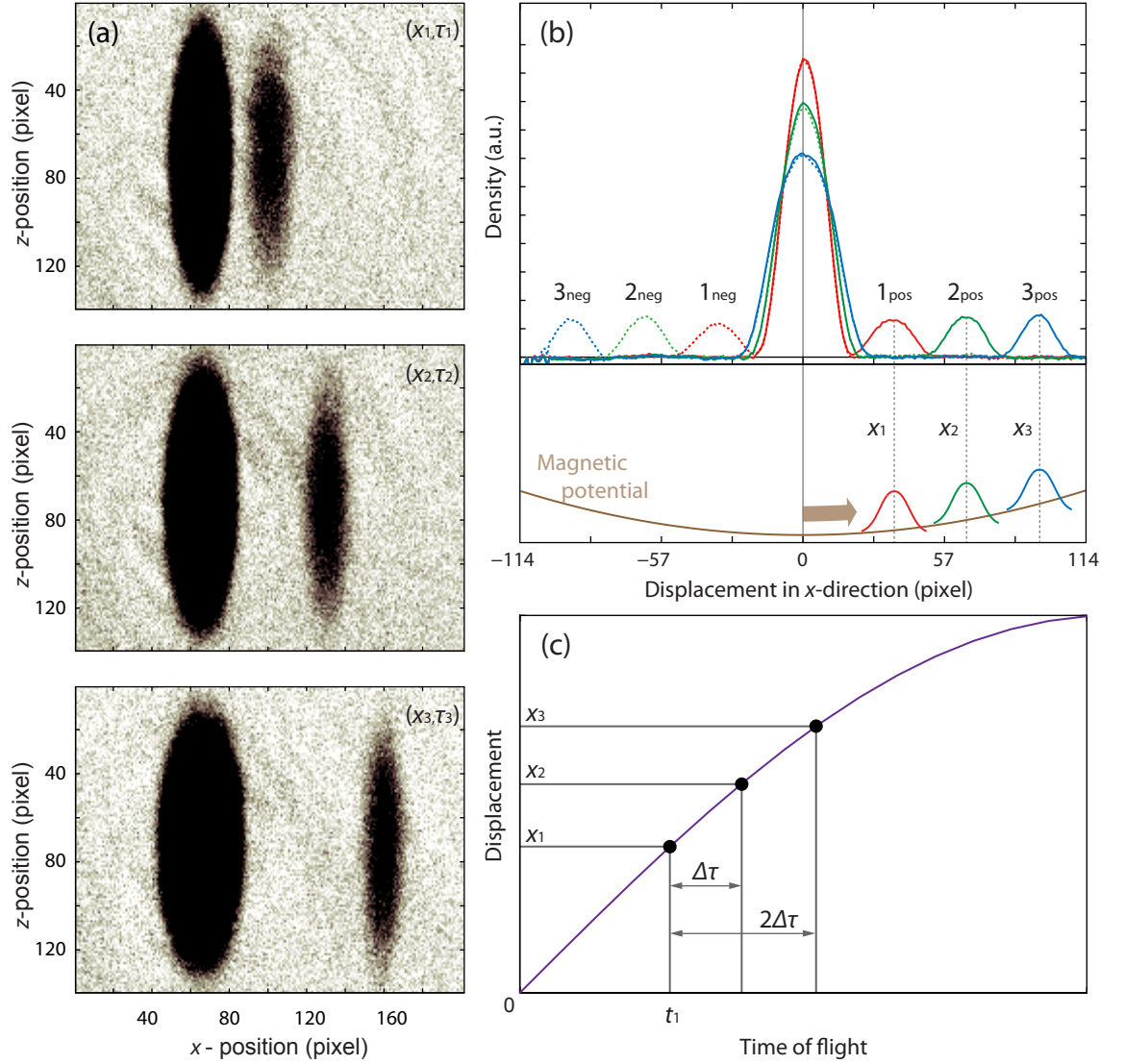


**Figure 4.3.2.:** Illustration of using Bragg spectroscopy as a tool for determining the magnification of our imaging system. The absorption images (a) show Bragg scattered clouds from a noninteracting Fermi gas in the positive  $x$ -direction for three expansion times,  $\tau_{1,2,3} = 0.7, 1.35, 2.0$  ms (red, green, blue line profiles in panel b). The centre-of-mass positions,  $x_{1,2,3}$ , of the scattered cloud fraction can be quantified via the line density profiles (b). The positive (negative) direction is indicated by solid (dashed) lines. The scattered clouds follow the trajectory of the harmonic oscillator potential of the magnetic trap, as schematically shown in (c) (not to scale). Once the reference time  $t_1$  is known, the centre-of-mass positions are fixed (see text).

#### 4. Precision measurement of the universal contact at unitarity

noticed during these measurements and was determined by including deceleration effects of the optical trapping potential ( $\omega_x = 2\pi \times 98.5$  Hz) on the Bragg scattered atoms<sup>2</sup>.

With the procedure described above, applied to all combinations of pairs of scattered cloud on either side of the (unperturbed) parent cloud, and averaging the outcomes, a magnification of  $M = 4.58 \pm 0.02$  was obtained. The effective pixel size of the imaging camera is therefore  $(2.84 \pm 0.02)$   $\mu\text{m}$ .

#### 4.3.3. Summary of the trapped cloud parameters

In the following, the calibration of the trapping frequencies and total atom number is described. These quantities appear in the Fermi wave vector,  $k_F = (24N)^{1/6} \sqrt{\frac{m\bar{\omega}}{\hbar}}$ . We use spin-balanced Fermi mixtures, that is, the total atom number  $N = N_\uparrow + N_\downarrow$  and  $N = 2N_\sigma$  ( $\sigma = \uparrow, \downarrow$ ). Also, a brief outline on how we obtain the relative temperature  $T/T_F$  of a trapped Fermi gas is given. Here,  $E_F = k_B T_F = (3N)^{1/3} \hbar \bar{\omega}$  is the Fermi energy in a harmonic trap.

**Trapping frequencies:** In our experiments, we produce elliptically shaped atomic clouds in a combined optical and magnetic trap. The radial confinement ( $x, y$ -plane) is created by the red-frequency detuned beam of a 10 W singlemode fibre laser at a wavelength of  $\lambda = 1064$  nm (cf. section 3.3.2). The trap operates at an effective optical power of 2.6 W. Trapping atoms in the axial direction ( $z$ -axis) is difficult to realise for large beam waists  $w_0$  as this frequency is by a factor of  $\lambda/(\sqrt{2}\pi w_0)$  smaller compared to its radial counterpart.<sup>3</sup> Instead, we make use of the residual magnetic field curvature of the Feshbach coils to confine atoms in the propagation direction of the laser beam (cf. section 3.2.2)

The radial trapping frequencies of the optical trap were determined by parametric heating the cloud [Lan76, Fri98]. As a deep optical potential is used in all Bragg experiments to ensure harmonic trapping ( $\sim 10$  times deeper than the Fermi energy  $E_F \sim 10$  kHz of the gas), we measure changes in cloud widths by applying a moderate modulation of the laser intensity (10% of the maximum intensity) while keeping the atom number constant. At a frequency close to twice the vibrational trapping frequency of the trap (and multiples of two) we observe an increase in cloud width, as shown in figure 4.3.3. In this way,

---

<sup>2</sup>The reason was that the Bragg pulse and the optical dipole trap were triggered by different computer output cards. As they have a small time delay, the optical dipole trap was still on for about 130  $\mu\text{s}$  after the Bragg pulse had been applied reducing the atom velocity from its initial value,  $v_{\text{rec}}$ , by 0.64 %.

<sup>3</sup>In our experiments, typical beam waist sizes are  $w_0 \sim 200$   $\mu\text{m}$  which corresponds to a factor of  $\sim 800$ .

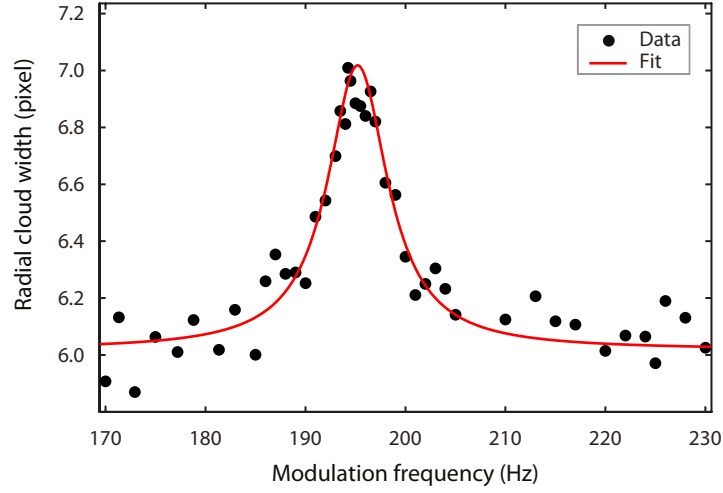


**Figure 4.3.3.:** The modulation frequency of the laser intensity of the optical dipole trap as a function of radial cloud width. The resonance is located at 195.08 Hz.

a strong resonance signal was found at  $2\omega_r = 2\pi \times 195.08\text{Hz}$ , and the radial trapping frequency amounts to  $\omega_r = 2\pi \times 97.5$  Hz. Including the magnetic trap, with frequencies of  $\omega_{\text{mag}(x,y)} = 24.5$  Hz and  $\omega_{\text{mag}(z)} = i 34.6$  Hz at 833 G, the combined trapping frequencies are

$$\omega_x = 2\pi \times 98.6 \text{ Hz}, \quad \omega_y = 2\pi \times 96.5 \text{ Hz}, \quad \omega_z = 2\pi \times 24.5 \text{ Hz}, \quad (4.3.2)$$

which gives a mean frequency of  $\bar{\omega} = 2\pi \times 61.5$  Hz and a trapping aspect ratio of 3.98. All three trapping frequencies were independently confirmed through measurements of cloud oscillations.

**Atom number:** We have employed two procedures to independently calibrate the total atom number: (i) precise measurements of the cloud size of a weakly interacting Fermi gas, and, (ii) absorption measurements of the atom number at very high and low imaging beam intensity and high and low optical densities.

In method (i) we obtained the Fermi radius  $R_F^{\text{BCS}}$  of cold clouds prepared in the weakly attractive BCS regime where the atomic distribution is well described by an ideal Fermi gas distribution with a perturbative correction to the Fermi radius. For  $1/(k_F|a|) \gg 1$ , where  $k_F = (48N_\sigma)^{1/6} \sqrt{m\bar{\omega}/\hbar}$  is the Fermi vector for a noninteracting gas at  $T = 0$  and  $a$  is the  $s$ -wave scattering length, the effect of interaction reduces the width of the Fermi

#### 4. Precision measurement of the universal contact at unitarity

radius according to [Gio08]

$$R_{F,i}^{\text{BCS}} = R_{F,i} \left( 1 - \frac{256}{315\pi^2} k_F |a| \right), \quad (4.3.3)$$

where  $R_{F,i} = (48N_\sigma)^{1/6} \sqrt{\hbar\bar{\omega}/(m\omega_i^2)}$  is the cloud radius of an ideal Fermi gas at  $T = 0$  and  $i = x, y, z$ .

We fit a finite temperature Thomas-Fermi distribution to the atomic density profile for very cold clouds ( $T < 0.05T_F$ ) prepared at a magnetic field of 920 G [ $1/(k_F a) = -1.4$ ]. With precise knowledge of the trapping frequencies and imaging magnification, we were able to determine  $R_{F,x}^{\text{BCS}}$  with an uncertainty of 1 %. Since the atom number is proportional to the 6th power of the radius this can be used to calculate the atom number with an error of 6 %.

Method (ii) involved absorption imaging with a broad range of imaging beam intensities,  $I$ , allowing us to see through optically dense clouds as described in section 3.4.1 and [Rei07]. This method relies on a precise determination of the effective saturation intensity  $I_{\text{sat}}$  which we accurately calibrated for our CCD camera (cf. section 3.4.4). To obtain the absolute atom numbers, we must also account for nonlinear effects that are known to occur at high atomic densities. These were quantified using techniques similar to those described in [Est08] by comparing atom number measurement using imaging beam intensities ranging from well above the saturation intensity ( $I/I_{\text{sat}} \sim 20$ ) to well below ( $I/I_{\text{sat}} \sim 0.1$ ) on clouds with optical depths ranging from 6 down to below 1. We used these measurements to calculate systematic shifts that occur at the optical density ( $\sim 5$ ) of our Bragg scattering experiments. The uncertainties in determining the systematic corrections are at the level of 3 % and the atom numbers determined after accounting for the systematic corrections were consistent with our calibration based on method (i) to better than  $\sim 2$  %.

As method (i) has the largest uncertainty but provides an absolute calibration independent of absorption cross-section, imaging beam intensity etc. we use its uncertainty (6 %) as the overall uncertainty in the atom number. When included with shot-to-shot fluctuations in atom number over the course of our measurements, which is  $\pm 18 \times 10^3$  or 5.8 %, the overall error bar on the atom number is 8 %. The atom number in one spin was measured to be  $N_\sigma = (300 \pm 25) \times 10^3$ . As  $k_F$  is proportional to  $N^{1/6}$ , this leads to an uncertainty of 1.5 % in  $k_F$ .

**Temperature:** We have performed thermometry on a harmonically trapped unitary Fermi gas to obtain its absolute temperature  $T$ . This was accomplished by fitting pressure curves to the equation of state (EoS) for a normal-state spin-1/2 unitary Fermi gas, which have recently been determined to a very high accuracy [vH12]. The result provides a good estimate for the relative temperature  $T/T_F$  of our system; here  $T_F$  is the temperature for a harmonic trapping potential.

Our procedure involves *in situ* imaging of a spin-balanced Fermi gas with a probe propagating in  $y$ -direction towards the CCD camera, and by integrating the resulting column density of atoms in the  $\sigma$ -spin state along the  $x$ -direction,  $\tilde{n}_\sigma(z) = \int n_\sigma(x, y, z) dx dy$ . In this way, the line density  $\tilde{n}_\sigma(z)$  provides direct access to the local (homogeneous) pressure along the axis of the trapped gas [Ho10, Nas10]. We have chosen to evaluate density profiles along the  $z$ -axis to take advantage of the very harmonic magnetic trap.

In the local density approximation, it is assumed that the trapped gas behaves locally as a homogeneous system with a local chemical potential  $\mu_\sigma(\mathbf{r}) = \mu_\sigma^0 - V(\mathbf{r})$ , where  $\mu_\sigma^0$  is the (constant) chemical potential at the trap centre,  $V(\mathbf{r}) = (m/2) \sum_i \omega_i^2 x_i^2$  the harmonic potential with trapping frequency  $\omega_i$  ( $i = x, y, z$ ), and  $m$  the atomic mass. For a harmonically trapped gas in thermal equilibrium, one has  $dx dy = -2\pi / (m\omega_x\omega_y) d\mu$  and the local pressure along the  $z$ -axis, at a given  $\mu_\sigma^0$  and  $T$ , can be expressed via the Gibbs-Duhem relation by

$$P[\mu_\sigma(z), T] = \int_{-\infty}^{\mu_\sigma(z)} n[\mu_\sigma(\mathbf{r}), T] d\mu = \frac{m\omega_x\omega_y}{2\pi} \tilde{n}_\sigma(z), \quad (4.3.4)$$

where  $\mu_\sigma(z) = \mu_\sigma^0 - (m/2)\omega_z^2 z^2$ .

We use equation 4.3.4 to fit the non-superfluid wings of the atomic density profiles on the pressure EoS with  $\mu_\sigma^0$  and  $T$  as fitting parameters. The EoS data, courtesy of [Wer13], was produced over a wide range of temperatures above the transition temperature for superfluidity. It was numerically computed by a combination of virial expansion [Liu09] and bold diagrammatic Monte Carlo calculations [vH13] at higher and lower temperatures, respectively. Note that for reliable results a high signal to noise in the acquired images is important as only the low-density signal from the normal-phase gas can be used for fitting (for the coldest clouds that is only a few percent from their peak atomic density).

With this method we find an absolute temperature of  $T = 29 \pm 2$  nK (and an overall chemical potential of  $\mu_\uparrow^0 \simeq k_B \times 25$  nK) for the coldest unitary clouds, which corresponds to  $T/T_F = 0.08 \pm 0.01$ . The relatively large error bar in the trapped relative temperature arises mainly from the uncertainty of the atom number (see above). Note that this fitting becomes more robust for hotter clouds with a larger normal fluid fraction.

## 4.4. Results at unitarity and the BEC-side of the crossover

In previous Bragg experiments at high momentum, the evolution of the density-density response of a spin-balanced  ${}^6\text{Li}$  gas in the BCS-BEC crossover ( $1/|k_F a| < 1$ ) was studied, showing a smooth transition in  $S(k, \omega)$  [Vee08]. In the BEC regime, where  $1/(k_F a) > 0$ , the observed spectra features a strong pairing peak whose amplitude grows when moving towards the BEC limit. This indicates the presence of bound pairs that more and more behave like molecules. At unitarity and above the resonance, where  $1/(k_F a) \leq 0$ , it was shown that pair scattering is present but the response drops off quickly on the BCS side of the crossover and resonant single-atom scattering dominates. Also, the many-body nature of pair excitations for  $1/(k_F a) \leq 0$  was clearly demonstrated.

In this section, I will present new precision measurements of density-density response functions of a strongly interacting Fermi gas using two-photon Bragg spectroscopy. By applying the procedure explained in section 4.2.2 we obtain spectral data that can be directly used to quantify dynamic and static properties related to pair correlations, without relying on fitting the data. These measurements represent significant improvements over previous results of our group. They enable us to precisely quantify the static structure factor and thereby the universal contact parameter of a unitary many-particle Fermi system [Hu12a].

### 4.4.1. Bragg excitation spectra of a trapped strongly interacting Fermi gas

In this section, the observed bosonic and fermionic excitations are described that determine the shape of the Bragg spectra obtained at two selected points in the BCS-BEC crossover. We have evaluated the centre-of-mass displacement of Bragg scattered clouds for a range of excitation energies  $\hbar\omega$  (cf. section 4.2.2). At the high momentum we use,  $k/k_F = 4.20$ , the transferred momentum  $\hbar k$  is direct proportional to the dynamic structure factor  $S(k, \omega)$ .

The purple solid lines in figure 4.4.1 represent measurements of the density-density response function (a) at unitarity and (b) at  $1/(k_F a) = 0.93$ , where  $k_F = 2.97 \pm 0.05 \mu\text{m}^{-1}$ . The uncertainty in  $k_F$  is dominated by the atom number uncertainty. Each open circle is the average of at least ten data points. The error bars represent one statistical standard deviation of the data at a particular frequency.

The measured spectra in figures 4.4.1 (a) and (b) exhibit a sharp quasielastic peak located at half the atomic recoil frequency  $\omega_{\text{rec}}/2$ . This is consistent with Bragg scattering pairs of twice the atomic mass. These pairs are composite bosons comprising correlated fermionic spin-up and spin-down atoms. The nature of these pairs varies with the interaction strength. At unitarity, where a moderate attractive interaction is present, weakly

#### 4.4. Results at unitarity and the BEC-side of the crossover

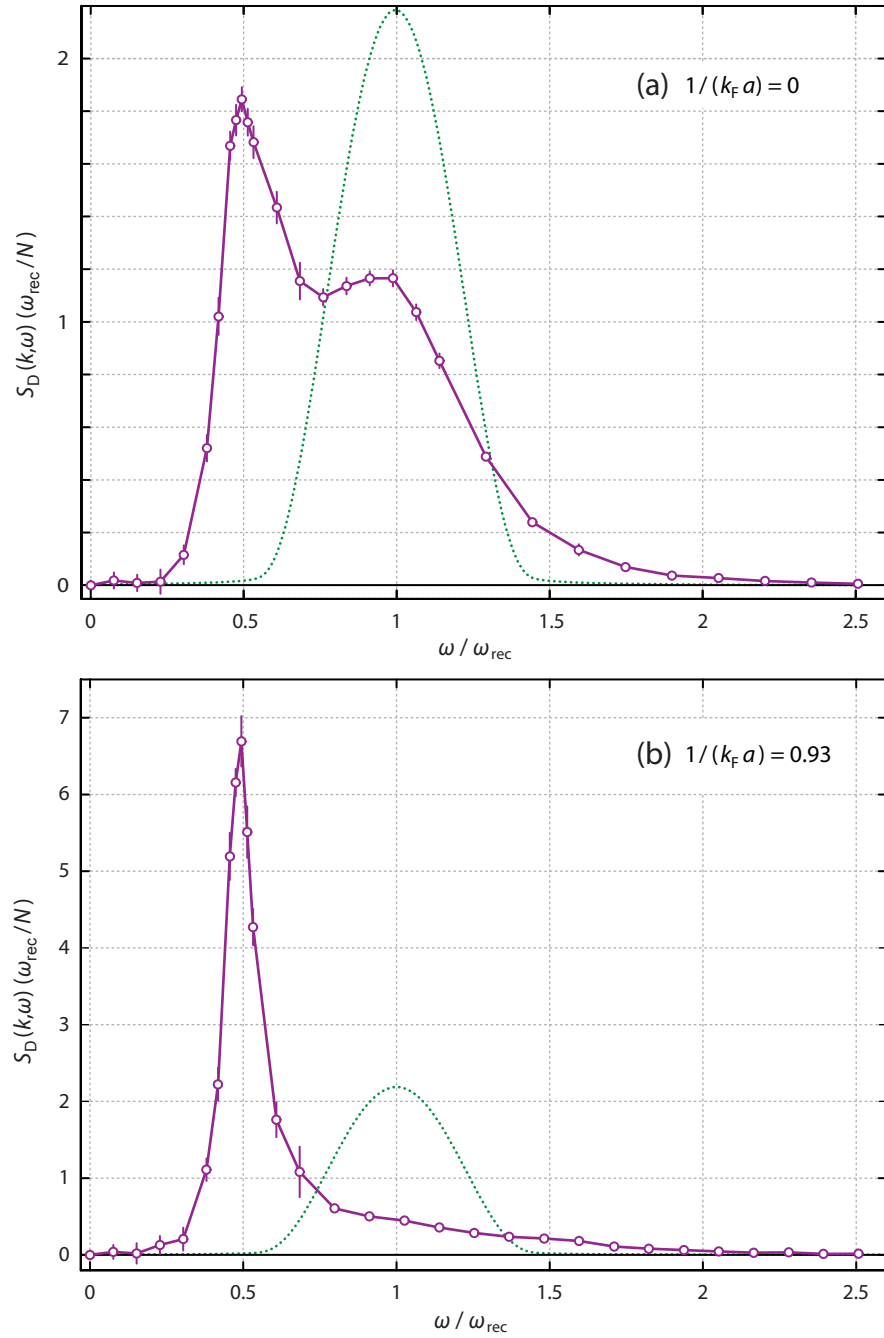


**Figure 4.4.1.:** Density-density response of a strongly interacting Fermi gas (a) at unitarity (833 G) and (b) at  $1/(k_F a) = 0.93$  (783 G) as a function of  $\omega/\omega_{\text{rec}}$  (purple). The data points are connected to guide the eye. The normalised spectra give the dynamic structure factor  $S(k, \omega)$  in units of  $\omega_{\text{rec}}/N$ . For comparison, the expected response for an ideal Fermi gas at  $k = 4.2 k_F$  is shown (green).

#### 4. Precision measurement of the universal contact at unitarity

bound Cooper pairs of size comparable to the interparticle spacing ( $\sim 1/k_F$ ) are scattered, while on the BEC side of the crossover the attraction between atoms increases so that scattered pairs resemble more and more tightly bound molecules (for  $\mu < 0$ ) with binding energy  $E_b = \hbar^2/(ma^2)$ . The pairs that contribute to the Bragg signal at high momentum have to be closely spaced (consistent with the definition of the contact parameter), that means in our case, the separation between correlated opposite-spin atoms has to be of order or less than the probing distance of the Bragg lattice given by  $2\pi/k \simeq 0.5 \mu\text{m}$ .

The pair excitation we observe at  $\omega_{\text{rec}}/2$  in the Bragg spectrum of the Fermi gas are referred to as collective mode [Com06b]. At low energy, this mode results from long-range fluctuations of a nonzero macroscopic order parameter<sup>4</sup> therefore is considered as a clear signature of a superfluid condensate [Min01]. Theoretically, a collective mode exists when the susceptibility diverges for a given  $\omega$  and  $k$ ; the mode is a coherent response of all particles in the system to the same excitation of the density fluctuation forming a discrete spectrum (discrete mode branch) [Pin66]. The spectra are obtained at temperatures well below  $T_c$  where a fraction of nonzero momentum pairs form a condensate<sup>5</sup>. The sharpness of the peak in the pairing response is a consequence of the narrow momentum distribution of the scattered pairs.

The collective mode of a Fermi gas with pairs follows a linear and quadratic energy-momentum dispersion relation at the respective low and high momentum [Com06b]; analogous to the dispersion relation of a true Bose gas [Oze05]. In the Fermi gas, however, pairs can decay into two fermionic excitations for Bragg energies exceeding a certain energy threshold, leading to the pair-breaking continuum which is inaccessible in a Bose gas. This continuum is the result of individual fermionic excitations and hence this part of a Bragg spectrum is referred to as the incoherent response of the Fermi gas. In addition, the collective mode continuously evolves from the gapless Bogoliubov-Anderson mode of a Fermi superfluid in the BCS regime into the Bogoliubov mode of molecules towards the BEC limit [Com06a].

---

<sup>4</sup>In the low-energy and long-wavelength limit,  $\lim_{\mathbf{k} \rightarrow 0} \omega(\mathbf{k}) = 0$ , the collective mode coincides with the gapless Goldstone mode which is basically a low-energy sound wave arising from oscillations of the superfluid order parameter. This mode is fundamentally related to spontaneous breakdown of the continuous gauge symmetry associated with the superfluid phase transition [Hau99]. It is expected to appear as a resonance in the density-density response function  $S(k, \omega)$  [Oha03b] (see also footnote on page 30).

<sup>5</sup>For example, the condensate fraction at  $1/(k_F a) = 0$  and 0.93 at the lowest temperatures is around 80% and 40%, respectively; inelastic losses however quickly deplete the pair condensate on the BEC side for long holding times of the cloud in the trap [Zwi04, Sal05].

When Bragg scattering a Fermi cloud at low momentum, one expects the collective mode to be a bulk excitation of the cloud (sound waves), whereas at high momenta the Bragg response corresponds to kicking pairs or molecules out of the cloud. Consequently, the energy dispersion at high momenta resembles the one of a free molecule,  $\omega(k) = \hbar k^2/(4m)$  (there is no simple physical picture available for a strongly interacting Fermi gas, so what happens exactly in this regime is not yet entirely clear though [Ran14]). Observing the pairing response in figures 4.4.1 (a) and (b) at  $\omega_{\text{rec}}/2$  indicates that the scattered pair picture is valid at the relatively high momentum we use. Note that there is actually a predicted small mean-field shift in the peak position ( $\sim$  kHz) due to repulsive interactions between composite bosons that we do not resolve in the measurements. The shift is proportional to the absolute value of the chemical potential, pushing the peak towards lower frequencies [Büc04, Com06a].

The single-atom continuum as a result of pair-breaking excitations emerges as a broad response at higher excitation frequencies centred approximately around  $\omega_{\text{rec}} \equiv \hbar k^2/(2m)$ , as seen in both Bragg spectra in figure 4.4.1 (a,b). This continuum marks the frequency range where Landau damping is present, that is, pairs may be broken into two single atoms; thus, the threshold frequency contains the pair binding energy and the kinetic energy due to the momentum transfer. In the BEC limit, this threshold can be quantified exactly to be  $E_b + \hbar^2 k^2/(4m)$  [Com06b]. As a result of damping, the response of a collective mode entering the continuum broadens and its peak height decreases. Note, multi-order excitations do not contribute to the spectra in figure 4.4.1 as high-order correlations seem to play no important role at the Bragg momentum considered here [Zou10], and, thermal single-particle excitations are essentially frozen out at such low temperatures [Ket99].

Figure 4.4.1 (a) shows that at unitarity the collective mode has merged with the single-atom continuum. It is very striking to observe such a clear pairing signature at the molecular dispersion ( $\omega_{\text{rec}}/2$ ) considering that the two-body binding energy is zero and no true molecules can form. In previous experiments, we have shown that unitary pairs are many-body in nature, and only exist in the presence of a dense cloud of interacting fermions [Vee08]. At high  $k$  when the mode overlaps with the continuum, pair excitations are coupled to the pair-breaking continuum allowing the dissipation of energy [Oha03a]. Thus, pairs can decay into two single Fermi atoms, one atom carrying away the Bragg momentum  $\hbar k$  while leaving a hole in the Fermi sea.

In figure 4.4.1 (b), the molecular mode appears to have merged with the continuum, hence it is possibly damped. However, theoretical calculations for a uniform spin-balanced Fermi gas at  $1/(k_F a) = 1$  predict the dispersion relation of the mode to be close to the

#### 4. Precision measurement of the universal contact at unitarity

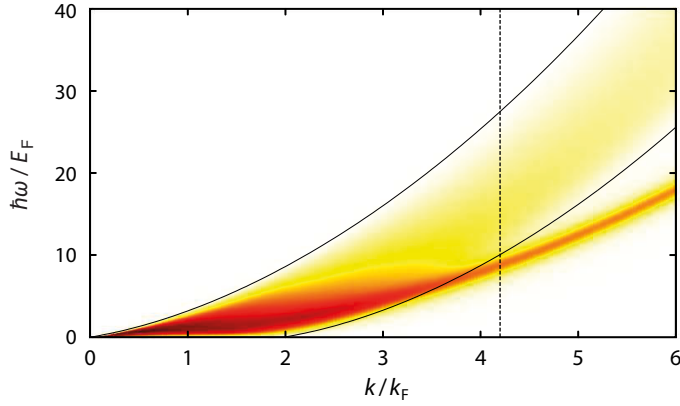


**Figure 4.4.2.:** The QMC predicted density dynamic structure factor at unitarity as a function of normalised momentum and energy transfer. The colour indicates the spectral weight of the response where red is maximum and white zero response. The vertical dashed line corresponds to the momentum transfer of our measured Bragg spectrum at unitarity. Taken from [Ast13].

continuum but not touching it, as observed by us. At  $1/(k_F a) > 1$  and more so deep in the BEC regime,  $1/(k_F a) > 2$ , the dispersion of the collective mode never meets the continuum and closely follows the result from Bogoliubov theory,  $\omega(k) = \sqrt{c^2 k^2 + [k^2/(4m)]^2}$ , where  $c$  is the speed of sound [Com06b]. Whether the mode is damped or not is hard to say as the measured Bragg spectra are broadened by several effects: The momentum spread of the inhomogeneous density distribution in the trap, contributions of Bragg scattering nonzero momentum pairs at finite  $T$  and the finite Bragg pulse duration. The large spectral weight of the pairing peak compared to the total spectrum indicates the dominance of long-lived molecules in the cloud though. Probing the response function of a homogeneous Fermi cloud at longer Bragg pulses may confirm a discrete mode branch of long-lived molecules.

For comparison, the normalised response of non-interacting Fermi gas is plotted in figure 4.4.1 (a) and (b) as a green dashed line to illustrate how the strong interactions affect the shape of an excitation spectrum in the crossover regime. We have not explored the BCS region since, at high momentum, the Bragg probe field is insensitive to the Bogoliubov-Anderson mode. This mode of largely overlapping Cooper pair excitations should only be visible at low  $k$ , whereas at high  $k$ , it has merged deep in the single-particle continuum and hence is strongly damped (i.e. very broad). We found in previous experiments that the spectrum for the BCS case looks quite similar to that of an ideal Fermi gas [Vee08].

In a recent theoretical study by [Ast13], spin and density dynamic responses of a reso-

nantly interacting two-component Fermi gas were calculated using quantum Monte Carlo ( $T = 0$ ). In this work, the results were compared with our measured dynamic structure factors (figure 4.4.1) and a good qualitative agreement was found. The study also involved the computation of the energy dispersion relation for a unitary Fermi gas in the density channel, which is reproduced in figure 4.4.2. I have included this plot as it nicely places the measured Bragg spectrum at unitarity into a broader context.

The  $(\omega, k)$ -plot shows the particle-hole continuum of pair-breaking excitations as a tapered, upwards bending band. The solid black lines encircle the possible energies of the quasiparticles due to Pauli blocking. In a two-component Fermi system, a quasiparticle is a particle-hole excitation created by breaking a pair and removing a single spin-up or spin-down atom from the Fermi sea as a result of the momentum transferred by the Bragg photon, leaving a hole in the sea. The upper line of the band indicates the maximum energy that can be excited at given  $k$ , whereas the lower line shows the minimum energy that is necessary to excite quasiparticles with momentum  $k - 2k_F$ . A fermionic (pair-breaking) excitation corresponding to a point inside the band at the bottom, means scattering an atom from just below the Fermi surface into an unoccupied momentum state just above the surface. In contrast, at high-momentum transfer,  $k > 2k_F$ , a quasiparticle is excited from an atom in a momentum state in the Fermi sea that is transferred into a momentum state far away from the Fermi surface. The spectral weight of the single-particle continuum has a maximum close to the atomic recoil energy; its exact shape depends strongly on the interactions in the Fermi gas.

The dispersion relation of the collective mode overlaps with the continuum at  $k \lesssim 4k_F$ , which means that the mode is damped, and evolves into a discrete branch at high  $k$  where the dispersion is decoupled from the continuum. The position of the branch is given by half the atomic recoil energy, consistent with scattering a pairs. The location of our measured Bragg spectrum at unitarity is marked by the vertical dashed line at  $k = 4.20k_F$ .

The two spectra in figure 4.4.1 exhibit universal behaviour at frequencies  $\omega \gg \omega_{\text{rec}}$ . The high-frequency tail is predicted to fall off  $\propto \omega^{-7/2}$ . This feature will be investigated in the next chapter. In the following sections, I will present the determination of a high-precision value of the universal contact parameter.

#### 4. Precision measurement of the universal contact at unitarity

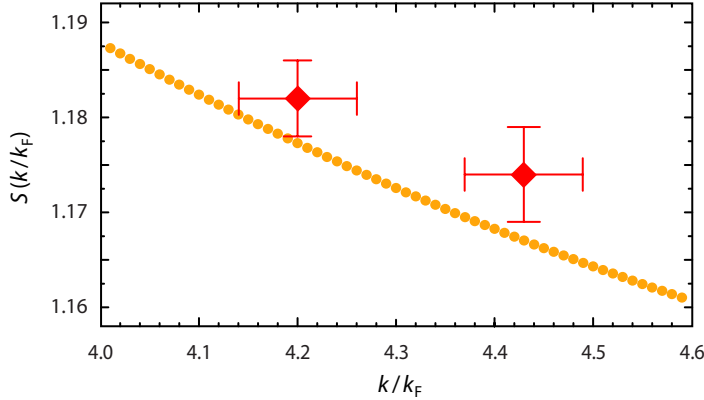


**Figure 4.4.3.:** Comparison of two experimentally measured static structure factors  $S(k)$  at  $k/k_F = 4.20$  and  $4.43$  (red diamonds) with trap-averaged QMC calculations of  $S(k)$  at unitarity as a function of  $k/k_F$ .

#### 4.4.2. Determining the trap-averaged contact $\mathcal{I}/(Nk_F)$

The integral of the normalised spectra in figure 4.4.1,  $S(k) = \int S(k, \omega) d\omega$ , over all frequencies provides a measure of the static structure factors, which we find to be

$$\begin{aligned} S(k) &= 1.182 \pm 0.004 & \text{at } 1/(k_F a) = 0.0, \text{ and} \\ S(k) &= 1.50 \pm 0.02 & \text{at } 1/(k_F a) = 0.93, \end{aligned}$$

representing a vast improvement in accuracy over our previous measurements. The errors account for the statistical uncertainties in the data of the spectra.

These results were compared with recent zero-temperature quantum Monte Carlo (QMC) calculations carried out by the theory group in Los Alamos. Details on this QMC can be found in [Car03, Gan11, Hoi13]. In these calculations, the static structure factor  $S(k/k_F^{\text{hom}})$  and contact  $\mathcal{C}/(nk_F^{\text{hom}})$ , where  $n$  is the (position dependent) density, for a strongly interacting homogeneous Fermi gas was determined. To include the harmonic trapping confinement, the local density approximation (LDA) is applied, assuming a locally homogeneous system on a length scale longer than the mean interparticle spacing. With this, the predicted trap-averaged static structure factor as a function of  $k$  is given by

$$S(k/k_F) = \int n(r) S[k/k_F^{\text{hom}}(r)] d^3r, \quad (4.4.1)$$

where  $k_F = (3N)^{1/3} \hbar \bar{\omega}$  is the Fermi wave vector in a harmonic trap,  $N$  the total atom number,  $\bar{\omega}$  the average trapping frequency,  $k_F^{\text{hom}}(r) = [3\pi^2 n(r)]^{1/3}$  the locally homogeneous Fermi wave vector and  $n(r)$  the density profile of a harmonically trapped gas [Hu11].

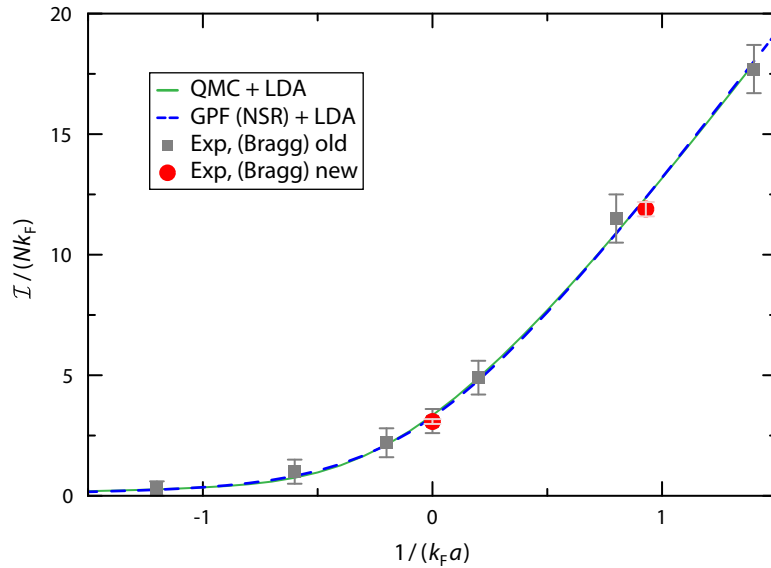


**Figure 4.4.4.:** The trap-averaged contact parameter as a function of  $k_F a$ . The red circles are the new experimental data and the grey squares are data from our previous Bragg measurements. The solid green and dashed blue lines show respective QMC and NSR calculations in combination with the LDA. At unitarity, the experimental result is  $\mathcal{I}/(Nk_F) = 3.06 \pm 0.08$ , compared with the QMC value, 3.336, and the NSR result, 3.26. At  $1/(k_F a) = 0.93$ , the experiment yields  $11.9 \pm 0.3$ , while the QMC and NSR values are  $\sim 12.35$ .

Figure 4.4.3 shows the measured unitary static structure factor  $S(k)$  at two relative wave vectors,  $k/k_F = 4.20$  and  $4.43$ . (For the latter value, we measured an additional Bragg spectrum of clouds in an optical dipole trap with slightly different trapping geometry. The spectrum is not shown here.) A comparison of our results with the QMC calculations shows good agreement at a level of better than one percent. The measurements lie slightly above the QMC predictions, possibly due to the approximations in the QMC model.

The static structure factor at large wave vector gives a direct measure of Tan’s universal contact parameter  $\mathcal{I}$  for a trapped gas at unitarity [Kuh10]. With the precise determination of  $S(k)$  we are hence able to specify a more reliable low temperature value of  $\mathcal{I}$ . The meaning of the contact was discussed in detail in section 2.3.5. In a nutshell, it quantifies the probability of finding closely spaced opposite-spin particles at separations small compared to  $1/k$ . At high momentum, the static structure factor is  $S(k) = S_{\uparrow\downarrow}(k) + 1$ , since  $S_{\uparrow\uparrow}(k \gg k_F) \simeq 1$ ; and the spin-antiparallel part  $S_{\uparrow\downarrow}(k)$  follows a universal law for  $k \gg k_F$ .

#### 4. Precision measurement of the universal contact at unitarity

Approach	$\mathcal{I}/(Nk_F)$	Group	Reference
Experiment	$3.4 \pm 0.2$	ENS	(1) [Nav10]
	$3.1 \pm 0.2$	Swinburne old	(2) [Kuh11b]
	<b><math>3.06 \pm 0.08</math></b>	Swinburne new	(3) [Hoi13]
	$2.8 \pm 0.4$		
	$2.2 \pm 0.5$	JILA	(4) [Ste10]
	$2.1 \pm 0.4$		
Experiment / Theory	3.4	Trento / Innsbruck	(5) [Li11, Gua13]
	$\sim 2$	Rice / ENS	(6) [Par05, Wer09]
Theory	3.26	Swinburne	(7) [Hu11]
	3.05	Camerino	(8) [Pal10]
	3.03	Munich	(9) [Hau09]

**Table 4.1.:** Comparison of recently published values of the contact of a harmonically trapped strongly-interacting Fermi gas at low or zero temperature. See text for details about measurements and theoretical models.

Using equation 2.3.24 on page 39, the dimensionless contact is given by

$$\frac{\mathcal{I}}{Nk_F} = \frac{4k}{k_F} \left[ \frac{S(k) - 1}{1 - 4/(\pi ka)} \right], \quad (4.4.2)$$

or simply  $\mathcal{I}/(Nk_F) = 4k/k_F[S(k) - 1]$  in the unitarity case where  $a \rightarrow \infty$ . Using equation 4.4.2, the results for a trapped Fermi gas at  $T = 0.08 T_F$  is  $\mathcal{I}/(Nk_F) = 3.06 \pm 0.08$  at unitarity and  $11.9 \pm 0.3$  for a gas with molecules at  $1/(k_F a) = 0.93 \pm 0.02$ . The error bars include the uncertainty in  $k_F$  as well as in  $S(k)$ .

In figure 4.4.4, our results for the contact are plotted relative to the solid green line of the QMC calculations combined with the LDA, and, for comparison the dashed blue line of a recent Nozières-Schmitt-Rink (NSR) Gaussian pair fluctuation (GPF) calculation [Hu11]. We find good agreement with theory, though the curves lie consistently above our data. The larger discrepancy at higher interaction strength might be due to the fact that our measurements were performed at nonzero temperature. The grey squares are experimental data from our previous Bragg measurements [Kuh11c].

Table 4.1 summarises recently published values of the contact parameter for a trapped unitary Fermi gas from experiments and theoretical predictions at  $T \lesssim 0.1 T_F$  and  $T = 0$ , respectively. It shows that our value (3, red) is somewhat below that obtained from measurements of the equation of state (1) and the frequency of collective oscillations (5)

but consistent with previous Bragg measurements (2); however, it is higher than found using radio-frequency spectroscopy (4) and photo-association data (6). A comparison with three established strong-coupling models (approximate many-body  $T$ -matrix theories), predicting the temperature dependence of the contact, shows that our measurement lies below the GPF calculation (7), yet is closest to, but slightly above, the recent non-self consistent  $G_0G_0$  (8) and the self consistent  $GG$  (9) calculation.

In the next section, I will use the result of the trapped contact parameter at unitarity to estimate the value for the zero-temperature homogeneous contact.

#### 4.4.3. Extracting the homogeneous contact density $\mathcal{C}/(nk_F)$ at $T = 0$

While our measurements were performed on a trapped (inhomogeneous) cloud, our result at unitarity can also provide a constraint on the zero-temperature homogeneous contact. At finite temperatures, the equation of state for the unitary Fermi gas is not known exactly, but, for  $T \ll T_c$  ( $\sim 0.22 T_F$ ) trap averaged measurements are only weakly affected by the small population in the high-temperature cloud wings. Several calculations of the temperature dependence of the trapped as well as homogeneous contact have recently been reported. Figure 4.4.5 depicts the homogeneous contact as a function of  $T/T_F$  as predicted by three strong-coupling theories [Hu11, Sag12]. The blue, purple, and green lines are results based on the respective GPF,  $G_0G_0$  and  $GG$  calculations. A plot showing these curves for a broader temperature range (up to  $T = 3 T_F$ ) and for the trapped case can be found in reference [Hu11].

While these predictions all vary significantly near  $T_c$ , at very low temperatures the predicted  $T$ -dependence is very similar. Comparing the ratios  $\mathcal{I}(T)/\mathcal{I}(0)$ , one finds a weak  $T$ -dependence with a relative difference of order 1% in the range  $0 < T/T_F < 0.08$  for the different models, as illustrated in the inset of figure 4.4.5 where the three curves for the trapped case are plotted. Thus, with knowledge of the trapped contact at a temperature  $T \ll T_c$ , we can extrapolate down to zero temperature and anticipate that systematics due to imprecise knowledge of the strong-coupling theories should be small.

Applying this extrapolation we obtain  $\mathcal{I}(0)/(Nk_F) = 3.15 \pm 0.09$  for the trapped contact as  $T \rightarrow 0$ . Furthermore, it can be shown that the trapped and homogeneous contact at zero temperature can be determined from each other through [Hu11, Hoi13]

$$\frac{\mathcal{I}}{Nk_F} = \frac{256}{105\pi} \xi^{-1/4} \frac{\mathcal{C}}{nk_F}, \quad (4.4.3)$$

where  $\xi = 0.370 \pm 0.005$  [Ku12, Zür13] is the universal Bertsch parameter [Blo08]. Using equation 4.4.3 then gives  $\mathcal{C}/(nk_F) = 3.17 \pm 0.09$  for the zero temperature homogeneous

#### 4. Precision measurement of the universal contact at unitarity

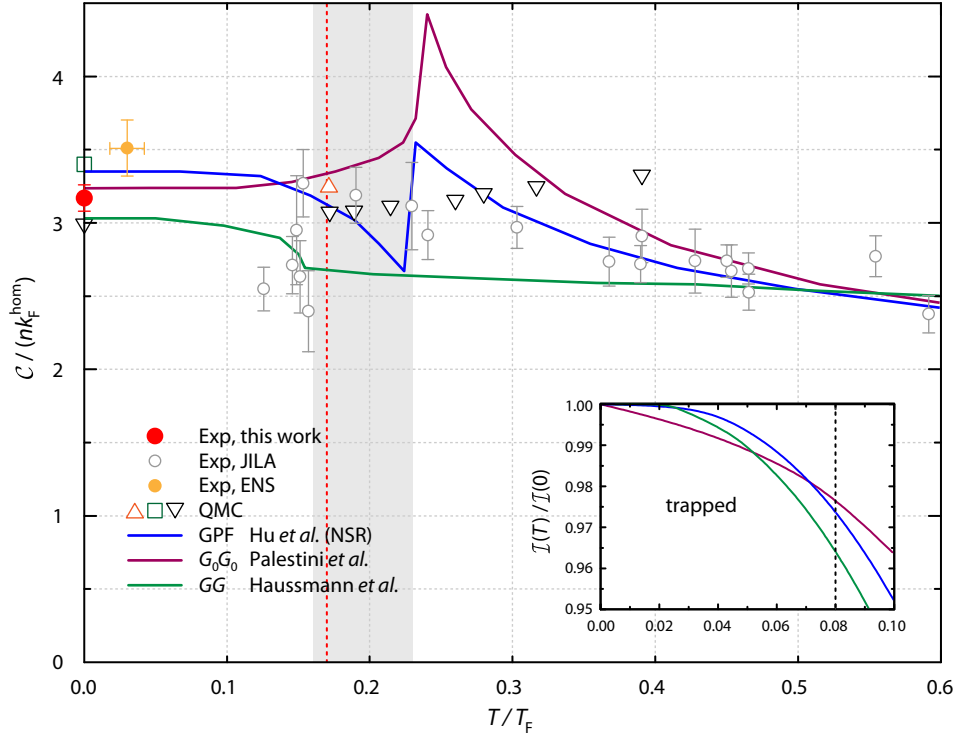


**Figure 4.4.5.:** Overview of recent experimental and theoretical results for the temperature dependence of the contact of a homogeneous unitary Fermi gas. The solid lines represent strong-coupling theories based on Gaussian pair-fluctuation (GPF) [Hu11], non-self consistent  $T$ -matrix ( $G_0G_0$ ) [Pal10] and self-consistent  $T$ -matrix ( $GG$ ) [Hau09] calculations. The QMC calculations are from [Gou10] (upright triangle), [Com06a] (square) and [Dru11] (inverted triangle). Experimental contact results are from JILA [Sag12] (grey open circles) and ENS [Nav10] (yellow solid circle). Our result at  $T = 0$  is given by the red solid circle. The predicted superfluid phase transition is marked by the grey area ( $T_c/T_F = 0.16 - 0.23$ ) [Hau07] whereas the red dotted line represents a recent measurement of  $T_c/T_F = 0.17$  [Ku12]. The inset shows how the normalised theoretical curves for a trap-averaged gas vary at very low temperatures. Main panel adapted from [Hu11, Sag12].

contact (density). The increased error bar is due to the uncertainty in the extrapolation to  $T = 0$ . The uncertainty in  $\xi$  barely impacts the overall error as it appears in equation 4.4.3 to the 1/4-th power.

An additional systematic arises from the fact that our measurement was performed at a magnetic field of 833.0 G which is not the exact field  $B_0$  at which  $|a| \rightarrow \infty$ . A recent determination found  $B_0 = 832.18 \pm 0.08$  G [Zür13], which, combined with the gradient of the QMC result in figure 4.4.4, would shift our result upwards by  $\sim 2.5\%$ .

With these considerations, we can compare our result with the predictions of the many-body theories at  $T = 0$  and find good agreement with the non-self consistent  $G_0G_0$  theory. This confirms our findings of the trapped contact at  $T = 0.08 T_F$ , which is also closest to the  $G_0G_0$  result. However, taking into account the correction due to the uncertainty of the Feshbach resonance our result lies closer to the GPF theory. Despite our measurements, and the measurements and QMC simulations of other groups summarised in figure 4.4.5, it remains unclear which of these strong-coupling theories most accurately describes the physics of unitary Fermi gases and further experiments in this direction would be required.

## 4.5. Summary

In summary we have presented a high precision determination of the low temperature dynamic and static structure factors and universal contact parameter of a strongly interacting Fermi gas at  $1/(k_F a) = 0$  and 0.93. These atomic systems provide an ideal testbed for validating different strong-coupling many-body calculations where exact predictions are not available. The measured high- $k/k_F$  Bragg spectra can provide experimental input for further developing QMC methods and dynamical strong-coupling theories.

To reach the high accuracy, we developed and implemented a number of technical and procedural improvements, including a new Bragg laser setup and improved data analysis for extracting the Bragg signal from absorption images. A detailed characterisation of all relevant experimental parameter was presented. To ensure linearity, the density response for a range of Bragg frequencies was measured as a function of Bragg laser intensities.

Our measurements are now at a level that can discriminate between several of the established numerical predictions, and the agreement with the latest QMC calculations is at the level of a few percent. The measurement at unitarity was used to provide a new benchmark for the  $T \rightarrow 0$  limit of the homogeneous contact density  $\mathcal{C}/(nk_F)$  with error bars at the 3% level.



# 5. Spin-Bragg spectroscopy of a strongly interacting ${}^6\text{Li}$ gas

## 5.1. Introduction

In this chapter, I will present the study of spin dynamic structure factors,  $S_S(\mathbf{k}, \omega)$ , of a strongly interacting Fermi gas, recently published in [Hoi12]. Precise spin responses were measured and analysed for a spin-balanced mixture of  ${}^6\text{Li}$  gas prepared in the two lowest ground states at unitarity and on the BEC side of the Feshbach resonance at  $1/(k_F a) \simeq 1$ . These spectra will be compared with the response of an ideal Fermi gas at  $T = 0$ .

I will show that spin dynamic structure factors can be obtained by applying essentially the same experimental procedure as used for measuring density dynamic structure factors,  $S_D(\mathbf{k}, \omega)$ , described in the preceding chapter. Using a Bragg momentum of  $k = 4.20 k_F$ , spectra of  $S_S(\mathbf{k}, \omega)$  were extracted by evaluating averaged differential centre-of-mass displacements of scattered atomic clouds as a function of the excitation energy  $\hbar\omega$  ranging from zero to  $3\hbar\omega_{\text{rec}}$ , where  $\omega_{\text{rec}}$  is the atomic recoil frequency. In addition, the Bragg spectra  $S_S(\mathbf{k}, \omega)$  and  $S_D(\mathbf{k}, \omega)$  were combined to give the profiles of the individual spin-parallel  $S_{\uparrow\downarrow}(\mathbf{k}, \omega)$  and antiparallel  $S_{\uparrow\uparrow}(\mathbf{k}, \omega)$  dynamic structure factors. As we can now fully characterise the components of the structure factor of the Fermi gas, I will give a physical interpretation of all features appearing in the obtained spectra at given  $k$ .

The control parameter we adjust to tune the relative coupling strength of the Bragg perturbation to the atomic spin states is the Bragg laser detuning. It will be shown that a selective measurement of either dynamic spin or density responses can be performed by an appropriate choice of the laser detunings. A careful check of the Bragg linearity was carried out, in the same way as for the density structure factor, to ensure the Bragg response remains linear while maximising the scattered signal in the absorption images.

The chapter concludes with a careful analysis of the same- and opposite-spin dynamic structure factors at high Bragg excitation energies  $\hbar\omega \gtrsim 2\hbar\omega_{\text{rec}}$  revealing a theoretically predicted universal power-law decaying proportional to  $\omega^{-5/2}$ .

## 5.2. Probing the spin response

The density and spin dynamic structure factors for a spin-balanced Fermi mixture in the states  $|\uparrow\rangle$  and  $|\downarrow\rangle$  are given, respectively, by [Com06a]

$$\begin{aligned} S_{\text{D}}(\mathbf{k}, \omega) &= 2[S_{\uparrow\uparrow}(\mathbf{k}, \omega) + S_{\uparrow\downarrow}(\mathbf{k}, \omega)], \\ S_{\text{S}}(\mathbf{k}, \omega) &= 2[S_{\uparrow\uparrow}(\mathbf{k}, \omega) - S_{\uparrow\downarrow}(\mathbf{k}, \omega)]. \end{aligned} \quad (5.2.1)$$

From these equations we see that for  $S_{\text{D}}(\mathbf{k}, \omega)$  correlations between atoms in both the same and opposite spin states contribute to the total response, whereas for  $S_{\text{S}}(\mathbf{k}, \omega)$  correlations from pairs of opposite-spin atoms are suppressed as the response is only sensitive to the pair-breaking continuum [Str09]. Knowing  $S_{\text{D,S}}(\mathbf{k}, \omega)$  for all  $\omega$  at given  $\mathbf{k}$ , the dynamic structure factors of the individual spin components,  $S_{\sigma\sigma'}(\mathbf{k}, \omega)$ , can be constructed. As will be shown in the following,  $S_{\uparrow\uparrow}(\mathbf{k}, \omega)$  and  $S_{\uparrow\downarrow}(\mathbf{k}, \omega)$  can be directly related to the measured response  $R(\mathbf{k}, \omega)$ , defined in equation 4.2.18 on page 87, by including the individual Bragg detunings,  $\Delta_{\uparrow,\downarrow}$ . This allows us to control the sign in the equations 5.2.1 by tuning the Bragg frequency and thereby to selectively access the spin and density channels.

In the experiments which follow, we work in a regime where the Bragg lasers are sufficiently weak to not significantly deplete the cloud. We also use a long Bragg pulse such that its Fourier width is narrow compared to the spectral features being measured. In this limit, the momentum  $\Delta P(\mathbf{k}, \omega)$  transferred by the Bragg lasers is proportional to the imaginary part of the dynamic susceptibility (see also section 4.2 on page 78 ff.)

$$\chi''_{\text{D,S}}(\mathbf{k}, \omega) = \pi[S_{\text{D,S}}(\mathbf{k}, \omega) - S_{\text{D,S}}(-\mathbf{k}, -\omega)], \quad (5.2.2)$$

where  $S_{\text{D,S}}(\mathbf{k}, \omega)$  are the dynamic structure factor of measurements in either the spin or density channel. When the magnitude of the Bragg wave vector  $|\mathbf{k}|$  is large compared to the Fermi wave vector ( $k_{\text{F}}$ ) and the inverse of the de Broglie wavelength ( $1/\lambda_{\text{dB}}$ ) then  $S_{\text{D,S}}(-\mathbf{k}, -\omega) \rightarrow 0$ , and only the positive term contributes to the measured response. Thus, we can directly obtain  $S_{\text{D,S}}(\mathbf{k}, \omega)$  from a measured Bragg spectrum.

The key to measuring the spin response in two-photon scattering experiments is to use Bragg lasers with different coupling to each of the spin states in the mixture. There are various theoretical proposals on how this can be achieved. For example, one possibility is using spin-flip Bragg spectroscopy [Rod02, Bru06, Guo10], where the rate of the momentum transfer imparted by the moving Bragg lattice is proportional to the scattering rate into the spin-flipped state. Alternatively, one can use polarisation sensitive coupling to either the total density or the spin density, where pair-breaking excitations are induced depending on the weight of the coupling [Car06].

These methods rely on atomic transitions between the two ground spin states coupled to a common excited state driven by the Bragg field. However, this cannot be easily realised between the two ground states of  ${}^6\text{Li}$  that we use since high external magnetic fields are present. As the nuclear spin almost fully decouples from the electronic states, the two Bragg transitions between the ground and excited states are effectively closed and can be treated independently (cf. appendix A).

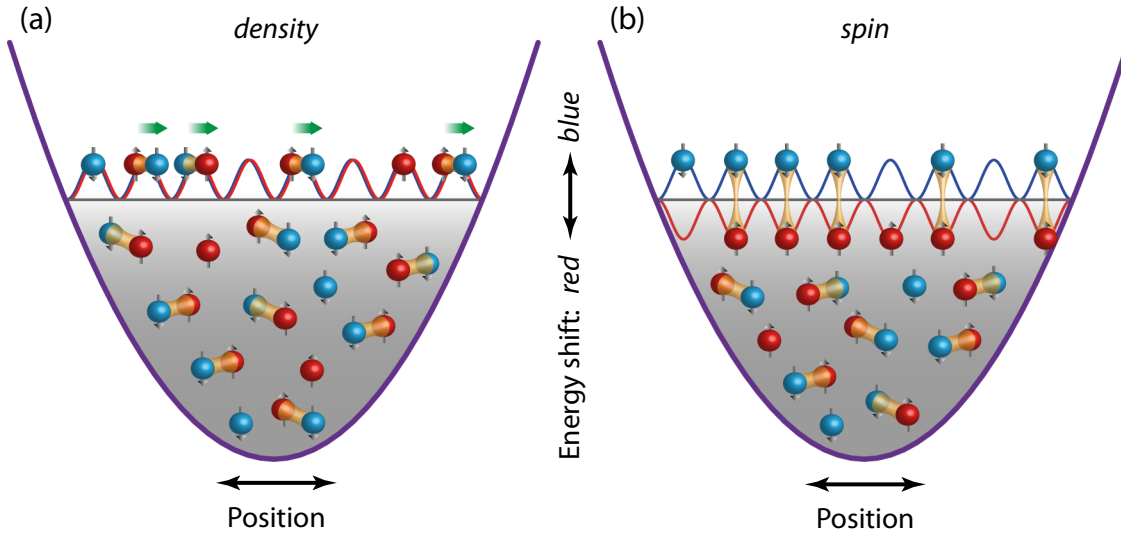
Instead, we use a different method which turns out to be almost ideal for our situation. It is straightforward to implement in our setup as we only need to alter the Bragg laser frequencies. The only disadvantage is enhanced spontaneous emission which limits the Bragg signal as we operate relatively close to the atomic transitions. The detunings are chosen such that the frequency of both Bragg lasers falls between the hyperfine states,  $\omega_{\uparrow\downarrow} \sim 80$  MHz, of the  $|\uparrow\rangle$  and  $|\downarrow\rangle$  states. This does not flip the electronic spin but results in a different relative coupling strength of the atoms in different states. Of particular interest is the case when the Bragg lasers are tuned precisely halfway between the two optical transition frequencies as this probes purely the spin-response function associated with  $S_S(\mathbf{k}, \omega)$ . A derivation of the dynamic structure factors  $S_D$  and  $S_S$  that includes the Bragg laser detuning  $\Delta_\sigma$  will be discussed in detail in the next section.

Figure 5.2.1 qualitatively illustrates the principles of our method. Atoms in the trap are represented by red (spin up) and blue (spin down) spheres, and a fraction of them are paired. The Bragg modulation is indicated by the red and blue sine waves. After switching on the Bragg potential, the density (grey shaded area) of the harmonically trapped cloud is perturbed resulting in a periodic energy shift of the electronic ground states of the perturbed atoms. Since the Bragg laser intensities are weak, to ensure linearity, the amplitude of the perturbation is small.

The Bragg perturbation affects single atoms (the constituents of pairs) in two different ways. Figure 5.2.1 (a) shows the situation when the Bragg field couples to the total density,  $\rho_D = \rho_\uparrow + \rho_\downarrow$ . In our case, both Bragg lasers are blue detuned relative to the atomic transitions of each spin state (cf. energy diagram for the blue-detuned Bragg lasers in figure 5.2.2). Since  $\Delta_\sigma \gg \omega_{\uparrow\downarrow}$ , both spin states couple in the same way to the field hence experience the same light shift. Consequently, the Bragg lasers can excite pairs close to the Bragg molecular resonance frequency,  $\omega_{\text{rec}}/2 \equiv \hbar^2 k^2 / (4m)$ , transferring energy and momentum. On average, the total energy of the system increases. This is in fact the scenario of conventional Bragg spectroscopy which has been used in all our previous experiments on two-component Fermi gases.

The situation changes dramatically when the Bragg lasers are tuned to lie between the

5. Spin-Bragg spectroscopy of a strongly interacting  ${}^6\text{Li}$  gas



**Figure 5.2.1.:** Schematic illustration of probing the density (a) and spin (b) response of a harmonically trapped strongly interacting spin-balanced Fermi mixture. The red (blue) lattice couples to the spin-up (spin-down) atoms represented in red (blue). Depending on the relative coupling between the Bragg lattice (sinusoidal lines) and atoms in the two spin states, the perturbation induces energy shifts in either the same (a) or opposite (b) direction relative to the energy of atoms and pairs in the reservoir. In the density case, the perturbation leads to the scatter of pairs (green arrows), whereas in the spin case the net perturbation and thus response for pairs is zero.

transition frequencies from the two spin states. Figure 5.2.1 (b) shows the extreme case when the Bragg lasers are detuned exactly to  $\omega_{\uparrow\downarrow}/2$ . In this case, the Bragg field entirely couples to the spin density,  $\rho_S = \rho_{\uparrow} - \rho_{\downarrow}$ , such that an out-of-phase perturbation affects the constituents of the pairs: Atoms in the spin-up state experience red-detuned Bragg light and the induced shift reduces the energy relative to the energy of the unperturbed atoms. Conversely, atoms in the opposite-spin state acquire the same light shift but in opposite direction as the Bragg lasers appear blue-detuned to them. Thus, the induced net perturbation for pairs is always zero and no pair scattering takes place. In the energetic picture, the effect of the Bragg potential for this scenario can also be understood as an “energetic distortion” of the individual atomic spin states in a symmetric but opposite way. Note, there can always be single-particle scattering (pair breaking) in the density and spin channel at higher Bragg excitation energies regardless of the sign of the Bragg perturbing potential.

### 5.2.1. Bragg perturbation including finite laser detunings

We can selectively probe either the density or spin channel by appropriately tuning the Bragg laser frequencies. To show how this works we derive expressions for the measured Bragg response,  $R_{D,S}(\mathbf{k}, \omega)$ , which explicitly includes the Bragg laser detunings ( $\Delta_{\uparrow, \downarrow}$ ), using a simple perturbative approach. This applies to linear two-photon Bragg spectroscopy at sufficiently weak atom-laser coupling. The total many-body hamiltonian for the trapped Fermi gas can be written as

$$\hat{H} = \hat{H}_0 + \hat{H}_{\text{Pert}}, \quad (5.2.3)$$

where  $\hat{H}_0$  is the hamiltonian of the unperturbed system including the kinetic energy, trapping potential and interactions, while  $\hat{H}_{\text{Pert}}$  is a small extra potential perturbing the gas (cf. equation 4.2.3 on page 80). For convenience, we represent  $\hat{H}_{\text{Pert}}$  in the framework of second quantisation as often found in literature [SK99, Min01, Bla02].

We start by writing  $\hat{H}_{\text{Pert}} = \hat{\Psi}^\dagger(\mathbf{r}) U_{\text{Br}} \hat{\Psi}(\mathbf{r})$ , where the row vector  $\hat{\Psi}^\dagger(\mathbf{r}) = [\hat{\psi}_\uparrow^\dagger(\mathbf{r}) \hat{\psi}_\downarrow^\dagger(\mathbf{r})]$  is the two-component fermionic field operator for the two different atomic ground internal states<sup>1</sup>, and  $U_{\text{Br}} = U_\sigma \exp[-i(\mathbf{k} \cdot \mathbf{r} - \omega t)]$  is the Bragg-modulation lattice created by the interference pattern of two intersecting plane waves with wave vectors  $\mathbf{k}_A$  and  $\mathbf{k}_B$  propagating through the cloud along the direction of the wave vector  $\mathbf{k} = \mathbf{k}_A - \mathbf{k}_B$ . The frequency difference of the two lasers is  $\omega$ , and  $\mathbf{r}$  denotes the position in space.

In the far-off-resonant regime, where  $|\Delta_\sigma| \gg |\Omega_{\text{Br}}|$  ( $\Omega_{\text{Br}}$  was defined on page 80), the coupling strength of the Bragg field to the atoms is determined by the light shift potential through [CT98]

$$U_\sigma = \frac{\hbar \Omega_{\text{R}}^2}{\Delta_\sigma} = \frac{|d_{\text{eg}}|^2 \sqrt{I_A I_B}}{\hbar \Delta_\sigma}, \quad (5.2.4)$$

where  $\Omega_{\text{R}} = |\langle e | \mathbf{d} \cdot \mathbf{E} | g \rangle| / \hbar$  is the Rabi frequency,  $\Delta_\sigma$  is the detuning from spin state  $|\sigma\rangle$ ,  $d_{\text{eg}}$  is the electric dipole operator for the  $m_J = -1/2$  to  $m_J = -3/2$  transition and  $I_{A,B}$  is the Bragg intensity. Note, in our case  $0.01 < |\Omega_{\text{Br}}| / |\Delta_\sigma| < 0.1$ . We assume no spatial dependency of the modulation strength  $U_\sigma$  since the beam diameters of the Bragg lasers are much larger than the cloud size. For the case of  ${}^6\text{Li}$  at large magnetic fields, both the  $|\uparrow\rangle$  and  $|\downarrow\rangle$  states have essentially identical dipole matrix elements  $d_{\text{eg}}$  for the corresponding Bragg transitions, therefore only the Bragg laser detunings  $\Delta_\uparrow$  and  $\Delta_\downarrow$  are relevant for setting the relative strength of the density and spin perturbations.

---

<sup>1</sup>In second quantisation, the field operator for state  $|\sigma\rangle$  can be expressed, for example, in the plane wave basis by  $\hat{\psi}_\sigma^\dagger(\mathbf{r}) = \sum_{\mathbf{q}} \langle \mathbf{q} | \mathbf{r} \rangle \hat{a}_{\mathbf{q}, \sigma}^\dagger$ , where  $\hat{a}_{\mathbf{q}, \sigma}^\dagger$  is the creation operator of a fermion with wave vector  $\mathbf{q}$  and spin  $\sigma$ , and  $\langle \mathbf{q} | \mathbf{r} \rangle = 1/\sqrt{V} \exp(-i\mathbf{q} \cdot \mathbf{r})$  is the single-particle wavefunction in a certain volume  $V$ .

## 5. Spin-Bragg spectroscopy of a strongly interacting ${}^6\text{Li}$ gas

In equation 5.2.3, the perturbation term of the two-component Fermi gas can be expressed in matrix form via [Rod02]

$$\hat{H}_{\text{Pert}} = \int \left[ \hat{\psi}_{\uparrow}^{\dagger}(\mathbf{r}) \hat{\psi}_{\downarrow}^{\dagger}(\mathbf{r}) \right] \begin{pmatrix} U_{\uparrow} & 0 \\ 0 & U_{\downarrow} \end{pmatrix} \begin{bmatrix} \hat{\psi}_{\uparrow}(\mathbf{r}) \\ \hat{\psi}_{\downarrow}(\mathbf{r}) \end{bmatrix} e^{-i(\mathbf{k}\cdot\mathbf{r}-\omega t)} d\mathbf{r} + \text{h.c.} \quad (5.2.5)$$

which of course is already diagonal in our case as the effect of the Bragg potential is merely a energy shift in each of the atomic states. If we, however, rewrite  $\hat{H}_{\text{Pert}}$  by expanding

$$\begin{pmatrix} U_{\uparrow} & 0 \\ 0 & U_{\downarrow} \end{pmatrix} = \left( \frac{U_{\uparrow} + U_{\downarrow}}{2} \right) \begin{pmatrix} 1 & 0 \\ 0 & 1 \end{pmatrix} + \left( \frac{U_{\uparrow} - U_{\downarrow}}{2} \right) \begin{pmatrix} 1 & 0 \\ 0 & -1 \end{pmatrix} \quad (5.2.6)$$

and identify the Fourier transform of the atomic density operator at wave vector  $\mathbf{k}$  for a given spin state,

$$\hat{\rho}_{\sigma}^{\dagger}(\mathbf{k}) = \int \hat{\psi}_{\sigma}^{\dagger}(\mathbf{r}) \hat{\psi}_{\sigma}(\mathbf{r}) e^{i\mathbf{k}\cdot\mathbf{r}} d\mathbf{r} = \sum_{\mathbf{q}} \hat{a}_{\mathbf{q}+\mathbf{k},\sigma}^{\dagger} \hat{a}_{\mathbf{q},\sigma}, \quad (5.2.7)$$

where  $\hat{a}_{\mathbf{q}}^{\dagger}$  ( $\hat{a}_{\mathbf{q}}$ ) is the creation (destruction) operator for an atom with momentum  $\hbar\mathbf{q}$ , then equation 5.2.5 reads

$$\hat{H}_{\text{Pert}} = \frac{(U_{\uparrow} + U_{\downarrow})}{2} \left[ \hat{\rho}_{\uparrow}^{\dagger}(\mathbf{k}) + \hat{\rho}_{\downarrow}^{\dagger}(\mathbf{k}) \right] e^{-i\omega t} + \frac{(U_{\uparrow} - U_{\downarrow})}{2} \left[ \hat{\rho}_{\uparrow}^{\dagger}(\mathbf{k}) - \hat{\rho}_{\downarrow}^{\dagger}(\mathbf{k}) \right] e^{-i\omega t} + \text{h.c.}, \quad (5.2.8)$$

showing that the perturbation introduced by the Bragg lasers can be expressed as the sum of two terms, one which couples to the total density  $\hat{\rho}^{\dagger}(\mathbf{k}) = \hat{\rho}_{\uparrow}^{\dagger}(\mathbf{k}) + \hat{\rho}_{\downarrow}^{\dagger}(\mathbf{k})$  and another one which couples to the  $z$ -projection of the total spin  $\hat{S}_z^{\dagger}(\mathbf{k}) = \hat{\rho}_{\uparrow}^{\dagger}(\mathbf{k}) - \hat{\rho}_{\downarrow}^{\dagger}(\mathbf{k})$ . The general definitions of these two quantities for spin- $\frac{1}{2}$  particles in Fourier space are given by [Sch08b]

$$\begin{aligned} \hat{\rho}^{\dagger}(\mathbf{k}) &= \sum_{\mathbf{q},\sigma,\sigma'} \mathbb{1}_{\sigma,\sigma'} \hat{a}_{\mathbf{q}+\mathbf{k},\sigma}^{\dagger} \hat{a}_{\mathbf{q},\sigma'} \quad \text{and} \\ \hat{S}_z^{\dagger}(\mathbf{k}) &= \sum_{\mathbf{q},\sigma,\sigma'} \boldsymbol{\sigma}_{\sigma,\sigma'} \hat{a}_{\mathbf{q}+\mathbf{k},\sigma}^{\dagger} \hat{a}_{\mathbf{q},\sigma'}, \end{aligned} \quad (5.2.9)$$

where  $\mathbb{1}_{\sigma,\sigma'}$  and  $\boldsymbol{\sigma}_{\sigma,\sigma'}$  are the respective matrix elements of the unit matrix and the Pauli matrices. The summation has to be carried out over all momentum and spin states of the system. To retain consistency with the standard notation for the spin operator  $\hat{\mathbf{S}}$ , we have chosen, for the remainder of this chapter, the  $z$ -axis parallel to the Feshbach field (quantisation axis) which is the natural orientation in this case.

For Fermi gases exposed to a moving Bragg lattice in the form of a plane wave, the dynamic structure factor  $S(\mathbf{k}, \omega)$  depends only on  $|\mathbf{k}| = k$ . With this, we arrive at our final expression for the effective Bragg

$$\hat{H}_{\text{Pert}} = \left[ I_{\text{eff}} \hat{\rho}^{\dagger}(k) + B_{\text{eff}} \hat{S}_z^{\dagger}(k) \right] e^{-i\omega t} + \left[ I_{\text{eff}} \hat{\rho}^{\dagger}(-k) + B_{\text{eff}} \hat{S}_z^{\dagger}(-k) \right] e^{+i\omega t}, \quad (5.2.10)$$

where we label  $I_{\text{eff}} = (U_{\uparrow} + U_{\downarrow})/2$  as an effective total intensity given by the sum of the light shifts for each spin state and  $B_{\text{eff}} = (U_{\uparrow} - U_{\downarrow})/2$  as an effective magnetic field given by the differential light shift [CT72]. On the right hand side of equation 5.2.10, the first term describes the energy and momentum transfer from the Bragg beams to the atoms, and vice versa for the second term.

As discussed in section 4.2.1, the system's response to a weak Bragg perturbation is proportional to the transferred momentum  $[\Delta P(k, \omega) \propto \hbar k]$  and energy ( $\hbar\omega$ ) to the atoms; and the probability per unit time and particle that this transfer occurs can be calculated by Fermi's golden rule,  $\mathcal{P}(k, \omega) = \frac{2\pi}{\mathcal{Z}N} \sum_{m,n} \exp(-\beta E_m) |\langle n | \hat{H}_{\text{Pert}} | m \rangle|^2 \delta(\omega - \omega_{nm})$ , where  $\mathcal{Z} = \sum_n \exp(-\beta E_n)$  is the partition function,  $\beta = 1/(k_B T)$  is the inverse temperature and  $\hbar\omega_{nm} = E_n - E_m$  is the transferred energy [Pin66]. We simplify the evaluation of the matrix element of the transition rate  $\mathcal{P}$  by explicitly ignoring the hermitian conjugate of the in equation 5.2.10. Consequently, we only take into account the  $S(k, \omega)$  term of the dynamic susceptibility. This assumption is valid at low temperatures  $T$  and high-momentum transfer ( $k \gg k_F, \lambda_{\text{dB}}^{-1}$ ) where momentum and energy transfer processes from the atomic cloud into the Bragg beams are strongly suppressed. We thus obtain

$$\mathcal{P}(k, \omega) = \frac{2\pi}{\mathcal{Z}N} \sum_{m,n} e^{-\beta E_m} \left[ I_{\text{eff}}^2 |\langle n | \hat{\rho}^{\dagger}(k) | m \rangle|^2 + B_{\text{eff}}^2 |\langle n | \hat{S}_z^{\dagger}(k) | m \rangle|^2 \right] \delta(\omega - \omega_{nm}), \quad (5.2.11)$$

where we also have made use of  $S_{\uparrow\uparrow}(k) \equiv S_{\downarrow\downarrow}(k)$  and  $S_{\uparrow\downarrow}(k) \equiv S_{\downarrow\uparrow}(k)$  for a spin-balanced Fermi gas [Com06a]. Further, recalling the definition of the individual components of the dynamic structure factors  $S_D$  and  $S_S$  [Bru01],

$$S_{\sigma\sigma'}(k, \omega) = \frac{1}{\mathcal{Z}N} \sum_{m,n} e^{-\beta E_m} \langle n | \hat{\rho}_{\sigma}^{\dagger}(k) | m \rangle \langle m | \hat{\rho}_{\sigma'}(k) | n \rangle \delta(\omega - \omega_{nm}), \quad (5.2.12)$$

we can rewrite equation 5.2.11 in the following form which now includes the individual spin-up/down structure factors and the corresponding light shift potentials,

$$\begin{aligned} \mathcal{P}(k, \omega) &= 2\pi \left[ I_{\text{eff}}^2 S_D(k, \omega) + B_{\text{eff}}^2 S_S(k, \omega) \right] \\ &= \frac{\pi}{2} \left[ (U_{\uparrow} + U_{\downarrow})^2 (S_{\uparrow\uparrow}(k, \omega) + S_{\downarrow\downarrow}(k, \omega)) + (U_{\uparrow} - U_{\downarrow})^2 (S_{\uparrow\uparrow}(k, \omega) - S_{\downarrow\downarrow}(k, \omega)) \right] \\ &= \pi \left[ (U_{\uparrow}^2 + U_{\downarrow}^2) S_{\uparrow\uparrow}(k, \omega) + 2U_{\uparrow}U_{\downarrow} S_{\uparrow\downarrow}(k, \omega) \right]. \end{aligned} \quad (5.2.13)$$

For Bragg measurements on  ${}^6\text{Li}$  in the BCS-BEC crossover, the Rabi frequencies for both spin states are essentially identical so that they cancel out when applying the  $f$ -sum normalisation. This gives the effective momentum transferred to the atoms by the Bragg

## 5. Spin-Bragg spectroscopy of a strongly interacting ${}^6\text{Li}$ gas

perturbation to be proportional to

$$\Delta P(k, \omega) = \hbar k \tau_{\text{Br}} \mathcal{P}(k, \omega) \propto \left( \frac{1}{\Delta_{\uparrow}^2} + \frac{1}{\Delta_{\downarrow}^2} \right) S_{\uparrow\uparrow}(k, \omega) + \frac{2}{\Delta_{\uparrow}\Delta_{\downarrow}} S_{\uparrow\downarrow}(k, \omega). \quad (5.2.14)$$

From equation 5.2.14 one can see that, using a large detuning from resonance such that  $\Delta_{\uparrow} \approx \Delta_{\downarrow} (\gg \omega_{\uparrow\downarrow})$ , the Bragg field couples primarily to the density channel as the coefficients in front of  $S_{\uparrow\uparrow}$  and  $S_{\uparrow\downarrow}$  will be approximately equal. Conversely, if  $\Delta_{\uparrow} \equiv -\Delta_{\downarrow}$  then the response will be entirely in the spin channel. Choosing detunings between these limits gives a variable contribution of both spin and density response.

Equation 5.2.14 relates to the (separate) measurements of the Bragg responses  $R_{\text{D,S}}(k, \omega)$  in the density and spin channels in the following way: To measure the spin response, we set the Bragg detuning to exactly half the hyperfine splitting of the atomic spin states ( $\omega_{\uparrow\downarrow}/2$ ) to recover the minus sign in equation 5.2.1. At a Feshbach magnetic field of 833 G this would be  $|\Delta_{\text{S}\sigma}| = 38.8$  MHz. The Bragg detuning for the density response, labelled  $\Delta_{\text{D}\sigma}$ , can be nearly anything as long the atoms in both spin states couple to the excited states sufficiently strong, and, the direction of the light shift is the same, and, the detuning is far-off resonant to minimise heating. Using equation 5.2.14 together with the  $f$ -sum rule, we find that the Bragg spectra in the respective density and spin channels relate to the responses of the individual spin components by

$$R_{\text{D}}(k, \omega) = S_{\uparrow\uparrow}(k, \omega) + \frac{2\Delta_{\text{D}\uparrow}\Delta_{\text{D}\downarrow}}{\Delta_{\text{D}\uparrow}^2 + \Delta_{\text{D}\downarrow}^2} S_{\uparrow\downarrow}(k, \omega) \equiv S_{\text{D}}(k, \omega) \quad \text{for } \Delta_{\text{D}\uparrow} \rightarrow \Delta_{\text{D}\downarrow}, \quad (5.2.15)$$

$$R_{\text{S}}(k, \omega) = S_{\uparrow\uparrow}(k, \omega) - S_{\uparrow\downarrow}(k, \omega) \equiv S_{\text{S}}(k, \omega).$$

As already pointed out in the preceding chapter (section 4.2.2 on page 87), the factor in front of the 2nd term on the right hand side of the equation for  $R_{\text{D}}(k, \omega)$  in 5.2.15 differs from unity by about 1% for the typical detunings we use for the density response of state  $|\uparrow\rangle$  ( $|\downarrow\rangle$ ), 568 MHz (644 MHz).

Note that  $R_{\text{D}}$  and  $R_{\text{S}}$  in equation 5.2.15, and thus  $S_{\text{D}}$  and  $S_{\text{S}}$ , also satisfy the  $f$ -sum rule as each of the components on the right hand side satisfies it according to [Guo10]

$$\int \omega S_{\uparrow\uparrow}(k, \omega) d\omega = \frac{\omega_{\text{rec}}}{\hbar} \quad (5.2.16)$$

$$\int \omega S_{\uparrow\downarrow}(k, \omega) d\omega = 0, \quad (5.2.17)$$

where  $\omega_{\text{rec}} = \hbar k^2/(2m)$  the atomic recoil frequency and  $m$  is the atom's mass. Therefore, the first energy weighted moment of any measured response must also satisfy the  $f$ -

sum rule which allows the accurate normalisation of our measured Bragg spectra (cf. section 4.2.2 on page 82).

Finally, we can rewrite the equations 5.2.15 to get normalised expressions for the respective spin-parallel and -antiparallel components of the dynamic structure factor with a correction for any Bragg laser detuning in the density channel, when the detunings for the spin channel were set to  $\Delta_{S\uparrow} \equiv -\Delta_{S\downarrow}$ :

$$S_{\uparrow\uparrow}(k, \omega) = \frac{1}{2} \left[ 1 - \left( \frac{\Delta_{D\uparrow} - \Delta_{D\downarrow}}{\Delta_{D\uparrow} + \Delta_{D\downarrow}} \right)^2 \right] R_D(k, \omega) + \frac{1}{2} \left[ 1 + \left( \frac{\Delta_{D\uparrow} - \Delta_{D\downarrow}}{\Delta_{D\uparrow} + \Delta_{D\downarrow}} \right)^2 \right] R_S(k, \omega) \quad (5.2.18)$$

and

$$S_{\uparrow\downarrow}(k, \omega) = \frac{\Delta_{D\uparrow}^2 + \Delta_{D\downarrow}^2}{(\Delta_{D\uparrow} + \Delta_{D\downarrow})^2} [R_D(k, \omega) - R_S(k, \omega)]. \quad (5.2.19)$$

### 5.2.2. Energy level diagram for spin-Bragg scattering ${}^6\text{Li}$ atoms

The preparation of the Fermi gas clouds for probing spin structure factors is equivalent to the one for measuring density responses. We produce an equal mixture of atoms in the  $|\uparrow\rangle$  and  $|\downarrow\rangle$  ground states and tune the magnetic field to either unitarity close to 833 G or any other point of interest in the BCS-BEC crossover where strong pair correlations are present. The atomic level diagram including the Bragg laser transitions for this setting is displayed in figure 5.2.2. Between the two ground states, where  $m_J = -1/2$ , the Zeeman splitting  $\omega_{\uparrow\downarrow}$  is approximately 80 MHz and the splitting between the branches of excited electronic states with different  $m_{J'}$  is of order of 1.5 GHz. Furthermore, the splitting between the  $|e_{\uparrow}\rangle$  and  $|e_{\downarrow}\rangle$  states in the lowest branch is below 2 MHz (cf. appendix A).

The Bragg beams are horizontally polarised which corresponds to a direction perpendicular to the Feshbach field. Therefore, only  $\sigma^-$  transitions from  $m_J = -1/2$  to  $m_{J'} = -3/2$  can be driven. This allows us to realise effectively close transitions and the atom-light interaction is equivalent to that of a two-level atom. The reason for this is that, at such high magnetic fields, the electronic and nuclear spins are almost fully decoupled and the nuclear spin projection  $m_I$ , which is 1 for  $|e_{\uparrow}\rangle$  and 0 for  $|e_{\downarrow}\rangle$ , cannot be flipped by the Bragg lasers. Therefore, the only possible excitations are to  $m_F = -1/2$  from state  $|\uparrow\rangle$  and to  $m_F = -3/2$  from state  $|\uparrow\rangle$ . In addition, due to the large Zeeman splitting in the excited states it is straightforward to selectively excite each of the ground states.

## 5. Spin-Bragg spectroscopy of a strongly interacting ${}^6\text{Li}$ gas

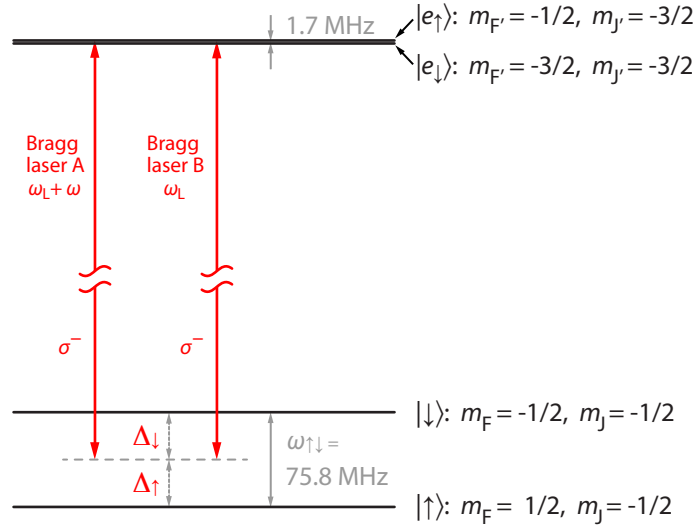


**Figure 5.2.2.:** Atomic energy diagram (not to scale) of  ${}^6\text{Li}$  and Bragg-laser transitions for probing the spin response at unitarity. Both Bragg lasers are detuned to precisely half the Zeeman splitting of the two ground states.

### 5.2.3. Bragg linearity for spin-response measurements

Similarly as for the density response, presented in the preceding chapter, we also carefully calibrated the Bragg intensities for the spin-response measurements to ensure linear momentum transfers at high Bragg signals. This check is of particular importance in the spin case since the Bragg detunings are close to the atomic resonances leading to a high spontaneous photon scattering rate. Perturbations in the non-linear regime could alter the spin correlations and distort the spectra. Our goal is therefore to find the highest possible laser intensities that still produce reliable spectra.

The atomic clouds are prepared at unitarity,  $1/(k_F a) = 0$ , and on the BEC side of the Feshbach resonance at  $1/(k_F a) = 0.93$ . The procedure for obtaining the linear-response data is essentially the same as described in section 4.2.5. The main differences are shorter Bragg pulse durations,  $\tau_{\text{Br}}$ , and a two orders of magnitude smaller intensity product of the Bragg lasers, corresponding to optical powers of  $2 - 4 \mu\text{W}/\text{beam}$  at  $1/(k_F a) = 0$  and  $\sim 6 \mu\text{W}/\text{beam}$  at  $1/(k_F a) = 0.93$ .

A shorter Bragg pulse was used in the spin channel to minimise spontaneous emission as follows. In the linear regime, the momentum imparted to the cloud by the Bragg lasers is proportional to the square of the laser intensities,  $I_A I_B$ , according to (equation 4.2.10)

$$\Delta P(\mathbf{k}, \omega) = 2\pi \hbar k \Omega_{\text{Br}}^2 \tau_{\text{Br}} S_S(\mathbf{k}, \omega), \quad (5.2.20)$$

where  $\Delta$  in  $\Omega_{\text{Br}} = \Gamma^2/(4\Delta)\sqrt{I_{\text{A}}I_{\text{B}}}/I_{\text{sat}}$  is assumed to have the same magnitude for both spin states. For a simple two-level atom, the number of spontaneously scattered photons in each spin state  $|\sigma\rangle$  can be calculated via

$$N_{\text{Ph},\sigma} = \frac{\Gamma\tau_{\text{Br}}}{2} \frac{I_{\text{tot}}/I_{\text{sat}}}{1 + I_{\text{tot}}/I_{\text{sat}} + (2\Delta_{\sigma}/\Gamma)^2}. \quad (5.2.21)$$

From equation 5.2.21 one can see that for  $I_{\text{A,B}} \ll I_{\text{sat}}$  the number of photons are approximately proportional to the sum of the intensities of both Bragg laser beams,  $I_{\text{tot}} = I_{\text{A}} + I_{\text{B}}$ , times the pulse duration  $\tau_{\text{Br}}$ . On the other hand, the Bragg signal in equation 5.2.20 is proportional to the intensity product multiplied by  $\tau_{\text{Br}}$ . Thus, a shorter pulse with higher intensities increases the ratio of Bragg signal to spontaneous emission.

As the spin dynamic structure factor  $S_{\text{S}}(\mathbf{k}, \omega)$  does not contain any narrow features (in contrast to the pairing peak in figure 4.4.1 on page 107), we are able to use a shorter Bragg pulse than for density response measurements ( $\tau_{\text{Br}} = 100 \mu\text{s}$ ). The pulse duration at unitarity is set to  $\tau_{\text{Br}} = 50 \mu\text{s}$ , and on the BEC side we chose  $\tau_{\text{Br}}$  to be  $25 \mu\text{s}$ . Even with the shortest pulse duration, the measured response, which extends over a frequency range of 400 kHz, will not be significantly altered as the Fourier width of the Bragg pulse does not exceed 35 kHz.

The figures in 5.2.3 depict the response in the spin channel for atom clouds at unitarity. Panel (a) shows the response for a wide range of squared intensities whereas (b) gives a more detailed view on the same data highlighting the region where linearity starts to break down. Bragg laser intensities are quoted in units of saturation intensity for the  $D_2$ -line of  ${}^6\text{Li}$  ( $I_{\text{sat}} = 2.54 \text{ mW}$ ). The different colours indicate different Bragg frequencies  $\omega$ . In contrast to the density case, the Bragg signal is now dominated by excitations at the atomic recoil frequency  $\omega_{\text{rec}}$  (red triangles). Pairing plays no important role anymore as shown by the data at  $\omega_{\text{rec}}/2$  (blue circles). At low,  $\omega_{\text{rec}}/4$  (green squares), and high frequencies,  $2\omega_{\text{rec}}$  (black inverted triangles), linearity persists to much higher values of the intensity product. For the actual spin-spectra at 833 G, we use Bragg squared intensities of  $0.6 \times 10^{-4} I_{\text{sat}}^2$  when probing around  $\omega_{\text{rec}}$ , whereas at the low and high frequency end we stay just below  $2 \times 10^{-4} I_{\text{sat}}^2$  to ensure linearity.

Figure 5.2.4 shows the spin-response at a magnetic field of 783 G. We find that the locations where linearity starts to break down are closer together in the BEC case than at unitarity. For an entire spin-spectrum on the BEC side, the squared intensity of Bragg lasers was therefore set to  $5 \times 10^{-4} I_{\text{sat}}^2$ .

We expect that the departure from linearity for spin-Bragg spectroscopy is dominated by spontaneous emission as there is no apparent dependence of the Bragg frequency and

5. Spin-Bragg spectroscopy of a strongly interacting  ${}^6\text{Li}$  gas

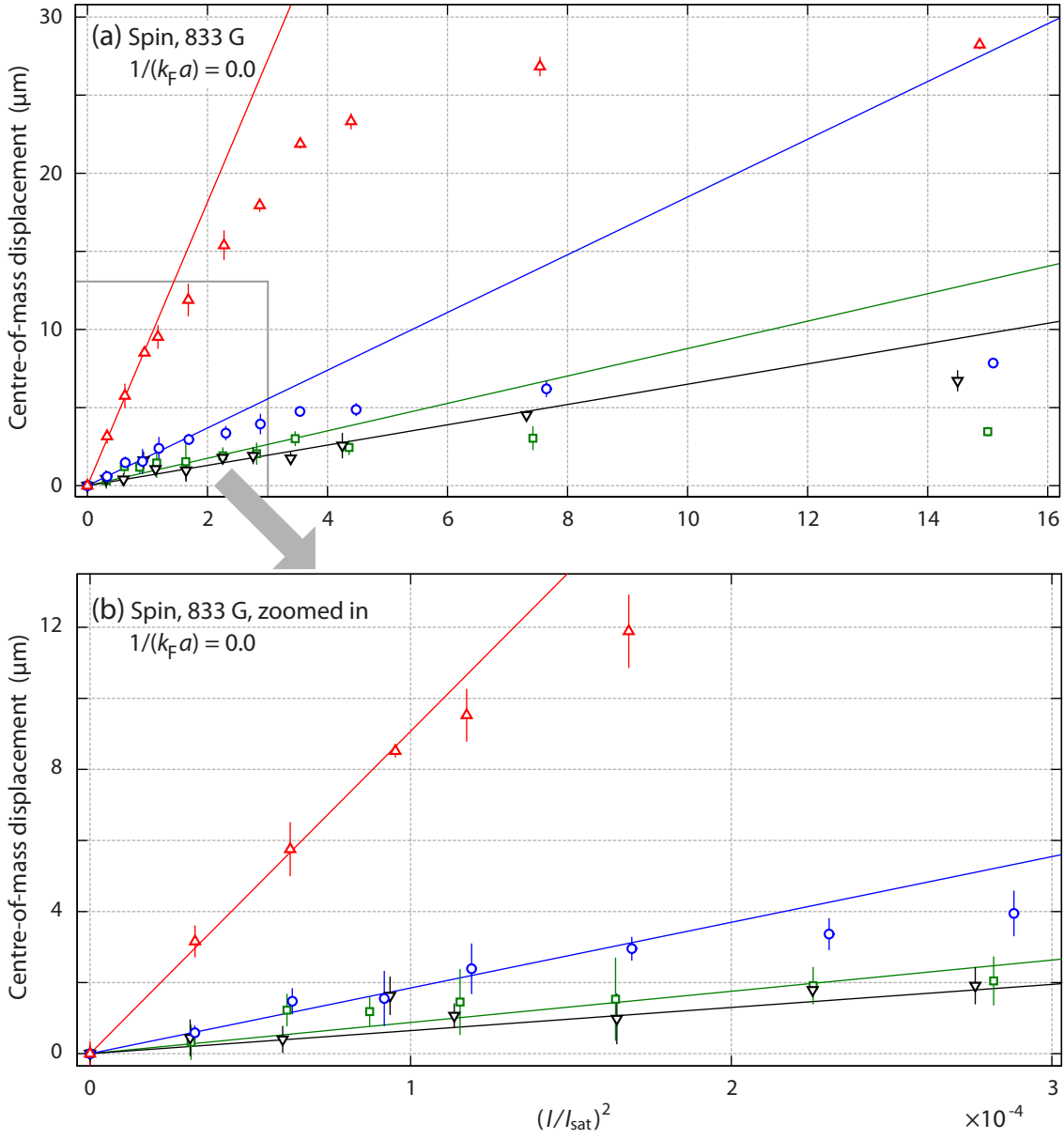


**Figure 5.2.3.:** Measurements of the centre-of-mass cloud displacement versus the squared Bragg laser intensity at four different frequencies. Shown are spin responses for a unitary Fermi gas. Green squares were taken at  $\omega = \omega_{\text{rec}}/4$ , blue circles at  $\omega = \omega_{\text{rec}}/2$ , red triangles at  $\omega = \omega_{\text{rec}} = 132$  kHz and black inverted triangles at  $\omega = 2\omega_{\text{rec}}$ . The straight lines are fits to the low intensity linear response portion of the data. Figure (a) shows data for squared intensities up to  $16 \times 10^{-4} I_{\text{sat}}^2$ . A zoomed in view on the data is given in figure (b).

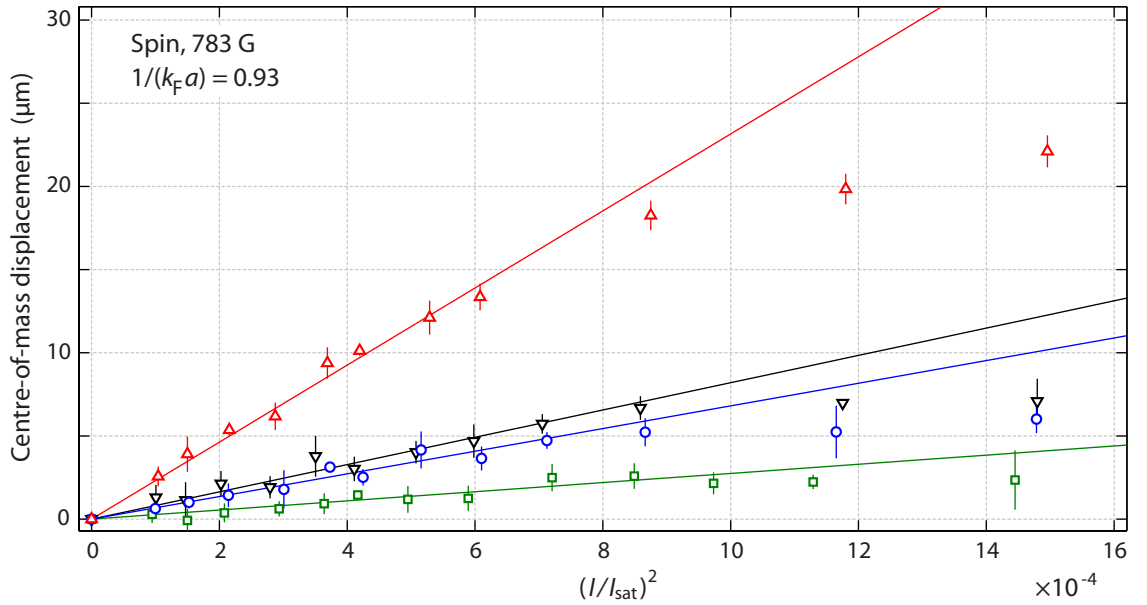


**Figure 5.2.4.:** Measurements of the centre-of-mass displacement of atomic clouds prepared at 783 G versus the squared intensity of the Bragg lasers for a selection of excitation frequencies  $\omega$  in units of the atomic recoil frequency  $\omega_{\text{rec}} = 132$  kHz. Green squares were taken at  $\omega = \omega_{\text{rec}}/4$ , blue circles at  $\omega = \omega_{\text{rec}}/2$ , red triangles at  $\omega = \omega_{\text{rec}}$  and black inverted triangles at  $\omega = 2\omega_{\text{rec}}$ . The straight lines are fits to the low intensity linear response portion of the data.

the spontaneous emission rates will be essentially constant for the relatively small range of Bragg frequencies. Additionally, we note that the squared intensities for which we see departure from the linear response in both the BEC and unitarity case are approximately a factor of four different. This is equivalent to a doubling of the total intensity, and hence a doubling of the spontaneous emission rate, but as the pulse duration for the BEC case was half that for unitarity, the total number of spontaneous emission events where the curves depart from linear will be roughly the same in both cases.

### 5.3. Results at unitarity and the BEC-side of the Feshbach resonance

The experimental investigation of the dynamic spin susceptibility provides valuable input for a better understanding of strongly interacting systems such as high- $T_c$  cuprate su-

## 5. Spin-Bragg spectroscopy of a strongly interacting ${}^6\text{Li}$ gas

perconductors, see for example the textbook [Pla10] for an overview. In ultracold Fermi gases, the dynamic spin response can be used to study the dynamics of pairing and molecule formation [Com06a, Str09]. Here, we measure the spin dynamic structure factor of a 3D two-component Fermi gas with  $s$ -wave pairing in the BCS-BEC crossover. Bragg spectra of  $S_S(k, \omega)$  and  $S_D(k, \omega)$  are combined to extract the dynamic spin-parallel,  $S_{\uparrow\uparrow}(k, \omega)$ , and spin-antiparallel,  $S_{\uparrow\downarrow}(k, \omega)$ , components of the response.

Bragg spectroscopy at high-momentum transfer was employed to obtain Bragg spectra of  $S_{D,S}(k, \omega)$ . The shape of the individual spin components were found to show excellent qualitative agreement with recent theoretical calculations for a harmonically trapped strongly interacting spin-balanced Fermi mixture. These calculations are based on high-temperature quantum virial expansions ( $T \gtrsim 0.4 T_F$ ) [Hu10a, Hu12b], and also on a random-phase approximation for a zero-temperature Fermi gas [Zou10].

The experimental setup and procedure are basically identical to that used for the precision measurements of the density response functions presented in the last chapter. Only the Bragg detunings are different in order to be sensitive to excitation processes that couple to the spin channel, and the Bragg pulse duration is shorter to increase the Bragg response signal. Thus, to avoid repetition, the experimental description is kept brief and the reader is referred to chapter 4 for more details.

### 5.3.1. Measuring spin dynamic structure factors

In these experiments, we used a balanced mixture of ultracold Fermi gases in the  $|\uparrow\rangle$  and  $|\downarrow\rangle$  states with  $N_{\uparrow} = N_{\downarrow} = 2 \times 10^5$  atoms per state. Details about atom cooling and preparation are given in section 3.3.3 on page 59 ff.. After evaporation, the cloud is loaded into the second trap, a single beam optical dipole trap with trapping frequencies of 97 and 24.5 Hz in the respective radial and axial directions. Before applying the Bragg pulse, the cloud was held for 500 ms in the final trap to allow for equilibration. We recorded several Bragg spectra at two different positions in the BCS-BEC crossover as a function of excitation energy ( $\hbar\omega$ ) at a fixed momentum transfer ( $\hbar k$ ). Results were obtained at magnetic fields close to unitarity and on the BEC-side of the Feshbach resonance [ $1/(k_F a) = 0.93$ ].

Bragg scattering is achieved by illuminating the cloud with two collimated laser beams intersecting at an angle of  $83.9^\circ$  yielding an atomic recoil frequency of  $\omega_{\text{rec}} = 2\pi \times 131.6$  kHz and a relative Bragg wave vector of  $k = 4.2 k_F$  (cf. section 4.2.3 on page 89 for the Bragg laser setup). We use Bragg laser detunings of  $\Delta_{\uparrow} = 39$  MHz and  $\Delta_{\downarrow} = -39$  MHz to be sensitive to excitations in the spin channel only.

Spin-spectra are obtained by applying a short Bragg pulse to a trapped atom cloud and

measuring the momentum imparted as a function of the Bragg frequency. The Bragg pulse durations are  $\tau_{\text{Br}} = 50 \mu\text{s}$  (unitarity) and  $\tau_{\text{Br}} = 25 \mu\text{s}$  (BEC side). Following the Bragg perturbation, the trap is immediately turned off and the atoms are allowed to expand for  $500 \mu\text{s}$  before an absorption image of atoms in state  $|\uparrow\rangle$  is taken. The imaging laser frequency is then rapidly ramped, by changing the reference frequency of the offset lock of the imaging laser, and a second image of atoms in state  $|\downarrow\rangle$  is taken  $850 \mu\text{s}$  after the first. Taking separate images of each spin state at different times allows us to measure the differential centre-of-mass cloud displacement which is insensitive to fluctuations in the dipole trap position (cf. section 4.2.2 on page 82). For the background image, taken last, the laser frequency is quickly ramped again, this time away from any atomic transition frequency within  $850 \mu\text{s}$  to avoid imaging remaining atoms in the region of interest. As we use a balanced mixture, and with the large collisional coupling between the two spin states, the order in which we image states  $|\uparrow\rangle$  and  $|\downarrow\rangle$  makes no difference to the measured spectra. We confirmed this by also taking spectra where the order of imaging both states was reversed.

Figure 5.3.1 shows Bragg spectra for both the spin (purple filled squares and circles) and density response (black dashed and dash-dotted lines) at unitarity and on the BEC side. Also shown for comparison is the calculated Bragg response of an ideal Fermi gas (green dotted line) centred at  $\omega_{\text{rec}}$ . The peak of the latter arises due to pair breaking excitations only, and the width is governed by the Fermi energy. This reference spectrum was calculated by the zero-temperature impulse approximation of the dynamic structure factor for large momentum transfer [Zam00].

The measured spectra were obtained at the lowest temperatures achievable with our experiment ( $\sim 0.08 T_{\text{F}}$  at unitarity). We apply our standard normalisation procedure to the spectra: Each spectrum is normalised such that the first energy weighted moment,  $\hbar^2 \int S(k, \omega) \omega d\omega$ , is set to be equal to unity. According to the  $f$ -sum rule [Pin66], this is equivalent to dividing each spectrum by the total number  $N$  of particles multiplied by the recoil energy  $\hbar\omega_{\text{rec}}$ . The measured Bragg signal  $\Delta X(k, \omega)$  is directly proportional to  $S(k, \omega)$ . Therefore, by normalising in this way, and expressing  $\omega$  in units of  $\omega_{\text{rec}}$ , we obtain the dynamic structure factor in units of  $1/N$  [Kuh10],

$$\frac{\Delta X(k, \omega)}{\int \Delta X(k, \omega) \frac{\omega}{\omega_{\text{rec}}} d\omega} = \hbar S(k, \omega). \quad (5.3.1)$$

Direct integration of the right hand side of equation 5.3.1 yields the static structure factor  $S(k) = \hbar \int S(k, \omega) d\omega$ . Note, for convenience we usually set  $\hbar \equiv 1$  when plotting dynamic structure factors.

## 5. Spin-Bragg spectroscopy of a strongly interacting ${}^6\text{Li}$ gas

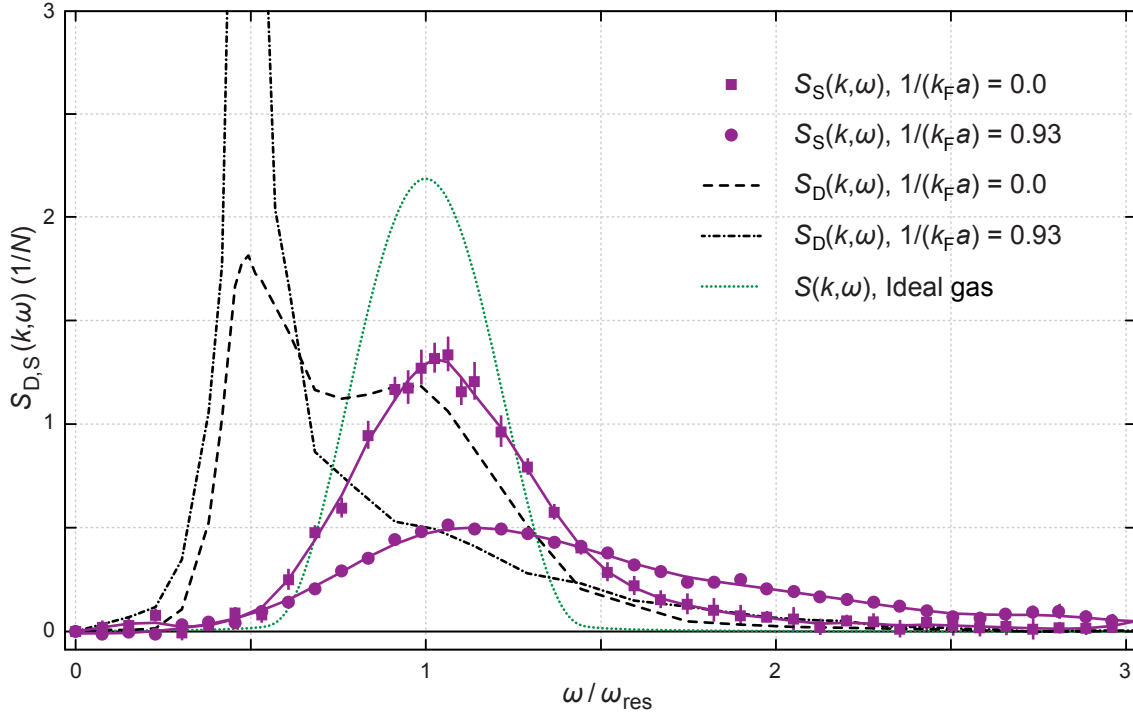


**Figure 5.3.1.:** Spin and density dynamic structure factors of a two-component Fermi gas. The spin (filled purple squares and circles) and density response (black dashed and dot dashed lines) were measured at  $1/(k_F a) = 0.0$  and  $1/(k_F a) = 0.93$ , respectively, and the dotted green line is the expected response of a noninteracting Fermi gas at  $T = 0$ . Solid lines are smoothed curves through the spin response data to guide the eye, and the responses have been normalised using the  $f$ -sum rule.

As figure 5.3.1 further shows, both the spin and density responses are significantly different to the ideal gas case indicating the strong correlations present both in the BEC and unitarity regimes. The density spectra  $S_D(k, \omega)$  show a strong response at  $\omega_{\text{rec}}/2$  due to the scattering of spin-up/spin-down pairs, as well as, a broad response at higher frequencies in the region of  $\omega_{\text{rec}}$  due to the scattering of single atoms (cf. section 4.4.1 on page 106 for a detailed discussion on the density response). At high momentum, the collective mode appears at  $\omega_{\text{rec}}/2$  [Com06a], which is clearly visible in both spectra, but more prominent on the BEC side due to the increased likelihood of finding spin-up/spin-down particles at small separation<sup>2</sup>.

<sup>2</sup>For  $k > k_F$ , the excitation of a collective mode physically corresponds to kicking pairs out of the pair

Spin-Bragg spectroscopy on the other hand is not sensitive to the collective mode as the positive and negative perturbations on the spin-up and spin-down particle, respectively, cancel each other, leaving no net perturbation on a pair (see illustration in figure 5.2.1). The spin response can only measure a signal when the excitation energy is high enough to break a pair whereas the density response probes the total density of the gas. Therefore, the spin response  $S_S(k, \omega)$  is suppressed at  $\omega_{\text{rec}}/2$  and instead only shows free atom excitations at higher energies.  $S_S(k, \omega)$  on the BEC side has a lower peak and is biased towards higher frequencies signalling a suppression of the spin susceptibility due to the increased energy required to remove atoms from bound pairs.

### 5.3.2. Spin-parallel and spin-antiparallel responses

The normalised spectra in figure 5.3.1 can be combined with the known Bragg laser detunings for the density measurements according to equations 5.2.18 and 5.2.19 to give the spin-parallel  $S_{\uparrow\uparrow}(k, \omega)$  (red upright triangles) and spin-antiparallel  $S_{\uparrow\downarrow}(k, \omega)$  (blue inverted triangles) components of the dynamic structure factor, plotted in figures 5.3.2 and 5.3.3 at  $1/(k_F a) = 0.0$  and  $0.93$ , respectively. These spectra reveal the response of the particle density in one state to a perturbation of the particle density in either the same or opposite spin states and show quite a complex structure. These interesting features will be discussed in the next section. We note that, in the absence of interactions, the spin-parallel response would be identical to the ideal gas response shown in figure 5.3.1 and the spin-antiparallel response would be zero for all  $\omega$  as the constituents of the gas are uncorrelated.

**Static structure factors:** According to equation 5.3.1, the spectra in figures 5.3.2 and 5.3.3 can be integrated to provide the static structure factors  $S(k)$  and hence  $S_{\sigma\sigma'}(k)$ . As these spectra are expressed in units of  $1/N$ , integration over  $\omega$  gives  $S(k)$  directly. We find the following results:

$$\begin{aligned} 1/(k_F a) = 0.0 : & \quad S_{\uparrow\uparrow}(k) = 1.02 \pm 0.04, \quad S_{\uparrow\downarrow}(k) = 0.17 \pm 0.04; \\ 1/(k_F a) = 0.93: & \quad S_{\uparrow\uparrow}(k) = 1.03 \pm 0.04, \quad S_{\uparrow\downarrow}(k) = 0.38 \pm 0.04. \end{aligned}$$

At the momentum used here,  $S_{\uparrow\uparrow}(k)$  is expected to be unity due to autocorrelation of fermionic atoms in identical spin states [Com06a, Hu10a] consistent with our findings. This also indicates that both the spin and density responses provide consistent measures for

---

condensate (single-particle regime of the energy dispersion) [Com06b].

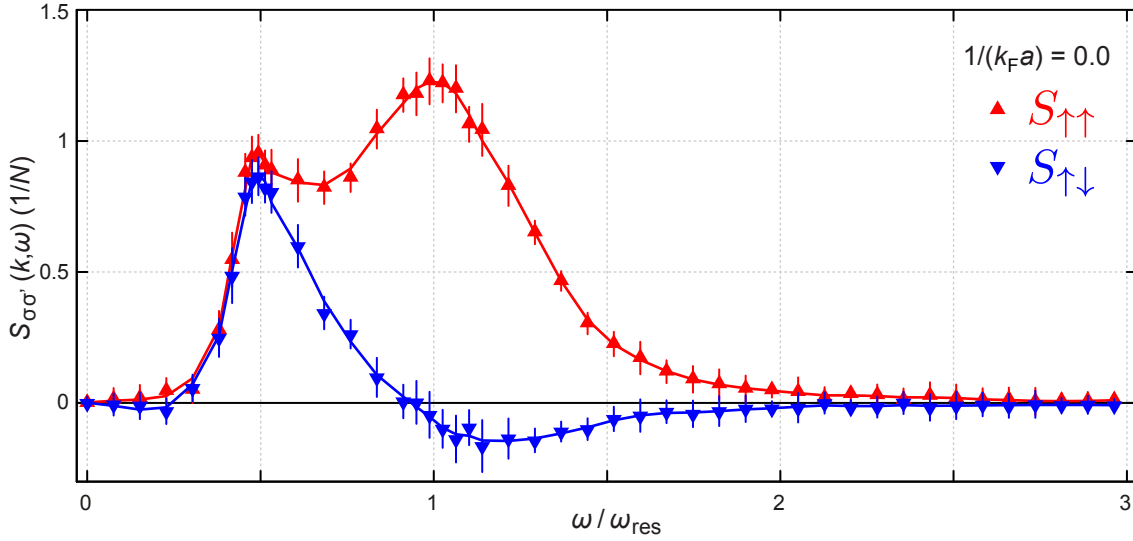


**Figure 5.3.2.:** Spin-parallel and spin-antiparallel components of the dynamic structure factor for a unitary Fermi gas at 833G. Red upright triangles are the spin-parallel structure factor  $S_{\uparrow\uparrow}$  and blue inverted triangles are the spin antiparallel response  $S_{\uparrow\downarrow}$ . Solid lines are a guide to the eye.

$S_{\uparrow\downarrow}(k)$  within our uncertainties. The uncertainties in the combined spectra are dominated by the uncertainty in the spin response, which was obtained at low intensities to minimise spontaneous emission. The situation could be improved by using a spin mixture with a larger energy separation such as  $|F = 1/2, m_F = 1/2\rangle$  and  $|F = 3/2, m_F = -3/2\rangle$  [Bar05], providing a hyperfine splitting of more than 150 MHz in the BCS-BEC crossover regime (cf. appendix A, energy levels of  ${}^6\text{Li}$ ).

### 5.3.3. Interpretation of the same- and opposite-spin response functions

The features seen in  $S_{\uparrow\uparrow}(k, \omega)$  and  $S_{\uparrow\downarrow}(k, \omega)$  can now be examined and attributed to different kinds of excitations. At frequencies ranging from zero to slightly above  $\omega_{\text{rec}}/2$ , both the spin-parallel and spin-antiparallel components are essentially identical for both interaction strengths. The emergence of a peak with same amplitude at  $\omega_{\text{rec}}/2$  in each response function impressively confirms that the correlations are dominated by pairs, composed of spin-up and spin-down atoms, and not just correlations by individual atoms. Each scattered pair contains a spin-up and spin-down particle, and, since the response is independent of the combination of spin states being probed at a given Bragg correlation length  $\propto 1/k$  and time  $\propto 1/\omega$ , the density-density correlations for either combination of

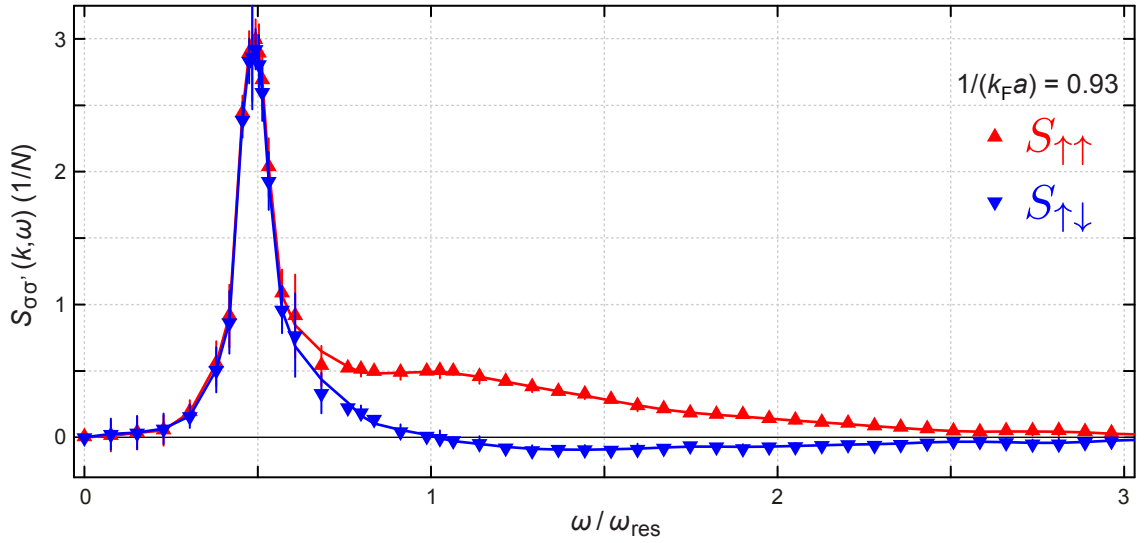


**Figure 5.3.3.:** Spin-parallel and spin-antiparallel components of the dynamic structure factor for a strongly interacting Fermi gas on the BEC side of the Feshbach resonance at 783G. Red upright triangles give the spin-parallel structure factor  $S_{\uparrow\uparrow}$  and blue inverted triangles are the spin anti-parallel response  $S_{\uparrow\downarrow}$ . Solid lines are a guide to the eye.

spin states are the same. In other words, each pair contains a spin-up and spin-down particle, therefore, correlations between pairs should be the same regardless of whether one looks at the spin-up or spin-down particles, as they scatter pairwise.

Comparing the  $\omega_{\text{rec}}/2$  responses at unitarity, figure 5.3.2, with the BEC regime, figure 5.3.3, it is clear that both the spin-parallel and spin-antiparallel are more dominated by a large pairing peak on the BEC side. This is because the pairs are more tightly bound and the gas behaves more like a gas of bound bosonic molecules, with a mass of twice the atomic mass, than a gas of interacting fermions. Recall, that  $\omega_{\text{rec}}$  goes inversely with the mass of the particle hence the response at  $\omega_{\text{rec}}/2$ .

At higher frequencies, however, the spin-parallel and spin-antiparallel response functions become very different with  $S_{\uparrow\uparrow}(k, \omega)$  showing a significant peak near  $\omega_{\text{rec}}$ , whereas  $S_{\uparrow\downarrow}(k, \omega)$  becomes negative for  $\omega \gtrsim \omega_{\text{rec}}$ . The positive peak in  $S_{\uparrow\uparrow}(k, \omega \approx \omega_{\text{rec}})$  is primarily due to the autocorrelation term, that arises from single particle scattering. This feature is not present in  $S_{\uparrow\downarrow}(k, \omega)$  that always involves correlations between two different particles in opposite spin states.  $S_{\uparrow\downarrow}(k, \omega)$  becomes negative at high frequencies as required to satisfy the  $f$ -sum rule,  $\int S_{\uparrow\downarrow}(k, \omega) \omega d\omega \equiv 0$ . This reveals an interesting feature of the relative

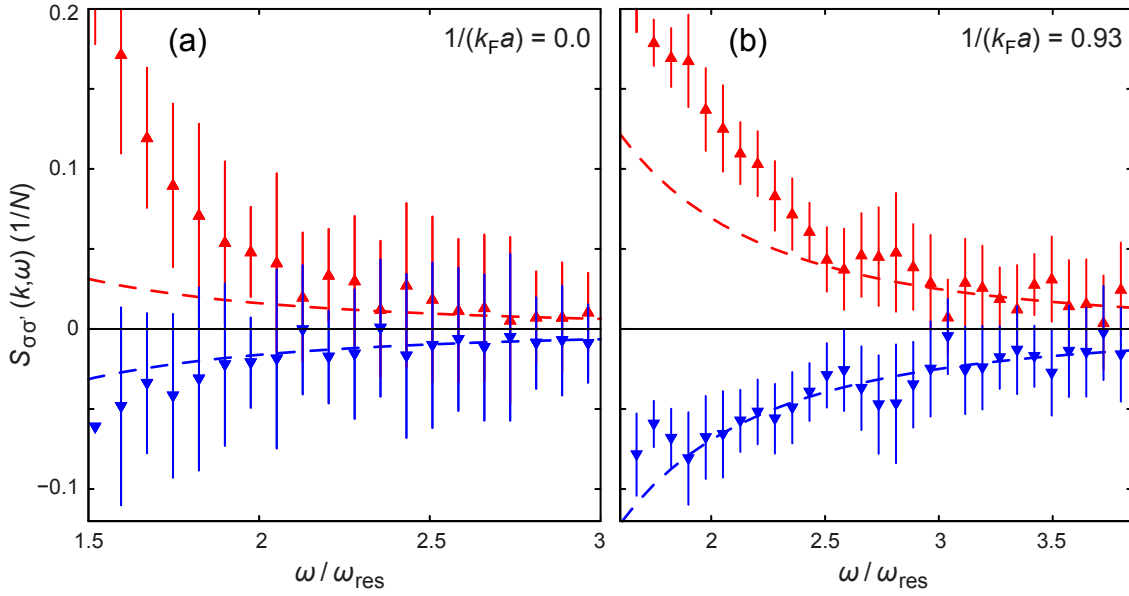


**Figure 5.3.4.:** Plots of the high-frequency region where  $S_{\uparrow\downarrow}(k, \omega)$  and  $S_{\uparrow\uparrow}(k, \omega)$  show universal behaviour. The tails at unitarity (a) and on the BEC side (b) drop off proportional to  $\omega^{-5/2}$ . The dashed blue lines are power law fits to  $S_{\uparrow\downarrow}(k, \omega > 2 \omega_{\text{rec}})$  (blue inverted triangles) and the dashed red lines are the negative of these fits. The red coloured fits indicate that  $S_{\uparrow\uparrow}(k, \omega)$  (red upright triangles) approaches the asymptotic universal behaviour only at higher  $\omega$ .

dynamics of spin-up/spin-down particles. A high-frequency fluctuation with momentum  $\hbar k$  of the spin-down density leads to an out-of-phase fluctuation of the spin-up particle density and vice versa. By recalling the definition of the dynamic structure factor, equation 4.2.5 on page 80, one can interpret the negative response as a result of the phase shift between the correlation function  $\langle \hat{\rho}_{\uparrow}(k, t) \hat{\rho}_{\downarrow}^{\dagger}(k, 0) \rangle$  and the complex phase factor ( $e^{i\omega t}$ ) at frequencies  $\gtrsim \omega_{\text{rec}}$ . These anti-correlations suppress the high frequency response in the density channel but enhance the high frequency spin response.

### 5.3.4. Universal behaviour of the high-frequency tail

For frequencies much greater than  $\omega_{\text{rec}}$  the individual spin components  $S_{\uparrow\uparrow}(k, \omega)$  and  $S_{\uparrow\downarrow}(k, \omega)$  are predicted to display a universal tail proportional to  $+\mathcal{I}/\omega^{5/2}$  and  $-\mathcal{I}/\omega^{5/2}$ , respectively, where  $\mathcal{I}$  is the contact parameter [Bra10, Hu12b, Nis12] (cf. section 2.3.5).

This can be seen in the high-frequency prediction for the spin dynamic structure factor,

$$\hbar\omega_{\text{rec}} \lim_{\omega \rightarrow \infty} S_S(k, \omega) = \left( \frac{\sqrt{2}}{3\pi^2} \right) \left( \frac{k_F}{k} \right) \left( \frac{\mathcal{I}}{Nk_F} \right) \left( \frac{\omega_{\text{rec}}}{\omega} \right)^{5/2} \simeq 0.0114 \frac{\mathcal{I}}{Nk_F} \tilde{\omega}^{-5/2}, \quad (5.3.2)$$

which is proportional to  $\omega^{-5/2}$  [Hu13]. On the right side of equation 5.3.2, the expression is evaluated for  $k = 4.20 k_F$  used in the experiments, and  $1/\tilde{\omega}$  is in units of  $\omega_{\text{rec}}$ .

For the density response, however, the leading order terms of  $S_{\uparrow\uparrow}$  and  $S_{\uparrow\downarrow}$  cancels leaving a universal  $\omega^{-7/2}$  tail given by [Son10, Tay10, Hu13]

$$\hbar\omega_{\text{rec}} \lim_{\omega \rightarrow \infty} S_D(k, \omega) = \left( \frac{16\sqrt{2}}{45\pi^2} \right) \left( \frac{k_F}{k} \right) \left( \frac{\mathcal{I}}{Nk_F} \right) \left( \frac{\omega_{\text{rec}}}{\omega} \right)^{7/2} \simeq 0.0121 \frac{\mathcal{I}}{Nk_F} \tilde{\omega}^{-7/2}, \quad (5.3.3)$$

where again  $k = 4.20 k_F$  was used. To my knowledge, the only time ever that a  $\omega^{-7/2}$  proportionality in the density response has been confirmed experimentally was in neutron scattering measurements on superfluid (bosonic)  $^4\text{He}$  [Gri93]. Because of the weaker power-law dependence, we decided to focus on the universal tail in  $S_S(k, \omega)$ , or equivalently, in the individual spin components.

Figure 5.3.4 (a) and (b) show zoomed-in plots of  $S_{\uparrow\uparrow}(k, \omega)$  and  $S_{\uparrow\downarrow}(k, \omega)$  at high frequency. Despite the small signal we find that the tail of  $S_{\uparrow\downarrow}(k, \omega)$  is well described by an  $\omega^{-5/2}$  dependence. A free power-law fit to the data (dashed blue line) for  $\omega > 2 \omega_{\text{rec}}$  yields

$$\begin{aligned} S_{\uparrow\downarrow}(k, \omega) &= (-0.14 \pm 0.10) \tilde{\omega}^{-2.7 \pm 0.8} && \text{at unitarity (a) and} \\ S_{\uparrow\downarrow}(k, \omega) &= (-0.39 \pm 0.11) \tilde{\omega}^{-2.5 \pm 0.3} && \text{on the BEC side (b),} \end{aligned}$$

consistent with  $\omega^{-5/2}$ .

In the limit that  $k, \omega \rightarrow \infty$ , the amplitude of the tails should provide a measure of the contact. However, our fit coefficients are approximately a factor of three larger than expected [Son10, Hu12b]. This can be partially attributed to the fact that the measured response is given by the convolution of the dynamic structure factor with a squared sinc function [Bru01, Bla02, Vee08] which will lift the data. However, we estimate that this effect alone would not explain the discrepancy. It is more likely that our experiments are not in the strict asymptotic high-momentum and high-frequency limit to obtain the contact even though the power law describes the data well.

We note that  $S_{\uparrow\uparrow}(k, \omega)$  only approaches the asymptotic behaviour at higher Bragg frequencies (dashed red line in figure 5.3.4) so we do not perform a separate fit to  $S_{\uparrow\uparrow}(k, \omega)$ , nor do we resolve the  $\omega^{-7/2}$  tail in  $S_D(k, \omega)$  in our measured frequency range.

## 5.4. Summary

In this chapter we have demonstrated that high-momentum Bragg spectroscopy with a differential coupling to each spin state can be used to measure the spin dynamic structure factor  $S_S(k, \omega)$  of a strongly interacting two-component Fermi gas. Differential coupling can be achieved by changing the detuning of the Bragg lasers in such way that for one spin state the laser appears red and for the other spin state blue detuned. Expressions were derived for the measured dynamic density and spin response functions  $R_D(k, \omega)$  and  $R_S(k, \omega)$ , respectively, based on a semi-classical perturbative approach to explicitly show their dependency on the finite detunings of the Bragg lasers.

Bragg spectra of the spin dynamic structure factor and the density dynamic structure factor, presented in the preceding chapter, were combined to extract  $S_{\uparrow\uparrow}(k, \omega)$  and  $S_{\uparrow\downarrow}(k, \omega)$  separately which allows us to understand the features of the density and spin response at different Bragg frequencies. The same- and opposite-spin components of the dynamic structure factor were seen to display a universal high-frequency tail  $\propto \omega^{-5/2}$ .

This work opens the way to measurements of  $S_{\uparrow\uparrow}(k, \omega)$  and  $S_{\uparrow\downarrow}(k, \omega)$  at any momentum; this will be particularly important for low-momentum Bragg spectroscopy ( $k < k_F$ ), where  $S_{\uparrow\uparrow}(k)$  cannot be assumed to be unity anymore since Pauli blocking reduces the number of states available to scatter into.

## 6. Summary and Outlook

In this thesis, I have presented precision studies of the dynamic density and spin response functions which have been used to explore a number of universal features of strongly interacting Fermi gases in the BCS-BEC crossover. Several experimental developments are described that led to dramatic improvements to our Bragg spectroscopic measurements compared with previous studies in our group, and a new method to obtain the spin response function by carefully setting the Bragg laser detuning was demonstrated. The main outcomes of this work are experimental results that can be used to benchmark many-body theories of strongly correlated fermions. All experiments described in this thesis were based on high-momentum ( $k = 4.2 k_F$ ) Bragg spectroscopy.

In chapter 4, the precision measurement of the density dynamic structure factor  $S(k, \omega)$  was described. This allowed the clear identification of the features associated with pair and single atom scattering in the response of a Fermi gas at unitarity. The pairing peak is very sharp and highly prominent in the response, which is at first surprising due to the fact that the Bragg recoil energy is more than a factor of ten larger than the pairing gap. However, this highlights the fact that, at low temperatures, pair correlations are very strong and the number of pairs whose total momentum is zero (i.e. that can scatter at  $\omega_{\text{rec}}/2$ ) is large, consistent with a significant condensate fraction. The integral of the measured dynamic structure factor directly provided the static structure factor,  $S(k)$ , which we were able to measure with an error bar of smaller than 1% at unitarity and 1.5% on the BEC side of the Feshbach resonance. When combined with the universal relation for the static structure factor, these results allowed the determination of Tan's contact parameter in a low temperature trapped gas with a better precision than has previously been available. Specifically, the error bar on our measurement at unitarity is now significantly smaller than the discrepancies between different theoretical predictions for the contact [Hu11].

In chapter 5, Bragg spectroscopy using light tuned close to the atomic transition frequencies was shown to be able to measure the spin response, i.e. the imaginary part of the dynamic spin susceptibility  $\chi_S''(k, \omega)$ , for a gas at unitarity and also on the BEC side of the Feshbach resonance. By setting the detuning of the Bragg lasers such that

## 6. Summary and Outlook

one state experienced a positive light shift potential (blue detuned) and the other state a negative light shift (red detuned) the Bragg lasers act as an effective magnetic field directly perturbing the spin operator  $\hat{S}_z$ . Based on a simple perturbative treatment, it was shown how the Bragg response depends on the Bragg laser detuning and how measurements for an arbitrary Bragg detuning allows for the reconstruction of the pure density and spin response functions. This method was used to extract the spin-parallel ( $S_{\uparrow\uparrow}$ ) and spin-antiparallel ( $S_{\uparrow\downarrow}$ ) dynamic and static structure factors at unitarity and in the BEC regime. The spin response was found to be suppressed at low energy due to pairing, particularly on the BEC side, but reveals pair breaking excitations at high energy. In addition, the predicted universal behaviour ( $\propto \omega^{-5/2}$ ) in the high-frequency limit was experimentally observed in the spin response for energies much greater than the recoil energy.

The techniques developed in this thesis open the way to a number of new directions for investigation. All experiments presented here involved measurements on an inhomogeneous gas confined in a harmonic trapping potential. In chapter 4, we used a trapped gas measurement to infer a homogeneous result for Tan's contact parameter based on some assumed knowledge about the finite temperature equation of state. Naturally it would be preferable to perform a homogeneous measurement directly as was reported recently by the JILA group who applied RF spectroscopy on a small sample of atoms near the centre of a trapped cloud where the density is approximately constant [Sag12]. The error bars on their measurement are still quite large and not at the level where one can use the results to distinguish between different theoretical predictions [Hu11].

Recently, our group has shown how Bragg spectroscopy can be performed in a way that allows access to the local value of the density dynamic structure factor [Lin14]. The basic idea is to confine the atoms in a harmonic trap that is elongated along the  $z$ -direction, where the confinement is weakest, apply a Bragg pulse in such a way that atoms are kicked perpendicular to the long axis of the cloud and measure the centre-of-mass displacement as a function of the coordinate  $z$ . In this way we obtain a line response function which represents the density-weighted response, integrated over  $x$  and  $y$ , but not  $z$  as would be the case for a trapped cloud measurement. We have then shown that taking a spatial derivative of this along  $z$  can provide the local homogeneous response, along the axis of the trap [Lin14]. This experimental protocol generalises an earlier scheme for obtaining the local pressure [Ho10, Nas10] and shows that it can be applied to other dynamical variables that cannot be accessed using an inverse Abel transform. In this work we showed a new signature of the emergence of a pair condensate in the unitary Fermi gas, however, the technique could also be applied to measure the temperature dependence of the contact.

Another significant direction that is now available thanks to the improvements described in this thesis is the possibility of low-momentum Bragg spectroscopy. Bragg scattering at low momentum ( $k < k_F$ ) is more challenging than the experiments described here (performed at  $k \sim 4k_F$ ) primarily due to the fact that the momentum imparted by the Bragg pulse is directly proportional to  $k$  so the measurable signal will be significantly smaller (cf. equation 4.2.10 on page 83). While longer expansion times would go part way to overcoming this difficulty, the whole cloud will also expand making the displacement relative to the overall cloud size smaller. Pauli suppression also plays a role in reducing the response for  $k < 2k_F$  as fermions are not able to scatter into states that are already occupied. Nonetheless there are very strong reasons to investigate the low- $k$  Bragg response as discussed below.

Firstly, low-momentum Bragg scattering allows the probing of collective excitations in the true sense. In particular, the Goldstone theorem states that for any spontaneous symmetry breaking transition, a gapless excitation (Goldstone mode) will exist that corresponds to a long wavelength deformation of the order parameter. In the case of a cold gas undergoing condensation, the condensate wavefunction acquires a macroscopic phase, but this phase does not appear in the hamiltonian (i.e. the ground state energy is independent of this phase) thus long wavelength variations in the phase cost little energy. In ultracold Fermi gases, this Goldstone mode (or Bogoliubov-Anderson mode) has been considered theoretically [Min01, Oha03b, Com06b] and was initially proposed as a means to identify the superfluid transition. At unitarity, the collective mode shows linear dispersion, below  $k \lesssim k_F$  and eventually merges with the continuum of single particle excitations where it becomes (Landau) damped and takes on the quadratic dispersion at higher  $k$  [Com06b]. The gradient of the dispersion relation of the Goldstone mode at low  $k$  gives the sound velocity.

The Bragg studies presented in this thesis already made use of the  $f$ -sum rule which relates the first energy-weighted moment of the dynamic structure factor to the number of particles and the recoil energy. This sum rule allowed the precise normalisation of Bragg spectra and has greatly improved the accuracy of our measurements [Kuh10, Hoi13]. At low momentum, Bragg spectroscopy will be aided by additional sum rules. For wavelengths longer than the mean interparticle spacing, the instantaneous or static response function due to a perturbation of the density by an external potential is equivalent to a measure of  $(\partial n / \partial \mu)$  which is proportional to the isothermal compressibility,  $\kappa = 1 / (m c_s^2)$ . The compressibility sum rule,  $\lim_{k \rightarrow 0} \int S(k, \omega) \omega^{-1} d\omega \equiv \kappa / 2$ , relates the first inverse energy weighted moment of the dynamic structure factor (or static response function) to the

## 6. Summary and Outlook

speed of sound ( $c_s$ ) [Pin66, Pit03]. Investigation of this sum rule in cold gases will be an important step as it offers a new way to measure the speed of sound. In combination with the  $f$ -sum rule (which applies at all momentum) these constraints will allow an accurate determination of  $c_s$ .

A further topic for investigation using low- $k$  Bragg scattering is the frequency dependent shear viscosity  $\eta(\omega)$  which can be used to study universal transport properties in strongly interacting Fermi gases. Several experiments have measured the static shear viscosity either through measurements of damping rates of collective oscillations [Cao11] or by measuring the evolution of the cloud size following release from an anisotropic trapping potential [Ell14]. By this it was demonstrated that at unitarity the ratio of the viscosity to the entropy density ( $\eta/s$ ), setting a scale for fluidity, is close to the predicted universal lower bound for quantum viscosity, i.e. a unitary Fermi gas behaves as a nearly perfect fluid [Tur08]. To date however, these studies have only probed static quantities. It would be very interesting to be able to probe the frequency dependent shear viscosity to learn more about the dynamics of the fluid. It turns out that shear viscosity for a unitary Fermi gas is directly proportional to the density dynamic structure factor at low  $k$ , according to [Tay10, Ens11]

$$\eta(\omega) = \lim_{\omega \rightarrow \infty} \lim_{k \rightarrow 0} \frac{3}{4\hbar} \frac{\omega^3}{k^4} S(\mathbf{k}, \omega). \quad (6.0.1)$$

From this it is easy to see that for high energies this quantity exhibits a universal behaviour scaling as  $\omega^{-1/2}$  since the high-frequency tail in  $S(\mathbf{k}, \omega)$  drops off as  $\omega^{-7/2}$ . Equation 6.0.1, together with the scheme mentioned above to obtain homogeneous quantities via Bragg scattering, may open a way to study local shear flows in a strongly correlated Fermi gas.

The shear viscosity also provides a sum rule (valid at small  $k$ ) involving the third moment of the dynamic structure factor [Tay10, Ens11]

$$\frac{2}{\pi} \int_0^\infty \left[ \eta(\omega) - \frac{\hbar^3/2\mathcal{C}}{15\pi\sqrt{m\omega}} \right] d\omega = \frac{2\mathcal{E}}{3} - \frac{\hbar^2\mathcal{C}}{6\pi ma} \quad (6.0.2)$$

which links the dynamic response of the gas to its thermodynamics via contact  $\mathcal{C}$  and energy density  $\mathcal{E}$ ; at unitarity this sum rule is equivalent to the equilibrium pressure. Sum rules provide important constraints on approximative many-body theories and the experimental verification of this shear viscosity sum rule hence also would be valuable.

# Appendix



## A. Electronic level structure of ${}^6\text{Li}$

${}^6\text{Li}$  is one of the two main workhorse elements for experiments on ultracold Fermi gases (the other being  ${}^{40}\text{K}$ ) and therefore its properties, relevant to laser cooling and trapping experiments have been well documented (see for example [Geh03] for an extensive review). Lithium is the lightest alkali atom (excluding hydrogen) and, like all alkalis, its atomic properties are dominated by the single valence electron. For convenience, we plot the energy levels relevant to the experiments described in this thesis for the ground  ${}^2S_{1/2}$  and excited  ${}^2P_{3/2}$  electronic states at low (fig. A.0.1) and high (fig. A.0.2) magnetic fields, respectively. Strong optical transitions between these two states are known as the  $D_2$ -line.

Due to the relatively small ground state hyperfine splitting of 228.2 MHz, the application of only modest magnetic fields ( $\sim 50$  G) leads to Zeeman shifts of comparable magnitude. At this point the coupling of the electronic and nuclear spin breaks down (Paschen-Back regime). In the excited  ${}^2P_{3/2}$  state the hyperfine splitting is even smaller, of order a few MHz, which effectively rules out polarisation gradient cooling mechanisms in magneto-optical traps. At the fields used in typical experiments ( $\sim 800$  G) the electronic and nuclear spins can essentially be considered fully decoupled which does provide some advantages for both imaging and Bragg scattering.

Consider optical transitions from the two lowest ground states used in our experiments,  $|F = 1/2, m_F = \pm 1/2\rangle$ , labelled  $|\uparrow\rangle$  and  $|\downarrow\rangle$  in figure A.0.1. At large fields the electron spins are parallel ( $m_S = -1/2$ ) and  $\sigma^-$  optical transitions to the  $m_S = -3/2$  excited state form a closed two-level system. Additionally, at such large fields the excited state Zeeman splittings are very large (fig. A.0.2) so that any light with the wrong polarisation will be far detuned from an optical transition and very unlikely to interact. This feature allow imaging of atoms in either spin state without the need for repumping light and, more importantly, without modifying the population in each state. It also enables the coupling of the Bragg lasers to the various energy levels to be easily controlled, as was described in section 4.2.4 on page 91 and 5.2.2 on page 127.

A. Electronic level structure of  ${}^6\text{Li}$

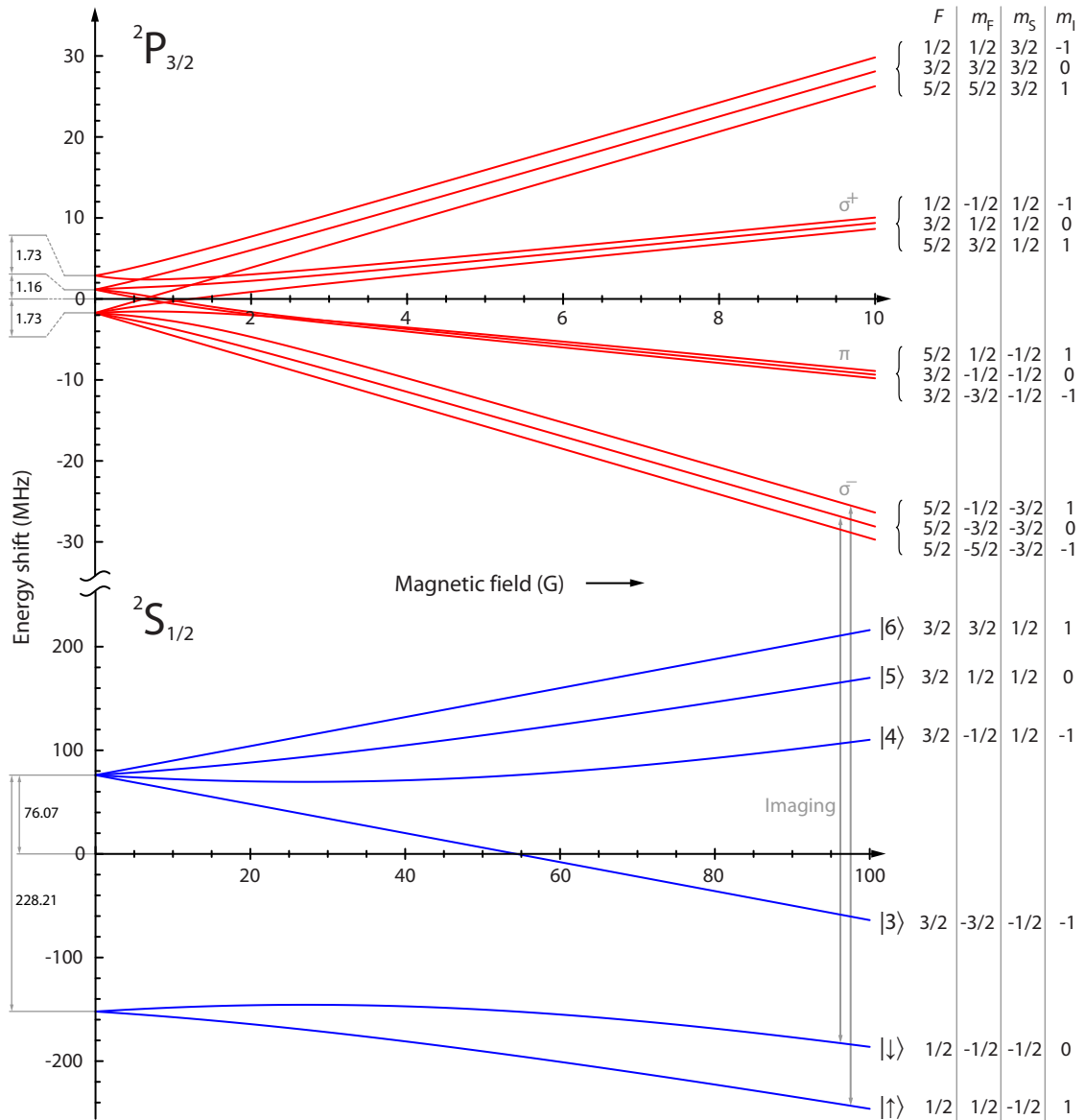


**Figure A.0.1.:** Electronic level structure of a  ${}^6\text{Li}$  atom in the ground  ${}^2S_{1/2}$  and excited  ${}^2P_{3/2}$  electronic states at low and moderate magnetic field ( $1\text{ G} = 10^{-4}\text{ T}$ ). Imaging as well as Bragg scattering use the  $\sigma^-$  optical transitions from the  $m_S = -1/2$  to the  $m_S = -3/2$  states.

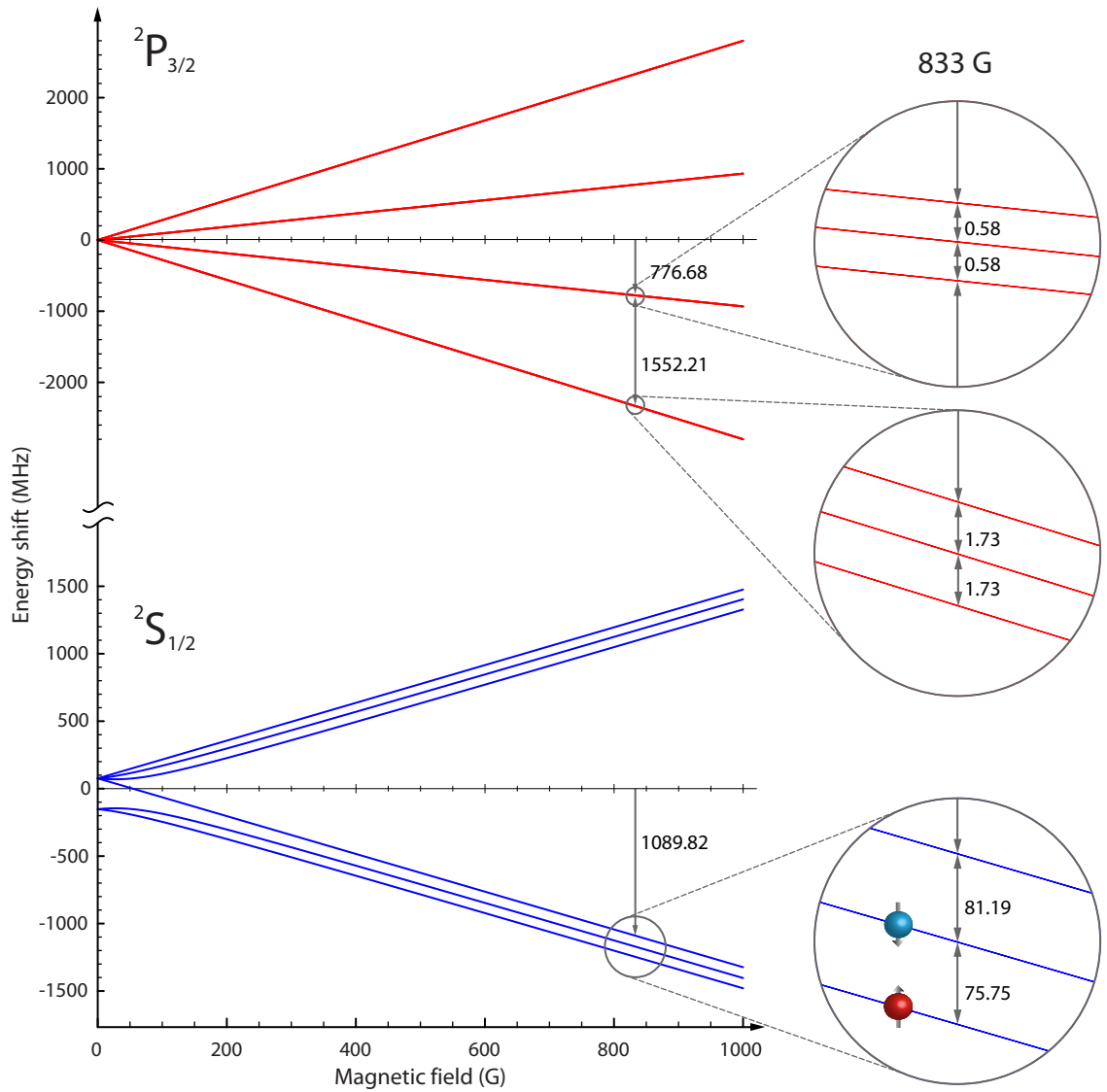


**Figure A.0.2.:** Electronic level structure of a  ${}^6\text{Li}$  atom at high magnetic field. Each branch of the ground and excited states forms a triplet. The energy shifts (MHz) relative to the zero axis as well as the level splittings (within the circles) were calculated at a magnetic field of 833 G near the Feshbach resonance (832.2 G) for  $|\uparrow\rangle$  and  $|\downarrow\rangle$ .



## B. Low-cost 4-channel digital direct synthesiser (DDS)

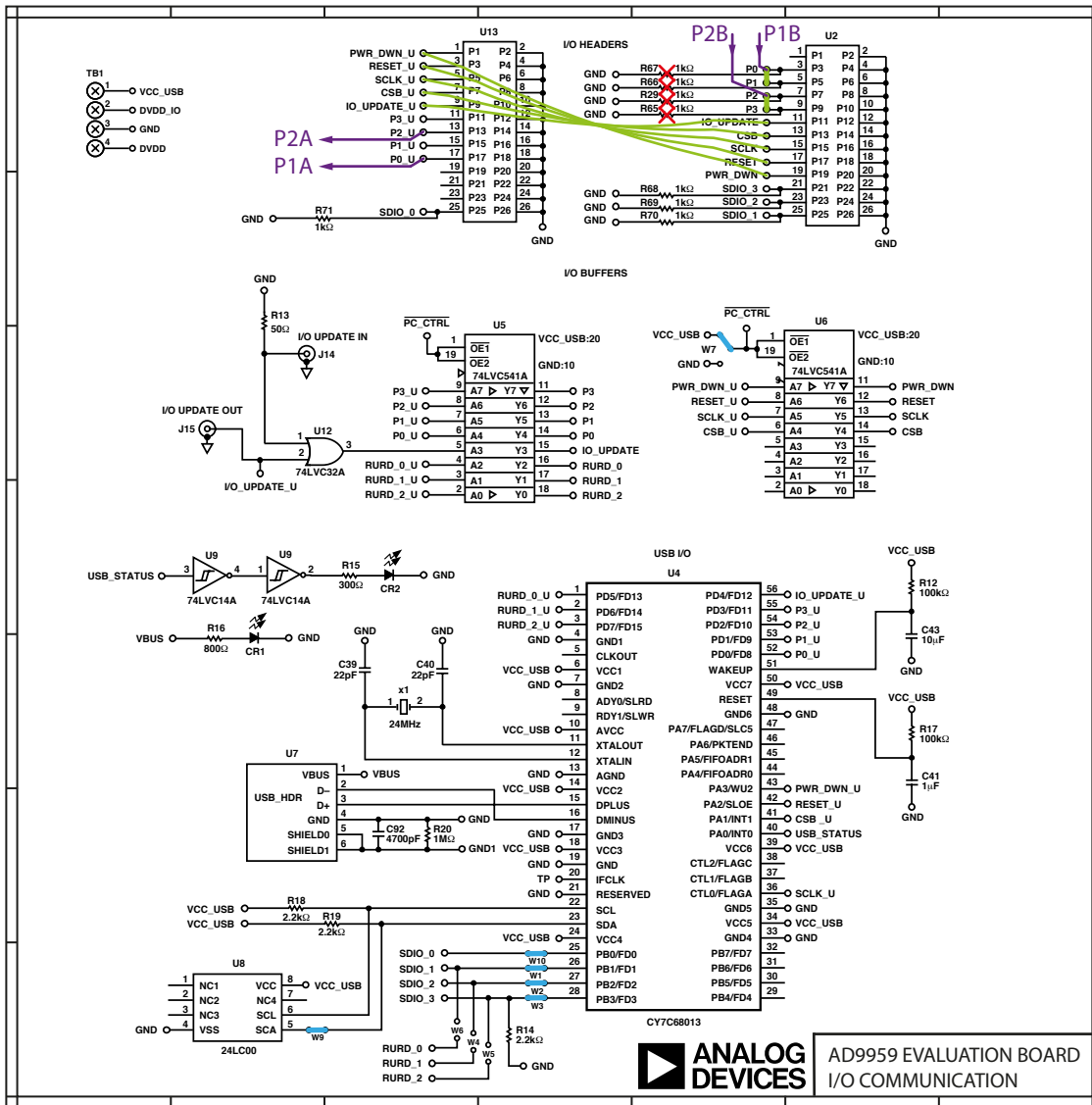
I will give a brief technical description of a simple but precise four-channel sine waveform generator that we use for controlling the RF amplitude and timing of the 88 MHz imaging AOM (cf. section 3.4.3 on page 70 ff.), and, for tuning the frequency difference  $\omega$  of the two Bragg lasers passing through two 80 MHz AOMs (cf. section 4.2.3 on page 89 ff.).

The generator consists of a commercially available plug-and-play evaluation printed circuit board (PCB) from Analog Devices featuring a 500 MHz four-channel AD9959 DDS chip accessible by an USB interface. Frequency, amplitude and phase of each channel can be independently controlled either by software (via USB interface) or hardware (via onboard header connectors). All channels share a common reference clock, therefore, they are inherently synchronised. Optionally, the RF output of the channels can be low-pass filtered. All RF connectors of the PCB are of SMA type. The frequency tuning resolution is 0.12 Hz, and the amplitude can be adjusted in 1024 steps (10 bit) from zero to maximum intensity. The RF output power of each channel at 80 MHz is typically  $-8$  dBm. The chip also features linear sweep capabilities of frequency, amplitude and phase which currently we do not use. An exhaustive description of the details of all features can be found in the datasheets for the AD9959.

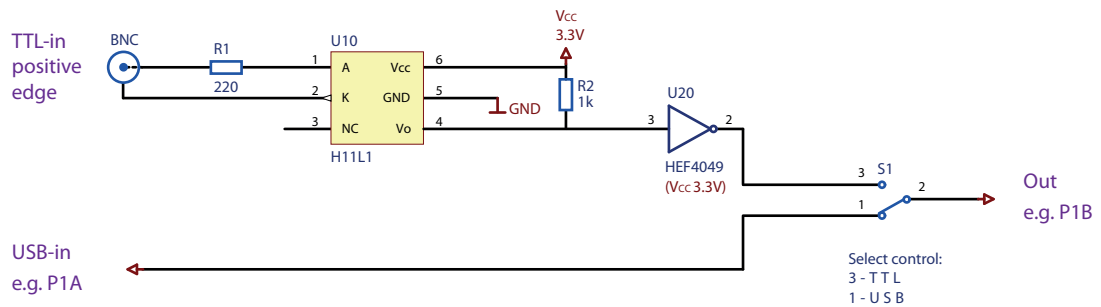
For our purposes, the DDS reference clock is generated by a standard external 30 MHz crystal oscillator (frequency stability  $\pm 20$  ppm). The frequency is internally multiplied by the DDS to set the system clock to 450 MHz. This suffices to run AOMs with a centre frequency of up to 200 MHz. For proper RF shielding, the PCB is placed into a die-cast aluminium box. The PCB electronics requires two voltage supplies, 1.8 and 3.3 V.

Figure B.0.1 shows the jumper configuration of the evaluation board and some additional minor modifications to make the DDS useful for our experiments. This enables either manual operation by mouse click via a software program or automatic operation through the experiment computer by simply flicking a switch. The jumper links W1-3,7,9,10, shown in blue, must be closed. Some pins of the headers connectors U2, U13

B. Low-cost 4-channel digital direct synthesiser (DDS)



**Figure B.0.1.:** Section of the circuit diagram of the AD9959 DDS evaluation board showing the required modifications to enable manual and automatic operation. Jumper links W1-3,7,9,10 are shown in blue, soldered wire links in green colour. The pull-down resistors R29, R65-67 are removed to enable soft- and hardware control via toggle switch. P1A and P1B refer to pin connections shown in figure B.0.2. The complete circuit diagram can be found in the datasheet of the AD9958/59 evaluation board from Analog Devices.



**Figure B.0.2.:** Circuit of the electrically isolated BNC input to protect the DDS chip from the outside world. The switch S1 selects between manual (USB) and automatic (TTL) triggering of the channels 0 and 1 (see text). P1A and P1B refer to pin connections shown in figure B.0.1.

are wire linked, as indicated in green. To be able to use a switch for soft- and hardware control, the pull-down resistors R29, R65-67 have to be removed. The channel outputs 0-3, not shown in the diagram, are triggered by the respective pins P0-3 on U2. Each of our applications, Bragg scattering and imaging, requires two concurrent channels, therefore P0 is wire linked to P1, and P2 is linked to P3 (green lines).

In a nutshell, controlling the DDS works as follows. For the board configuration described above, the DDS can be triggered either manually by software (USB) or by hardware (TTL), selectable through a switch (see figure B.0.2). The required signals to run the DDS are available at pins of the header connector U13. These pins, except the ones for triggering the channel outputs, are wire linked to U2 according to figure B.0.1.

To trigger channel 0 and 1 manually, the switch S1 in figure B.0.2 is set to USB, connecting pin P0\_U on U13 to P0 and P1 on U2, as shown in figure B.0.1. For hardware control, S1 is set to TTL, connecting the BNC input to P0 and P1 via the optical isolator U10. An identical circuit applies to switching channel 2 and 3, not shown here. Optical isolators are highly recommended to prevent the DDS chip from electrostatic discharge or faulty experiment electronics. In TTL mode, the positive edge of a 5 to 10 V electronic pulse is required. For convenience, an inverter U20 was inserted to switch the RF signal on when a trigger signal is applied. Note, the use of the optical insulator causes a fixed time delay of  $\sim 1 \mu\text{s}$  between the positive edge at the trigger input and the response at the RF output depending on the impedance of the device providing the trigger pulse. This may have to be taken into account when programming imaging sequences.

## B. Low-cost 4-channel digital direct synthesiser (DDS)

Channel 0 and 1 are used for driving the Bragg AOMs (cf. figure 4.2.4 on page 90). These two channels operate in “single-frequency mode”, that is, the amplitude of both channels is constant (the different operational modes of the DDS are explained in the datasheet of the evaluation board). In a Bragg experiment, we only tune the frequency of either channel 0 or 1 while leaving the frequency of the other unchanged. That means in practice, one channel frequency is set to 80 MHz while the other channel is tuned to  $[80 + \omega/(2\pi)]$  MHz, where  $\omega/(2\pi)$  typically ranges between zero and a few hundred kHz.

Channel 2 and 3 are used for generating RF pulses with two different amplitudes for driving the imaging AOM, selectable by an RF switch. In this case, the DDS operates in “amplitude mode”, that is, both channels are set to the same frequency of 88 MHz but differ in amplitude (cf. figure 3.4.4 on page 72 for a technical overview).

## References

- [Ada12] A. Adams, L. D. Carr, T. Schäfer, P. Steinberg, and J. E. Thomas, *Strongly correlated quantum fluids: Ultracold quantum gases, quantum chromodynamic plasmas and holographic duality*, New J. Phys. **14**, 115009 (2012).
- [Alf08] M. G. Alford, A. Schmitt, K. Rajagopal, and T. Schäfer, *Color superconductivity in dense quark matter*, Rev. Mod. Phys. **80**, 1455 (2008).
- [Ast13] G. E. Astrakharchik, J. Boronat, E. Krotscheck, and T. Lichtenegger, *Dynamic structure function of a cold Fermi gas at unitarity*, arXiv:1304.6831 (2013).
- [Bar57] J. Bardeen, L. N. Cooper, and J. R. Schrieffer, *Theory of superconductivity*, Phys. Rev. **108**, 1175 (1957).
- [Bar94] F. Bardou, B. Saubamea, J. Lawall, K. Shimizu, O. Émile, C. Westbrook, A. Aspect, and C. Cohen-Tannoudji, *Sub-recoil laser cooling with precooled atoms*, C. R. Acad. Sci. Paris **318**, 877 (1994).
- [Bar04] M. Bartenstein, A. Altmeyer, S. Riedl, S. Jochim, C. Chin, J. H. Denschlag, and R. Grimm, *Crossover from a molecular Bose-Einstein condensate to a degenerate Fermi gas*, Phys. Rev. Lett. **92**, 120401 (2004).
- [Bar05] M. Bartenstein, A. Altmeyer, S. Riedl, R. Geursen, S. Jochim, C. Chin, J. H. Denschlag, R. Grimm, A. Simoni, E. Tiesinga, C. J. Williams, and P. S. Julienne, *Precise determination of  $^6\text{Li}$  cold collision parameters by radio-frequency spectroscopy on weakly bound molecules*, Phys. Rev. Lett. **94**, 103201 (2005).
- [Bau09] D. M. Bauer, M. Lettner, G. R. Christoph Vo, and S. Dürr, *Control of a magnetic Feshbach resonance with laser light*, Nat. Phys. **5**, 339 (2009).
- [Ber87] T. Bergeman, G. Erez, and H. J. Metcalf, *Magnetostatic trapping fields for neutral atoms*, Phys. Rev. A **35**, 1535 (1987).
- [Bla02] P. B. Blakie, R. J. Ballagh, and C. W. Gardiner, *Theory of coherent Bragg spectroscopy of a trapped Bose-Einstein condensate*, Phys. Rev. A **65**, 033602 (2002).
- [Blo08] I. Bloch, J. Dalibard, and W. Zwerger, *Many-body physics with ultracold gases*, Rev. Mod. Phys. **80**, 885 (2008).

## REFERENCES

- [Blu12] D. Blume, *Few-body physics with ultracold atomic and molecular systems in traps*, Rep. Prog. Phys. **75**, 046401 (2012).
- [Boh58] A. Bohr, B. R. Mottelson, and D. Pines, *Possible analogy between the excitation spectra of nuclei and those of the superconducting metallic state*, Phys. Rev. **110**, 936 (1958).
- [Bou04] T. Bourdel, L. Khaykovich, J. Cubizolles, J. Zhang, F. Chevy, M. Teichmann, L. Tarruell, S. J. J. M. F. Kokkelmans, and C. Salomon, *Experimental study of the BEC-BCS crossover region in lithium 6*, Phys. Rev. Lett. **93**, 050401 (2004).
- [Bra08] E. Braaten, M. Kusunoki, and D. Zhang, *Scattering models for ultracold atoms*, Ann. Phys. (Amsterdam) **323**, 1770 (2008).
- [Bra09] E. Braaten, *How the tail wags the dog in ultracold atomic gases*, Physics **2**, 9 (2009).
- [Bra10] E. Braaten, D. Kang, and L. Platter, *Short-time operator product expansion for rf spectroscopy of a strongly interacting Fermi gas*, Phys. Rev. Lett. **104**, 223004 (2010).
- [Bra12] E. Braaten, *Universal relations for fermions with large scattering length*, in: W. Zwerger, ed., *The BEC-BCS crossover and the unitary Fermi gas*, Springer-Verlag, Berlin, 2012.
- [Bru01] A. Brunello, F. Dalfovo, L. Pitaevskii, S. Stringari, and F. Zambelli, *Momentum transferred to a trapped Bose-Einstein condensate by stimulated light scattering*, Phys. Rev. A **64**, 063614 (2001).
- [Bru04] G. M. Bruun, *Universality of a two-component Fermi gas with a resonant interaction*, Phys. Rev. A **70**, 053602 (2004).
- [Bru06] G. M. Bruun and G. Baym, *Bragg spectroscopy of cold atomic Fermi gases*, Phys. Rev. A **74**, 033623 (2006).
- [Büc04] H. P. Büchler, P. Zoller, and W. Zwerger, *Spectroscopy of superfluid pairing in atomic Fermi gases*, Phys. Rev. Lett. **93**, 080401 (2004).
- [But97] D. A. Butts and D. S. Rokhsar, *Trapped Fermi gases*, Phys. Rev. A **55**, 4346 (1997).
- [Cao11] C. Cao, E. Elliott, J. Joseph, H. Wu, J. Petricka, T. Schäfer, and J. E. Thomas, *Universal Quantum Viscosity in a Unitary Fermi Gas*, Science **331**, 58 (2011).
- [Car03] J. Carlson, S.-Y. Chang, V. R. Pandharipande, and K. E. Schmidt, *Superfluid Fermi gases with large scattering length*, Phys. Rev. Lett. **91**, 050401 (2003).

- [Car06] I. Carusotto, *Bragg scattering and the spin structure factor of two-component atomic gases*, J. Phys. B **39**, S211 (2006).
- [Cas07] Y. Castin, *Basic theory tools for degenerate Fermi gases*, in: M. Inguscio, W. Ketterle, and C. Salomon, eds., *Ultracold Fermi gases: Proceedings of the international school of physics (Enrico Fermi)*, IOS Press, 2007.
- [Che05] Q. Chen, J. Stajic, S. Tan, and K. Levin, *BCS-BEC crossover: From high temperature superconductors to ultracold superfluids*, Phys. Rep. **412**, 1 (2005).
- [Chi04] C. Chin, M. Bartenstein, A. Altmeyer, S. Riedl, S. Jochim, J. H. Denschlag, and R. Grimm, *Observation of the pairing gap in a strongly interacting Fermi gas*, Science **305**, 1128 (2004).
- [Chi10] C. Chin, R. Grimm, P. Julienne, and E. Tiesinga, *Feshbach resonances in ultracold gases*, Rev. Mod. Phys. **82**, 1225 (2010).
- [Chu86] S. Chu, J. E. Bjorkholm, A. Ashkin, and A. Cable, *Experimental observation of optically trapped atoms*, Phys. Rev. Lett. **57**, 314 (1986).
- [Com06a] R. Combescot, S. Giorgini, and S. Stringari, *Molecular signatures in the structure factor of an interacting Fermi gas*, Europhys. Lett. **75**, 695 (2006).
- [Com06b] R. Combescot, M. Y. Kagan, and S. Stringari, *Collective mode of homogeneous superfluid Fermi gases in the BEC-BCS crossover*, Phys. Rev. A **74**, 042717 (2006).
- [Coo56] L. N. Cooper, *Bound electron pairs in a degenerate Fermi gas*, Phys. Rev. **104**, 1189 (1956).
- [Cou98] P. Courteille, R. S. Freeland, D. J. Heinzen, F. A. van Abeelen, and B. J. Verhaar, *Observation of a Feshbach resonance in cold atom scattering*, Phys. Rev. Lett. **81**, 69 (1998).
- [CT72] C. Cohen-Tannoudji and J. Dupont-Roc, *Experimental study of Zeeman light shifts in weak magnetic fields*, Phys. Rev. A **5**, 968 (1972).
- [CT98] C. Cohen-Tannoudji, J. Dupont-Roc, and G. Grynberg, *Atom-Photon Interactions*, Wiley, New York, 1998.
- [DeM99] B. DeMarco and D. S. Jin, *Onset of Fermi degeneracy in a trapped atomic gas*, Science **285** (1999).
- [DeM01] B. DeMarco, S. B. Papp, and D. S. Jin, *Pauli Blocking of Collisions in a Quantum Degenerate Atomic Fermi Gas*, Phys. Rev. Lett. **86**, 5409 (2001).
- [Dri02] V. Dribinski, A. Ossadtchi, V. A. Mandelshtam, and H. Reisler, *Reconstruction of Abel-transformable images: The Gaussian basis-set expansion Abel transform*

## REFERENCES

- method*, Rev. Sci. Instrum. **73**, 2634 (2002).
- [Dru11] J. E. Drut, T. A. Lähde, and T. Ten, *Momentum distribution and contact of the unitary Fermi gas*, Phys. Rev. Lett. **106**, 205302 (2011).
- [Du08] X. Du, L. Luo, B. Clancy, and J. E. Thomas, *Observation of anomalous spin segregation in a trapped Fermi gas*, Phys. Rev. Lett. **101**, 150401 (2008).
- [Dua11] P. M. Duarte, R. A. Hart, J. M. Hitchcock, T. A. Corcovilos, T.-L. Yang, A. Reed, and R. G. Hulet, *All-optical production of a lithium quantum gas using narrow-line laser cooling*, Phys. Rev. A **84**, 061406 (2011).
- [Dui04] R. A. Duine and H. T. C. Stoof, *Atom-molecule coherence in Bose gases*, Phys. Rep. **396**, 115 (2004).
- [Dyk10] P. Dyke, *Quasi two-dimensional  $^6\text{Li}$  Fermi gas*, Ph.D. thesis, Swinburne University of Technology (2010).
- [Eag69] D. M. Eagles, *Possible pairing without superconductivity at low carrier concentrations in bulk and thin-film superconducting semiconductors*, Phys. Rev. **186**, 456 (1969).
- [Ell14] E. Elliott, J. A. Joseph, and J. E. Thomas, *Observation of conformal symmetry breaking and scale invariance in expanding Fermi gases*, Phys. Rev. Lett. **112**, 040405 (2014).
- [Eng97] J. R. Engelbrecht, M. Randeria, and C. A. R. Sáde Melo, *BCS to Bose crossover: Broken-symmetry state*, Phys. Rev. B **55**, 15153 (1997).
- [Ens11] T. Enss, R. Haussmann, and W. Zwerger, *Viscosity and scale invariance in the unitary Fermi gas*, Ann. Phys. (Amsterdam) **326**, 770 (2011).
- [Est08] J. Estève, C. Gross, A. Weller, S. Giovanazzi, and M. K. Oberthaler, *Squeezing and entanglement in a Bose-Einstein condensate*, Nature (London) **455**, 1216 (2008).
- [Fan61] U. Fano, *Effects of configuration interaction on intensities and phase shifts*, Phys. Rev. **124**, 1866 (1961).
- [Fer08] F. Ferlaino, S. Knoop, and R. Grimm, *Ultracold Feshbach molecules*, arXiv:0809.3920 (2008).
- [Fer12] D. R. Fernandes, F. Sieversand, N. Kretzschmar, S. Wu, C. Salomom, and F. Chevy, *Sub-Doppler laser cooling of fermionic  $^40\text{K}$  atoms in three-dimensional gray optical molasses*, Europhys. Lett. **100**, 63001 (2012).
- [Fes62] H. Feshbach, *A unified theory of nuclear reactions. II*, Ann. Phys. (Amsterdam) **19**, 287 (1962).

- [Fri98] S. Friebel, C. D'Andrea, J. Walz, M. Weitz, and T. W. Hänsch, *CO<sub>2</sub>-laser optical lattice with cold rubidium atoms*, Phys. Rev. A **57**, R20 (1998).
- [Fu13] Z. Fu, P. Wang, L. Huang, Z. Meng, H. Hu, and J. Zhang, *Optical control of a magnetic Feshbach resonance in an ultracold Fermi gas*, Phys. Rev. A **88**, 041601 (2013).
- [Fuc09] J. Fuchs, *Molecular Bose-Einstein condensates and p-wave Feshbach molecules of <sup>6</sup>Li<sub>2</sub>*, Ph.D. thesis, Swinburne University of Technology (2009).
- [Fuk07] N. Fukushima, Y. Ohashi, E. Taylor, and A. Griffin, *Superfluid density and condensate fraction in the BCS-BEC crossover regime at finite temperatures*, Phys. Rev. A **75**, 033609 (2007).
- [Gan11] S. Gandolfi, K. E. Schmidt, and J. Carlson, *BEC-BCS crossover and universal relations in unitary Fermi gases*, Phys. Rev. A **83**, 041601 (2011).
- [Geh03] M. E. Gehm, *Preparation of an optically-trapped degenerate Fermi gas of <sup>6</sup>Li: Finding the route to degeneracy*, Ph.D. thesis, Duke University (2003).
- [Gio08] S. Giorgini, L. P. Pitaevskii, and S. Stringari, *Theory of ultracold atomic Fermi gases*, Rev. Mod. Phys. **80**, 1215 (2008).
- [Gly92] H. R. Glyde, *Density and quasiparticle excitations in liquid <sup>4</sup>He*, Phys. Rev. B **45**, 7321 (1992).
- [Gou10] O. Goulko and M. Wingate, *Thermodynamics of balanced and slightly spin-imbalanced Fermi gases at unitarity*, Phys. Rev. A **82**, 053621 (2010).
- [Gra02] S. R. Granade, M. E. Gehm, K. M. O'Hara, and J. E. Thomas, *All-Optical production of a degenerate Fermi gas*, Phys. Rev. Lett. **88**, 120405 (2002).
- [Gre03] M. Greiner, C. A. Regal, and D. S. Jin, *Emergence of a molecular Bose-Einstein condensate from a Fermi gas*, Nature **426**, 537 (2003).
- [Gri93] A. Griffin, *Excitations in a Bose condensed liquid*, Cambridge University Press, 1993.
- [Gri00] R. Grimm, M. Weidemüller, and Y. Ovchinnikov, *Optical dipole traps for neutral atoms*, arXiv:9902072, Adv. At. Mol. Opt. Phys. **42**, 95 (2000).
- [Gri13] A. T. Grier, I. Ferrier-Barbut, B. S. Rem, M. Delehaye, L. Khaykovich, F. Chevy, and C. Salomon,  *$\Lambda$ -enhanced sub-Doppler cooling of lithium atoms in D<sub>1</sub> gray molasses*, Phys. Rev. A **87**, 063411 (2013).
- [Gua13] E. R. S. Guajardo, M. K. Tey, L. A. Sidorenkov, and R. Grimm, *Higher-nodal collective modes in a resonantly interacting Fermi gas*, Phys. Rev. A **87**, 063601 (2013).

## REFERENCES

- [Guo10] H. Guo, C.-C. Chien, and K. Levin, *Establishing the presence of coherence in atomic Fermi superfluids: Spin-flip and spin-preserving Bragg scattering at finite temperatures*, Phys. Rev. Lett. **105**, 120401 (2010).
- [Gur07] V. Gurarie and L. Radzihovsky, *Resonantly paired fermionic superfluids*, Ann. Phys. (Amsterdam) **322**, 2 (2007).
- [Had02] Z. Hadzibabic, C. A. Stan, K. Dieckmann, S. Gupta, M. W. Zwierlein, A. Görlitz, and W. Ketterle, *Two-species mixture of quantum degenerate Bose and Fermi gases*, Phys. Rev. Lett. **88**, 160401 (2002).
- [Han86] J. P. Hansen and I. R. McDonald, *Theory of simple liquids*, Academic Press, 1986, 2. edn.
- [Han09] T. M. Hanna, H. Martay, and T. Köhler, *Theory of ultracold Feshbach molecules*, in: R. Krems, B. Friedrich, and W. C. Stwalley, eds., *Cold molecules: Theory, experiment, applications*, Taylor & Francis, 2009.
- [Hau99] R. Haussmann, *Self-consistent quantum-field theory and bosonization for strongly correlated electron systems*, Springer-Verlag, Berlin, 1999.
- [Hau07] R. Haussmann, W. Rantner, S. Cerrito, and W. Zwerger, *Thermodynamics of the BCS-BEC crossover*, Phys. Rev. A **75**, 023610 (2007).
- [Hau09] R. Haussmann, M. Punk, and W. Zwerger, *Spectral functions and rf response of ultracold fermionic atoms*, Phys. Rev. A **80**, 063612 (2009).
- [Hei01] H. Heiselberg, *Fermi systems with long scattering lengths*, Phys. Rev. A **63**, 043606 (2001).
- [Ho04] T.-L. Ho, *Universal thermodynamics of degenerate quantum gases in the unitarity limit*, Phys. Rev. Lett. **92**, 090402 (2004).
- [Ho10] T.-L. Ho and Q. Zhou, *Obtaining the phase diagram and thermodynamic quantities of bulk systems from the densities of trapped gases*, Nat. Phys. **6**, 131 (2010).
- [Hoi12] S. Hoinka, M. Lingham, M. Delehaye, and C. J. Vale, *Dynamic spin response of a strongly interacting Fermi gas*, Phys. Rev. Lett. **109**, 050403 (2012).
- [Hoi13] S. Hoinka, M. Lingham, K. Fenech, H. Hu, C. J. Vale, J. E. Drut, and S. Gandolfi, *Precise determination of the structure factor and contact in a unitary Fermi gas*, Phys. Rev. Lett. **110**, 055305 (2013).
- [Hou98] M. Houbiers, H. T. C. Stoof, W. I. McAlexander, and R. G. Hulet, *Elastic and inelastic collisions of  $^6\text{Li}$  atoms in magnetic and optical traps*, Phys. Rev. A **57**, R1497 (1998).

- [Hu07] H. Hu, P. D. Drummond, and X.-J. Liu, *Universal thermodynamics of strongly interacting Fermi gases*, Nature Phys. **3**, 469 (2007).
- [Hu10a] H. Hu, X.-J. Liu, and P. D. Drummond, *Dynamic response of strongly correlated Fermi gases in the quantum virial expansion*, Phys. Rev. A **81**, 033630 (2010).
- [Hu10b] H. Hu, X.-J. Liu, and P. D. Drummond, *Static structure factor of a strongly correlated Fermi gas at large momenta*, Europhys. Lett. **91**, 20005 (2010).
- [Hu11] H. Hu, X.-J. Liu, and P. D. Drummond, *Universal contact of strongly interacting fermions at finite temperatures*, New J. Phys. **13**, 035007 (2011).
- [Hu12a] H. Hu, *Many-body theories of density response for a strongly correlated Fermi gas*, Front. Phys. **7**, 98 (2012).
- [Hu12b] H. Hu and X.-J. Liu, *Universal dynamic structure factor of a strongly correlated Fermi gas*, Phys. Rev. A **85**, 023612 (2012).
- [Hu13] H. Hu, *Private communication* (2013).
- [Ing99] M. Inguscio, S. Stringari, and C. E. Wieman, eds., *Bose-Einstein condensation in atomic gases: Proceedings of the international school of physics (Enrico Fermi)*, IOS Press, 1999.
- [Ing07] M. Inguscio, W. Ketterle, and C. Salomon, eds., *Ultracold Fermi gases: Proceedings of the international school of physics (Enrico Fermi)*, IOS Press, 2007.
- [Ino98] S. Inouye, M. R. Andrews, J. Stenger, H.-J. Miesner, D. M. Stamper-Kurn, and W. Ketterle, *Observation of Feshbach resonances in a Bose-Einstein condensate*, Nature **392**, 151 (1998).
- [Joc03a] S. Jochim, M. Bartenstein, A. Altmeyer, G. Hendl, C. Chin, J. H. Denschlag, and R. Grimm, *Pure gas of optically trapped molecules created from fermionic atoms*, Phys. Rev. Lett. **91**, 240402 (2003).
- [Joc03b] S. Jochim, M. Bartenstein, A. Altmeyer, G. Hendl, S. Riedl, C. Chin, J. Hecker Denschlag, and R. Grimm, *Bose-Einstein condensation of molecules*, Science **302**, 2101–2103 (2003).
- [Jof93] M. A. Joffe, W. Ketterle, A. Martin, and D. E. Pritchard, *Transverse cooling and deflection of an atomic beam inside a Zeeman slower*, J. Opt. Soc. Am. B **10**, 2257 (1993).
- [Kap38] P. Kapitza, *Viscosity of liquid Helium below the  $\lambda$ -point*, Nature **141**, 74 (1938).
- [Kel68] L. V. Keldysh and A. N. Kozlov, *Collective properties of excitons in semiconductors*, Sov. Phys. JETP **27**, 521 (1968).
- [Ket99] W. Ketterle, D. S. Durfee, and D. M. Stamper-Kurn, *Making, probing and*

## REFERENCES

- understanding Bose-Einstein condensates*, in: M. Inguscio, S. Stringari, and C. E. Wieman, eds., *Bose-Einstein condensation in atomic gases: Proceedings of the international school of physics (Enrico Fermi)*, IOS Press, 1999.
- [Ket07] W. Ketterle and M. W. Zwierlein, *Making, probing and understanding ultracold Fermi gases*, in: M. Inguscio, W. Ketterle, and C. Salomon, eds., *Ultracold Fermi gases: Proceedings of the international school of physics (Enrico Fermi)*, IOS Press, 2007.
- [Kin04] J. Kinast, S. L. Hemmer, M. E. Gehm, A. Turlapov, and J. E. Thomas, *Evidence for superfluidity in a resonantly interacting Fermi gas*, *Phys. Rev. Lett.* **92**, 150402 (2004).
- [Kin06] J. M. Kinast, *Thermodynamics and superfluidity of a strongly interacting Fermi gas*, Ph.D. thesis, Duke University (2006).
- [Köh06] T. Köhler, K. Góral, and P. S. Julienne, *Production of cold molecules via magnetically tunable Feshbach resonances*, *Rev. Mod. Phys.* **78**, 1311 (2006).
- [Koz99] M. Kozuma, L. Deng, E. W. Hagley, J. Wen, R. Lutwak, K. Helmerson, S. L. Rolston, and W. D. Phillips, *Coherent splitting of Bose-Einstein condensed atoms with optically induced Bragg diffraction*, *Phys. Rev. Lett.* **82**, 871 (1999).
- [Kre09] R. Krems, B. Friedrich, and W. C. Stwalley, eds., *Cold molecules: Theory, experiment, applications*, Taylor & Francis, 2009.
- [Ku12] M. J. H. Ku, A. T. Sommer, L. W. Cheuk, and M. W. Zwierlein, *Revealing the superfluid lambda transition in the universal thermodynamics of a unitary Fermi gas*, *Science* **335**, 563 (2012).
- [Kuh10] E. D. Kuhnle, H. Hu, X.-J. Liu, P. Dyke, M. Mark, P. D. Drummond, P. Hannaford, and C. J. Vale, *Universal behavior of pair correlations in a strongly interacting Fermi gas*, *Phys. Rev. Lett.* **105**, 070402 (2010).
- [Kuh11a] E. D. Kuhnle, *Studies of universality in strongly interacting  ${}^6\text{Li}$  Fermi gases with Bragg spectroscopy*, Ph.D. thesis, Swinburne University of Technology (2011).
- [Kuh11b] E. D. Kuhnle, S. Hoinka, P. Dyke, H. Hu, P. Hannaford, and C. J. Vale, *Temperature dependence of the universal contact parameter in a unitary Fermi gas*, *Phys. Rev. Lett.* **106**, 170402 (2011).
- [Kuh11c] E. D. Kuhnle, S. Hoinka, H. Hu, P. Dyke, P. Hannaford, and C. J. Vale, *Studies of the universal contact in a strongly interacting Fermi gas using Bragg spectroscopy*, *New J. Phys* **13**, 055010 (2011).

- [Lan76] L. D. Landau and E. M. Lifshitz, *Mechanics*, vol. 1, Butterworth-Heinemann, 1976.
- [Lee57] T. D. Lee, K. Huang, and C. N. Yang, *Eigenvalues and eigenfunctions of a Bose system of hard spheres and its low-temperature properties*, Phys. Rev. **106**, 1135 (1957).
- [Leg80] A. J. Leggett, *Diatomic molecules and Cooper pairs*, in: A. Pekalski, J. Przys-tawa, eds., Modern trends in the theory of condensed matter, Springer, Berlin, 1980.
- [Leg06] A. J. Leggett, *Quantum liquids - Bose condensation and Cooper pairing in condensed-matter systems*, Oxford University Press, 2006.
- [Let88] P. D. Lett, R. N. Watts, C. I. Westbrook, W. D. Phillips, P. L. Gould, and H. J. Metcalf, *Observation of atoms laser cooled below the Doppler limit*, Phys. Rev. Lett. **61**, 169 (1988).
- [Lev12] K. Levin, A. L. Fetter, and D. M. Stamper-Kurn, eds., *Ultracold bosonic and fermionic gases (series: Contemporary concepts of condensed matter science)*, vol. 5, Elsevier, 2012.
- [Lew07] M. Lewenstein, A. Sanpera, V. Ahufinger, B. Damski, A. Sen(De), and U. Sen, *Ultracold atomic gases in optical lattices: Mimicking condensed matter physics and beyond*, Adv. Phys. **56**, 243 (2007).
- [Li11] Y. Li and S. Stringari, *Universal contact and collective excitations of a strongly interacting Fermi gas*, Phys. Rev. A **84**, 023628 (2011).
- [Lin14] M. G. Lingham, K. Fenech, S. Hoinka, and C. J. Vale, *Local observation of pair condensation in a Fermi gas at unitarity*, Phys. Rev. Lett. **112**, 100404 (2014).
- [Liu09] X.-J. Liu, H. Hu, and P. D. Drummond, *Virial expansion for a strongly correlated Fermi gas*, Phys. Rev. Lett. **102**, 160401 (2009).
- [Lon38] F. London, *The  $\lambda$ -phenomenon of liquid Helium and the Bose-Einstein degeneracy*, Nature **141**, 643 (1938).
- [Mag11] P. Magierski, G. Wlazłowski, and A. Bulgac, *Onset of a pseudogap regime in ultracold Fermi gases*, Phys. Rev. Lett. **107**, 145304 (2011).
- [Mak14] P. Makotyn, C. E. Klauss, D. L. Goldberger, E. A. Cornell, and D. S. Jin, *Universal dynamics of a degenerate unitary Bose gas*, Nat Phys **19**, 116 (2014).
- [Mar88] P. J. Martin, B. G. Oldaker, A. H. Miklich, and D. E. Pritchard, *Bragg scattering of atoms from a standing light wave*, Phys. Rev. Lett. **60**, 515 (1988).
- [Met99] H. J. Metcalf and P. van der Straten, *Laser cooling and trapping*, Springer-

## REFERENCES

- Verlag, New York, 1999.
- [Mig59] A. B. Migdal, *Superfluidity and the moments of inertia of nuclei*, Nucl. Phys. **13**, 655 (1959).
- [Min01] A. Minguzzi, G. Ferrari, and Y. Castin, *Dynamic structure factor of a superfluid Fermi gas*, Eur. Phys. J. D **17**, 49 (2001).
- [Moe95] A. J. Moerdijk, B. J. Verhaar, and A. Axelsson, *Resonances in ultracold collisions of  $^6\text{Li}$ ,  $^7\text{Li}$ , and  $^{23}\text{Na}$* , Phys. Rev. A **51**, 4852 (1995).
- [Mor06] O. Morsch and M. Oberthaler, *Dynamics of Bose-Einstein condensates in optical lattices*, Rev. Mod. Phys. **78**, 179 (2006).
- [Nas10] S. Nascimbène, N. Navon, K. J. Jiang, F. Chevy, and C. Salomon, *Exploring the thermodynamics of a universal Fermi gas*, Nature (London) **463**, 1057 (2010).
- [Nav10] N. Navon, S. Nascimbène, F. Chevy, and C. Salomon, *The equation of state of a low-temperature Fermi gas with tunable interactions*, Science **328**, 729 (2010).
- [Nis12] Y. Nishida, *Probing strongly interacting atomic gases with energetic atoms*, Phys. Rev. A **85**, 053643 (2012).
- [Noz85] P. Nozières and S. Schmitt-Rink, *Bose condensation in an attractive fermion gas: From weak to strong coupling superconductivity*, J. Low Temp. Phys. **59**, 195 (1985).
- [O'H02] K. M. O'Hara, S. L. Hemmer, M. E. Gehm, S. R. Granade, and J. E. Thomas, *Observation of a strongly interacting degenerate Fermi gas of atoms*, Science **298**, 2179 (2002).
- [Oha03a] Y. Ohashi and A. Griffin, *Superfluid transition temperature in a trapped gas of Fermi atoms with a Feshbach resonance*, Phys. Rev. A **67**, 033603 (2003).
- [Oha03b] Y. Ohashi and A. Griffin, *Superfluidity and collective modes in a uniform gas of Fermi atoms with a Feshbach resonance*, Phys. Rev. A **67**, 063612 (2003).
- [Oze05] R. Ozeri, N. Katz, J. Steinhauer, and N. Davidson, *Bulk Bogoliubov excitations in a Bose-Einstein condensate*, Rev. Mod. Phys. **77**, 187 (2005).
- [Pal10] F. Palestini, A. Perali, P. Pieri, and G. C. Strinati, *Temperature and coupling dependence of the universal contact intensity for an ultracold Fermi gas*, Phys. Rev. A **82**, 021605 (2010).
- [Par05] G. B. Partridge, K. E. Strecker, R. I. Kamar, M. W. Jack, and R. G. Hulet, *Molecular probe of pairing in the BEC-BCS crossover*, Phys. Rev. Lett. **95**, 020404 (2005).
- [Pet03] D. S. Petrov, *Three-body problem in Fermi gases with short-range interparticle*

- interaction*, Phys. Rev. A **67**, 010703 (2003).
- [Pet04] D. S. Petrov, C. Salomon, and G. V. Shlyapnikov, *Weakly bound dimers of fermionic atoms*, Phys. Rev. Lett. **93**, 090404 (2004).
- [Pet08] C. J. Pethick and H. Smith, *Bose-Einstein condensation in dilute gases*, Cambridge University Press, 2008, 2. edn.
- [Pet13] D. S. Petrov, *The few-atom problem*, vol. 94, in: C. Salomon, and G. Schlyapnikov, and L. V. Cugliandolo, eds., Many-body physics with ultracold gases: Lecture notes of the Les Houches summer school, Oxford University Press, 2013.
- [Phi82] W. D. Phillips and H. Metcalf, *Laser deceleration of an atomic beam*, Phys. Rev. Lett. **48**, 596 (1982).
- [Pin66] D. Pines and P. Nozières, *The theory of quantum liquids*, vol. Vol. I, Benjamin, New York, 1966.
- [Pit03] L. Pitaevskii and S. Stringari, *Bose-Einstein condensation*, Clarendon Press, Oxford, 2003.
- [Pla10] N. Plakida, *High-temperature cuprate superconductors: Experiment, theory and applications*, vol. 166, Springer-Verlag, Berlin, 2010.
- [Pre96] D. W. Preston, *Doppler-free saturated absorption: Laser spectroscopy*, Am. J. Phys. **64**, 1432 (1996).
- [Pri04] L. Pricoupenko and Y. Castin, *One particle in a box: The simplest model for a Fermi gas in the unitary limit*, Phys. Rev. A **69**, 051601 (2004).
- [Ran92] M. Randeria, N. Trivedi, A. Moreo, and R. T. Scalettar, *Pairing and spin gap in the normal state of short coherence length superconductors*, Phys. Rev. Lett. **69**, 2001 (1992).
- [Ran96] M. Randeria, *Crossover from BCS theory to Bose-Einstein condensation*, A. Griffin, and D. W. Snoke, and S. Stringari, eds., Bose-Einstein condensation, Cambridge University Press, 1996.
- [Ran14] M. Randeria and E. Taylor, *Crossover from Bardeen-Cooper-Schrieffer to Bose-Einstein condensation and the unitary Fermi gas*, Annu. Rev. Condens. Matter Phys. **5**, 209 (2014).
- [Reg04] C. A. Regal, M. Greiner, and D. S. Jin, *Observation of resonance condensation of fermionic atom pairs*, Phys. Rev. Lett. **92**, 040403 (2004).
- [Rei07] G. Reinaudi, T. Lahaye, Z. Wang, and D. Guéry-Odelin, *Strong saturation absorption imaging of dense clouds of ultracold atoms*, Opt. Lett. **32** (2007).

## REFERENCES

- [Rod02] M. Rodriguez and P. Törmä, *Laser-induced collective excitations in a two-component Fermi gas*, Phys. Rev. A **66**, 033601 (2002).
- [Sag12] Y. Sagi, T. E. Drake, R. Paudel, and D. S. Jin, *Measurement of the homogeneous contact of a unitary Fermi gas*, Phys. Rev. Lett. **109**, 220402 (2012).
- [Sak94] J. J. Sakurai, *Modern quantum mechanics*, Addison-Wesley, 1994.
- [Sal05] L. Salasnich, N. Manini, and A. Parola, *Condensate fraction of a Fermi gas in the BCS-BEC crossover*, Phys. Rev. A **72**, 023621 (2005).
- [Sal13] C. Salomon, G. Schlyapnikov, and L. V. Cugliandolo, eds., *Many-body physics with ultracold gases: Lecture notes of the Les Houches summer school*, vol. 94, Oxford University Press, 2013.
- [San10] C. Sanner, E. J. Su, A. Keshet, R. Gommers, Y.-i. Shin, W. Huang, and W. Ketterle, *Suppression of density fluctuations in a quantum degenerate Fermi gas*, Phys. Rev. Lett. **105**, 040402 (2010).
- [San11] C. J. Sansonetti, C. E. Simien, J. D. Gillaspay, J. N. Tan, S. M. Brewer, R. C. Brown, S. Wu, and J. V. Porto, *Absolute transition frequencies and quantum interference in a frequency comb based measurement of the  $^{6,7}\text{Li}$  D-lines*, Phys. Rev. Lett. **107**, 023001 (2011).
- [Sch99] U. Schünemann, H. Engler, R. Grimm, M. Weidemüller, and M. Zielonkowski, *Simple scheme for tunable frequency offset locking of two lasers*, Rev. Sci. Instrum. **70**, 242 (1999).
- [Sch00] D. V. Schroeder, *An introduction to thermal physics*, Addison-Wesley, 2000.
- [Sch01] F. Schreck, L. Khaykovich, K. L. Corwin, G. Ferrari, T. Bourdel, J. Cubizolles, and C. Salomon, *Quasipure Bose-Einstein condensate immersed in a Fermi sea*, Phys. Rev. Lett. **87**, 080403 (2001).
- [Sch08a] A. Schirotzek, Y.-i. Shin, C. H. Schunck, and W. Ketterle, *Determination of the superfluid gap in atomic Fermi gases by quasiparticle spectroscopy*, Phys. Rev. Lett. **101**, 140403 (2008).
- [Sch08b] F. Schwabl, *Advanced quantum mechanics*, Springer-Verlag, Berlin, 2008.
- [Sch09] T. Schäfer and D. Teaney, *Nearly perfect fluidity: From cold atomic gases to hot quark gluon plasmas*, Rep. Prog. Phys. **72**, 126001 (2009).
- [SdM08] C. A. R. Sá de Melo, *When fermions become bosons: Pairing in ultracold gases*, Physics Today **61**, 45 (2008).
- [Shi07] Y. Shin, C. H. Schunck, A. Schirotzek, and W. Ketterle, *Tomographic rf spectroscopy of a trapped Fermi gas at unitarity*, Phys. Rev. Lett. **99**, 090403 (2007).

- [Sim05] S. Simonucci, P. Pieri, and G. C. Strinati, *Broad vs. narrow Fano-Feshbach resonances in the BCS-BEC crossover with trapped Fermi atoms*, Europhys. Lett. **69**, 713 (2005).
- [SK99] D. M. Stamper-Kurn, A. P. Chikkatur, A. Görlitz, S. Inouye, S. Gupta, D. E. Pritchard, and W. Ketterle, *Excitation of phonons in a Bose-Einstein condensate by light scattering*, Phys. Rev. Lett. **83**, 2876 (1999).
- [Son10] D. T. Son and E. G. Thompson, *Short-distance and short-time structure of a unitary Fermi gas*, Phys. Rev. A **81**, 063634 (2010).
- [Ste99] J. Stenger, S. Inouye, A. P. Chikkatur, D. M. Stamper-Kurn, D. E. Pritchard, and W. Ketterle, *Bragg spectroscopy of a Bose-Einstein condensate*, Phys. Rev. Lett. **82**, 4569 (1999).
- [Ste08] J. P. G. Stewart, J. T. and D. S. Jin, *Using photoemission spectroscopy to probe a strongly interacting Fermi gas*, Nature **454**, 744 (2008).
- [Ste10] J. T. Stewart, J. P. Gaebler, T. E. Drake, and D. S. Jin, *Verification of universal relations in a strongly interacting Fermi gas*, Phys. Rev. Lett. **104**, 235301 (2010).
- [Str03] K. E. Strecker, G. B. Partridge, and R. G. Hulet, *Conversion of an atomic Fermi gas to a long-lived molecular Bose gas*, Phys. Rev. Lett. **91**, 080406 (2003).
- [Str09] S. Stringari, *Density and spin response function of a normal Fermi gas at unitarity*, Phys. Rev. Lett. **102**, 110406 (2009).
- [Suo96] K.-A. Suominen, *Theories for cold atomic collisions in light fields*, J. Phys. B **29**, 5981 (1996).
- [Tan08a] S. Tan, *Energetics of a strongly correlated Fermi gas*, Ann. Phys. (Amsterdam) **323**, 2952 (2008).
- [Tan08b] S. Tan, *Generalized virial theorem and pressure relation for a strongly correlated Fermi gas*, Ann. Phys. (Amsterdam) **323**, 2987 (2008).
- [Tan08c] S. Tan, *Large momentum part of a strongly correlated Fermi gas*, Ann. Phys. (Amsterdam) **323**, 2971 (2008).
- [Tay10] E. Taylor and M. Randeria, *Viscosity of strongly interacting quantum fluids: Spectral functions and sum rules*, Phys. Rev. A **81**, 053610 (2010).
- [The04] M. Theis, G. Thalhammer, K. Winkler, M. Hellwig, G. Ruff, R. Grimm, and J. H. Denschlag, *Tuning the scattering length with an optically induced Feshbach resonance*, Phys. Rev. Lett. **93**, 123001 (2004).

## REFERENCES

- [Tie93] E. Tiesinga, B. J. Verhaar, and H. T. C. Stoof, *Threshold and resonance phenomena in ultracold ground-state collisions*, Phys. Rev. A **47**, 4114 (1993).
- [Tru01] A. G. Truscott, K. E. Strecker, W. I. McAlexander, G. B. Partridge, and R. G. Hulet, *Observation of Fermi pressure in a gas of trapped atoms*, Science **291**, 2570 (2001).
- [Tur08] A. Turlapov, J. Kinast, B. Clancy, L. Luo, J. Joseph, and J. E. Thomas, *Is a gas of strongly interacting atomic fermions a nearly perfect fluid?*, J. Low Temp. Phys. **150**, 567 (2008).
- [Vee08] G. Veeravalli, E. Kuhnle, P. Dyke, and C. J. Vale, *Bragg spectroscopy of a strongly interacting Fermi gas*, Phys. Rev. Lett. **101**, 250403 (2008).
- [Vee09] G. Veeravalli, *Bragg spectroscopy of a strongly interacting Fermi gas*, Ph.D. thesis, Swinburne University of Technology (2009).
- [vH54] L. van Hove, *Correlations in space and time and Born approximation scattering in systems of interacting particles*, Phys. Rev. **95**, 249 (1954).
- [vH12] K. van Houcke, F. Werner, E. Kozik, N. Prokof'ev, B. Svistunov, M. J. H. Ku, A. T. Sommer, L. W. Cheuk, A. Schirotzek, and M. W. Zwierlein, *Feynman diagrams versus Fermi-gas Feynman emulator*, Nat. Phys. **8**, 366 (2012).
- [vH13] K. van Houcke, F. Werner, N. V. Prokof'ev, and B. V. Svistunov, *Bold diagrammatic Monte Carlo for the resonant Fermi gas*, arXiv:1305.3901 (2013).
- [Viv04] L. Viverit, S. Giorgini, L. Pitaevskii, and S. Stringari, *Momentum distribution of a trapped Fermi gas with large scattering length*, Phys. Rev. A **69**, 013607 (2004).
- [Vol90] D. Vollhardt and P. Wölfle, *The superfluid phases of helium 3*, Taylor & Francis, London, 1990.
- [Web03] T. Weber, J. Herbig, M. Mark, H.-C. Nägerl, and R. Grimm, *Bose-Einstein Condensation of Cesium*, Science **299**, 232 (2003).
- [Wei99] J. Weiner, V. S. Bagnato, S. Zilio, and P. S. Julienne, *Experiments and theory in cold and ultracold collisions*, Rev. Mod. Phys. **71**, 1 (1999).
- [Wer09] F. Werner, L. Tarruell, and Y. Castin, *Number of closed-channel molecules in the BEC-BCS crossover*, Eur. Phys. J. B **68**, 401 (2009).
- [Wer13] F. Werner, *Private communication* (2013).
- [Win79] D. J. Wineland and W. M. Itano, *Laser cooling of atoms*, Phys. Rev. A **20**, 1521 (1979).
- [Wla13] G. Wlazłowski, P. Magierski, J. E. Drut, A. Bulgac, and K. J. Roche, *Cooper*

- pairing above the critical temperature in a unitary Fermi gas*, Phys. Rev. Lett. **110**, 090401 (2013).
- [Wri07] M. J. Wright, S. Riedl, A. Altmeyer, C. Kohstall, E. R. S. Guajardo, J. H. Denschlag, and R. Grimm, *Finite-temperature collective dynamics of a Fermi gas in the BEC-BCS crossover*, Phys. Rev. Lett. **99**, 150403 (2007).
- [Yan62] C. N. Yang, *Concept of off-diagonal long-range order and the quantum phases of liquid He and of superconductors*, Rev. Mod. Phys. **34**, 694 (1962).
- [Zam00] F. Zambelli, L. Pitaevskii, D. M. Stamper-Kurn, and S. Stringari, *Dynamic structure factor and momentum distribution of a trapped Bose gas*, Phys. Rev. A **61**, 063608 (2000).
- [Zha09] S. Zhang and A. J. Leggett, *Universal properties of the ultracold Fermi gas*, Phys. Rev. A **79**, 023601 (2009).
- [Zou10] P. Zou, E. D. Kuhnle, C. J. Vale, and H. Hu, *Quantitative comparison between theoretical predictions and experimental results for Bragg spectroscopy of a strongly interacting Fermi superfluid*, Phys. Rev. A **82**, 061605 (2010).
- [Zür13] G. Zürn, T. Lompe, A. N. Wenz, S. Jochim, P. S. Julienne, and J. M. Hutson, *Precise characterization of  $^6\text{Li}$  Feshbach resonances using trap-sideband-resolved RF spectroscopy of weakly bound molecules*, Phys. Rev. Lett. **110**, 135301 (2013).
- [Zwe12] W. Zwerger, ed., *The BEC-BCS crossover and the unitary Fermi gas*, vol. 836, Springer-Verlag, Berlin, 2012.
- [Zwi03] M. W. Zwierlein, C. A. Stan, C. H. Schunck, S. M. F. Raupach, S. Gupta, Z. Hadzibabic, and W. Ketterle, *Observation of Bose-Einstein condensation of molecules*, Phys. Rev. Lett. **91**, 250401 (2003).
- [Zwi04] M. W. Zwierlein, C. A. Stan, C. H. Schunck, S. M. F. Raupach, A. J. Kerman, and W. Ketterle, *Condensation of pairs of fermionic atoms near a Feshbach resonance*, Phys. Rev. Lett. **92**, 120403 (2004).
- [Zwi05] M. W. Zwierlein, J. R. Abo-Shaeer, A. Schirotzek, C. H. Schunck, and W. Ketterle, *Vortices and superfluidity in a strongly interacting Fermi gas*, Nature **435**, 1047 (2005).



## Publications of the author

*Local observation of pair condensation in a Fermi gas at unitarity*

M. G. Lingham, K. Fenech, S. Hoinka, and C. J. Vale,  
Phys. Rev. Lett. **112**, 100404 (2014).

*Precise determination of the structure factor and contact in a unitary Fermi gas*

Sascha Hoinka, Marcus Lingham, Kristian Fenech, Hui Hu, Chris J. Vale, Joaquín E. Drut,  
and Stefano Gandolfi,  
Phys. Rev. Lett. **110**, 055305 (2013).

*Precision studies of Fermi gases using Bragg spectroscopy*

S. Hoinka, M. G. Lingham, K. Fenech, H. Hu, M. Delehay, P. Hannaford, and C. J. Vale,  
EPJ Web of Conferences **57**, 01003 (2013).

*Dynamic spin response of a strongly interacting Fermi gas*

S. Hoinka, M. Lingham, M. Delehay, and C. J. Vale,  
Phys. Rev. Lett. **109**, 050403 (2012).

*Temperature dependence of the contact in a unitary Fermi gas*

E. D. Kuhnle, S. Hoinka, P. Dyke, H. Hu, P. Hannaford, and C. J. Vale,  
Phys. Rev. Lett. **106**, 170402 (2011).

*Studies of the universal contact in a strongly interacting Fermi gas using Bragg spectroscopy*

E. D. Kuhnle, S. Hoinka, P. Dyke, P. Hannaford, and C. J. Vale,  
New J. Phys. **13**, 055010 (2011).

*Universal structure of a strongly interacting Fermi gas*

Eva Kuhnle, Paul Dyke, Sascha Hoinka, Michael Mark, Hui Hu, Xia-Ji Liu, Peter Drummond, Peter Hannaford, and Chris Vale,  
Journal of Physics: Conference Series **264**, 012013 (2011).

*Direct observation of shell structure in a quasi-2D Fermi gas*

P. Dyke, E. D. Kuhnle, S. Whitlock, H. Hu, M. Mark, S. Hoinka, M. Lingham, P. Hannaford, and C. J. Vale,  
Phys. Rev. Lett. **106**, 105304 (2011).

## Acknowledgements

I would like to express my sincere gratitude to everyone who has contributed to the success of this research work at the Centre for Quantum and Optical Science (CQOS), formerly known as the Centre for Atom Optics and Ultrafast Spectroscopy (CAOUS).

First and foremost I wish to thank Chris Vale and Peter Hannaford for their excellent supervision and unfailing scientific and general support. It has been a great pleasure for me to work in the Fermi gas lab. Chris' intuition in physics and approach to unravel the oddities in experimental data is very inspiring. Countless discussions with him about new ideas or just the usual lab stuff has taught me, so I hope, a good deal about the essentials in research. And I always most welcome Peter's advice given his wealth of experience.

I want to thank Peter Drummond and the members of his group for providing theoretical support for our Fermi gas experiments. In particular, the many discussions with Hui Hu and Xia-Ji Liu are highly appreciated. They were very helpful for me to gain a bit more insight into the tough field of strongly interacting many-body fermions.

A big thanks goes to the entire Fermi gas lab team for the joyful and productive time: Marcus Lingham, Kristian Fenech and Tyson Pepler, my former lab colleague Eva Kuhnle and former-and-now-current colleague Paul Dyke. All of them had and have been excelling themselves to make the  $^6\text{Li}$  experiment as successful as it is today. A special thanks to Marion Delehaye for her contributions to our group, and for showing me around Paris.

During my research I had the opportunity to collaborate with Joaquín Drut and Stefano Gandolfi from the theory group in Los Alamos. Thank you for your exciting contributions!

For making sure that university life runs smoothly, and for patiently explaining again and again which form to fill out for which purpose, a big thank you to Tatiana Tchernova. And of course to all other members of CQOS for the pleasant working environment.

I wish to thank my former colleagues for the memorable time during my stay at the University of Otago in New Zealand prior to moving to Australia. To Tzahi Grunzweig for endless discussions about how to take good pictures with a DSLR and our excursions around Dunedin, and to Ana Rakonjac for being a great lab mate back then and for keeping me up to date on the progress of the BEC experiment.

I want to take the opportunity to thank my teachers Peter Ziller for his ability to unveil the beauty of physics and Barbara Ganter for her candid encouragements. It is to a great deal because of them that I found my passion for physics and pursue a career in this field.

For staying in touch with me while being far away from home I want to thank my dear friends back in Germany: Gerhard, Bettina, Jochen, Martin Ressler and their families.

Finally, I would like to express my deepest gratitude to my family, to whom I dedicate this thesis: To my parents Rosemarie and Gerhard who have always been extremely supportive in my decisions. To my sister Jasmin, who is just awesome, and to Micha and Andy. To Sara my wonderful partner for her unconditional love and support. I cannot thank her enough for being part of my life. To Sara's parents Forough and Hossein and her lovely sister Sandra. Thank you all for your great support!

